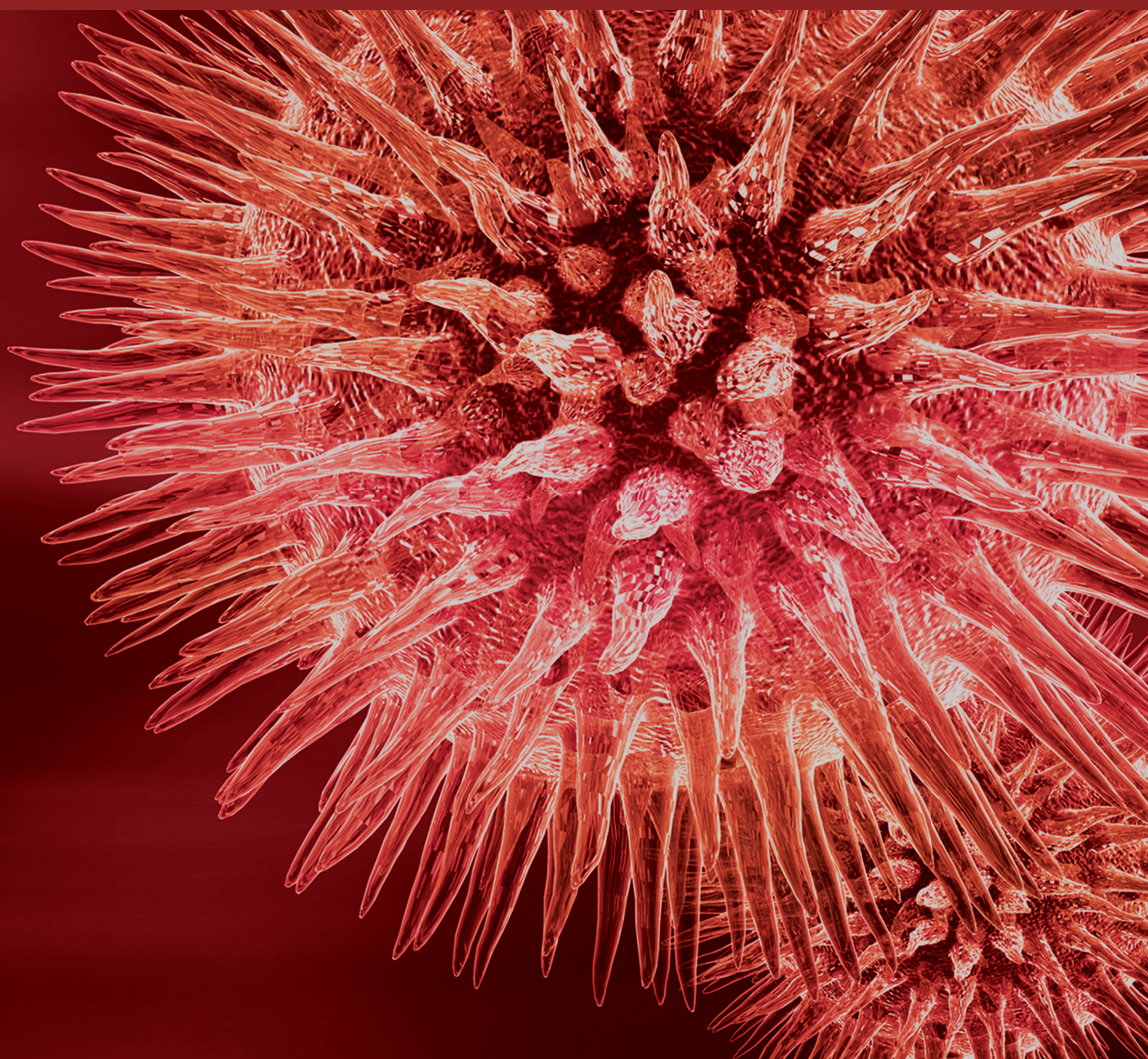# Translational and Emerging Clinical Applications of Medical Ultrasound

Lead Guest Editor: Yongjin Zhou
Guest Editors: Zhihong Huang and Weibao Qiu

Translational and Emerging Clinical Applications of Medical Ultrasound

Translational and Emerging Clinical Applications of Medical Ultrasound

Lead Guest Editor: Yongjin Zhou
Guest Editors: Zhihong Huang and Weibao Qiu

Contents

Editorial

Translational and Emerging Clinical Applications of Medical Ultrasound

Yongjin Zhou ORCID,[1] Weibao Qiu,[2] and Zhihong Huang[3]

[1]*Shenzhen University, Guangdong, China*
[2]*Shenzhen Institutes of Advanced Technology, Chinese Academy of Sciences, Shenzhen, China*
[3]*University of Dundee, Dundee, UK*

Correspondence should be addressed to Yongjin Zhou; yjzhou@szu.edu.cn

Wide and active usage of medical ultrasound can date back to the 1960s, yet it is not low-tech or obsolete. After decades of cooperative efforts from clinicians, researchers, and engineers, medical ultrasound is experiencing rapid developments in fields including optical-acoustic imaging, ultrasound elastography, advanced materials/technologies in ultrasonic transducers, ultrasound neuromodulation, ultrasound-guided interventions, and ultrafast ultrasound imaging. In this special issue on medical ultrasound, we have invited 13 papers that address translational and emerging clinical applications of medical ultrasound.

Specifically speaking, five papers in this special issue are more of novel engineering techniques in medical ultrasound. The only transducer paper titled "A High Frequency Geometric Focusing Transducer Based on 1-3 Piezocomposite for Intravascular Ultrasound Imaging" introduces a high frequency geometric focusing piezocomposite transducer, which can output high axial and lateral resolution and subsequently improve the imaging quality. Then two papers titled "A Modified 2D Multiresolution Hybrid Algorithm for Ultrasound Strain Imaging" and "A Normalized Shear Deformation Indicator for Ultrasound Strain Elastography in Breast Tissues: An *In Vivo* Feasibility Study" are both focused on ultrasound elastography. The first introduced a novel 2D multiresolution hybrid method for displacement estimation, to deal with the high compression scenario, while the second one proposed a normalized shear deformation indicator, which is proposed to boost breast lesion differentiation via a subsample speckle tracking algorithm. Another two

papers titled "Machine Learning in Ultrasound Computer-Aided Diagnostic Systems: A Survey" and "Differentiation of the Follicular Neoplasm on the Gray-Scale US by Image Selection Subsampling along with the Marginal Outline Using Convolutional Neural Network" both apply machine learning/artificial intelligence in medical ultrasound. The first one is a review paper while the second is more specifically dealing with thyroid cancer.

Eight more papers are included in this special issue, covering various new clinical applications of medical ultrasound. Yet, four of them are more converged to musculoskeletal studies, while the others are more diversified for applications. Specifically speaking, the first paper titled "Correlation between Pathological Characteristics and Young's Modulus Value of Spastic Gastrocnemius in a Spinal Cord Injury Rat Model" is about the pathological characteristics and muscle stiffness of in rats with spinal cord injury using shear wave sonoelastography technology. The second paper titled "Automatic Myotendinous Junction Tracking in Ultrasound Images with Phase-Based Segmentation" aims at automatic localizing and tracking of the myotendinous junction, which is crucial to quantify the interactive length changes of muscle and tendon for understanding the mechanics and pathological conditions of the muscle-tendon unit during motion muscle contraction. The phase congruency was employed to perceive and enhance ridge-like features in the detection of tendinous tissues with Radon transform. The third paper titled "Gear Shifting of Quadriceps during Isometric Knee Extension Disclosed Using Ultrasonography" is also about

image processing applications on muscle sonography, where it is found that quadriceps contract with a gear-shifting pattern under the protocol of isometric knee extension. The fourth and the last paper on muscle that is titled "Musculoskeletal Ultrasonography Assessment of Functional Magnetic Stimulation on the Effect of Glenohumeral Subluxation in Acute Poststroke Hemiplegic Patients" is more clinical oriented and presented the application of musculoskeletal ultrasonography on evaluation of the efficacy of functional magnetic stimulation (FMS) in the treatment of glenohumeral subluxation (GHS) in acute hemiplegic patients.

The last four papers are on prenatal diagnostics, cancellous bone, prostate cancer, and needle biopsy, respectively. The first one titled "Ultrasound in Prenatal Diagnostics and Its Impact on the Epidemiology of Spina Bifida in a National Cohort from Denmark with a Comparison to Sweden" is believed to cover the impact of prenatal ultrasound screening on the incidence of a major malformation on a national level. The second paper titled "Variability in Ultrasound Backscatter Induced by Trabecular Microstructure Deterioration in Cancellous Bone" investigates the relationship between ultrasonic backscatter and cancellous bone microstructure deterioration and indicated that the ultrasonic backscatter could be affected by cancellous bone microstructure deterioration direction. The third paper titled "The Use of Ultrasound Imaging in the External Beam Radiotherapy Workflow of Prostate Cancer Patients" provides an updated review on the status of prostate cancer ultrasound-guided external beam radiotherapy treatments. The last paper titled "Contrast-Enhanced Ultrasound Improves the Pathological Outcomes of US-Guided Core Needle Biopsy That Targets the Viable Area of Anterior Mediastinal Masses" presents results on ultrasound-guided core needle biopsy to harvest sufficient tissue with more cellularity that could be used for underlying ancillary molecular studies and improve the pathologic yield.

Yongjin Zhou
Weibao Qiu
Zhihong Huang

Clinical Study

Musculoskeletal Ultrasonography Assessment of Functional Magnetic Stimulation on the Effect of Glenohumeral Subluxation in Acute Poststroke Hemiplegic Patients

Chengyuan Yang,[1] Ping Chen,[2,3] Wenjie Du,[2] Qingmei Chen,[2] Huilin Yang [ID],[1] and Min Su [ID][2]

[1]*Department of Orthopedics, The First Affiliated Hospital of Soochow University, Suzhou, China*
[2]*Department of Physical Medicine & Rehabilitation, The First Affiliated Hospital of Soochow University, Suzhou, China*
[3]*Department of Physical Medicine & Rehabilitation, Wuxi Tongren International Rehabilitation Hospital, Wuxi, China*

Correspondence should be addressed to Huilin Yang; suzhouspine@163.com and Min Su; sumin@139.com

Chengyuan Yang and Ping Chen contributed equally to this work.

Background. Glenohumeral subluxation (GHS) is common in patients with acute hemiplegia caused by stroke. GHS and upper limb function are closely related. *Objective*. Using musculoskeletal ultrasonography (MSUS) to objectively evaluate the efficacy of functional magnetic stimulation (FMS) in the treatment of GHS in acute hemiplegic patients after stroke. *Methods*. The study used prospective case control study. Stroke patients with GHS were recruited and assigned to control group and FMS group. Control group received electrode stimulation at the supraspinatus and deltoid muscles of the hemiplegic side, while FMS group was stimulated at the same locations. Before and after treatment, the distances of the acromion-greater tuberosity (AGT), acromion-lesser tuberosity (ALT), acromiohumeral distance (AHD), supraspinatus thickness (SST), and deltoid muscle thickness (DMT) in patients' bilateral shoulder joint were measured by MSUS, respectively. Meanwhile, Fugl-Meyer Assessment (FMA) was used to evaluate the improvement of upper limb function. *Results*. 30 patients were recruited. After FMS treatment, there was a significant decrease in the difference value between ipsilateral side and contralateral side of AGT [$t = 8.595$, $P < 0.01$], ALT [$t = 11.435$, $P < 0.01$], AHD [$t = 8.375$, $P < 0.01$], SST [$t = 15.394$, $P < 0.01$], and DMT [$t = 24.935$, $P < 0.01$], and FMA score increased [$t = -13.315$, $P < 0.01$]. Compared with control group, FMS group decreased more significantly in the difference value between ipsilateral side and contralateral side of AGT [$t = 2.161$, $P < 0.05$], ALT [$t = 3.332$, $P < 0.01$], AHD [$t = 8.768$, $P < 0.01$], SST [$t = 6.244$, $P < 0.01$], and the DMT [$t = 3.238$, $P < 0.01$], and FMA score increased more significantly in FMS group [$t = 7.194$, $P < 0.01$]. *Conclusion*. The study preliminarily shows that the MSUS can objectively and dynamically evaluate the treatment effect of GHS in hemiplegic patients. Meanwhile, compared with control group, the FMS is more effective and has fewer side effects, and the long-term effect of FMS is worth further study. This trial is registered with ChiCTR1800015352.

1. Introduction

Glenohumeral subluxation (GHS) is common in patients with stroke and has an effect on the recovery of upper limb motor function [1–3]. The incidence of GHS has been reported from 17% to 84%; such a difference is mainly due to different measurement methods [4, 5]. Musculoskeletal ultrasonography (MSUS) plays an important role in the nervous system, orthopedics, and rehabilitation as an imaging model [5]. Its advantages include high accuracy, low cost, real-time imaging, contralateral immediate comparison, and radiation-free [6]. In recent years, it has replaced palpation and plain radiograph [7] and become the main means to assess shoulder abnormalities.

GHS can be assessed by measuring the distance between the acromion and the humerus. Kumar et al. have confirmed that MSUS measurement of acromion-greater tuberosity (AGT) distance is reliable and effective in assessing GHS in

hemiplegic patients [2, 8]. Park et al. found that increased acromion-lesser tuberosity (ALT) distance was highly correlated with GHS [4]. Previous studies have demonstrated the validity and reliability of using MSUS to measure acromio-humeral distance (AHD) for assessing GHS [9–13]. Nozoe et al. have elucidated that the recovery of limbs function can be assessed by measuring changes in the thickness of dominated muscles before and after the treatments [14, 15]. Some researchers have confirmed the validity and accuracy of using MSUS to measure muscle thickness [16–18]. Therefore, we measured the change of AGT, ALT, AHD, and the supraspinatus thickness (SST) and deltoid muscles thickness (DMT) to evaluate the improvement of GHS and upper limb function before and after the treatments.

Among reasons for GHS, the denervation of shoulder muscles caused by brain injury is the main cause and, under the action of gravity, the humeral head downward out of the glenoid fossa [19]. Without timely and effective treatment, GHS will get worse over time and eventually become irreversible [20]. Thus, the treatment of GHS is suggested as early and effectively as possible [21]. A number of methods have been reported for the treatment of GHS, such as shoulder slings, shoulder strapping, positioning, and electrical stimulation [7, 22, 23]. Many studies have shown that functional electrical stimulation (FES) is effective for the treatment of GHS in acute hemiplegic patients [21, 22, 24, 25]. According to electromyographic studies, the supraspinatus and deltoid muscles are the two key muscles that maintain the head of the humerus in the glenoid fossa, so they are the target spots of the FES treatment [21, 22]. However, FES has some adverse reactions, for example, inducing pain, dermatitis, and even skin burns. In addition, the role of FES is very weak for the deep muscles and nerves, because its stimulating scope is shallow [26, 27]. And FES is invalid in chronic hemiplegic patients. Therefore, it is necessary to find an alternative method.

Functional magnetic stimulation (FMS) has been used to stimulate the muscles and peripheral nerves to promote function recovery. A lot of researches have confirmed the effectiveness of FMS in the aspects of gastric emptying, neurogenic bowel, respiratory muscle conditioning, dysphagia, urinary incontinence, and so on [28–32]. Okudera et al. have confirmed that FMS can improve upper limb motor function in healthy adults [27]. So we hypothesize that FMS may reduce GHS and promote the recovery of upper limb function in hemiplegic patients.

The purpose of our study was to, using MSUS, objectively quantify the effect of FMS treatment on GHS in hemiplegic patients with acute stroke. Compared with electrical stimulation, maybe FMS can achieve the same or even better therapeutic effects with lesser side effects.

2. Methods

2.1. Participants.
Patients who were inpatient or outpatient at the Physical Medicine & Rehabilitation Department of the First Affiliated Hospital of Soochow University were screened from August 2016 to May 2017. The inclusion criteria were as follows: (1) stroke onset time of less than one month, (2) less than or equal to grade 3 of the upper limb muscle strength in hemiplegic side, (3) stable vital signs, (4) without aphasia or cognitive dysfunction, and (5) able to sit upright independently (or with one person's assistance). And exclusion criteria were as follows: (1) history of shoulder dysfunction, (2) combined with myogenic diseases or the peripheral nervous system disease, (3) combined with severe heart, liver, or kidney dysfunction, (4) pacemaker or metal implantation, and (5) combined with severe coagulation dysfunction.

The finger breadth palpation methods were used for GHS diagnosis; that is, AHD is 1/2 fingerbreadth or more. The degree of GHS is defined as follows: 0 degrees = no subluxation, 1 degree = 1/2 fingerbreadth gap, 2 degrees = 1 fingerbreadth gap, 3 degrees = 1 1/2 fingerbreadth gap, 4 degrees = 2 fingerbreadth gap, and 5 degree = 2 1/2 fingerbreadth gap [5, 33]. Patients with a dislocation of 2 degree or more were included in the study.

2.2. Study Design.
The study is a prospective case control study. The recruited patients were assigned to control group and FMS group. Basic information including age, gender, duration of stroke, affected side, and type of stroke were collected from patients and their guardians. The informed consent was signed by patients themselves, and to those who were unable to sign, their guardians were authorized to sign. The study was approved by the Ethics Committee of the First Affiliated Hospital of Soochow University. Screening of eligible patients and collection of basic information were done by one person in the research team.

2.3. Treatments.
Both groups received conventional rehabilitation including active and passive motion, weight bearing exercise, grasp, hold and release activities, and ADL activities, 45 minutes a day, consecutive 5 days a week, total for 4 weeks. The conventional rehabilitation of all patients was done by one therapist.

On the basis of conventional rehabilitation, control group received stimulation by electrode stimulation device (BA2008-III, Benao, China). Four electrodes were attached to the places of the supraspinatus and deltoid muscles of the hemiplegic side. And pulse of 200 and micro/s, duty cycle of 1 : 2, wave rise/wave drop of 2 s, and current of 50 mA were applied. The FMS group used magnetic stimulator (MagPro R30, Medtronic A/S, Denmark) connected with a 75 mm figure-of-eight water-cooled coil (MCF-B65) to stimulate the supraspinatus and deltoid muscles of the hemiplegic side. Frequency of 5 Hz with the stimulus intensity at 100% of the resting motion threshold (MT) was applied. Each site of each patient was stimulated for 20 minutes a day in both groups. The treatments were consecutively conducted 5 days a week for a total of 4 weeks. During the treatments, patients were seated upright independently (or with one person's assistance) in a chair with forearms placing on their laps. Two special therapists were, respectively, trained in one of the treatments, to complete the patients' treatment programs. In FMS group no patient withdrawn during the treatments, but in control group, there are 4 patients who failed to persist in electrical stimulation due to pain.
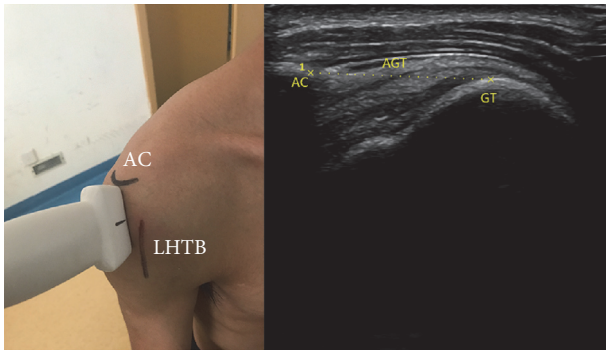
Figure 1: Anatomical structures: AC (acromion); LHTB (long head tendon of biceps); the position and orientation of transducer; and the ultrasound image: GT (greater tuberosity) and AGT (acromion-greater tuberosity).

Figure 2: Anatomical structures; the position and orientation of transducer; and the ultrasound image: LT (lesser tuberosity) and ALT (acromion-lesser tuberosity).

2.4. Clinical Evaluations. A portable diagnostic ultrasound system (M-Turbo, ICTx, SonoSite, America) connected with a 6–13 MHz linear array transducer was used to assess the changes of GHS, AGT, ALT, AHD, SST, and DMT, respectively, in the hemiplegic side and healthy side of shoulder before and after the treatments. At the same time, we used Fugl-Meyer Assessment (FMA) Scale to assess upper limb function of the hemiplegic side in acute poststroke patients.

In the process of measuring these parameters, each patient was placed in a standardized position [2]. Patients were seated upright in a chair with their forearms placed on their laps and the elbows unsupported. Each parameter was measured three times and took the average by the same specially trained sonographer before and after the treatments. The parameters were measured on the frozen image using the caliper on the screen. The depth of the ultrasonic transducer was set at 3.5 cm for each measurement.

AGT. Place transducer on the lateral edge of acromion and the lateral edge of long head tendon of biceps; scan the shoulder along longitudinal axis of humerus. When the lateral edge of acromion and the upper edge of greater tuberosity simultaneously appear in the screen freeze the image and measure AGT. We calculated the difference value of AGT between ipsilateral side and contralateral side and recorded (Figure 1).

ALT. Place transducer on the lateral edge of acromion and the medial edge of long head tendon of biceps; scan the shoulder along longitudinal axis of humerus. When the lateral edge of acromion and the upper edge of lesser tuberosity simultaneously appear in the screen freeze the image and measure ALT. We calculated the difference value of ALT between ipsilateral side and contralateral side and recorded (Figure 2).

AHD. Place transducer on the anterior edge of acromion in the coronal plane. When acromion and humerus head simultaneously appear in the screen freeze the image and measure the shortest distance between acromion and humerus. We calculated the difference value of AHD between ipsilateral side and contralateral side and recorded (Figure 3).
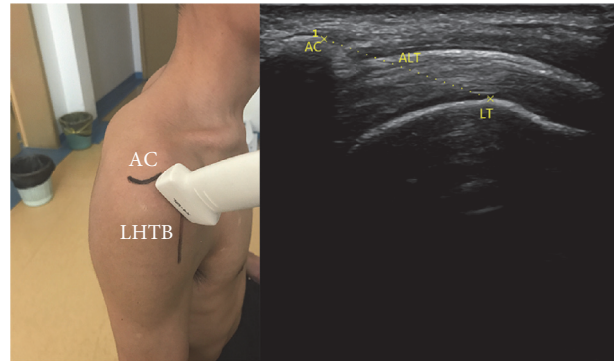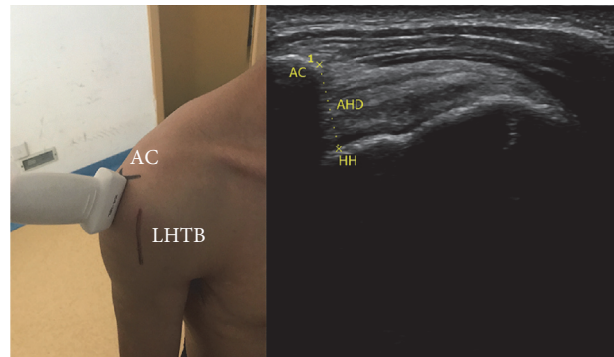
Figure 3: Anatomical structures; the position and orientation of transducer; and the ultrasound image: HH (humerus head) and AHD (acromiohumeral distance).

SST. Place transducer vertically at the midpoint of the mesoscapula. Move transducer in parallel until identifying the thickest cross section of supraspinatus, freeze the image, and measure the distance of the thickest part of supraspinatus. We calculated the difference value of SST between ipsilateral side and contralateral side and recorded (Figure 4).

DMT. We measure the thickness of the middle bundle representing DMT in our research. Place transducer vertically at the midpoint of the connection of acromion lateral edge and deltoid tuberosity. Move transducer in parallel until identifying the thickest cross section of deltoid muscle, freeze the image, and measure the distance of the thickest part of deltoid muscle. We calculated the difference value of DMT between ipsilateral side and contralateral side and recorded (Figure 5).

2.5. Statistical Analysis. Using SPSS19.0 software to do data statistics and analysis, the data were expressed as mean value ± standard deviation. *T* test was used to compare data and $P < 0.05$ was statistically significant.

TABLE 1: Patients' demographics.

Type of variable	Control group	FMS group	P value
Age (years)	67.20 ± 10.72	63.67 ± 15.09	0.146
Gender			0.418
Male	11.00	12.00	
Female	4.00	3.00	
Duration of stroke (days)	15.47 ± 2.72	13.87 ± 3.36	0.359
Affected side			0.224
Left	6.00	7.00	
Right	9.00	8.00	
Type of stroke			1.000
Hemorrhage	5.00	6.00	
Ischemia	10.00	9.00	
Degree of GHS			0.603
2 degrees	2.00	3.00	
3 degrees	11.00	11.00	
4 degrees	2.00	1.00	
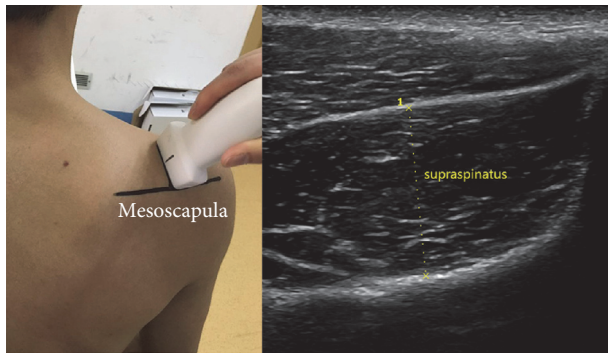
FIGURE 4: Anatomical structures: mesoscapula; the position and orientation of transducer; and the ultrasound image: SST (supraspinatus thickness).
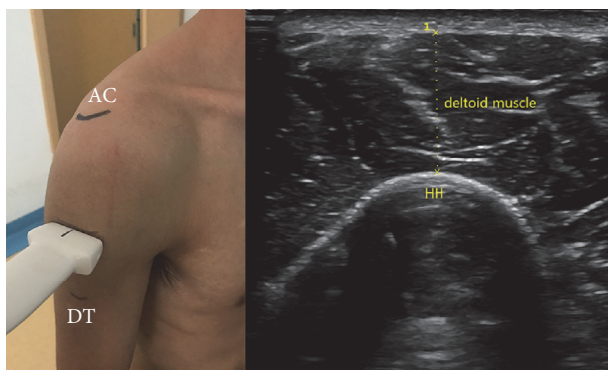
FIGURE 5: Anatomical structures: DT (deltoid tuberosity); the position and orientation of transducer; and the ultrasound image: DMT (deltoid muscle thickness).

3. Results

3.1. General Information.
A total of 34 patients were evaluated and treated, and 4 patients who failed to persist in electrical stimulation due to pain were excluded. Finally, 30 patients (23 men, 7 women) with a mean age of 65 years (range from 38 to 84 years) were eligible for the study. The mean duration after onset was 15 days (range from 7 to 21 days). A summary of the demographic characteristics of the patients is shown in Table 1. There is no difference between the two groups with regard to age, gender, duration of stroke, affected side, type of stroke, and degree of GHS ($P > 0.05$).

3.2. The Results of MSUS Measurement.
Before treatments, there were no differences statistical significance ($P > 0.05$) in the value of AGT, ALT, AHD, SST, and DMT between control group and FMS group. After treatments, there was a significantly decrease in the difference value between ipsilateral side and contralateral side of AGT, ALT, AHD, SST, and DMT in both groups (Tables 2 and 3 and Figures 6(a)–6(d)). After 4-week treatment, compared with control group, FMS group decreased more significantly in the difference value between ipsilateral side and contralateral side of AGT, ALT, AHD, SST, and DMT (Table 4 and Figures 6(a)–6(d)).

3.3. The Results of FMA Assessments.
We used the Simplified Fugl-Meyer Motor Function Assessment Scale to assess the hemiplegic upper limb function before and after the treatments, respectively. Before treatments, there was no differences statistical significance ($P > 0.05$) in FMA score between control group and FMS group. After the treatments, FMA score increased in both control group and FMS group (Tables 2 and 3 and Figure 6(f)). After 4-week treatment, compared with control group, FMA increased more significantly in FMS group (Table 4 and Figure 6(f)).

4. Discussion

In our study, the results of MSUS preliminary proved in FMS group, the gap between the ipsilateral side and contralateral side of AGT, ALT, and AHD significantly decreased, and SST and DMT obviously increased. At the same time, FMA

TABLE 2: Comparison between posttreatment and pretreatment in control group.

	Pretreatment	Posttreatment	t value	P value
Difference value of AGT	15.05 ± 2.41	8.70 ± 1.43	8.766	0.000
Difference value of ALT	12.15 ± 2.55	6.22 ± 1.17	8.170	0.000
Difference value of AHD	3.11 ± 0.37	2.20 ± 0.15	8.762	0.000
Difference value of SST	6.61 ± 0.63	3.37 ± 0.64	14.010	0.000
Difference value of DMT	8.76 ± 0.39	5.00 ± 0.58	20.986	0.000
FMA score	20.00 ± 2.17	25.40 ± 2.69	6.045	0.000

TABLE 3: Comparison between posttreatment and pretreatment in FMS group.

	Pretreatment	Posttreatment	t value	P value
Difference value of AGT	13.75 ± 3.44	5.70 ± 1.15	8.595	0.000
Difference value of ALT	12.30 ± 2.64	3.93 ± 1.03	11.435	0.000
Difference value of AHD	2.78 ± 0.72	0.90 ± 0.49	8.375	0.000
Difference value of SST	6.54 ± 0.73	2.44 ± 0.73	15.394	0.000
Difference value of DMT	8.45 ± 0.36	4.13 ± 0.57	24.935	0.000
FMA score	22.00 ± 2.54	33.47 ± 2.17	13.315	0.000

TABLE 4: Comparison between FMS group and control group.

	FES	FMS	t value	P value
Difference value of AGT	6.35 ± 1.49	8.05 ± 2.66	2.161	0.039
Difference value of ALT	5.93 ± 2.21	8.37 ± 1.78	3.332	0.002
Difference value of AHD	0.91 ± 0.31	1.88 ± 0.29	8.768	0.000
Difference value of SST	3.24 ± 0.44	4.09 ± 0.29	6.244	0.000
Difference value of DMT	3.76 ± 0.60	4.32 ± 0.29	3.238	0.003
FMA score	5.40 ± 1.80	11.47 ± 2.72	7.194	0.000

substantially improved in the hemiplegic upper limb. These results show that the short time FMS treatment (4 weeks) can obviously improve GHS of the hemiplegic patients with acute stroke and promote the functional recovery of the patients' paralyzed upper limbs. The changes in several indicators by MSUS measurement, such as AGT, ALT, and AHD, as well as SST and DMT, are consistent with the function of paralyzed upper limb. These coincide with our previous assumptions.

Researches have shown that, in acute poststroke hemiplegic patients, paralysis muscles around the shoulder cannot resist the gravity of upper limb and gradually result in GHS [20, 23]. Soft tissue around the shoulder such as muscles, ligaments, and capsule is going to be overstretched, leading to the dysfunction of upper limb [2]. Therefore, our goal is to use simple and effective rehabilitation therapies to restore the activity of the paralyzed muscles, enhance its ability to resist gravity, reduce GHS, and ultimately achieve the recovery of upper limb function.

Electrical stimulation and magnetic stimulation techniques have been widely used in the field of rehabilitation. Our study results are consistent with previous studies that FES is effective on reducing GHS and promoting the recovery of upper limb function in acute hemiplegic patients [21, 22, 24, 25]. After electrical stimulation treatment in control group, the AGT and AHD of hemiplegic side were remarkably decreased and FMA increased obviously in our study. However, the mechanism has not yet been fully

understood. Perhaps by the stimulation of the muscle fibers and peripheral nerves, the muscles contraction increases and the coordination between agonist and antagonist muscles improve and eventually achieve functional and beneficial movement [20, 25], although the FES is effective on GHS in acute (<6 months) hemiplegic patients but is not valid in chronic (>6 months) ones [26, 34]. Perhaps the soft tissue around the shoulder overstretched for too long time, and the muscles atrophy is very serious, so it induced the GHS quite difficult to recover. Several studies have also found that the GHS can hardly get further improved after 6 weeks of FES treatment [22, 35]. And follow-up studies have also shown that there is no a positive long-term effect after FES [21, 34]. Because of the limitations and complications in the skin and other aspects, its clinical application is limited.

While repeat transcranial magnetic stimulation (rTMS) is a kind of brain stimulation techniques which has become promising for the recovery of limbs function in hemiplegic patients [36], it stimulates the cerebral cortex to regulate the excitability of the central nervous system [37, 38]. Sohn et al. have confirmed that rTMS has a certain effect on the recovery of upper limb function in hemiplegic patients [36, 37]; however, there have some side effects to be reported, such as induced epilepsy, tinnitus, and headache [39]. In order to avoid these complications, more and more researchers have studied its use in stimulating peripheral nerves and muscles, and it is called functional magnetic stimulation (FMS).

(a)

(b)

(c)

(d)

(e)

(f)
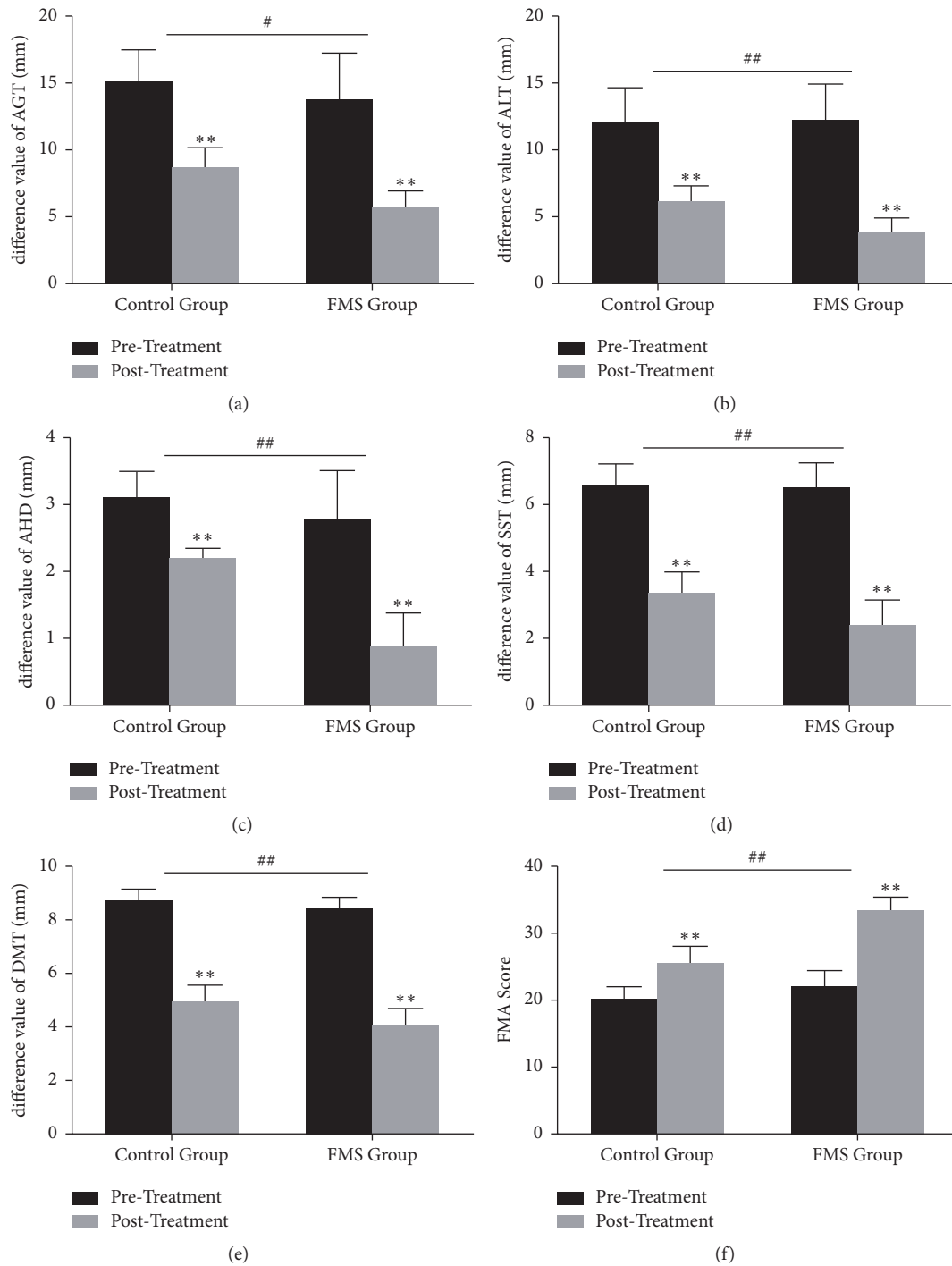
FIGURE 6: Comparison within control group and FMS group, respectively, and comparison between control group and FMS group. Comparison within groups: $^{*}P < 0.05$ and $^{**}P < 0.01$. Comparison between groups: $^{#}P < 0.05$ and $^{##}P < 0.01$.

The FMS has been applied in some aspects of rehabilitation and achieved some curative effects [28–32]. Since the FMS does not paste on the skin directly, it seldom causes skin problems. However, the applications of FMS in reducing GHS and promoting the recovery of upper limb function have not yet been reported. Inspired by previous researches, our team speculated that the FMS used in local hemiplegic shoulders

maybe produce the same or even better effect as electrical stimulation. And this was confirmed in our study. After the treatments for 4 weeks, compared with control group the AGT and AHD in the hemiplegic side were significantly reduced and the FMA scores increased in FMS groups. These trends are more pronounced and coincide with our previous assumptions. Since the magnetic field of FMS does

not attenuate through the skin, it can act on deeper muscles and peripheral nerves than electrical stimulation [40]. And it is painless and causes no damage to the skin. In our study, we found that pain and dermatitis appeared more or less in the stimulation area of patients in control group, which did not appear in FMS group.

Our previous studies have shown that MSUS measurement of AGT is reliable and valid in assessing GHS in patients with hemiplegia, which is in agreement with many other researchers [41]. A lot of researches are done by Bladel et al., and they found that it was valid and reliable to evaluate the therapeutic effect of GHS by measuring changes in AHD [9, 10]. McCreesh et al. have confirmed that MSUS is a reliable and sensitive tool to identify AHD change [10–13]. From our study it can be found the AGT, ALT, and AHD consistently reduced after the treatments, especially in FMS group. The results not only show that FMS is more effective than electrical stimulation, but also further illustrate the correlation between ALT and GHS. The greater tuberosity and the lesser tuberosity are adjacent, and the brachial biceps long head tendon goes through the gap between them. It is not difficult to measure ALT with MSUS. So, in addition to measuring AGT and AHD with MSUS, we also assess GHS by measuring ALT. It may be used as a supplement or even become a more sensitive indicator. Although it has been reported that ALT was highly correlated with GHS [4], its validity and reliability of assessing GHS by ALT alone need our further specialized researches to verify.

Muscle thickness affects muscle function and further affects limb function [15]. CT and MRI have been the standard methods for accurate measurement of muscle thickness [6, 18]. But it has shortcomings of radio action, cost too much, inconvenience, and so on. Nozoe et al. have pointed out that MSUS measurement of muscle thickness is an effective way to assess the limb function of hemiplegic patients [14]. Therefore, we considered whether it was possible to evaluate the effect of FMS on the recovery of upper limb function in GHS patients by measuring the SST and DMT by MSUS. Dupont et al. have verified that MSUS can be used to measure SST and DMT [18]. Our study shows that the thickness of the two muscles significantly increase in both groups, especially in FMS group. By stimulating the muscles and peripheral nerves, FMS and FES can, on the one hand, maintain muscles and peripheral nerves excitability and reduce disuse atrophy and, on the other hand, feedback regulate and remodel the corresponding functional areas of the cerebral cortex to restore muscle contraction. The FMS can act on deeper muscles and peripheral nerves than electrical stimulation, making FMS a better treatment.

In addition, previous studies have shown that the change of muscle thickness could be used as an indicator of muscle atrophy [18]. However, in this study the change of muscle thickness around the shoulder in hemiplegic patients is not only caused by muscle atrophy alone. Because the recruited patients were all at the early stage of hemiplegia, muscle atrophy was not obvious in a short time. We have reasons to believe that the more important reason is the paralyzed muscles around the shoulder which are elongated due to the separation of bone structure in GHS, making the muscles

become thinner. Therefore, from this point of view, SST and DMT can also predict the extent of the GHS. Furth more, in both control group and FMS group, the FMA scores of upper limb function in hemiplegic side were significantly improved after the treatments. Compared with control group, it improved more significantly in FMS group. This is consistent with the results of MSUS, thus further verifying the relationship between each indicators of MSUS measurement and limb function. These indicators may be used as an objective basis for monitoring the degree of GHS.

Recently, some researchers have studied the synergistic effects of different therapies on limb function recovery after stroke and found that they were more pronounced than single treatment [7, 42]. So the next step, we will study the synergistic effects of FMS and some other therapies on GHS and upper limb function in hemiplegic patients.

Of course, our research also has many limitations. First, the sample size is not large enough. Second, the further follow-up is needed to assess the long-term effect. Third, whether FMS is effective in GHS in patients with chronic hemiplegia is not validated. These questions deserved further exploration and study.

5. Conclusion

The FMS is effective in the treatment of GHS in patients with early hemiplegia, and compared with the electrical stimulation, it is more effective. The mechanism, effectiveness in chronic hemiplegia, long-term efficacy, and so on of the new way, FMS, need further exploration. Meanwhile, the changes in several indicators by MSUS measurement, such as AGT, ALT, and AHD, as well as SST and DMT, are consistent with the function of paralyzed upper limb. These indicators may be used as an objective basis for monitoring the degree of GHS. Furthermore, the validity and reliability of ALT, SST, and DMT in assessing GHS and upper limb functional require further proof.

Conflicts of Interest

The authors declare that there are no conflicts of interest regarding the publication of this article.

Acknowledgments

References

[1] R. Y. Wang, Y. R. Yang, M. W. Tsai, W. T. Wang, and R. C. Chan, "Effects of functional electric stimulation on upper limb motor function and shoulder range of motion in hemiplegic patients," *American Journal of Physical Medicine & Rehabilitation*, vol. 81, no. 4, pp. 283–290, 2002.

[2] P. Kumar, R. Cruziah, M. Bradley, S. Gray, and A. Swinkels, "Intra-rater and inter-rater reliability of ultrasonographic measurements of acromiongreater tuberosity distance in patients with post-stroke hemiplegia," *Topics in Stroke Rehabilitation*, vol. 23, no. 3, pp. 147–153, 2016.

[3] M. Paci, L. Nannetti, P. Taiti, M. Baccini, and L. Rinaldi, "Shoulder subluxation after stroke: relationships with pain and motor recovery.," *Physiotherapy research international : the journal for researchers and clinicians in physical therapy*, vol. 12, no. 2, pp. 95–104, 2007.

[4] G.-Y. Park, J.-M. Kim, S.-I. Sohn, I.-H. Shin, and M. Y. Lee, "Ultrasonographic measurement of shoulder subluxation in patients with post-stroke hemiplegia," *Journal of Rehabilitation Medicine*, vol. 39, no. 7, pp. 526–530, 2007.

[5] P. Kumar, M. Mardon, M. Bradley, S. Gray, and A. Swinkels, "Assessment of glenohumeral subluxation in poststroke hemiplegia: Comparison between ultrasound and fingerbreadth palpation methods," *Physical Therapy in Sport*, vol. 94, no. 11, pp. 1622–1631, 2014.

[6] C. K. English, K. A. Thoirs, L. Fisher, H. McLennan, and J. Bernhardt, "Ultrasound is a reliable measure of muscle thickness in acute stroke patients, for some, but not all anatomical sites: a study of the intra-rater reliability of muscle thickness measures in acute stroke patients," *Ultrasound in Medicine & Biology*, vol. 38, no. 3, pp. 368–376, 2012.

[7] M. Paci, L. Nannetti, and L. A. Rinaldi, "Glenohumeral subluxation in hemiplegia: An overview," *Journal of Rehabilitation Research and Development* , vol. 42, no. 4, pp. 557–568, 2005.

[8] P. Kumar, M. Bradley, S. Gray, and A. Swinkels, "Reliability and validity of ultrasonographic measurements of acromiongreater tuberosity distance in poststroke hemiplegia," *Archives of Physical Medicine and Rehabilitation*, vol. 92, no. 5, pp. 731–736, 2011.

[9] A. Van Bladel, G. Lambrecht, K. M. Oostra, G. Vanderstraeten, and D. Cambier, "Arandomized controlled trial on the immediate and long-term effects of arm slings on shoulder subluxation in stroke patients," *European Journal of Physical and Rehabilitation Medicine*, vol. 53, no. 3, pp. 400–409, 2017.

[10] K. M. McCreesh, J. M. Crotty, and J. S. Lewis, "Acromiohumeral distance measurement in rotator cuff tendinopathy: Is there a reliable, clinically applicable method? A systematic review," *British Journal of Sports Medicine*, vol. 49, no. 5, pp. 298–305, 2015.

[11] Y.-S. Lin, M. L. Boninger, K. A. Day, and A. M. Koontz, "Ultrasonographic measurement of the acromiohumeral distance in spinal cord injury: Reliability and effects of shoulder positioning," *The Journal of Spinal Cord Medicine*, vol. 38, no. 6, pp. 700–708, 2015.

[12] F. Desmeules, L. Minville, B. Riederer, C. H. Côté, and P. Frémont, "Acromio-humeral distance variation measured by ultrasonography and its association with the outcome of rehabilitation for shoulder impingement syndrome," *Clinical Journal of Sport Medicine*, vol. 14, no. 4, pp. 197–205, 2004.

[13] N. Kalra, A. L. Seitz, N. D. Boardman, and L. A. Michener, "Effect of posture on acromiohumeral distance with arm elevation in subjects with and without rotator cuff disease using ultrasonography," *Journal of Orthopaedic & Sports Physical Therapy*, vol. 40, no. 10, pp. 633–640, 2010.

[14] M. Nozoe, H. Kubo, A. Furuichi et al., "Validity of Quadriceps Muscle Thickness Measurement in Patients with Subacute

Stroke during Hospitalization for Assessment of Muscle Wasting and Physical Function," *Journal of Stroke and Cerebrovascular Diseases*, vol. 26, no. 2, pp. 438–441, 2017.

[15] P. Liu, Y. Wang, H. Hu, Y. Mao, D. Huang, and L. Li, "Change of muscle architecture following body weight support treadmill training for persons after subacute stroke: Evidence from Ultrasonography," *BioMed Research International*, vol. 2014, Article ID 270676, 2014.

[16] A. Schneebeli, M. Egloff, A. Giampietro, R. Clijsen, and M. Barbero, "Rehabilitative ultrasound imaging of the supraspinatus muscle: Intra- and interrater reliability of thickness and cross-sectional area," *Journal of Bodywork and Movement Therapies*, vol. 18, no. 2, pp. 266–272, 2014.

[17] T. I. Yi, I. S. Han, J. S. Kim, J. R. Jin, and J. S. Han, "Reliability of the supraspinatus muscle thickness measurement by ultrasonography," *Annals of Rehabilitation Medicine*, vol. 36, no. 4, pp. 488–495, 2012.

[18] A.-C. Dupont, E. E. Sauerbrei, P. V. Fenton, P. C. Shragge, G. E. Loeb, and F. J. R. Richmond, "Real-time sonography to estimate muscle thickness: Comparison with MRI and CT," *Journal of Clinical Ultrasound*, vol. 29, no. 4, pp. 230–236, 2001.

[19] S.-W. Huang, S.-Y. Liu, H.-W. Tang, T.-S. Wei, W.-T. Wang, and C.-P. Yang, "Relati onship between severity of shoulder subluxati on and soft-tissue injury in hemiplegic stroke patients," *Journal of Rehabilitation Medicine*, vol. 44, no. 9, pp. 733–739, 2012.

[20] J. B. Manigandan, G. S. Ganesh, M. Pattnaik, and P. Mohanty, "Effect of electrical stimulation to long head of biceps in reducing gleno humeral subluxation after stroke," *NeuroRehabilitation*, vol. 34, no. 2, pp. 245–252, 2014.

[21] L. Ada and A. Foongchomcheay, "Efficacy of electrical stimulation in preventing or reducing subluxation of the shoulder after stroke: a meta-analysis," *Australian Journal of Physiotherapy*, vol. 48, no. 4, pp. 257–267, 2002.

[22] D. Stolzenberg, G. Siu, and E. Cruz, "Current and future interventions for glenohumeral subluxation in hemiplegia secondary to stroke," *Topics in Stroke Rehabilitation*, vol. 19, no. 5, pp. 444–456, 2012.

[23] S. Chatterjee, K. A. Hayner, N. Arumugam et al., "The california tri-pull taping method in the treatment of shoulder subluxation after stroke: A randomized clinical trial," *North American Journal of Medical Sciences*, vol. 8, no. 4, pp. 175–182, 2016.

[24] P. Gu and J. J. Ran, "Electrical Stimulation for Hemiplegic Shoulder Function: A Systematic Review and Meta-Analysis of 15 Randomized Controlled Trials," *Archives of Physical Medicine and Rehabilitation*, vol. 97, no. 9, pp. 1588–1594, 2016.

[25] E. Koyuncu, G. F. Nakipoğlu-Yüzer, A. Doğan, and N. Özgirgin, "The effectiveness of functional electrical stimulation for the treatment of shoulder subluxation and shoulder pain in hemiplegic patients: a randomized controlled trial," *Disability and Rehabilitation*, vol. 32, no. 7, pp. 560–566, 2010.

[26] J. Lee, L. L. Baker, R. E. Johnson, and J. K. Tilson, "Effectiveness of neuromuscular electrical stimulation for management of shoulder subluxation post-stroke: a systematic review with meta-analysis," *Clinical Rehabilitation*, vol. 31, no. 11, pp. 1431–1444, 2017.

[27] Y. Okudera, T. Matsunaga, M. Sato et al., "The impact of high-frequency magnetic stimulation of peripheral nerves: Muscle hardness, venous blood flow, and motor function of upper extremity in healthy subjects," *Biomedical Research (Japan)*, vol. 36, no. 2, pp. 81–87, 2015.

[28] V. W.-H. Lin, K. H. Kim, I. Hsiao, and W. Brown, "Functional magnetic stimulation facilitates gastric emptying," *Archives of Physical Medicine and Rehabilitation*, vol. 83, no. 6, pp. 806–810, 2002.

[29] P.-Y. Tsai, C.-P. Wang, F.-Y. Chiu, Y.-A. Tsai, Y.-C. Chang, and T.-Y. Chuang, "Efficacy of functional magnetic stimulation in neurogenic bowel dysfunction after spinal cord injury," *Journal of Rehabilitation Medicine*, vol. 41, no. 1, pp. 41–47, 2009.

[30] V. W. Lin, I. N. Hsiao, E. Zhu, and I. Perkash, "Functional magnetic stimulation for conditioning of expiratory muscles in patients with spinal cord injury," *Archives of Physical Medicine and Rehabilitation*, vol. 82, no. 2, pp. 162–166, 2001.

[31] R. Momosaki, M. Abo, S. Watanabe, W. Kakuda, N. Yamada, and K. Mochio, "Functional magnetic stimulation using a parabolic coil for dysphagia after stroke," *Neuromodulation: Technology at the Neural Interface*, vol. 17, no. 7, pp. 637–641, 2014.

[32] D. D. Chandi, P. M. Groenendijk, and P. L. Venema, "Functional extracorporeal magnetic stimulation as a treatment for female urinary incontinence: 'The chair,'" *BJU International*, vol. 93, no. 4, pp. 539–542, 2004.

[33] J. Hall, B. Dudgeon, and M. Guthrie, "Validity of clinical measures of shoulder subluxation in adults with poststroke hemiplegia.," *The American journal of occupational therapy. : official publication of the American Occupational Therapy Association*, vol. 49, no. 6, pp. 526–533, 1995.

[34] A. K. Vafadar, J. N. Côté, and P. S. Archambault, "Effectiveness of functional electrical stimulation in improving clinical outcomes in the upper arm following stroke: a systematic review and meta-analysis," *BioMed Research International*, vol. 2015, Article ID 729768, 14 pages, 2015.

[35] R.-Y. Wang, R.-C. Chan, and M.-W. Tsai, "Functional electrical stimulation on chronic and acute hemiplegic shoulder subluxation," *American Journal of Physical Medicine & Rehabilitation*, vol. 79, no. 4, pp. 385–390, 2000.

[36] Y. H. Sohn and M. Hallett, "Motor evoked potentials," *Physical Medicine and Rehabilitation Clinics of North America*, vol. 15, no. 1, pp. 117–131, 2004.

[37] S.-I. Izumi, T. Kondo, and K. Shindo, "Transcranial magnetic stimulation synchronized with maximal movement effort of the hemiplegic hand after stroke: A double-blinded controlled pilot study," *Journal of Rehabilitation Medicine*, vol. 40, no. 1, pp. 49–54, 2008.

[38] Y. Inukai, K. Saito, R. Sasaki et al., "Comparison of three non-invasive transcranial electrical stimulation methods for increasing cortical excitability," *Frontiers in Human Neuroscience*, vol. 10, no. 2016, article no. 668, 2016.

[39] E. M. Khedr, M. A. Ahmed, N. Fathy, and J. C. Rothwell, "Therapeutic trial of repetitive transcranial magnetic stimulation after acute ischemic stroke," *Neurology*, vol. 65, no. 3, pp. 466–468, 2005.

[40] C. Paquette and A. Thiel, "Rehabilitation interventions for chronic motor deficits with repetitive transcranial magnetic stimulation," *Journal of Neurosurgical Sciences*, vol. 56, no. 4, pp. 299–306, 2012.

[41] J. Feng, W. Yang, M. Su, C. Liu, and D. Zhang, "Reliability and validity of ultrasound measurement of acromion-greater tuberosity distance for assessing glenohumeral subluxation in hemiplegic patients," *Chinese Journal of Rehabilitation Medicine*, vol. 30, no. 1, pp. 38–40, 2015.

[42] S. Etoh, T. Noma, Y. Takiyoshi et al., "Effects of repetitive facilitative exercise with neuromuscular electrical stimulation, vibratory stimulation and repetitive transcranial magnetic stimulation of the hemiplegic hand in chronic stroke patients," *International Journal of Neuroscience*, vol. 126, no. 11, pp. 1007–1012, 2016.

Research Article

Automatic Myotendinous Junction Tracking in Ultrasound Images with Phase-Based Segmentation

Guang-Quan Zhou [iD],[1,2] Yi Zhang,[1,2] Ruo-Li Wang [iD],[3,4] Ping Zhou,[1,2] Yong-Ping Zheng,[5] Olga Tarassova,[6] Anton Arndt,[6,7] and Qiang Chen[1,2]

[1]*School of Biological Science and Medical Engineering, Southeast University, Nanjing, China*
[2]*National Demonstration Center for Experimental Biomedical Engineering Education, Southeast University, Nanjing, China*
[3]*Department of Women's and Children's Health, Karolinska Institute, Stockholm, Sweden*
[4]*BioMEX Center and Department of Mechanics, Royal Institute of Technology, Stockholm, Sweden*
[5]*Department of Biomedical Engineering, The Hong Kong Polytechnic University, Hung Hom, Hong Kong*
[6]*The Swedish School of Sport and Health Sciences, Stockholm, Sweden*
[7]*Department of Clinical Intervention and Technology, Karolinska Institute, Stockholm, Sweden*

Correspondence should be addressed to Guang-Quan Zhou; guangquan.zhou@seu.edu.cn

Displacement of the myotendinous junction (MTJ) obtained by ultrasound imaging is crucial to quantify the interactive length changes of muscles and tendons for understanding the mechanics and pathological conditions of the muscle-tendon unit during motion. However, the lack of a reliable automatic measurement method restricts its application in human motion analysis. This paper presents an automated measurement of MTJ displacement using prior knowledge on tendinous tissues and MTJ, precluding the influence of nontendinous components on the estimation of MTJ displacement. It is based on the perception of tendinous features from musculoskeletal ultrasound images using Radon transform and thresholding methods, with information about the symmetric measures obtained from phase congruency. The displacement of MTJ is achieved by tracking manually marked points on tendinous tissues with the Lucas-Kanade optical flow algorithm applied over the segmented MTJ region. The performance of this method was evaluated on ultrasound images of the gastrocnemius obtained from 10 healthy subjects (26.0 ± 2.9 years of age). Waveform similarity between the manual and automatic measurements was assessed by calculating the overall similarity with the coefficient of multiple correlation (CMC). *In vivo* experiments demonstrated that MTJ tracking with the proposed method (CMC = 0.97 ± 0.02) was more consistent with the manual measurements than existing optical flow tracking methods (CMC = 0.79 ± 0.11). This study demonstrated that the proposed method was robust to the interference of nontendinous components, resulting in a more reliable measurement of MTJ displacement, which may facilitate further research and applications related to the architectural change of muscles and tendons.

1. Introduction

The muscle-tendon unit (MTU) that consists of muscles and tendons plays an important role in force generation and energetics during human movement [1]. The force generated by the contractions of muscle fascicles is transmitted to bones via tendons to control and regulate body motions. The interaction between muscles and tendons takes place in response to the effective utilization of the force and tendon elasticity in mechanical demands during specific movement tasks [2, 3]. Nevertheless, the MTU length calculated using body segment length and joint kinematics is not a good predictor of the muscle and tendon and their interaction [4]. Recently, ultrasound imaging has become a prospective field of research in comprehending the adaptation of muscles and tendons as well as evaluating their function and pathological status by monitoring the architectural changes among muscles and tendons. Sonography has been used to
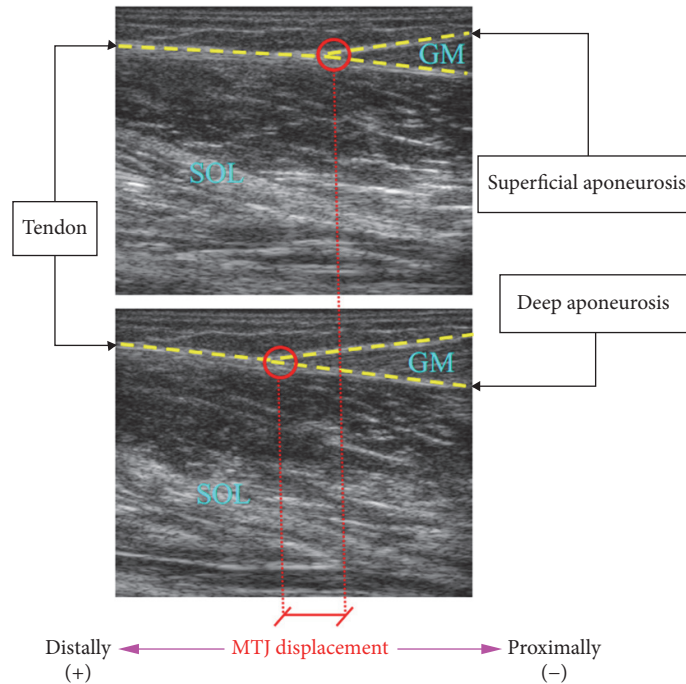
FIGURE 1: Typical ultrasound image of GM MTJ.

examine muscle-tendon architectural changes in response to motion [2, 3, 5, 6], contraction [7, 8], aging [9, 10], pathologies [11], and physical training [12, 13]. Ultrasound imaging shows great potential in both diagnosis and rehabilitation by assessing geometrical changes in muscles and tendons *in vivo* [14–16].

Changes in tendon length and fascicle length are the most often used structural parameters in ultrasound images to quantify the modulation of interaction between muscles and tendons and estimate the mechanical properties of tendons. Using ultrasound to measure dynamic tendon length changes, the Achilles tendon has been figured out to recoil and stretch in the stance period of walking and take up most of the MTU lengthening [17]. On the other hand, during early stance of walking, the muscle fascicle operates over the highest force region of the force-length curve with the advantage of relatively greater force generation [3, 5]. The rapid shortening of tendon structures has also been found at the first stage of plantar flexion in the fast stretch-shortening cycle exercise, enabling the working muscles to develop more tension in relation to their force-velocity properties [18]. Previous research has pointed out that the mechanical energy generated by the muscle was mainly stored in the tendinous tissue which acts as a spring to store and return elastic energy during human motion [2, 3, 5]. These morphometric parameters are therefore of great importance to understanding muscle-tendon architecture as well as its mechanism. However, the analysis used in most of the previously reported studies relied on the manual method that is time-consuming and potentially prone to human error. Although some automatic approaches have been developed to estimate the muscle fascicle changes [19–29], there is still a lack of methods

for measuring the change of tendinous tissues. Moreover, the muscular and tendinous structures are often obscured by speckle noise, making it difficult to measure these morphometric parameters accurately.

Tendon length changes *in vivo* are usually estimated by tracking the displacement of the myotendinous junction (MTJ) (Figure 1), where the muscle is connected to the tendon, that is, the distal end of the muscle [30]. Motion between sequential images could be applied to quantify the MTJ displacement with the optical flow technique that has been widely used in fields of computer vision such as object segmentation and motion detection [31]. Spatial cross-correlation has been employed to track the tendinous displacement [32]. However, the regions of interest used in the cross-correlation method may undergo irregular changes in appearance or intensity, causing the failure to track the displacement continuously. On the other hand, under the assumption of homogeneous affine transformations in the region of interest, the global affine transformation parameters can be obtained to derive the changes of muscular and tendinous structures using the Lucas-Kanade optical flow algorithm [31]. The changes in fascicle length have been identified with the Lucas-Kanade method by regarding the selected fascicle region as a whole patch [20–22]. Recently, the Lucas-Kanade method was adopted to track the aponeurosis of the rectus femoris for estimating the muscle thickness [24]. Nonetheless, as shown in Figure 1, the motion of different tissues connected in MTJ, including gastrocnemius medialis (GM), gastrocnemius lateralis (GL), soleus (SOL), and Achilles tendon, might violate the assumption of homogeneous affine transformations, resulting in an inaccurate estimation of MTJ displacement when using the Lucas-Kanade method.

In this study, a novel automatic method is presented to estimate the MTJ displacement in consecutive ultrasound images of GM by utilizing prior knowledge on the tendinous tissues and MTJ. Based on the observation that the tendinous tissues are distributed as continuous hyperechoic bands in ultrasound images [33], the symmetric features were first measured with the phase congruency, enabling the segmentation of the effective MTJ region using the localized Radon transform (LRT) and thresholding techniques. Under the assumption of homogeneous affine transformations, the global affine transform parameters are then calculated over the effective MTJ region, addressing the limitations of currently available Lucas-Kanade approaches. The displacement of MTJ was finally estimated by tracking the connection of muscle to Achilles tendon, that is, the intersection of two aponeuroses. The automatic method for MTJ displacement estimation is described in detail in the following section and was tested with real ultrasound image sequences of the GM MTJ during the passive rotation of the ankle joint.

2. Materials and Methods

The flowchart of our proposed method for measuring MTJ is illustrated in Figure 2. The musculoskeletal ultrasound image was first preprocessed with the phase congruency [34] to measure the symmetric features, contributing to the detection of tendinous tissues. As shown in Figure 1, the MTJ was defined as the intersection of two aponeuroses, that is, near the distal end of the muscle. The region containing the visible MTJ structure can then be separated from preprocessed data using the prior anatomical information of MTJ to localize the Radon transform [25] and Otsu method [35]. Under the assumptions of homogeneous affine transformations, the global affine transform parameters were calculated between successive images from the Lucas-Kanade method [36] over the segmented region, termed the effective MTJ region. After the displacements of the predefined points on the tendon and aponeuroses were calculated from the global affine transform parameters, the MTJ was finally determined according to the intersection of two aponeuroses (Figure 1). In cases where the MTJ moved out of the view of ROI, the MTJ was estimated by linearly extrapolating both paths of aponeuroses in ROI.

2.1. Preprocessing with Phase Congruency. In musculoskeletal ultrasound images, the tendinous tissues, including aponeuroses and tendons, depict ridge-like hyperechoic bands [33], representing an axis of local symmetry (Figure 1). Phase congruency is a well-known illumination and contrast invariant measure of symmetric features based on the local-energy model [37]. Under the observation that the Fourier series at points of symmetry is either at minima or maxima of their cycle, symmetry in image intensity gives rise to special patterns using phase congruency [34]. After the publication of the phase congruency method [34], it has been investigated extensively to construct descriptors for the ridge-like bone surface localization [38, 39] and cardiac border enhancement [40] in ultrasound images. In this work, we proposed to use the phase congruency as a sensitive feature for the measure of ridge-like tendinous tissues in ultrasound images.
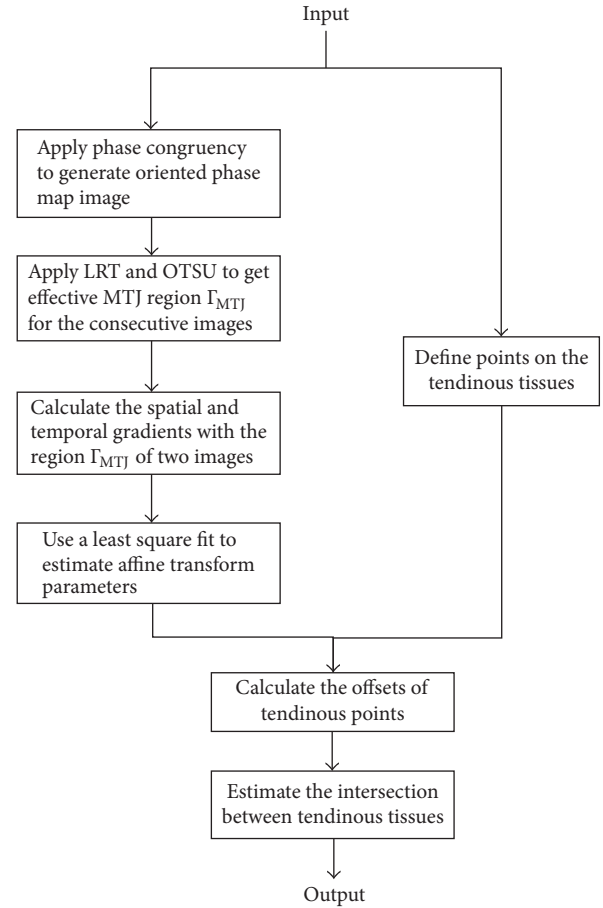
FIGURE 2: Flowchart of the proposed tracking algorithm.

The current state-of-the-art method is to use a quadrature pair of filters to calculate the phase congruency [41–44]. The log Gabor wavelet is the most common choice of quadrature filters because it can achieve good feature localization and noise compensation [41]. By taking the responses of log Gabor wavelet over multiple scales and orientations, the symmetric phase measure at each point in the image can be calculated according to the following equation [41]:

$$PS(x, y) = \frac{\sum_r \sum_s W(x, y) \lfloor A_{rs}(x, y) [|e_{rs}(x, y)| - |o_{rs}(x, y)|] - T_r \rfloor}{\sum_r \sum_s A_{rs}(x, y) + \varepsilon},$$

where $e_{rs}(x, y)$ is the even symmetric part and $o_{rs}(x, y)$ is the odd symmetric part of the filter at orientation r and scale s. At a point of symmetry, the absolute value of e_{rs} will approach 1 and the absolute value of o_{rs} will be near 0, and vice versa. ε is a small real number to avoid division by zero, T_r is the noise threshold, and $\lfloor \cdot \rfloor$ denotes the operation $\lfloor z \rfloor = z$ if $z > 0$; otherwise, $\lfloor z \rfloor = 0$. $W(x, y)$ is the weighting factor based on frequency spread that reduces phase congruency at locations with a narrow frequency component. $A_{rs}(x, y)$ is the amplitude of wavelet response with a given scale and orientation at point (x, y).

(a)   (b)
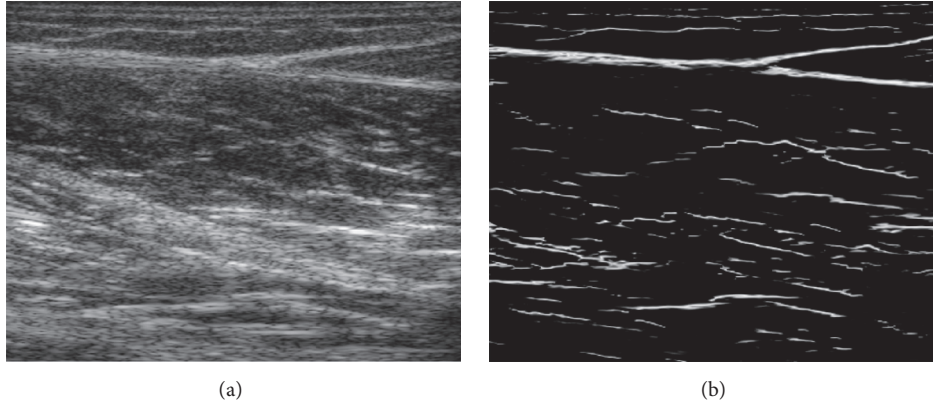
FIGURE 3: An example showing the oriented phase map: (a) original musculoskeletal ultrasound image contains MTJ; (b) the oriented phase map of the image.

Moreover, the angular range of tendinous tissues has been reported to be about $-10°$ to $10°$ [45]. Phase congruency with specified central orientation, called oriented phase congruency, could be used to further measure ridge-like tendinous tissues, which is calculated as follows:

$$
\text{PS}_{\text{Orient}}(x, y) = \frac{\sum_s W(x, y) \left\lfloor A_{r_{\text{spec}}s}(x, y) \left[\left| e_{r_{\text{spec}}s}(x, y) \right| - \left| o_{r_{\text{spec}}s}(x, y) \right| \right] - T_{r_{\text{spec}}} \right\rfloor}{\sum_s A_{r_{\text{spec}}}(x, y) + \varepsilon},
\tag{2}
$$

where r_{spec} is the specified orientation range covering $[-10°, 10°]$. The parameters used in computing phase congruency, such as $W(x, y)$, $A_{rs}(x, y)$, and T_r, were based on those presented in [41]. Figures 3(a) and 3(b) show an example of an original image and its corresponding oriented phase map, respectively.

2.2. Effective MTJ Region Segmentation. Both aponeuroses and fascicles are distributed as line-like structures in musculoskeletal ultrasound images [19, 20]. The oriented phase congruency thus enhanced the ridge-like features of not only tendinous tissue but also part of fascicles in GM and SOL muscles. Nevertheless, the tendinous tissues are represented as continuous hyperechoic bands in the ultrasound image [33], while the fascicles are usually not uniformly distributed as line-like structures [46], which makes the depiction of tendinous tissue quite distinct from that of fascicles in the oriented phase map (Figure 3(b)). Moreover, the MTJ is the site of connection between tendons and muscles. As illustrated in Figure 1, the MTJ was observed to be the intersection of two aponeuroses, being used to localize the Radon transform over the oriented phase map. Motivated by the aforementioned observation on tendinous tissues and MTJ, the LRT was employed to roughly determine the MTJ region from the oriented phase map [25]. The LRT over Euclidean space is defined as

$$
R_{\text{LOC}}(\theta, \rho) = \int_{x_{\min}}^{x_{\max}} \int_{y_{\min}}^{y_{\max}} \text{PS}_{\text{Orient}}(x, y)
$$
$$
\cdot \delta(\rho - x\cos\theta - y\sin\theta)\, dx\, dy,
\tag{3}
$$

where $\text{PS}_{\text{Orient}}(x, y)$ is the oriented phase map at position (x, y) and δ is the Dirac delta function. ρ and θ denote the distance from the center of the image to the straight line and the angle between the x-axis and the line perpendicular to the straight line, respectively. Only the points $x_{\min} \leq x \leq x_{\max}$ and $y_{\min} \leq y \leq y_{\max}$ in image space and $\theta_{\min} \leq \theta \leq \theta_{\max}$ in Radon space are calculated in LRT. The same revoting strategy [47] was conducted to extract line features one by one and remove all phase maps close to the detected lines. According to a previous study [45], the angular range was set to be $-10° \leq \theta \leq 10°$ for performing LRT. In addition, based on the prior knowledge on MTJ structure (Figure 1), the position and orientation of the detected lines were used to determine the proper range of the locations and the orientation where other aponeuroses and tendons are supposed to be found. Moreover, the average diameter of tendinous tissues of GM tendon and aponeuroses has been reported to be about 2.5 mm [48]. The removing width was then empirically determined to be 2 mm in this study.

After localization and revoting procedure, lines intersecting near MTJ could be identified from the Radon space obtained from the oriented phase map. Figure 4(a) presents an example of LRT on the oriented phase map as shown in Figure 3(b). However, a common limitation of phase-based techniques is the poor localization on blurred features, affecting the localization of detected lines and MTJ. As illustrated in Figure 4(b), the intersection determined by the lines from the phase map was not well located at the actual MTJ. Therefore, in this study, instead of directly locating the MTJ by LRT, the effective region of MTJ was segmented

(a)

(b)

(c)

(d)
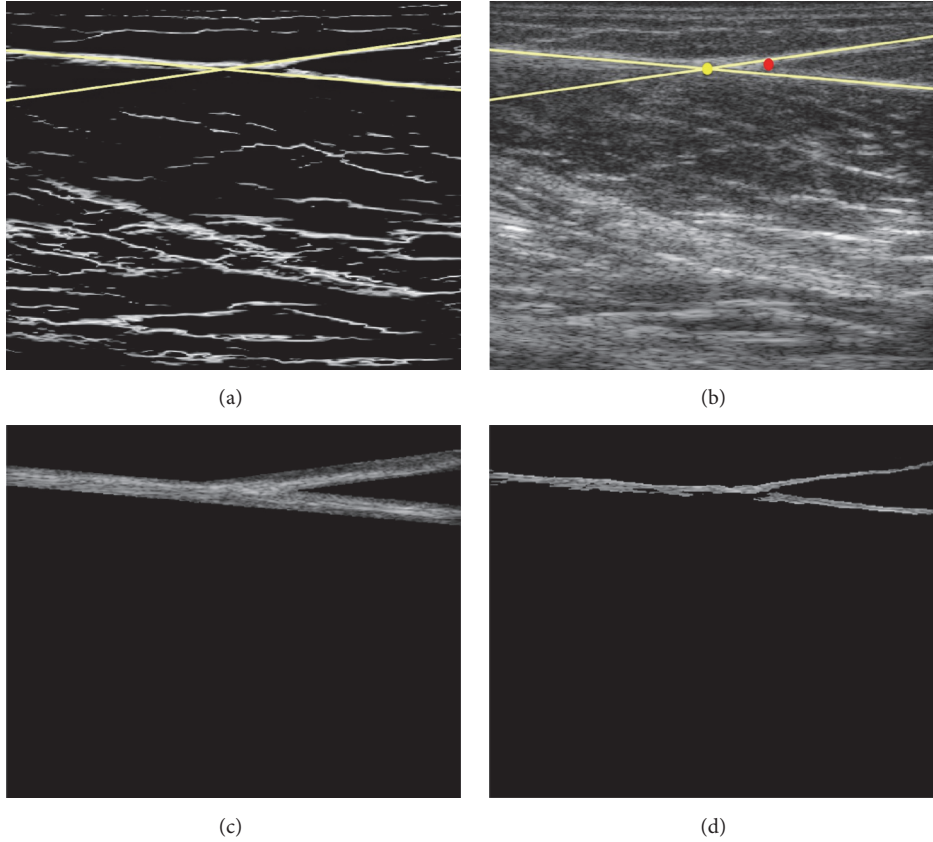
FIGURE 4: An example of effective MTJ region segmentation from the image shown in Figure 3: (a) the LRT results on the oriented phase map shown in Figure 3(b); (b) the intersection of LRT on the image shown in Figure 3(a); (c) the result of the tendinous region; (d) the effective MTJ region segmentation result. Yellow lines are the lines detected by LRT on the oriented phase map. The circles of yellow and red represent the MTJ identified by the intersections of LRT and manual measurements, respectively.

from the oriented phase map by combining the LRT and Otsu method, enabling the reliable tracking of MTJ with the Lucas-Kanade method. Based on previously reported average diameters of tendinous tissues [48], a distance threshold T_d to the detected lines was firstly set to 2.5 mm to exclude the nontendinous region and determine the tendinous region Γ_T. The Otsu method was then employed to calculate the global threshold T_{Otsu} on the oriented phase map over the tendinous region Γ_T. The final effective MTJ region $\Gamma_{MTJ}(x, y)$ was derived as follows:

$$\Gamma_{MTJ}(x, y)$$
$$= \begin{cases} 1, & (x, y) \in \Gamma_T, \ PS_{Orient}(x, y) \le T_{Otsu} \\ 0, & \text{otherwise.} \end{cases} \quad (4)$$

Figures 4(c) and 4(d) illustrate the tendinous region Γ_T and the corresponding effective MTJ region Γ_{MTJ} on the ultrasound image (Figure 3(a)), respectively.

2.3. Automatic MTJ Tracking Using Lucas-Kanade Optical Flow Method. The MTJ could be identified as the intersection of two aponeuroses near the distal end of the muscle (Figure 1). The points on the aponeuroses were used to

determine the position of MTJ, which could be manually defined by identifying the aponeuroses skeleton in the first frame, and then tracked using the Lucas-Kanade method for the subsequent images. Let $I(x, y)$ denote the gray-level value at pixel (x, y); the image constraint equation between time t and $t + \Delta t$ is

$$I(x, y, t) = I(x + \Delta x, y + \Delta y, t + \Delta t). \quad (5)$$

With the assumption of small movement between adjacent images, the image constraint at $I(x, y, t)$ with Taylor series can be expressed as

$$I(x + \Delta x, y + \Delta y, t + \Delta t)$$
$$= I(x, y, t) + \frac{\partial I}{\partial x}\Delta x + \frac{\partial I}{\partial y}\Delta y + \frac{\partial I}{\partial t}\Delta t + \varepsilon, \quad (6)$$

where ε is the higher-order term. It follows that

$$\frac{\partial I}{\partial x}\Delta x + \frac{\partial I}{\partial y}\Delta y + \frac{\partial I}{\partial t}\Delta t = I_x V_x + I_y V_y + I_t V_t = 0, \quad (7)$$

where V_x and V_y are the x and y components of the velocity or optical flow of $I(x, y, t)$ and I_x, I_y, and I_t are the derivatives of I with respect to x, y, and t. In Lucas-Kanade optical

flow method [21], the image velocity is defined by six affine transform parameters:

$$\left(V_x, V_y\right) = \begin{bmatrix} x & y & 1 \end{bmatrix} \times \begin{bmatrix} d+s1 & s2+r \\ s2-r & d-s1 \\ vxt & vyt \end{bmatrix}, \qquad (8)$$

where the affine flow parameters vxt and vyt are the optical flow at the origin in the x- and y-directions, respectively, d is the rate of dilation, r is the rate of rotation, $s1$ is the shear along the main image axis, and $s2$ is the shear along the diagonal axis.

Under the assumption of homogeneous affine transformations, the six affine transform parameters could be determined from a least square fit using the given spatial and temporal gradients over the whole region between adjacent images [31]. The x and y grids along with the spatial and temporal gradients were resampled (every 3 pixels) to reduce the computation cost in the least square fit [21]. However, the visible nontendinous components and speckle noise in the selected region were not taken into account in this resampling method, which may violate the hypothesis of homogeneous affine transformations in the whole selected region, resulting in the inaccurate estimation of the global affine flow parameters. Therefore, we proposed a simple and automatic method to calculate the affine transform parameters over the effective MTJ region Γ_{MTJ} obtained using the prior information of MTJ, to achieve both reliable calculation and economical computation cost for the least square fitting process. Only the spatial and temporal gradients in Γ_{MTJ} were applied to calculate the affine transform parameters via a least square fit, which could reduce the error caused by the nontendinous components and speckle noises. The predefined points were then applied to determine the position of aponeuroses by calculating their displacements from the affine transform parameters. Finally, according to the definition of MTJ (Figure 1), the intersection of two aponeuroses was calculated to measure the displacement of MTJ. In cases where the MTJ moved out of the view of ROI, the MTJ was estimated by linearly extrapolating both paths of aponeuroses in ROI.

2.4. Experiment. Ten healthy adults (age: 26.0 ± 2.9 years; 6 males and 4 females; weight: 70.4 ± 11.5 kg; body mass index: 22.8 ± 2.2 kg/m^2) with no history of musculoskeletal injury were recruited in an experimental study to demonstrate the feasibility of the proposed method. This study was approved by the Regional Ethics Committee, Stockholm, Sweden. All subjects signed informed consent before participation in the study.

The subjects were instructed to lie in a prone position with their knee flexed at 20° and their foot fixated to a footplate connected to a dynamometer (Figure 5). Only the right foot was tested in the convenience of the experimental setup. Shoulders, hips, legs, and the tested foot were adequately fixated, while paying special attention to securely strapping the foot to the footplate. The ankle joint was carefully aligned with the dynamometer axis of rotation using a laser device. In the initial position, the footplate was positioned
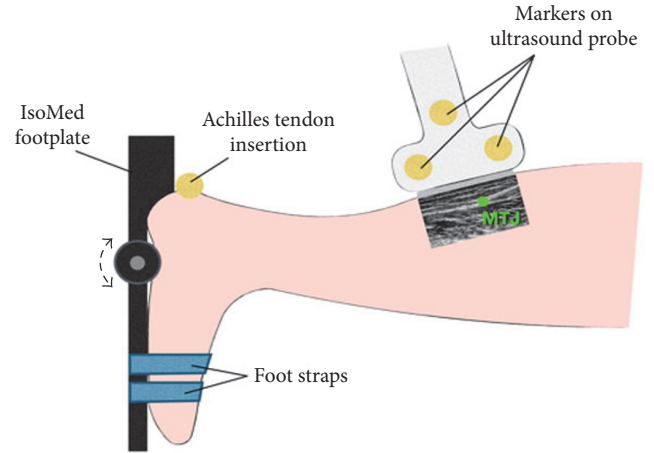
FIGURE 5: Illustration of the experimental setup during the passive rotation test of the ankle joint.

perpendicularly to the tibia of the subject, which was defined as 0° ankle rotation. In the following, plantar flexion of the foot will be expressed in negative (−) angles, and dorsiflexion of the foot will be expressed in positive (+) angles. The ankle of all participants was passively rotated between −20° and 10° several times to familiarize the movement. For the actual experiment, the ankle was rotated five consecutive times at a constant velocity of 5°/s within the range of motion (ROM). All participants were instructed to stay relaxed during the passive rotation experiments.

During the passive ankle rotation, the excursion of the MTJ of GM was recorded using an ultrasonography system, while the corresponding ankle angle was recorded by the dynamometer at 5 kHz. The position of MTJ at 0° ankle rotation was selected for the initial position to calculate MTJ displacement. The positive (+) displacement expresses that the MTJ moves distally during dorsiflexion and vice versa (Figure 1). An ultrasound scanner (Vivid Q, GE Healthcare, Milwaukee, WI, USA) with a linear transducer was utilized to capture MTJ excursion, which was sampled at 40 frames/s with an image resolution of 0.11 mm/pixel. The ultrasound transducer probe with a frequency of 3.5–10 MHz and a field of view of 53 mm was optimally positioned parallel to the tendon in the sagittal plane, and the ultrasound image plane was therefore aligned with the longitudinal axis of the tendon. The MTJ displacement was automatically estimated with our proposed approach developed using Visual Studio (Microsoft Corporation, Washington, USA) in the present study. To evaluate the performance of our proposed method, the traditional Lucas-Kanade method [36] was also applied to track the MTJ displacement. Moreover, manual measurements of MTJ displacement were performed three times in each image by a single expert who was experienced in ultrasound imaging of muscles and blind to the automatic measurement results. According to the definition of MTJ displacement, line segments representing tendinous tissues were manually drawn in each ultrasound image to obtain an estimate of MTJ and its movement. The mean value of the manual displacement measurements was used to compare with the automatic measurements.

TABLE 1: The CMC values between the manual and automatic methods for the measurement of MTJ displacement.

Subject	CMC value between manual measurement and automatic measurement by the Lucas-Kanade method	CMC value between manual measurement and automatic measurement by the proposed method
A	0.88	0.97
B	0.91	0.99
C	0.57	0.94
D	0.72	0.96
E	0.73	0.97
F	0.95	0.96
G	0.87	0.97
H	0.79	0.99
I	0.70	0.94
J	0.78	0.97

FIGURE 6: The MTJ displacement obtained with the proposed method, the traditional Lucas-Kanade approach, the LRT with phase map, and the manual method during the passive rotation test of the ankle joint for subject H.

2.5. Data Analysis. Values were reported as mean ($\pm$SD) for all subjects unless otherwise stated. The manual measurements of MTJ displacement were used as a reference for comparison with the automatic measurements. The intraclass correlation coefficient (ICC) was used to test the intraobserver repeatability of manual measurement [49]. The waveform similarity between the manual and automatic measurements was assessed by calculating the overall similarity with the coefficient of multiple correlations (CMC) [50, 51], with a range of 0 and 1. More similar waveforms have higher CMC values, whereas highly dissimilar waveforms can result in a CMC near 0. Student's paired t-test was applied to test the difference between the CMC values of the proposed method and the Lucas-Kanade method. Moreover, Bland and Altman's method of differences [52] was applied to test the agreement between the manual and automatic measurements. In addition, polynomial regression analysis was applied to describe the association between the ankle angle rotation and MTJ displacement. Pearson's product-moment correlation (r) was calculated for the regression analysis. The level of significance was accepted at $p < 0.05$.

3. Results

As shown in Table 1, the CMC value (0.79 ± 0.11) determined by the Lucas-Kanade method ranged from 0.57 and 0.95, while the proposed method had a CMC value (0.97 ± 0.02) ranging from 0.94 to 0.99. The difference in the CMC value between these two approaches was significant ($p < 0.05$). Figure 6 shows a typical example of MTJ displacement measured with the proposed approach, for which Lucas-Kanade method failed to track the excursion in MTJ. Since the tendinous structures in the image were not taken into account, such errors could not be avoided when the whole selected region was used to estimate the affine transform parameters (Figures 7(b) and 7(c)). On the other hand, our proposed tracking approach only used the effective tendinous region to calculate the affine transform parameters, thus
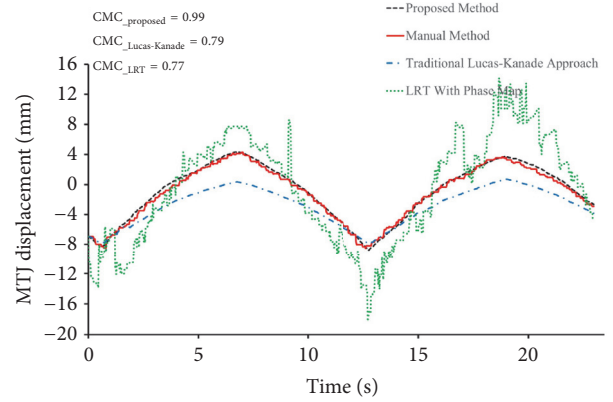
avoiding the influence of nontendinous components and speckle noise (Figures 8(b) and 8(c)). The CMC values also suggested that the automatic measurement with the proposed method was more consistent with the manual measurement compared with the Lucas-Kanade method. Figure 6 also illustrated that the poor localization of phase-based techniques degraded the accuracy of MTJ localization when directly using LRT to detect the MTJ on the oriented phase map. As shown in Figure 9, the Bland-Altman plot between the manual and automatic measurements indicated a low mean difference (0.2 mm) and the symmetrically distributed difference around mean difference was within limits (± 1.96 SD = 0.65 mm), suggesting a good agreement between the measurements obtained by our proposed method and the manual method. Additionally, the intraobserver tests of manual MTJ measurements showed good repeatability, with the ICC being 0.91 ± 0.03 ($p < 0.001$). These results support the conclusion that the proposed approach was reliable for the estimation of MTJ displacement.

The MTJ displacement shifted nonlinearly with the change of ankle angle during passive ankle rotation. Figure 10 demonstrates the changes MTJ with the change in ankle angle for one typical subject. When the ankle angle was rotated from $-19.26 \pm 0.06°$ to $11.64 \pm 0.05°$, the MTJ measured with the proposed method was moved from -8.22 ± 2.03 mm (proximally) to 3.97 ± 1.27 mm (distally) and was correlated with the ankle joint angle ($r = 0.99 \pm 0.01$, all $p < 0.001$). Also, the average computation time for the estimation of fascicle length with the proposed method in the ~400 × 400 pixel region was about 2~3 sec for each frame using a computer with an Intel Core 7 2.60 GHz processor and 4 GB of memory.

4. Discussion

We have developed a novel automatic method to track the MTJ displacement in sequential musculoskeletal ultrasound images. The combination of phase congruency with LRT made it feasible to segment the effective MTJ region from

(a)

(b)

(c)
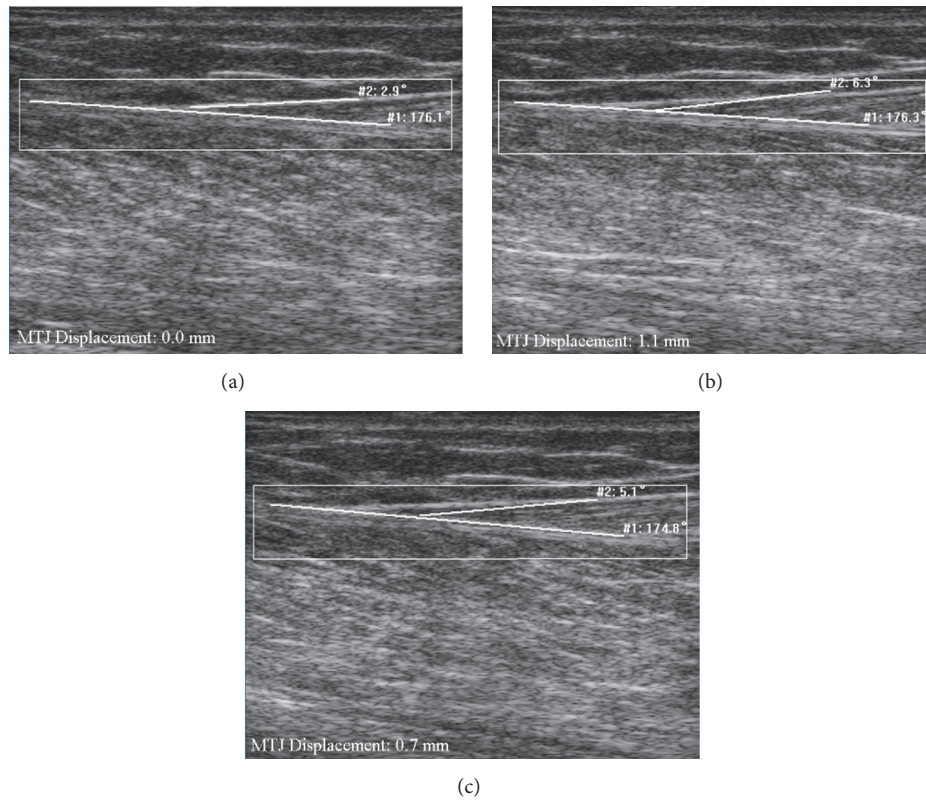
FIGURE 7: The measurement of MTJ displacement for subject H using traditional Lucas-Kanade approach: (a) the MTJ in the 1st frame manually defined with the lines (white line); (b) the measurement of MTJ at frame 275; (c) the measurement of MTJ at frame 764.

(a)

(b)

(c)
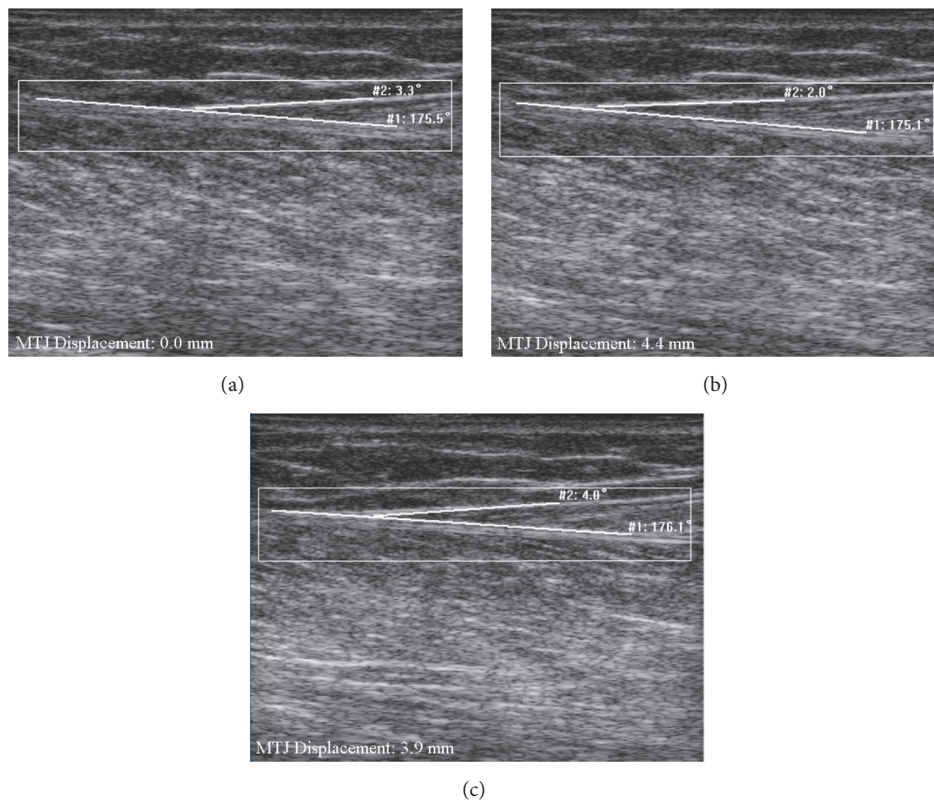
FIGURE 8: The measurement of MTJ displacement for subject H using the proposed approach: (a) the MTJ in the 1st frame manually defined with the lines (white line); (b) the measurement of MTJ at frame 275; (c) the measurement of MTJ at frame 764.
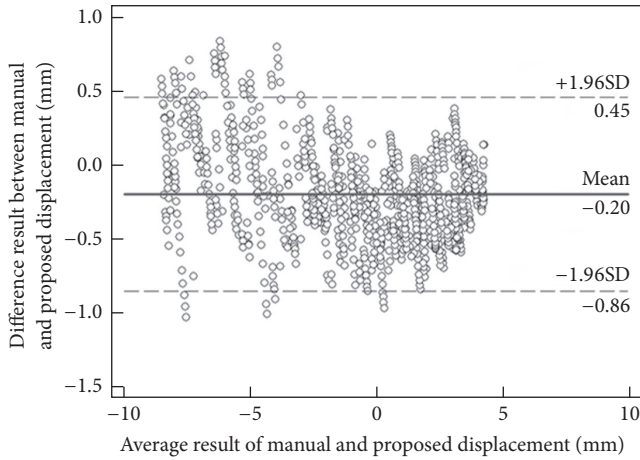
FIGURE 9: Bland-Altman plot of the MTJ displacement measured with the proposed method and manual measurements.

ultrasound images using the prior knowledge of MTJ structure. A more reliable calculation of global affine transform parameters was then achieved using the Lucas-Kanade optical flow algorithm over the effective MTJ region since it precluded the influence of nontendinous components as well as speckle noise on the motion estimation of points on the tendinous tissues. The *in vivo* experiment results show that MTJ could be reliably tracked in continuous ultrasound images, which were in good agreement with those obtained by manual measurement and correlated well with kinematic data, such as ankle angle.

The key element in the proposed method is to utilize prior knowledge of MTJ structures in the musculoskeletal ultrasound images. Tendons are made up of collagen fibers and flattened wide tendons are known as aponeuroses that are often found in series with a tendon [33, 53]. Both tendons and aponeuroses are distributed as continuous hyperechoic bands with specified orientation in the ultrasound image [33, 45], representing an axis of local symmetry. As an illumination and contrast invariant measure of symmetric structures, phase congruency can be employed to perceive and enhance ridge-like features [34], which is beneficial for the detection of tendinous tissues using Radon transform. Moreover, MTJ is the specific site of connection between tendons and muscles [54], which can be identified as the intersection of two aponeuroses in ultrasound images [55, 56]. With the consideration of the poor localization of phase-based techniques, the locations and the orientation of tendinous tissues and MTJ were used to facilitate the segmentation of MTJ obtained with LRT and Otsu methods. The prior knowledge of MTJ structures, therefore, allows for easier detection of the effective MTJ region from the musculoskeletal ultrasound images, which can be applied as a preprocessing step for the tracking of MTJ displacement.

The estimation of affine flow parameters over the effective MTJ region could avoid the accumulation of errors caused by inhomogeneous deformation across the area of interest between consecutive images. The proposed method segments

(a)

$$y = 0.04x^2 + 2.23x + 2.41$$
$$r = 0.99$$

(b)
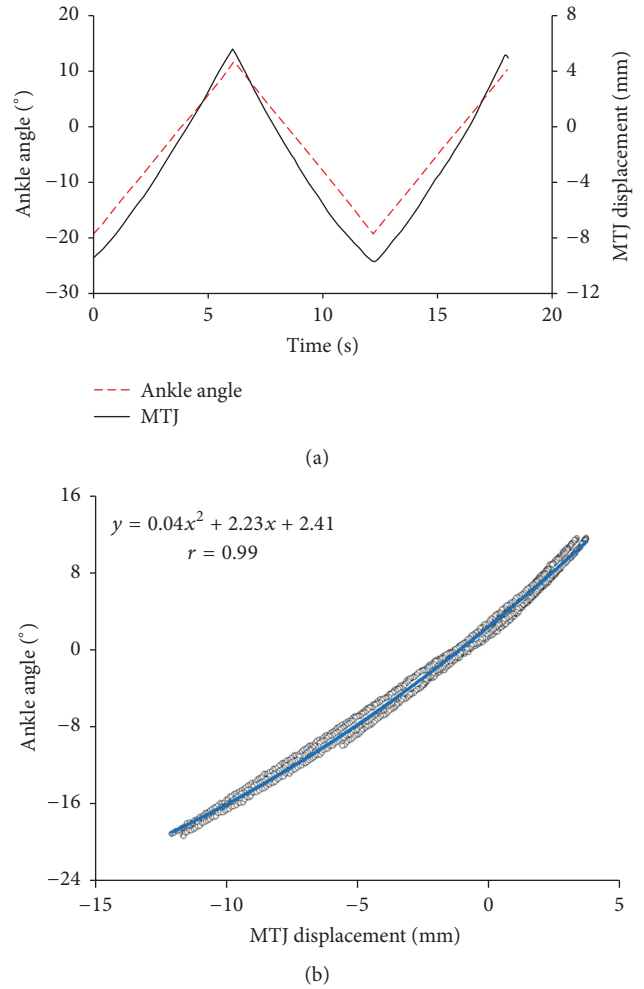
FIGURE 10: The displacement of MTJ during the passive rotation test of the ankle joint for subject A: (a) the change of MTJ and ankle angle with time; (b) the cross-correlation between MTJ displacement and ankle angle.

visible MTJ structures from the whole image for the calculation of global affine transform parameters, thus obviating the impact the nontendinous components and speckle noise. On the other hand, the original Lucas-Kanade method with the whole region, including MTJ structure, nontendinous components, and speckle noise, might cause the inaccurate estimation of affine transform parameters, resulting in accumulated measurement errors of MTJ displacement. The overall high CMC value (0.97 ± 0.02) demonstrated that the results of the proposed method were more consistent with the manual than that of the original Lucas-Kanade method (0.79 ± 0.11). The significantly larger CMC value for the proposed method ($p < 0.05$), compared with the Lucas-Kanade method, also suggested that this approach had a better performance in tracking MTJ displacement.

In this study, the average excursion of MTJ was -8.22 ± 2.03 mm with the plantar flexion angle reaching $19.26 \pm 0.06°$, and MTJ was moved distally by 3.97 ± 1.27 mm for an ankle angle of $11.64 \pm 0.05°$. These results were in line with those reported in previous work [56, 57]. The average displacement

of MTJ was reported to be 14 mm from 20° plantar flexion to 10° dorsiflexion [56]. Additionally, the greater displacement in the females reported in [57] was also found in our study, implying lower muscle stiffness in females than in males [57, 58]. In the previous study of muscles and tendons, the changes in tendon length can be obtained by subtracting MTJ displacement from MTU length change estimated using ankle joint angle [59]. Therefore, it is feasible to generalize the use of MTJ displacement into tendon length change analysis with the proposed method, which would facilitate an improved understanding of the structural and bioelectrical properties of muscles and tendons during motion.

However, the method proposed in this study still had some limitations. Firstly, errors might be introduced if the assumption that tendinous tissues being tracked conform to homogeneous affine transformations does not hold. Given the promising results, it seems that this assumption holds true when tracking the planar movement of tendinous tissues during passive motion. Further studies should be conducted to take account of both changes in local shape and global shape, thus improving the tracking accuracy of MTJ. In addition, manual initialization of points on the tendinous tissues might also affect the results of MTJ estimation. The automatic initialization should be further investigated in future studies with better detection of line and corner features in musculoskeletal ultrasound images. Furthermore, a two-point representation may not properly account for the Achilles tendon curvature. The Achilles tendon is almost straight in the dorsiflexion region; as the ankle joint angle changes, the Achilles tendon becomes slightly curved, resulting in an approximately 3% underestimation of tendon length with the plantar flexion angle reaching 30° [55]. Thus, this effect is likely to be a minor factor in measuring MTJ and tendon length in daily human movements. Nevertheless, it would be ideal if the algorithm was able to track multiple points along a tendinous tissue for curvature measurement in the future.

5. Conclusions

We have successfully developed a robust method for automatically tracking MTJ displacement in a series of GM ultrasound images with the prior knowledge about the distribution and shape of tendinous tissues and MTJ. The proposed method, therefore, precluded the influence of nontendinous components on the calculation of affine transform parameters over effective MTJ region segmented by combining phase congruency with LRT and thresholding methods, resulting in a more reliable estimation of MTJ displacement. The results showed a good agreement between the automatic and manual measurements. This approach obviated subjective manual measurements, reducing the variations in measurements. We expected that the proposed method would provide an effective way to analyze the functionality of muscle-tendon unit in human kinetics as well as force generation analysis. Future studies with a large cohort of subjects, including patients with musculoskeletal abnormalities, will be conducted to further illustrate the potential of this new approach for the full understanding of muscle as well as tendon mechanism.

The performance of the newly proposed method can also be further enhanced by taking account of both changes in local shape and global shape in future studies.

Conflicts of Interest

The authors declare that there are no conflicts of interest.

Acknowledgments

Supplementary Materials

The Supplementary Materials include one sample video showing the MTJ tracking results obtained by our proposed method. *(Supplementary Materials)*

References

[1] N. J. Cronin, R. A. Klint, M. J. Grey, and T. Sinkjaer, "Ultra-sonography as a tool to study afferent feedback from the muscle-tendon complex during human walking," *Journal of Electromyography & Kinesiology*, vol. 21, no. 2, pp. 197–207, 2011.

[2] M. Ishikawa, J. Pakaslahti, and P. V. Komi, "Medial gastrocnemius muscle behavior during human running and walking," *Gait & Posture*, vol. 25, no. 3, pp. 380–384, 2007.

[3] T. Fukunaga, Y. Kawakami, K. Kubo, and H. Kanehisa, "Muscle and tendon interaction during human movements," *Exercise and Sport Sciences Reviews*, vol. 30, no. 3, pp. 106–110, 2002.

[4] N. J. Cronin and G. Lichtwark, "The use of ultrasound to study muscle-tendon function in human posture and locomotion," *Gait & Posture*, vol. 37, no. 3, pp. 305–312, 2013.

[5] G. A. Lichtwark and A. M. Wilson, "Interactions between the human gastrocnemius muscle and the Achilles tendon during incline, level and decline locomotion," *Journal of Experimental Biology*, vol. 209, no. 21, pp. 4379–4388, 2006.

[6] G. Zhou, Y. Zheng, and P. Zhou, "Measurement of Gender Differences of Gastrocnemius Muscle and Tendon Using Sonomyography during Calf Raises: A Pilot Study," *BioMed Research International*, vol. 2017, pp. 1–10, 2017.

[7] C. N. Maganaris and J. P. Paul, "Tensile properties of the in vivo human gastrocnemius tendon," *Journal of Biomechanics*, vol. 35, no. 12, pp. 1639–1646, 2002.

[8] A. Arampatzis, S. Stafilidis, G. DeMonte, K. Karamanidis, G. Morey-Klapsing, and G. P. Brüggemann, "Strain and elongation of the human gastrocnemius tendon and aponeurosis during maximal plantarflexion effort," *Journal of Biomechanics*, vol. 38, no. 4, pp. 833–841, 2005.

[9] M. V. Narici, N. Maffulli, and C. N. Maganaris, "Ageing of human muscles and tendons," *Disability and Rehabilitation*, vol. 30, no. 20–22, pp. 1548–1554, 2008.

[10] N. D. Reeves, C. N. Maganaris, and M. V. Narici, "Effect of strength training on human patella tendon mechanical properties of older individuals," *The Journal of Physiology*, vol. 548, no. 3, pp. 971–981, 2003.

[11] P. Hoang, J. P. Saboisky, S. C. Gandevia, and R. D. Herbert, "Passive mechanical properties of gastrocnemius in people with multiple sclerosis," *Clinical Biomechanics*, vol. 24, no. 3, pp. 291–298, 2009.

[12] J. Duclay, A. Martin, A. Duclay, G. Cometti, and M. Pousson, "Behavior of fascicles and the myotendinous junction of human medial gastrocnemius following eccentric strength training," *Muscle & Nerve*, vol. 39, no. 6, pp. 819–827, 2009.

[13] A. Foure, A. Nordez, and C. Cornu, "Effects of plyometric training on passive stiffness of gastrocnemii muscles and achilles tendon," *European Journal of Applied Physiology*, vol. 112, no. 8, pp. 2849–2857, 2012.

[14] S. Jonhagen, K. Halvorsen, and D. L. Benoit, "Muscle activation and length changes during two lunge exercises: implications for rehabilitation," *Scandinavian Journal of Medicine Science in Sports*, vol. 19, no. 4, pp. 561–568, Aug 2009.

[15] H. Gao, Q. Huang, X. Xu, and X. Li, "Wireless and sensorless 3D ultrasound imaging," *Neurocomputing*, vol. 195, pp. 159–171, 2016.

[16] W. Qiu, J. Zhou, Y. Chen et al., "A Portable Ultrasound System for Non-Invasive Ultrasonic Neuro-Stimulation," *IEEE Transactions on Neural Systems and Rehabilitation Engineering*, vol. 25, no. 12, pp. 2509–2515, 2017.

[17] T. Fukunaga, K. Kubo, Y. Kawakami, S. Fukashiro, H. Kanehisa, and C. N. Maganaris, "In vivo behaviour of human muscle tendon during walking," *Proceedings of the Royal Society B Biological Science*, vol. 268, no. 1464, pp. 229–233, 2001.

[18] K. Kubo, H. Kanehisa, D. Takeshita, Y. Kawakami, S. Fukashiro, and T. Fukunaga, "In vivo dynamics of human medial gastrocnemius muscletendon complex during stretch-shortening cycle exercise," *Acta Physiologica Scandinavica*, vol. 170, no. 2, pp. 127–135, 2000.

[19] G.-Q. Zhou, P. Chan, and Y.-P. Zheng, "Automatic measurement of pennation angle and fascicle length of gastrocnemius muscles using real-time ultrasound imaging," *Ultrasonics*, vol. 57, no. C, pp. 72–83, 2015.

[20] G.-Q. Zhou and Y.-P. Zheng, "Automatic Fascicle Length Estimation on Muscle Ultrasound Images With an Orientation-Sensitive Segmentation," *IEEE Transactions on Biomedical Engineering*, vol. 62, no. 12, pp. 2828–2836, 2015.

[21] N. J. Cronin, C. P. Carty, R. S. Barrett, and G. Lichtwark, "Automatic tracking of medial gastrocnemius fascicle length during human locomotion," *Journal of Applied Physiology*, vol. 111, no. 5, pp. 1491–1496, 2011.

[22] J. Darby, B. Li, N. Costen, I. Loram, and E. Hodson-Tole, "Estimating skeletal muscle fascicle curvature from B-mode ultrasound image sequences," *IEEE Transactions on Biomedical Engineering*, vol. 60, no. 7, pp. 1935–1945, 2013.

[23] J. Li, Y. Zhou, K. Ivanov, and Y.-P. Zheng, "Estimation and visualization of longitudinal muscle motion using ultrasonography: A feasibility study," *Ultrasonics*, vol. 54, no. 3, pp. 779–788, 2014.

[24] Q. Li, D. Ni, W. Yi, S. Chen, T. Wang, and X. Chen, "Use of optical flow to estimate continuous changes in muscle thickness from ultrasound image sequences," *Ultrasound in Medicine & Biology*, vol. 39, no. 11, pp. 2194–2201, 2013.

[25] H. Zhao and L.-Q. Zhang, "Automatic tracking of muscle fascicles in ultrasound images using localized radon transform," *IEEE Transactions on Biomedical Engineering*, vol. 58, no. 7, pp. 2094–2101, 2011.

[26] M. Rana, G. Hamarneh, and J. M. Wakeling, "Automated tracking of muscle fascicle orientation in B-mode ultrasound images," *Journal of Biomechanics*, vol. 42, no. 13, pp. 2068–2073, 2009.

[27] Y. Zhou and Y.-P. Zheng, "Estimation of muscle fiber orientation in ultrasound images using revoting Hough transform (RVHT)," *Ultrasound in Medicine & Biology*, vol. 34, no. 9, pp. 1474–1481, 2008.

[28] Y. Zhou, J.-Z. Li, G. Zhou, and Y.-P. Zheng, "Dynamic measurement of pennation angle of gastrocnemius muscles during contractions based on ultrasound imaging," *Biomedical Engineering Online*, vol. 11, article no. 63, 2012.

[29] J. Darby, E. F. Hodson-Tole, N. Costen, and I. D. Loram, "Automated regional analysis of B-mode ultrasound images of skeletal muscle movement," *Journal of Applied Physiology*, vol. 112, no. 2, pp. 313–327, 2012.

[30] A. Konrad and M. Tilp, "Increased range of motion after static stretching is not due to changes in muscle and tendon structures," *Clinical Biomechanics*, vol. 29, no. 6, pp. 636–642, 2014.

[31] S. Baker and I. Matthews, "Lucas-Kanade 20 years on: a unifying framework," *International Journal of Computer Vision*, vol. 56, no. 3, pp. 221–255, 2004.

[32] I. D. Loram, C. N. Maganaris, and M. Lakie, "Use of ultrasound to make noninvasive in vivo measurement of continuous changes in human muscle contractile length," *Journal of Applied Physiology*, vol. 100, no. 4, pp. 1311–1323, 2006.

[33] A. Del Buono, O. Chan, and N. Maffulli, "Achilles tendon: Functional anatomy and novel emerging models of imaging classification," *International Orthopaedics*, vol. 37, no. 4, pp. 715–721, 2013.

[34] P. Kovesi, "Symmetry and Asymmetry from Local Phase," *in Tenth Australian Joint Converence on Artificial Intelligence*, p. 2, 1997.

[35] N. Otsu, "A threshold selection method from gray-level histograms," *IEEE Transactions on Systems, Man, and Cybernetics*, vol. 9, no. 1, pp. 62–66, 1979.

[36] B. D. Lucas and T. Kanade, "An iterative image registration technique with an application to stereo vision," in *Proceedings of the in Proceedings of the 7th international joint conference on Artificial intelligence - Volume 2*, pp. 674–679, Vancouver, BC, Canada, 1981.

[37] M. C. Morrone and R. A. Owens, "Feature detection from local energy," *Pattern Recognition Letters*, vol. 6, no. 5, pp. 303–313, 1987.

[38] I. Hacihaliloglu, R. Abugharbieh, A. J. Hodgson, and R. N. Rohling, "Bone surface localization in ultrasound using image phase-based features," *Ultrasound in Medicine & Biology*, vol. 35, no. 9, pp. 1475–1487, 2009.

[39] I. Hacihaliloglu, A. Rasoulian, R. N. Rohling, and P. Abolmaesumi, "Local phase tensor features for 3-D ultrasound to statistical shape+pose spine model registration," *IEEE Transactions on Medical Imaging*, vol. 33, no. 11, pp. 2167–2179, 2014.

[40] A. Belaid, D. Boukerroui, Y. Maingourd, and J.-F. Lerallut, "Phase-based level set segmentation of ultrasound images," *IEEE Transactions on Information Technology in Biomedicine*, vol. 15, no. 1, pp. 138–147, 2011.

[41] P. Kovesi, "Phase congruency: a low-level image invariant," *Psychological Research*, vol. 64, no. 2, pp. 136–148, 2000.

[42] M. Felsberg and G. Sommer, "The monogenic signal," *IEEE Transactions on Signal Processing*, vol. 49, no. 12, pp. 3136–3144, 2001.

[43] G.-Q. Zhou, W.-W. Jiang, K.-L. Lai, and Y.-P. Zheng, "Automatic Measurement of Spine Curvature on 3-D Ultrasound Volume

Projection Image with Phase Features," *IEEE Transactions on Medical Imaging*, vol. 36, no. 6, pp. 1250–1262, 2017.

[44] Q. Huang, Y. Luo, and Q. Zhang, "Breast ultrasound image segmentation: a survey," *International Journal for Computer Assisted Radiology and Surgery*, vol. 12, no. 3, pp. 493–507, 2017.

[45] D. A. Lansdown, Z. Ding, M. Wadington, J. L. Hornberger, and B. M. Damon, "Quantitative diffusion tensor MRI-based fiber tracking of human skeletal muscle," *Journal of Applied Physiology*, vol. 103, no. 2, pp. 673–681, 2007.

[46] G. P. Pappas, D. S. Asakawa, S. L. Delp, F. E. Zajac, and J. E. Drace, "Nonuniform shortening in the biceps brachii during elbow flexion," *Journal of Applied Physiology*, vol. 92, no. 6, pp. 2381–2389, 2002.

[47] Y. Zhou and Y.-P. Zheng, "Enhancement of muscle fibers in ultrasound images using gabor filters," in *Proceedings of the 2009 IEEE International Ultrasonics Symposium, IUS 2009*, Italy, September 2009.

[48] A. Arampatzis, G. D. Monte, and K. Karamanidis, "Effect of joint rotation correction when measuring elongation of the gastrocnemius medialis tendon and aponeurosis," *Journal of Electromyography & Kinesiology*, vol. 18, no. 3, pp. 503–508, 2008.

[49] G. Rankin and M. Stokes, "Reliability of assessment tools in rehabilitation: an illustration of appropriate statistical analyses," *Clinical Rehabilitation*, vol. 12, no. 3, pp. 187–199, 1998.

[50] M. P. Kadaba, H. K. Ramakrishnan, M. E. Wootten, J. Gainey, G. Gorton, and G. V. B. Cochran, "Repeatability of kinematic, kinetic, and electromyographic data in normal adult gait," *Journal of Orthopaedic Research*, vol. 7, no. 6, pp. 849–860, 1989.

[51] J. J. Kavanagh, S. Morrison, D. A. James, and R. Barrett, "Reliability of segmental accelerations measured using a new wireless gait analysis system," *Journal of Biomechanics*, vol. 39, no. 15, pp. 2863–2872, 2006.

[52] J. M. Bland and D. G. Altman, "Statistical methods for assessing agreement between two methods of clinical measurement," *The Lancet*, vol. 1, no. 8476, pp. 307–310, 1986.

[53] V. M. Zatsiorsky and B. I. Prilutsky, *Biomechanics of Skeletal Muscles*, Human Kinetics, 2012.

[54] J. A. Trotter, S. Eberhard, and A. Samora, "Structural connections of the muscle-tendon junction," *Cell Motility*, vol. 3, no. 5, pp. 431–438, 1983.

[55] A. Fukutani, S. Hashizume, K. Kusumoto, and T. Kurihara, "Influence of neglecting the curved path of the achilles tendon on achilles tendon length change at various ranges of motion," *Physiological Reports*, vol. 2, no. 10, Article ID e12176, 2014.

[56] Y. Kawakami, H. Kanehisa, and T. Fukunaga, "The relationship between passive ankle plantar flexion joint torque and gastrocnemius muscle and achilles tendon stiffness: Implications for flexibility," *Journal of Orthopaedic & Sports Physical Therapy*, vol. 38, no. 5, pp. 269–276, 2008.

[57] C. I. Morse, "Gender differences in the passive stiffness of the human gastrocnemius muscle during stretch," *European Journal of Applied Physiology*, vol. 111, no. 9, pp. 2149–2154, 2011.

[58] T. Muraoka, K. Chino, T. Muramatsu, T. Fukunaga, and H. Kanehisa, "In vivo passive mechanical properties of the human gastrocnemius muscle belly," *Journal of Biomechanics*, vol. 38, no. 6, pp. 1213–1219, 2005.

[59] D. Grieve, S. Pheasant, and P. Cavanagh, "Prediction of gastrocnemius length from knee and ankle joint posture," *Biomechanics Vi-A*, vol. 2, pp. 405–412, 1978.

Research Article

Gear Shifting of Quadriceps during Isometric Knee Extension Disclosed Using Ultrasonography

Shu Zhang,[1] **Weijian Huang,**[1] **Yu Zeng,**[1] **Wenxiu Shi,**[1] **Xianfen Diao,**[1]
Xiguang Wei ⬤,[2] **and Shan Ling** ⬤[3]

[1]*School of Biomedical Engineering, Shenzhen University, Shenzhen, China*
[2]*Department of Electrical and Electronic Engineering, Hong Kong University, Pok Fu Lam, Hong Kong*
[3]*Department of Biomedical Engineering, Case Western Reserve University, Cleveland, OH, USA*

Correspondence should be addressed to Xiguang Wei; xgwei@eee.hku.hk and Shan Ling; sxl1174@case.edu

Ultrasonography has been widely employed to estimate the morphological changes of muscle during contraction. To further investigate the motion pattern of quadriceps during isometric knee extensions, we studied the relative motion pattern between femur and quadriceps under ultrasonography. An interesting observation is that although the force of isometric knee extension can be controlled to change almost linearly, femur in the simultaneously captured ultrasound video sequences has several different piecewise moving patterns. This phenomenon is like quadriceps having several forward gear ratios like a car starting from rest towards maximal voluntary contraction (MVC) and then returning to rest. Therefore, to verify this assumption, we captured several ultrasound video sequences of isometric knee extension and collected the torque/force signal simultaneously. Then we extract the shapes of femur from these ultrasound video sequences using video processing techniques and study the motion pattern both qualitatively and quantitatively. The phenomenon can be seen easier via a comparison between the torque signal and relative spatial distance between femur and quadriceps. Furthermore, we use cluster analysis techniques to study the process and the clustering results also provided preliminary support to the conclusion that, during both ramp increasing and decreasing phases, quadriceps contraction may have several forward gear ratios relative to femur.

1. Introduction

Muscle behavior in vivo is an essential problem to be resolved. Commonly used techniques for measuring muscle activities from different aspects include electromyography (EMG) [1], dynamometers, and ultrasonography [2]. Surface EMG is the most widely used tool for indirect assessment of mechanical activity of muscle, but it fails to disclose muscle's morphological changes. Dynamometers are devices for quantitative measurement of muscle, such as torque and power, but they cannot provide muscle's morphological information yet. Due to the quality of real-time imaging, widespread availability, and low cost, ultrasonography has been increasingly employed as a clinical and research tool to study the in vivo behavior of the quadriceps muscle from the morphological point of view, such as architectural changes

of thickness [3–6], fascicle length [2, 6–10], pennation angle [2, 7, 8, 10–12], and cross-sectional area [2, 13, 14]. Dick and Wakeling recorded medial gastrocnemius tendon length, fascicle length, pennation angle, and thickness using ultrasonography and muscle activation using surface EMG during cycling [15]. They identified muscle force, and not velocity, as the mechanistic driving factor to allow muscle gearing to vary depending on the contractile conditions. All these works show the potential of using data and quantitative approaches to help understand the nature and functional implications of in vivo dynamic body movement. Quadriceps is always a focus as it is crucial in walking, running, jumping, and squatting. Wei et al. reported an image-based method to find the contour of the center tendon of rectus femoris quantitatively [16]. However, the knowledge about relative movement between quadriceps and femur during dynamic

contraction remains unclear. The aim of this study is to quantify this movement for further understanding of muscle contraction mechanism.

As a matter of fact, in the data from a previous study [16], a phenomenon like shifting gear of a car was observed visually from time to time. Simply speaking, when the torque increases linearly, femur is frequently noticed to move around several relatively fixed positions. To verify this assumption, we repeated the experiment and recorded both the torque signal and the movement of femur under ultrasonography. Then, some established image processing techniques were used to disclose the gear shifting phenomenon.

2. Materials and Methods

2.1. Subjects and Experiment Protocol. Eight healthy male subjects (mean ± SD, age = 28.5±0.6 years; body weight 67.3± 1.7 kg; height = 171.8 ± 0.6 cm) volunteered to participate in this study. No participants had a history of neuromuscular disorders, and all were aware of experimental purposes and procedures. The human subject ethical approval was obtained from the relevant committee in the authors' institution, and informed consent was obtained from subjects prior to the experiment.

The testing position of the subject was in accordance with the User's Guide of a Norm dynamometer (Humac/ Norm Testing and Rehabilitation System, Computer Sports Medicine, Inc., Massachusetts, USA). Each subject was required to put forth his maximal effort of isometric plantar flexion for a period of 3 seconds with verbal encouragement provided. The maximal voluntary contraction (MVC) was defined as the highest value of torque recorded during the entire isometric contraction. The MVC torque was then calculated by averaging the two recorded highest torque values from the two tests. The subject was instructed to generate a torque waveform up to 90% of his MVC, using ankle plantar flexion movements in prone position. The torque was measured by the aforementioned dynamometer and the reason for choosing 90% MVC as the highest value was to avoid muscle fatigue.

2.2. Data Acquisition and Data Processing. A real-time B-mode ultrasonic scanner (EUB-8500, Hitachi Medical Corporation, Tokyo, Japan) with a 10 MHz electronic linear array probe (L53L, Hitachi Medical Corporation, Tokyo, Japan) was used to obtain ultrasound images of muscles. The long axis of the ultrasound probe (EUB-8500) was arranged perpendicularly to the long axis of the thigh on its superior aspect, 40% distally from the knee. As the position of probe-quadriceps is fixed, the movement of femur reflects the contraction of quadriceps. The ultrasound probe was fixed by a custom-designed foam container with fixing straps, and a very generous amount of ultrasound gel was applied to secure acoustic coupling between the probe and skin during muscle contractions, as shown in Figure 1. The probe was adjusted to optimize the contrast of muscle fascicles in ultrasound images. Then the B-mode ultrasound images were digitized by a video card (NI PCI-1411, National Instruments, Austin, USA) at a rate of 25 frame/s for later analysis.
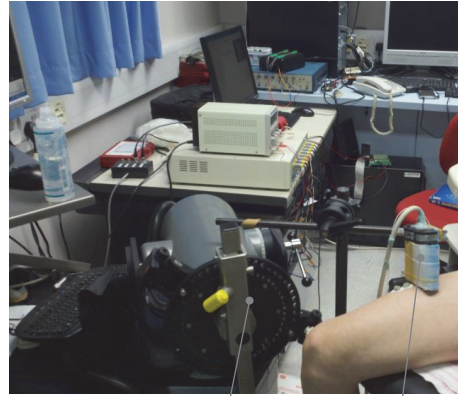
Figure 1: Experimental setup including the torque and ultrasound image data collection modules.

Eight sequences of musculoskeletal ultrasound images were acquired and the number of frames per sequence was 240 images. All images were cropped to remove equipment tags in the images and keep the image content only using a home-made software. All data were processed offline using programs written in Matlab R2010b (Math Works, Natick, MA, USA) on a Windows-based computer with a P4 (3 GHz) processor and 2 GB memory.

2.3. Image Filtering and Femur Segmentation. In this study, the shapes of femur are extracted automatically by two steps. The ultrasound images are first denoised using guided filter. Then, the femur in a sequence is segmented by using an active contour model, named implicit active contours driven by local binary fitting energy (LBF) [17]. To reduce the computation time and improve the accuracy of femur extraction, we located the region of interest (ROI) as a rectangle which could enclose the femur of the whole image sequence, and the subsequent operations are applied on this region rather than the whole image. The rectangle is expected to be small but able to contain the femur of the sequence.

Ultrasound images are usually affected by speckle noise [18], and the edges of femur are not clear in most images, which make it hard for the segmentation algorithm to recognize the accurate boundaries of femur. To handle this problem, we use a filtering algorithm, named guided filtering, for image smoothing and noise reduction before the segmentation step. This filter has edge-preserving smoothing property like bilateral filter but does not suffer from the gradient reversal artifacts. The derivation and details of the guided filtering algorithm can be found in Appendix A.

Although images are smoothed after guided filtering, intensity inhomogeneity still exists in ultrasound frames. Hence, we adopted implicit active contours driven by local binary fitting energy (LBF), to extract boundaries of femur from ultrasound images. In this model, a kernel function is introduced into a data fitting energy, so that intensity information in local regions is extracted to guide the motion of the contour, which thereby enables the model to cope with

intensity inhomogeneity. The details and implementation of the LBF model are introduced in Appendix A. In this study, level set of each frame is initialized as two rectangles enclosing the femur. Then contours of femur will be extracted by evolving the level set iteratively using LBF model.

2.4. Analysis of Femur Motion. To study the motion of femur, we use the contours in the previous step to generate corresponding segmentation images for the femur. Figure 5 is an overlapped plot of segmentation results in a knee extension process. In this figure, different color represents the duration time of the femur staying at this location and one may easily observe that the femur mainly stays at several positions. Figure 6 is a schematic drawing of a cross-sectional view of the quadriceps in which A, B, and C are different stages of femur motion. To see the motion in detail, we draw the overlapped plot of femur movement in both muscle contraction and relaxation stages in Figure 8(a) and plot an example of torque signal and related x y coordinates in Figures 8(b) and 8(c). In order to further study the process, we used optimal detection of change-points (ODC) algorithm [19] to cut the process into different clusters. The reason of using ODC is that the motion is a temporal continuous process and ODC algorithm can cover this continuity by design. The results and discussion of clustering can be found in the next section.

The flowchart of the proposed strategy mentioned above is illustrated in Figure 2.

3. Results and Discussion

3.1. Image Filtering and Femur Segmentation. After acquisition of ultrasound frames, images were focused on the ROI, and then guided filter and LBF model were applied to smooth the image and extract the femur, respectively. In our numerical experiments, window radius r and regularization parameter ε for guided filter are selected as 8 and 0.4^2, respectively. And for femur segmentation using LBF model we empirically adopted parameters as follows: $\lambda_1 = 1$, $\lambda_2 = 2$, $\nu = 0.001 \times 255 \times 225$, $\mu = 1$, $\sigma = 10$, and time step $\Delta t = 0.1$. All parameters are empirical values and applied to frames of all subjects. The explanation and usage for mentioned parameters can be found in the Appendices.

A representative example of selected ROI, filtered image, and segmented femur are shown in Figure 3. And a representative example of femur segmentation process using LBF evolution model is shown in Figure 4.

3.2. Discussion. After segmentation of femur, an interesting phenomenon could be found where (shown in Figure 5), corresponding to one ramp increasing and decreasing of quadriceps, femur relative to the ultrasound sensor in a sequence mainly concentrated at several positions which are shown as *A, *B, and *C. To further investigate the detailed motion and its relationship to torque changing, in Figure 8, we draw the overlapped plot of femur movement in both muscle contraction and relaxation stages in (a), plot the torque signal in (b), and plot the x y coordinates of the femur centroid movement in (c). Then we use optimal detection of
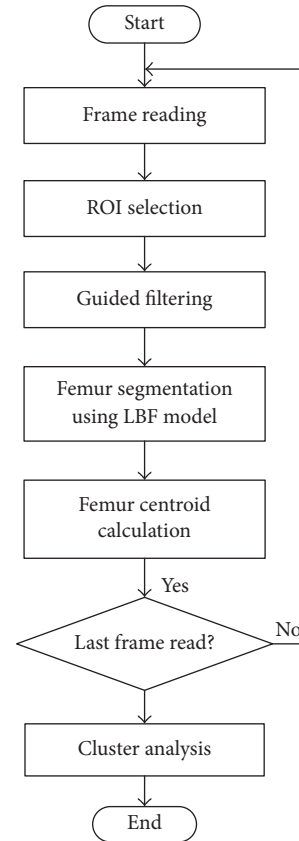
FIGURE 2: Flowchart of the proposed strategy for processing an ultrasound image sequence.
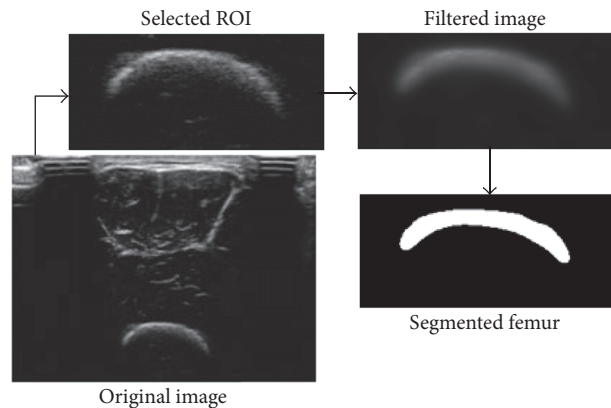
FIGURE 3: A representative result of ROI selection, guided filtering, and femur segmentation.

change-points (ODC) method [19] to cut whole process into different stages using torque signal and x y coordinates. We can see the motion of femur and the torque changing have very different behaviors. The torque signal, which is shown in Figure 8(b), can be mainly divided into three stages which are corresponding to muscle contraction, relaxation, and resting, respectively, and, in each stage, the torque changes almost linearly, while, in Figures 8(c) and 8(d), the plotted x and y coordinates of femur centroid movement can be viewed as

(a)

(b)

(c)
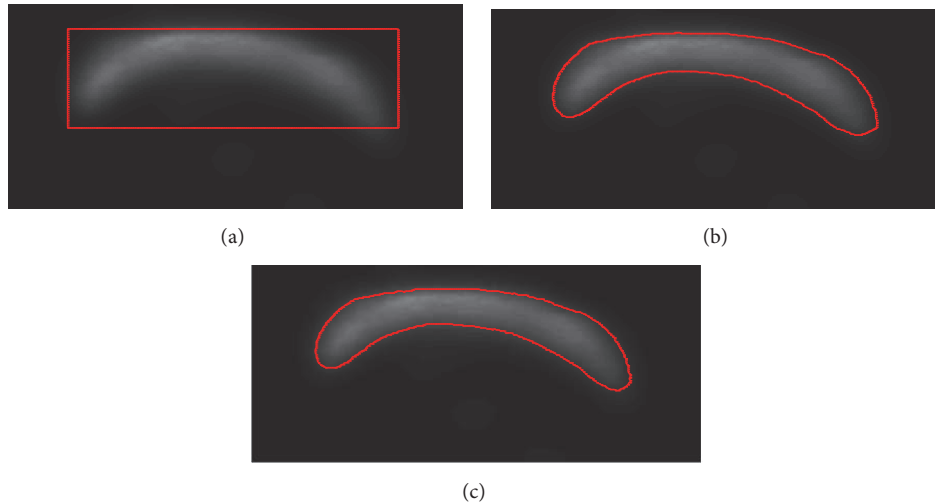
FIGURE 4: A representative set of results of LBF model for femur segmentation. (a) Original image with initial contour. (b) Curve evolution result after 2 iterations. (c) Final contour after evolving stopped.
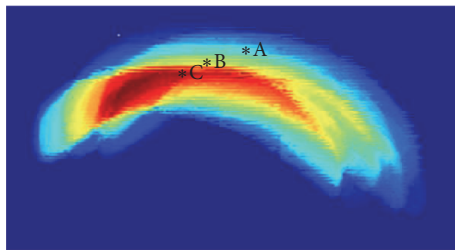
FIGURE 5: A representative statistical result of femur position in a sequence, where ∗A, ∗B, and ∗C are the positions the femur mainly stay at.
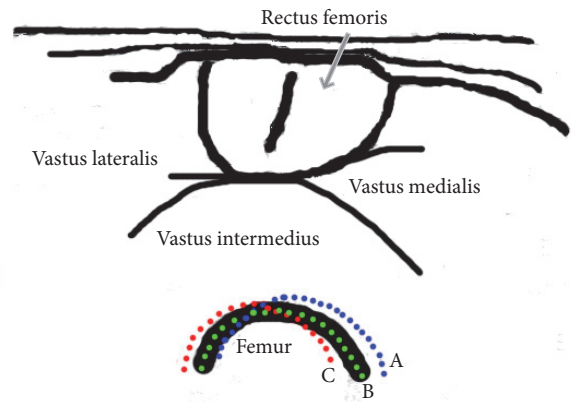
FIGURE 6: Schematic drawing of a cross-sectional view of the quadriceps shows the femur movement during a contraction-relaxation process of quadriceps, where A, B, and C are the main stages of femur movement.

more stages than torque changing. When the torque signal changes into another stage, the motion of femur also changes to another stage which makes sense. Interestingly, we can observe that when the torque linearly increases or decreases in a stage, the trend of femur movement is not fixed and can be further divided into several stages. This stage changing reminds us of gear shifting in a car where there might also be a gear shifting of femur in the extension process. Therefore, to further investigate this phenomenon quantitatively, we use cluster analysis methods to study the behavior of femur movement. We first cut the process using torque signal into three stages, that is, contraction, relaxation, and resting. (The contraction stage and relaxation stage are separated by peak torque while the relaxation stage changes to resting stage when the torque signal reduced to less than 0.05.)

As we are studying the extension process, we only focus on contraction and relaxation stages. Both contraction and relaxation stages are clustered into three phases by ODC. Clustering results are displayed in Figure 7 and the six clusters are represented by #A, #B, #C, #C′, #B′, and #A′, in which #A, #B, and #C correspond to beginning, middle, and ending of contraction stage and #A′, #B′, and #C′ correspond to beginning, middle, and ending of relaxing stage. In Table 1, we

first summarized the variances of each cluster in all subjects. In this table, we also included their rankings. Interestingly, in the relaxation phase, we find that #B′ has the largest variances for 7/8 subjects, #C′ has the median variances for 6/8 subjects, and #A′ has the smallest variances for 7/8 subjects. The variance of a group represents the moving speed of the femur in this cluster and we may conclude that the moving speed of femur changes in a fixed pattern in relaxation phase. In the contraction phase, the property is not very clear, but we can still notice that the femur generally moves faster in #A than in #B and #C. At all events, from the clustering results, we can find that the clusters in the same contraction or relaxation phase have different properties whereas the torque signal keeps linear changing. #A and #A′, #B and #B′, and #C and #C′ are considered as pairs as they have similar torque signal

TABLE 1: Variances of clusters.

Subject	#A		#B		#C		#C'		#B'		#A'	
1	15.4	Medium	18.7	Large	3.9	Small	8.6	Medium	24.0	Large	5.5	Small
2	3.9	Small	26.8	Medium	76.5	Large	2.3	Small	18.8	Large	8.6	Medium
3	19.0	Large	4.3	Small	15.3	Medium	5.8	Small	36.0	Large	10.1	Medium
4	28.1	Medium	6.7	Small	55.6	Large	7.1	Small	10.3	Medium	11.0	Large
5	27.0	Large	5.0	Medium	3.1	Small	8.5	Small	19.0	Large	14.2	Medium
6	69.9	Large	14.1	Medium	1.3	Small	3.4	Small	41.9	Large	10.2	Medium
7	7.2	Small	17.9	Large	15.7	Medium	4.0	Small	24.3	Large	9.7	Medium
8	16.2	Large	7.3	Small	15.1	Medium	4.0	Medium	31.7	Large	4.0	Small

TABLE 2: Cluster distance between contraction group and relaxation group.

Subject	Euclidean distance (mm)		
	#A-#A'	#B-#B'	#C-#C'
1	17.3	13.6	3.1
2	14.6	13.5	10.8
3	16.9	2.1	6.6
4	12.6	17.5	8.3
5	26.2	4.7	5.8
6	12.1	2.7	2.3
7	2.9	9.8	6.6
8	5.2	0.4	6.7
Mean	11.3	5.0	5.7
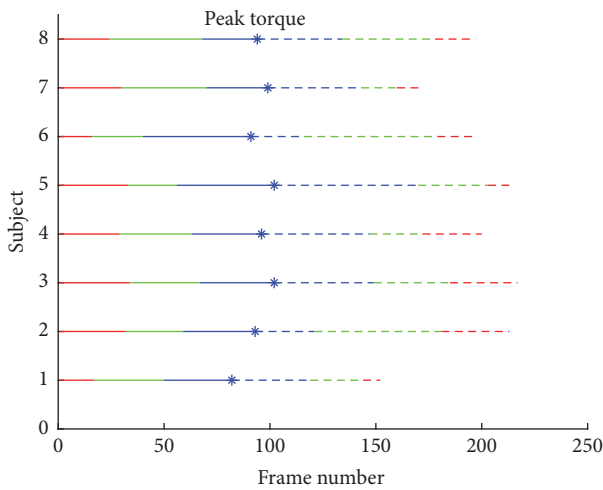
FIGURE 7: Classification results of all subjects.

(a) Overlapped plot of femora movement in both muscle contraction and relaxation stages

(b) Torque signal

(c) x y coordinates of femur centroids
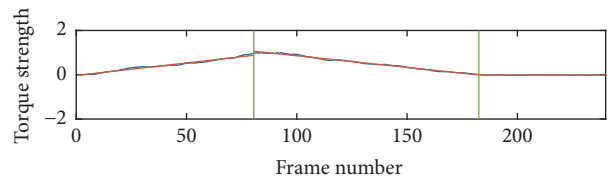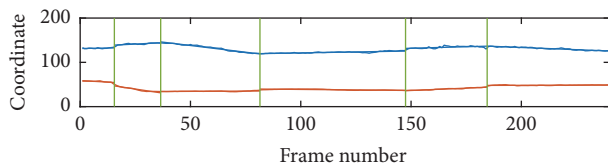
— x coordinate
— y coordinate

FIGURE 8: (a) Overlapped plot of muscle contraction and relaxation stages, (b) torque signal, and (c) x y coordinates of femur centroids.

and, therefore, in Table 2, we also summarized the distances among them. Another interesting phenomenon can be seen from Table 2 that distances between clusters #A and #A' are much larger than distances of other pairs. This can support the early suggestion that complete relaxation of muscle takes time. In many cases, muscle morphology has not returned to the initial condition although torque has done.

To sum up the points which we have just indicated, the main finding of this study could conclude that quadriceps movement is nonlinear and the relative position between the quadriceps and femur is piecewise with the change of torque during one contraction-relaxation. In other words, the contraction of quadriceps may have gear shifting mechanism during isometric knee extension.

4. Conclusion

In this paper, we observed a gear shifting pattern of quadriceps. To validate our observation, we proposed a systematic strategy to analyze the isometric knee extension process via ultrasonography, video processing, and related signal processing techniques. Analysis results provide preliminary support for the phenomenon. To our knowledge, the present study is the first report to describe the gear shifting motion pattern during quadriceps contractions in human skeletal muscles.

However, there are still several limitations of this study. The number of participants is small. In future work, larger dataset would allow making further validation.

Appendix

A. Details of Guided Filtering Algorithm

The key assumption of the guided filter is that the filter output q is a linear transform of the guidance image I in a window ω_k centered at the pixel k:

$$q_i = a_k I_i + b_k, \quad \forall i \in \omega_k, \tag{A.1}$$

where (a_k, b_k) are some linear coefficients assumed to be constant in a square window ω_k with a radius r.

To determine the linear coefficients, the following cost function is minimized in the window:

$$E(a_k, b_k) = \sum_{i \in \omega_k} \left((a_k I_i + b_k - p_i)^2 + \varepsilon a_k^2 \right). \tag{A.2}$$

Here ε is a regularization parameter, I and q are identical and given as the input ultrasound image. The solution to (A.2) can be given by linear regression:

$$a_k = \frac{(1/|\omega|) \sum_{i \in \omega_k} I_i p_i - \mu_k \overline{p}_k}{\sigma_k^2 + \varepsilon} \tag{A.3}$$

$$b_k = \overline{p}_k - a_k \mu_k.$$

Here, μ_k and σ_k^2 are the mean and variance of I in ω_k, $|\omega|$ is the number of pixels in ω_k, and $\overline{p}_k = (1/|\omega|) \sum_{i \in \omega_k} p_i$ is the mean of p in ω_k.

So after computing (a_k, b_k) for all patches ω_k in the image, we compute the filter output by

$$q_i = \frac{1}{|\omega|} \sum_{k: i \in \omega_k} (a_k I_i + b_k). \tag{A.4}$$

B. Details of Local Binary Fitting Model

Consider the input image $I : \Omega \rightarrow \mathfrak{N}^2$, where Ω is the image domain. Let ϕ be the level set of a Lipschitz function; the gradient decent flow equation of the LBF energy functional is defined as

$$\frac{\partial \phi}{\partial t} = -\delta_\varepsilon(\phi)(\lambda_1 e_1 - \lambda_2 e_2) + \nu \delta_\varepsilon(\phi)$$
$$\cdot \operatorname{div}\left(\frac{\nabla \phi}{|\nabla \phi|}\right) + \mu \left(\nabla^2 \phi - \operatorname{div}\left(\frac{\nabla \phi}{|\nabla \phi|}\right)\right), \tag{B.1}$$

where λ_1, λ_2, ν, and μ are positive constants, K_σ is a Gaussian kernel function with parameter σ, δ_ε is the smooth Dirac function with parameter $\varepsilon = 1.0$, and e_1 and e_2 are the functions as follows:

$$e_1(x) = \int_\Omega K_\sigma(y - x) |I(x) - f_1(y)|^2 \, dy$$
$$e_2(x) = \int_\Omega K_\sigma(y - x) |I(x) - f_2(y)|^2 \, dy. \tag{B.2}$$

where K_σ is the Gaussian kernel with standard deviation σ, and f_1, f_2 are given by

$$f_1(x) = \frac{K_\sigma(x) * [H_\varepsilon(\phi(x)) I(x)]}{K_\sigma(x) * H_\varepsilon(\phi(x))}$$
$$f_2(x) = \frac{K_\sigma(x) * [1 - H_\varepsilon(\phi(x)) I(x)]}{K_\sigma(x) * [1 - H_\varepsilon(\phi(x))]}. \tag{B.3}$$

In practice, the Heaviside function H is approximated by a smooth function H_ε defined by

$$H_\varepsilon(x) = \frac{1}{2}\left[1 + \frac{2}{\pi} \arctan\left(\frac{x}{\varepsilon}\right)\right]. \tag{B.4}$$

The derivative of H_ε is the following smooth function:

$$\delta_\varepsilon(x) = H_\varepsilon'(x) = \frac{1}{\pi}\frac{\varepsilon}{\varepsilon^2 + \pi^2}. \tag{B.5}$$

Conflicts of Interest

The authors have no conflicts of interest.

Authors' Contributions

Shu Zhang and Weijian Huang contributed equally to the work.

Acknowledgments

References

[1] J. Basmajian and C. Deluca, *Muscle Alives*, Williams & Wilkins, Baltimore, Md, USA, 1985.

[2] M. V. Narici, T. Binzoni, E. Hiltbrand, J. Fasel, F. Terrier, and P. Cerretelli, "In vivo human gastrocnemius architecture with changing joint angle at rest and during graded isometric contraction," *The Journal of Physiology*, vol. 496, no. 1, pp. 287–297, 1996.

[3] P. Han, Y. Chen, L. Ao et al., "Automatic thickness estimation for skeletal muscle in ultrasonography: Evaluation of two enhancement methods," *Biomedical Engineering Online*, vol. 12, no. 1, article no. 6, 2013.

[4] P. W. Hodges, L. H. M. Pengel, R. D. Herbert, and S. C. Gandevia, "Measurement of muscle contraction with ultrasound imaging," *Muscle & Nerve*, vol. 27, no. 6, pp. 682–692, 2003.

[5] S. Ling, Y. Zhou, Y. Chen, Y.-Q. Zhao, L. Wang, and Y.-P. Zheng, "Automatic tracking of aponeuroses and estimation of muscle thickness in ultrasonography: A feasibility study," *IEEE Journal of Biomedical and Health Informatics*, vol. 17, no. 6, pp. 1031–1038, 2013.

[6] G. Misuri, S. Colagrande, M. Gorini et al., "In vivo ultrasound assessment of respiratory function of abdominal muscles in normal subjects," *European Respiratory Journal*, vol. 10, no. 12, pp. 2861–2867, 1997.

[7] T. Fukunaga, Y. Ichinose, M. Ito, Y. Kawakami, and S. Fukashiro, "Determination of fascicle length and pennation in a contracting human muscle in vivo," *Journal of Applied Physiology*, vol. 82, no. 1, pp. 354–358, 1997.

[8] M. Ito, Y. Kawakami, Y. Ichinose, S. Fukashiro, and T. Fukunaga, "Nonisometric behavior of fascicles during isometric contractions of a human muscle," *Journal of Applied Physiology*, vol. 85, no. 4, pp. 1230–1235, 1998.

[9] L. Mademli and A. Arampatzis, "Behaviour of the human gastrocnemius muscle architecture during submaximal isometric fatigue," *European Journal of Applied Physiology*, vol. 94, no. 5-6, pp. 611–617, 2005.

[10] C. N. Maganaris, V. Baltzopoulos, and A. J. Sargeant, "Repeated contractions alter the geometry of human skeletal muscle," *Journal of Applied Physiology*, vol. 93, no. 6, pp. 2089–2094, 2002.

[11] Y. Zhou, J.-Z. Li, G. Zhou, and Y.-P. Zheng, "Dynamic measurement of pennation angle of gastrocnemius muscles during contractions based on ultrasound imaging," *Biomedical Engineering Online*, vol. 11, article no. 63, 2012.

[12] Y. Zhou and Y.-P. Zheng, "Estimation of muscle fiber orientation in ultrasound images using revoting Hough transform (RVHT)," *Ultrasound in Medicine & Biology*, vol. 34, no. 9, pp. 1474–1481, 2008.

[13] C. N. Maganaris, V. Baltzopoulos, and A. J. Sargeant, "Human calf muscle responses during repeated isometric plantarflexions," *Journal of Biomechanics*, vol. 39, no. 7, pp. 1249–1255, 2006.

[14] N. D. Reeves, C. N. Maganaris, and M. V. Narici, "Ultrasonographic assessment of human skeletal muscle size," *European Journal of Applied Physiology*, vol. 91, no. 1, pp. 116–118, 2004.

[15] T. J. Dick and J. M. Wakeling, "Shifting gears: dynamic muscle shape changes and force-velocity behavior in the medial gastrocnemius," *Journal of Applied Physiology*, vol. 123, no. 6, pp. 1433–1442, 2017.

[16] X. Wei, J. Zhang, S.-C. Chan, H.-C. Wu, Y. Zhou, and Y.-P. Zheng, "Automatic Extraction of Central Tendon of Rectus Femoris (CT-RF) in Ultrasound Images Using a New Intensity-Compensated Free-Form Deformation-Based Tracking Algorithm with Local Shape Refinement," *IEEE Journal of Biomedical and Health Informatics*, vol. 21, no. 4, pp. 1058–1068, 2017.

[17] C. Li, C.-Y. Kao, J. C. Gore, and Z. Ding, "Implicit active contours driven by local binary fitting energy," in *Proceedings of the IEEE Computer Society Conference on Computer Vision and Pattern Recognition (CVPR '07)*, Minneapolis, Minn, USA, June 2007.

[18] X. Feng, X. Guo, and Q. Huang, "Systematic evaluation on speckle suppression methods in examination of ultrasound breast images," *Applied Sciences*, vol. 7, no. 1, p. 37, 2017.

[19] R. Killick, P. Fearnhead, and I. A. Eckley, "Optimal detection of changepoints with a linear computational cost," *Journal of the American Statistical Association*, vol. 107, no. 500, pp. 1590–1598, 2012.

Review Article

Machine Learning in Ultrasound Computer-Aided Diagnostic Systems: A Survey

Qinghua Huang [ID],[1,2] Fan Zhang,[3] and Xuelong Li[4]

[1]School of Mechanical Engineering and Center for OPTical IMagery Analysis and Learning (OPTIMAL),
 Northwestern Polytechnical University, Xi'an, Shaanxi 710072, China
[2]College of Information Engineering, Shenzhen University, Shenzhen 518060, China
[3]School of Electronic and Information Engineering, South China University of Technology, Guangzhou 510641, China
[4]Center for OPTical IMagery Analysis and Learning (OPTIMAL), Xi'an Institute of Optics and Precision Mechanics,
 Chinese Academy of Sciences, Xi'an, Shaanxi 710119, China

Correspondence should be addressed to Qinghua Huang; enicarwhw@qq.com

The ultrasound imaging is one of the most common schemes to detect diseases in the clinical practice. There are many advantages of ultrasound imaging such as safety, convenience, and low cost. However, reading ultrasound imaging is not easy. To support the diagnosis of clinicians and reduce the load of doctors, many ultrasound computer-aided diagnosis (CAD) systems are proposed. In recent years, the success of deep learning in the image classification and segmentation led to more and more scholars realizing the potential of performance improvement brought by utilizing the deep learning in the ultrasound CAD system. This paper summarized the research which focuses on the ultrasound CAD system utilizing machine learning technology in recent years. This study divided the ultrasound CAD system into two categories. One is the traditional ultrasound CAD system which employed the manmade feature and the other is the deep learning ultrasound CAD system. The major feature and the classifier employed by the traditional ultrasound CAD system are introduced. As for the deep learning ultrasound CAD, newest applications are summarized. This paper will be useful for researchers who focus on the ultrasound CAD system.

1. Introduction

For decades, ultrasound image has been extensively applied in the detection of different diseases because of its high safety and high efficiency [1–3], such as the breast cancer, the liver cancer, the gastroenteric disease [4], the cardiovascular diseases [5], spine curvature [6], and the muscle disease [7, 8]. However, it requires years of experience and training to read ultrasound image. The amount of training to be an excellent radiologist is high. In this background, the CAD became a powerful tool to assist radiologists diagnosing. The original CAD system was used to diagnose the breast tumor in the 1960s [9]. The CAD system helps the doctors and radiologists to diagnose from two views. One view is their experience; the other is the view of the computer. The application of CAD system improves the accuracy of diagnosis, reduces the time consumption, and decreases the load of doctors [10].

There are two important aspects of CAD research which are "Detection" and "Diagnosis," respectively [11]. "Detection" is defined as the technology to locate the lesion region of the image. It aims to reduce the observational burden of medical staffs. "Diagnosis" means the technology to identify the potential diseases. It aims to provide additional support for clinicians. In most of the CAD systems, the "Detection" and "Diagnosis" are associated. In the "Detection" phase, the lesion is segmented from the normal tissues, and in the "Diagnosis" phase, the lesion is evaluated to produce a diagnosis.

The ultrasound CAD system also consists of "Detection" and "Diagnosis." The ultrasound CAD system can be divided into four phases: image preprocessing, image segmentation, feature extraction, and lesion classification. Figure 1 shows the general flowchart of ultrasound CAD system.
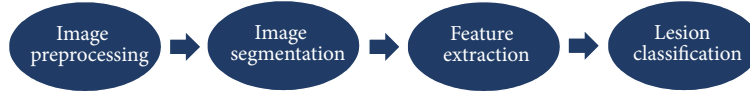
FIGURE 1: The general flowchart of CAD system.

In this article, we present an overview of recent developments in ultrasound CAD to support future studies. There have been many studies which summarized the research of ultrasound CAD [10, 12, 13]. Reference [10] presents a detailed overview of the breast ultrasound CAD research, and [12] presents an overview of liver ultrasound CAD researches. However, both of them ignored many new technologies of the deep learning which is one of the most revolutionary technologies in recent years. In this study, we present an overview of the traditional ultrasound CAD system and the ultrasound CAD system which applies deep learning technology. As for the traditional CAD system, this study focuses on the feature and the classifier. As for the deep learning ultrasound CAD system, the newest applications of deep learning technology in ultrasound CAD system are summarized.

2. Traditional Ultrasound CAD System

2.1. Feature. As for the traditional ultrasound CAD system, the feature selection and extraction are indispensable steps [29]. The effective features can improve the accuracy and decrease the computational complexity of the system. As for ultrasound CAD system, the collection of data is difficult. If the dimension of features is high and the size of the dataset is small, there will be "curse of dimensionality" occurring [30]. Thus, the selection of features is an important step for traditional ultrasound CAD system. The feature adopted by traditional ultrasound CAD can be divided into four categories: texture, morphologic, model-based, and descriptor features.

2.1.1. Texture. The texture is one of the most common features in the ultrasound CAD system. Texture features can reflect the character of the lesion surface. A few general utilized features are shown as follows.

Laws Texture Energy (LTE). This feature utilizes the local masks to detect the texture types [31]. In general, the size of masks is 5×5. The energy of texture is calculated by the local masks and represented by a vector.

Contrast of Gray Level Values. This feature is a measure of local variations in the image. It can be defined as

$$\text{CON} = \sum_{i,j} (i - j)^2 P_d(i, j),\tag{1}$$

where $P_d(i, j)$ is the probability of the pixel value (i, j) lying at distance d in the image.

Gray Level Cooccurrence Matrix (GLCM). GLCM reflects the distribution of cooccurring pixel grayscale values at a given offset. GLCM is a common feature in CAD system. The methods in [32, 33] have utilized GLCM to extract the texture features for breast tumor classification. The GLCM can be defined as

$$\text{COR} = \frac{\sum ij P_d(i, j) - m_x m_y}{\sqrt{S_x^2 S_y^2}},\tag{2}$$

where m_x, m_y, S_x^2, and S_y^2 are defined as

$$
\begin{aligned}
m_x &= \sum_i i \sum_j P_d(i, j), \\
m_y &= \sum_j j \sum_i P_d(i, j), \\
S_x^2 &= \sum_i i \sum_j P_d(i, j) - m_x^2, \\
S_y^2 &= \sum_j j \sum_i P_d(i, j) - m_y^2.
\end{aligned}
\tag{3}
$$

Local Binary Pattern (LBP). LBP is proposed by T. Ojala, M. Pietikäinen, and D. Harwood. It can reflect the local texture of ultrasound image. The LBP is defined in a 3×3 neighborhood. The center of the neighborhood is taken as the threshold. The other 8 gray values are compared to the threshold. If the value is larger than the threshold, that pixel will be marked by 1; otherwise, it will be marked by 0. In this approach, every 3×3 neighborhood will be transformed into an 8-bit binary number [34]. LBP possesses the rotation invariance and gray scale invariance.

Wavelet Features. This feature is derived from the wavelet transform of the ultrasound image. The wavelet transform is a generally used method in ultrasound image processing. The method in [21] utilized the wavelet packet transform to extract texture feature for the liver disease classification.

2.1.2. Morphology. Compared with the texture feature, the morphologic feature is more focused on the lesion. We summarized some common morphologic features as follows.

Spiculation. This feature reflects the smoothness of lesion margin. Reference [35] proposed a method to measure the speculation, which defined the spiculation as the ratio of low-frequency area to high-frequency area. This value is proportional to the possibility of the tumor being malignant.
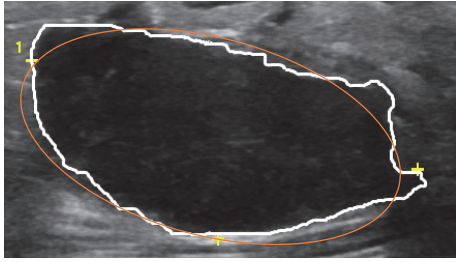
FIGURE 2: The equivalent ellipse (orange line) of a benign breast lesion.

Depth-to-Width Ratio. Depth-to-width ratio is an active feature for the classification of many tumors, which has been widely employed by many studies [1, 36]. The depth is defined as the largest difference between the y-axis values of two points on the margin of the tumor. The width means the largest difference between the x-axis values of two points on the margin of the tumor. As for the malignant tumor, the depth-to-width ratio is usually larger than 1, and the ratio of benign tumor is usually smaller than 1.

Elliptic-Normalized Circumference (ENC). ENC is the circumference ratio of the equivalent ellipse of the tumor which is defined as the ratio of the circumference of the ellipse to its diameter [3]. Figure 2 shows an example of equivalent ellipse of a benign breast lesion.

Elliptic-Normalized Skeleton (ENS). ENS is the number of skeleton points which are normalized by the perimeter of the equivalent ellipse. The larger the ENS is, the higher the possibility of malignancy is [3].

Long Axis-to-Short Axis Ratio (L : S). This feature is defined as the ratio of long axis to short axis. The long axis is the major axis of the equivalent ellipse, and the short axis is the minor axis of the ellipse [3].

2.1.3. The Feature Based on Statistical Model of the Backscattered Echo. The model-based feature is one of the unique features of ultrasound images. It reflects the character of the backscattered echo from tissues. Scholars utilized different models to simulate the echo of backscatter. The parameters of these models are employed as tools to classify the tumors.

Nakagami Model-Based Features. Nakagami model is one of the most common models of backscattered echo, which can be utilized to simulate different backscattered distributions. The parameter of Nakagami model is defined by the statistics of the backscattered echoes. The authors in [37] have attempted to utilize the Nakagami parameter as a feature to classify the breast lesion.

K-Distribution Model-Based Features. The feature based on K-distribution model is also widely used in ultrasound CAD system. Reference [38] utilized the parameter of log-compressed K distribution to classify the breast tumor. The experiment in [38] compared the performance of the method

employing K-α feature to the method without K-α feature. The result shows that the performance of method utilizing K-α feature is higher than the method without K-α feature.

2.1.4. Descriptor Features. The descriptor feature is usually summarized from the experience of clinicians. As for different applications, the descriptor feature is different. For example, as for the breast tumor, most of the descriptor features come from the breast imaging reporting and data system (BI-RADS) lexicon. But as for the thyroid nodules, most of the descriptors are attributes in thyroid imaging reporting and data system (TI-RADS) lexicon.

Shape (Round, Oval, or Irregular). Shape is a universal descriptor feature for classification of many tumors [2]. The regular shape like round and oval usually means that the tumor is benign. The shape of malignant tumor is always irregular.

Calcifications (Absent or Present). In general, there are more calcifications or microcalcifications in malignant tumor than in benign tumor.

Posterior Shadow or Posterior Echo. The posterior shadow or posterior echo reflects the characteristic of the posterior region of the tumor, where gray value is smaller than the region of the surrounding.

Echo Characteristic. This feature reflects the model of echo in the ultrasound image including hypoechoic, isoechoic, hyperechoic, and complex. The echo signal of different tissues shows different characteristic in the ultrasound image [39].

2.2. Classifiers. Most of ultrasound CAD systems are designed to classify the lesion such as the breast tumor, liver fibrosis, and thyroid nodules. The classifier is one of the most important parts in the lesion classification. After the selection and extraction of features, many classifiers are adopted to classify the ultrasound images. This section introduced the major classifiers employed by the ultrasound CAD system.

2.2.1. Linear Classifier. Linear discrimination analysis (LDA) [40] and logistic regression (LOGREG) [41] are two of the most widely used linear classifiers in the ultrasound CAD system. LDA is proposed by Fisher and is extensively used in medical image analysis [32, 42]. It aims to find the best linear combination of the features to divide the data into several categories. LOGREG is proposed by David Cox. It is a regression method which takes the feature as the argument and takes the category as the dependent variable. Both of the LDA and LOGREG are widely applied in medical field [43, 44]. However, the performance of the linear classifier is limited by the distribution of data. If the data is nonlinearly separable, the performance of linear classifier will be unsatisfactory.

2.2.2. Bayesian Classifier. The Bayesian classifier is one of the most frequently used methods in the machine learning field.

It can utilize the prior information of data to estimate the posterior information. The most famous Bayesian classifier is the Naïve Bayesian Classifier (NBC). NBC is based on the Bayesian theorem. It hypothesizes that the feature of samples is conditionally independent. There are only a few parameters of NBC which are required for estimation through the statistics of samples. Due to the advantage of insensitivity to data, NBC is widely applied in social information analysis and medical field. Reference [45] utilized the NBC as a classifier to distinguish the cardiovascular US images. The accuracy of the method reached 96.59% [45].

2.2.3. Support Vector Machine. The support vector machine (SVM) is a method in statistics and computer science to analyze data and recognize pattern. It is a supervised learning method which can be applied in both of classification and regression. The target of SVM is to build a hyperplane to divide the sample into different categories [46]. It utilized the kernel functions to map the original data into the higher dimensional space to find the decision hyperplane. SVM is widely applied in the analysis of ultrasound images [15, 47–49]. SVM can perform well in both of small dataset and large dataset. However, as the size of dataset increases, the complexity of SVM also grows. Meanwhile, the choice of kernel function also influences the performance of SVM.

2.2.4. Decision Tree. The decision tree is an effective algorithm for classification of ultrasound images [25, 50]. It can learn a classification rule from disorder data. Decision trees algorithm adopts the divide-and-conquer strategy to divide search space of problem into several subsets. The structure of decision tree is a flowchart. From top to bottom, every node calculates the feature value of input sample to decide which node to go to next. In leaf nodes, the final result of classification is given [51]. When the size of data is small and the feature value is not diverse, the construction of decision tree is simple and fast. However, if the size of data is large and the feature value is various, the complexity of decision tree algorithm will be huge.

2.2.5. Artificial Neural Network. Artificial neural network (ANN) is the machine learning model which is designed according to the human nervous system. In general, the architecture of ANN can be divided into three layers: the input layer, the hidden layer, and the output layer. The layer consists of the neuron. The number of the hidden layers and the number of the neurons in each layer are flexible. One of the most famous ANN is the back-propagation neural network (BPNN) [52]. BPNN is a feed-forward ANN with supervised learning process. It is widely used in the medical image analysis [53–55]. The train of ANN is a self-adaptive process. If the architecture is complex, it will take plenty of time to train the network.

2.2.6. AdaBoost. AdaBoost is one of the most popularly used ensemble methods proposed and has the ability to improve the classification accuracy by integrating multiple weak classifiers. AdaBoost method generates a series of weak classifiers firstly and builds a powerful classifier through weighted majority voting of the classes predicted by weak classifiers. Reference [38] utilized the multiclass AdaBoost to distinguish carcinomas, fibro adenomas, and cysts.

3. Ultrasound CAD System with Deep Learning Technology

In 2006, the professor of the University of Toronto, Hinton, and his student published the paper which utilized the neural network to reduce the dimensionality of data [56]. This paper is widely regarded as the beginning of the research in deep learning. In the following years, deep learning was extensively applied in many fields, such as image recognition, semantic analysis, and disease detection. The ultrasound CAD system is always a highly anticipated field where the deep learning can be applied. Many scholars have attempted to utilize the deep learning to assist the clinician.

The largest change from the traditional ultrasound CAD to deep learning ultrasound CAD is that the feature employed by deep learning ultrasound CAD system is not artificial. In the traditional ultrasound CAD system, most of the features are human-crafted, such as gray features and texture features. However, with the development of deep learning, the researchers noted that the feature extracted by the deep neural network is sometimes more effective than the feature designed by the human.

In this section, the newest applications of deep learning on the ultrasound CAD system are introduced. The major application field includes the breast lesion diagnosis, the liver lesion diagnosis, the fetal ultrasound standard plane detection, the thyroid nodule diagnosis, and the carotid ultrasound image classification.

3.1. The Breast Lesion Diagnosis. The breast tumor is one of the most common cancers for women. Thousands of women suffer from breast tumor all over the world. The early detection can decrease the death rate of the breast cancer significantly [57]. The ultrasonography is a safe and convenient scheme to detect the early breast lesion [58]. To support the clinician in diagnosis, many scholars attempted to utilize the deep learning technology to classify the breast lesion. Han et al. utilized the GoogLeNet to classify the breast image and the accuracy reached 90% [16]. They employed 4254 benign samples and 3154 malignant samples to train the deep neural network. The sufficient data support the GoogLeNet to reach an acceptable performance. However, more researchers cannot acquire enough data like Han et al. [16]. Most of them employed other deep learning methods to classify the breast lesion. Zhang et al. utilized the point-wise gated Boltzmann machine (PGBM) to extract the feature from shear-wave elastography (SWE) to classify the breast tumor [17]. The deep learning feature reached 93.4% accuracy. Cheng et al. utilized stacked denoising autoencoder (SDAE) technology to encode the ultrasound image and employed the softmax layer to classify the breast lesion [18]. Shi et al. employed the deep polynomial network to extract the textural feature from the ultrasound image and reach the accuracy of 90.40% [19].

The deep learning technology is widely applied in the breast ultrasound image. However, most of the studies are limited by the number of samples. Methods adopted by these studies usually utilized the deep learning technology as a tool to generate the representation of images. Only [16] utilized the convolutional neural network (CNN) like GoogLeNet to classify the ultrasound image directly.

3.2. The Liver Lesion Diagnosis. The liver disease has been a menace to humans for a long time. The incidence and mortality of the liver disease grow yearly. The ultrasonography is one of the most common techniques to detect the liver disease. Many researchers have attempted to employ deep learning technology to support the doctor diagnosis by liver ultrasound image. Reference [22] utilized the sparse autoencoder to acquire the representation of the liver ultrasound image and utilized the softmax layer to distinguish different focal liver diseases. Compared with support vector machines method, the method proposed in [22] reaches higher accuracy.

Liver fibrosis classification is also a high profile field of research. Meng et al. utilized the VGGNet and fully connected network (FCN) to differentiate the level of liver fibrosis [23]. To address the shortage of samples, Meng et al. employed the transfer learning (TL) technology. Meng et al. divided the liver fibrosis level into three phases: normal, early stage fibrosis (S1–S3), and late-stage fibrosis (S4). The accuracy of their method reached 93.90%. Similarly to Meng et al., Liu et al. utilized deep learning technology to diagnose the cirrhosis [24]. In the study of Liu et al., CNN is employed as a tool to generate features from ultrasound images. Liu et al. adopted the SVM as the classifier to distinguish the normal liver and the diseased liver, and the accuracy of the proposed method reached 96.8% which is much higher than the accuracy of low-level features.

The deep learning is a powerful tool to detect the liver diseases from ultrasound liver images. According to the experiment result of [23, 24], the application of deep learning technology can significantly improve the accuracy of liver diseases diagnosis.

3.3. The Fetal Ultrasound Standard Plane Detection. The ultrasound imaging is one of the most common technologies in the prenatal examination for being economic and safe. Standard plane selection is one of the necessary phases in the ultrasound examination [59, 60]. The clinician can estimate subsequent biometric information of fetus from the fetal ultrasound standard plane. Many scholars have attempted to utilize the machine learning technology to detect the fetal ultrasound standard plane automatically. With the popularity of deep learning, the researchers began to utilize the deep learning to distinguish the fetal ultrasound plane. The fetal facial standard plane is one type of the fetal ultrasound standard plane. From the fetal facial standard plane, the doctor can measure the biparietal diameter of the fetus and detect the malformation. Yu et al. employed the CNN to classify the fetal ultrasound plane. Their method reached the accuracy of 93.03% which is much higher than the accuracy of the traditional method [61]. However, the time consumption

of training which often takes more than 80 hours for the method is very expensive.

The study of Yu et al. focuses on one type of the fetal ultrasound standard plane. Their method cannot distinguish other types of the fetal ultrasound standard plane. Chen et al. proposed a deep learning framework which can detect different types of the fetal ultrasound standard plane [62]. Chen et al. employed the CNN and long short-term memory (LSTM) model to classify the fetal abdominal standard plane (FASP), the fetal face axial standard plane (FFASP), and the fetal four-chamber view standard plane (FFVSP). The CNN is responsible for extracting features from ROI images, and the LSTM model is responsible for the classification. Although the method proposed by Chen et al. [62] can classify different types of the fetal ultrasound standard, its performance is slightly lower than the method in [61]. The accuracy of FASP is 90.80%, the accuracy of FFASP is 86.70%, and the accuracy of FFVSP is 86.70%.

Besides the fetal ultrasound standard plane, the deep learning was also applied in the detection of fetal neurosonographic diagnostic plane. The fetal neurosonographic diagnostic plane can help the clinician to estimate the growth of fetal head and detect the serious central nervous system anomalies. Reference [63] proposed a method which employed CNN to detect the fetal neurosonographic diagnostic plane. The experiment result shows that the method in [63] has a similar accuracy to a specialist's performance.

The fetal ultrasound standard plane detection is one of the research fields where the deep learning can be applied. Unlike the breast lesions diagnosis and liver diseases diagnosis, the collection of the fetal ultrasound standard plane samples is more convenient. There are sufficient samples which can be utilized to train the deep learning network.

3.4. The Thyroid Nodule Diagnosis. The thyroid nodule is a common disease upon a world scale. The ultrasound imaging is a widely employed scheme to detect the thyroid nodule. To support the doctor to diagnose the thyroid nodule, many CAD systems were proposed. With the breakthrough of deep learning, many scholars focus on the method which employs the deep learning to classify the thyroid nodule. Chi et al. employed the GoogLeNet to classify the thyroid nodule [27]. To address the shortage of data, Chi et al. utilized the Deep Learning Caffe library [64] to fine-tune the GoogLeNet. The accuracy of their method reached 99.13%. Reference [28] presented a method which employed cascade CNN to detect and classify the thyroid nodule. The cascade CNN in [28] includes two CNNs. The first CNN was responsible for the segmentation of thyroid nodules, and the second CNN was utilized to classify the thyroid nodules. The experiment shows that the cascade CNN method outperforms other traditional machine learning methods.

The deep learning can improve the performance of thyroid nodule diagnosis significantly. However, the time consumption of train the deep learning network is also enormous. In [28], the training time of cascade CNN which is accelerated by GPU is more than 106 hours. The more complex the model is, the larger the cost of training is.

3.5. The Carotid Ultrasound Image Classification. The mortality of cardiovascular diseases increases yearly. The atherosclerotic plaque is the major reason of cardiovascular diseases. In the early detection of atherosclerosis, the intima-media thickness (IMT) of the carotid artery is an important indicator. IMT is the distance between the lumen-intima interface (LII) and the media-adventitia interface (MAI). The doctor usually utilized the ultrasound image to measure the IMT. To support the diagnosis of doctors, the researcher has attempted to utilize the deep learning to acquire the IMT automatically. Reference [65] utilized the autoencoder to segment LII and MAI. The IMT was acquired by calculating the distance between two levels. The error of the method in [65] is much smaller than traditional methods.

Besides the calculation of IMT, the deep learning method also is applied to detect the composition of plaque. Reference [66] utilized CNN to classify different tissues of plaque including lipid core, fibrous tissue, and calcified tissue. The experiment shows that the classification accuracy of CNN is much better than SVM.

3.6. Other Applications. Besides the application mentioned above, there are some other applications of deep learning on the ultrasound CAD system. The study in [67] applied CNN to classify the type of myositis including inclusion body myositis (IBM), polymyositis (PM), and dermatomyositis (DM). Reference [67] compared the performances of CNN and random forests. The accuracy of CNN for normal versus affected tissues (DM, PM, and IBM) reached 76.2% which is 3.9% higher than this value of random forests. Hetherington et al. designed a spine level identification system employing CNN [68]. The system can accurately detect the vertebral level so that the anesthesiologist can find the right site to inject the anaesthetic. Cheng and Malhi utilized CNN to classify the abdominal ultrasound images [69]. In the paper, Cheng and Malhi divided the abdominal ultrasound images into 11 categories including liver left longitudinal, liver left transverse, liver right longitudinal, liver right transverse, spleen, pancreas, kidney left longitudinal, kidney left transverse, kidney right longitudinal, kidney right transverse, and gallbladder. The mean accuracy of classification reached 77.9%.

4. Performance Summary

In this section, we summarized the performance of various techniques in the different application fields. Table 1 shows the performance of breast ultrasound CAD system. Table 2 shows the performance of liver ultrasound CAD system. Table 3 shows the performance of thyroid ultrasound CAD system.

5. Discussion and Conclusions

In this study, we summarized the literature about the ultrasound CAD system. This study divided the ultrasound CAD system into two categories. One is the traditional ultrasound CAD system which employs the manmade feature. The major feature and major classifier adopted by the traditional

ultrasound CAD system are introduced. Another category is the deep learning ultrasound CAD system which employs the deep neural network to extract features and classify them. The newest applications of deep learning on the ultrasound CAD system were summarized.

As for the traditional ultrasound CAD system, the selection of feature impacts the performance of final diagnosis. The common feature employed by traditional ultrasound CAD system can be divided into four categories: textural features, morphologic features, model-based features, and descriptor features. The textural feature is one of the earliest adopted features in the ultrasound CAD system. TEM, GLDS, GLCM, and other textual features are widely applied in the classification of liver diseases and breast lesions. The morphologic feature is a powerful feature in the traditional ultrasound CAD system. It contains the prior knowledge of clinicians. Morphologic features like spiculation and depth-to-width ratio are designed according to the experience of clinicians. These features are extracted from the ultrasound image automatically and are extensively adopted in the ultrasound CAD system. Model-based features are based on the backscattered echo of ultrasound images. Nakagami model-based features and *K*-distribution model-based features are two common model-based features. The descriptor feature is usually summarized from clinical experience. As for the different application, the descriptor feature is different.

The classifiers employed by traditional ultrasound CAD system are divided into 6 categories: linear classifier, Bayesian method, SVM, decision tree, ANN, and AdaBoost. Both of the linear classifier and Bayesian method are common classifiers in the machine learning field. These two classifiers are convenient to use. However, the performance of them is not stable on all of the data. The decision tree is also a simple algorithm, and the complexity of it is low. The SVM is a powerful classifier. It can perform well even in the small dataset. As for ANN, there is no certain rule in the design of ANN. It is flexible and widely applicable. The AdaBoost can integrate the output of weak classifiers to get a robust classification result.

The largest difference between the deep learning ultrasound CAD system and traditional ultrasound CAD system is the approach of extracting features. In the traditional ultrasound CAD system, the feature is designed by the human. But in the deep learning ultrasound CAD system, the feature is extracted by deep learning network automatically. This paper introduced the newest application of deep learning on the ultrasound CAD system. The application field includes the breast lesion diagnosis, the liver lesion diagnosis, the fetal ultrasound standard plane detection, the thyroid nodule diagnosis, and the carotid ultrasound image classification.

This study summarized the performance of ultrasound CAD in three fields including breast tumor classification, liver diseases, and thyroid nodule diagnosis. It can be seen that the dataset employed by these studies is different. There are huge differences in the size and the modality of the dataset employed by different methods. It is hard to fairly evaluate the performance of different methods utilizing different datasets. The construction of standard dataset for different ultrasound CAD applications is an important task in further studies.

Table 1: The performance summary of breast ultrasound CAD system.

Reference	Dataset	Features	Classifiers	Performance
[14]	88 benign 90 malignant	Textural features + morphologic features	ANN (BPNN)	Accuracy: 95.86% Sensitivity: 95.14% Specificity: 96.58%
[15]	70 benign 50 malignant	Textural features + morphologic features	SVM	Accuracy: 95.83% Sensitivity: 96% Specificity: 95.71%
[16]	4254 benign 3154 malignant	GoogLeNet		Accuracy: 91.23% Sensitivity: 84.29% Specificity: 96.07%
[17]	135 benign 92 malignant	Boltzmann machine		Accuracy: 93.4% Sensitivity: 88.6% Specificity: 97.1%
[18]	275 benign 245 malignant	Stacked denoising Autoencoder (SDAE)		Accuracy: 82.4% Sensitivity: 78.7% Specificity: 85.7%
[19]	100 benign 100 malignant	Deep polynomial network	SVM	Accuracy: 92.40% Sensitivity: 92.67% Specificity: 91.36%

Table 2: The performance summary of liver ultrasound CAD system.

Reference	Dataset	Features	Classifiers	Performance
[20]	50 normal 50 fatty liver disease (FLD)	Textural features	ANN	Accuracy: 98% Sensitivity: 100% Specificity: 96%
[21]	15 normal 16 cirrhotic 25 hepatocellular carcinoma (HCC)	Textural features	SVM	Accuracy: 88.8%
[22]	44 cyst 18 hemangioma 30 HCC 16 normal	Sparse autoencoder		Accuracy: 90.50% Sensitivity: 91.60% Specificity: 88.50%
[23]	79 normal 89 early-stage fibrosis 111 late-stage fibrosis	VGGNet	FCN	Accuracy: 93.90% Sensitivity: 88.6% Specificity: 97.1%
[24]	47 cirrhosis 44 normal	CNN	SVM	Accuracy: 86.9%

Table 3: The performance summary of thyroid ultrasound CAD system.

Reference	Dataset	Features	Classifiers	Performance
[25]	48 benign 223 malignant	Textural features	Decision tree: C4.5	Accuracy: 94.3%
[26]	10 benign 10 malignant	Textural features	AdaBoost	Accuracy: 100% Sensitivity: 100% Specificity: 100%
[27]	71 benign 357 malignant	GoogLeNet		Accuracy: 99.13% Sensitivity: 99.70% Specificity: 95.80%
[28]	465 normal 9957 thyroid nodular lesions	CNN (15 convolutional layers)	CNN (4 convolutional layers)	AUC: 0.986

On the other hand, the collection of ultrasound data is also a problem. Deep learning methods require plenty of samples to train the network. However, the size of the dataset employed by most of the studies mentioned above is still small. The shortage of ultrasound samples is one of the obstacles in the way of applying deep learning.

Conflicts of Interest

The authors declare that they have no conflicts of interest.

References

[1] K. Drukker, M. L. Giger, K. Horsch, M. A. Kupinski, C. J. Vyborny, and E. B. Mendelson, "Computerized lesion detection on breast ultrasound," *Medical Physics*, vol. 29, no. 7, pp. 1438–1446, 2002.

[2] B. Sahiner, H.-P. Chan, M. A. Roubidoux et al., "Malignant and benign breast masses on 3D US volumetric images: effect of computer-aided diagnosis on radiologist accuracy," *Radiology*, vol. 242, no. 3, pp. 716–724, 2007.

[3] C.-M. Chen, Y.-H. Chou, K.-C. Han et al., "Breast lesions on sonograms: computer-aided diagnosis with nearly setting-independent features and artificial neural networks," *Radiology*, vol. 226, no. 2, pp. 504–514, 2003.

[4] X. Wang, V. Seetohul, R. Chen et al., "Development of a mechanical scanning device with high-frequency ultrasound transducer for ultrasonic capsule endoscopy," *IEEE Transactions on Medical Imaging*, vol. 36, no. 9, pp. 1922–1929, 2017.

[5] W. Qiu, X. Wang, Y. Chen et al., "Modulated Excitation Imaging System for Intravascular Ultrasound," *IEEE Transactions on Biomedical Engineering*, vol. 64, no. 8, pp. 1935–1942, 2017.

[6] G.-Q. Zhou, W.-W. Jiang, K.-L. Lai, and Y.-P. Zheng, "Automatic Measurement of Spine Curvature on 3-D Ultrasound Volume Projection Image with Phase Features," *IEEE Transactions on Medical Imaging*, vol. 36, no. 6, pp. 1250–1262, 2017.

[7] G.-Q. Zhou and Y.-P. Zheng, "Automatic Fascicle Length Estimation on Muscle Ultrasound Images With an Orientation-Sensitive Segmentation," *IEEE Transactions on Biomedical Engineering*, vol. 62, no. 12, pp. 2828–2836, 2015.

[8] G.-Q. Zhou, P. Chan, and Y.-P. Zheng, "Automatic measurement of pennation angle and fascicle length of gastrocnemius muscles using real-time ultrasound imaging," *Ultrasonics*, vol. 57, no. C, pp. 72–83, 2015.

[9] R. Takahashi and Y. Kajikawa, "Computer-aided diagnosis: A survey with bibliometric analysis," *International Journal of Medical Informatics*, vol. 101, pp. 58–67, 2017.

[10] H. D. Cheng, J. Shan, W. Ju, Y. Guo, and L. Zhang, "Automated breast cancer detection and classification using ultrasound images: a survey," *Pattern Recognition*, vol. 43, no. 1, pp. 299–317, 2010.

[11] A. Mansoor, U. Bagci, B. Foster et al., "Segmentation and image analysis of abnormal lungs at CT: Current approaches, challenges, and future trends," *RadioGraphics*, vol. 35, no. 4, pp. 1056–1076, 2015.

[12] M. Y. Jabarulla and H.-N. Lee, "Computer aided diagnostic system for ultrasound liver images: A systematic review," *Optik - International Journal for Light and Electron Optics*, vol. 140, pp. 1114–1126, 2017.

[13] Q. Huang, Y. Luo, and Q. Zhang, "Breast ultrasound image segmentation: a survey," *International Journal for Computer Assisted Radiology and Surgery*, vol. 12, no. 3, pp. 493–507, 2017.

[14] B. K. Singh, K. Verma, and A. S. Thoke, "Fuzzy cluster based neural network classifier for classifying breast tumors in ultrasound images," *Expert Systems with Applications*, vol. 66, pp. 114–123, 2016.

[15] K. M. Prabusankarlal, P. Thirumoorthy, and R. Manavalan, "Assessment of combined textural and morphological features for diagnosis of breast masses in ultrasound," *Human-centric Computing and Information Sciences*, vol. 5, no. 1, 2015.

[16] S. Han, H. K. Kang, J. Y. Jeong et al., "A deep learning framework for supporting the classification of breast lesions in ultrasound images," *Medicine & Biology*, 2017.

[17] Q. Zhang, Y. Xiao, W. Dai et al., "Deep learning based classification of breast tumors with shear-wave elastography," *Ultrasonics*, vol. 72, pp. 150–157, 2016.

[18] J.-Z. Cheng, D. Ni, Y.-H. Chou et al., "Computer-Aided Diagnosis with Deep Learning Architecture: Applications to Breast Lesions in US Images and Pulmonary Nodules in CT Scans," *Scientific Reports*, vol. 6, Article ID 24454, 2016.

[19] J. Shi, S. Zhou, X. Liu, Q. Zhang, M. Lu, and T. Wang, "Stacked deep polynomial network based representation learning for tumor classification with small ultrasound image dataset," *Neurocomputing*, vol. 194, pp. 87–94, 2016.

[20] U. R. Acharya, H. Fujita, V. K. Sudarshan et al., "An integrated index for identification of fatty liver disease using radon transform and discrete cosine transform features in ultrasound images," *Information Fusion*, vol. 31, pp. 43–53, 2016.

[21] J. Virmani, V. Kumar, N. Kalra, and N. Khandelwal, "SVM-based characterization of liver ultrasound images using wavelet packet texture descriptors," *Journal of Digital Imaging*, vol. 26, no. 3, pp. 530–543, 2013.

[22] T. M. Hassan, M. Elmogy, and E.-S. Sallam, "Diagnosis of Focal Liver Diseases Based on Deep Learning Technique for Ultrasound Images," *Arabian Journal for Science and Engineering*, vol. 42, no. 8, pp. 3127–3140, 2017.

[23] D. Meng, L. Zhang, G. Cao, W. Cao, G. Zhang, and B. Hu, "Liver Fibrosis Classification Based on Transfer Learning and FCNet for Ultrasound Images," *IEEE Access*, vol. 5, pp. 5804–5810, 2017.

[24] X. Liu, J. Song, J. S. Hong Wang, J. Zhao, and Y. Chen, "Learning to diagnose cirrhosis with liver capsule guided ultrasound image classification," *Sensors*, vol. 17, no. 1, article no. 149, 2017.

[25] U. R. Acharya, P. Chowriappa, H. Fujita et al., "Thyroid lesion classification in 242 patient population using Gabor transform features from high resolution ultrasound images," *Knowledge-Based Systems*, vol. 107, pp. 235–245, 2016.

[26] U. R. Acharya, O. Faust, S. V. Sree, F. Molinari, and J. S. Suri, "ThyroScreen system: High resolution ultrasound thyroid image characterization into benign and malignant classes using novel combination of texture and discrete wavelet transform," *Computer Methods and Programs in Biomedicine*, vol. 107, no. 2, pp. 233–241, 2012.

[27] J. Chi, E. Walia, P. Babyn, J. Wang, G. Groot, and M. Eramian, "Thyroid Nodule Classification in Ultrasound Images by Fine-Tuning Deep Convolutional Neural Network," *Journal of Digital Imaging*, vol. 30, no. 4, pp. 477–486, 2017.

[28] J. Ma, F. Wu, T. Jiang, J. Zhu, and D. Kong, "Cascade convolutional neural networks for automatic detection of thyroid nodules in ultrasound images," *Medical Physics*, vol. 44, no. 5, pp. 1678–1691, 2017.

[29] R. Ravindraiah and K. Tejaswini, "A survey of image segmentation algorithms based on fuzzy clustering," *International Journal of Computer Science and Mobile Computing*, vol. 2, no. 7, pp. 200–206, 2013.

[30] V. Cherkassky and F. Mulier, "Learning from Data: Concepts, Theory, and Methods: Second Edition," *Learning from Data: Concepts, Theory, and Methods: Second Edition*, pp. 1–538, 2006.

[31] K. I. Laws, "Texture Energy Measures," in *Image Understanding Workshop*, pp. 47–51, 1979.

[32] W. Gómez, W. C. A. Pereira, and A. F. C. Infantosi, "Analysis of co-occurrence texture statistics as a function of gray-level quantization for classifying breast ultrasound," *IEEE Transactions on Medical Imaging*, vol. 31, no. 10, pp. 1889–1899, 2012.

[33] Q. Zhang, C. Li, H. Han et al., "Spatio-Temporal Quantification of Carotid Plaque Neovascularization on Contrast Enhanced Ultrasound: Correlation with Visual Grading and Histopathology," *European Journal of Vascular and Endovascular Surgery*, vol. 50, no. 3, pp. 289–296, 2015.

[34] M. Abdel-Nasser, J. Melendez, A. Moreno, O. A. Omer, and D. Puig, "Breast tumor classification in ultrasound images using texture analysis and super-resolution methods," *Engineering Applications of Artificial Intelligence*, vol. 59, pp. 84–92, 2017.

[35] S. Joo, Y. S. Yang, W. K. Moon, and H. C. Kim, "Computer-aided diagnosis of solid breast nodules: use of an artificial neural network based on multiple sonographic features," *IEEE Transactions on Medical Imaging*, vol. 23, no. 10, pp. 1292–1300, 2004.

[36] K. Horsch, M. L. Giger, L. A. Venta, and C. J. Vyborny, "Computerized diagnosis of breast lesions on ultrasound," *Medical Physics*, vol. 29, no. 2, pp. 157–164, 2002.

[37] P. M. Shankar, V. A. Dumane, J. M. Reid et al., "Classification of ultrasonic B-mode images of breast masses using Nakagami distribution," *IEEE Transactions on Ultrasonics, Ferroelectrics and Frequency Control*, vol. 48, no. 2, pp. 569–580, 2001.

[38] A. Takemura, A. Shimizu, and K. Hamamoto, "Discrimination of breast tumors in ultrasonic images using an ensemble classifier based on the adaboost algorithm with feature selection," *IEEE Transactions on Medical Imaging*, vol. 29, no. 3, pp. 598–609, 2010.

[39] M. Costantini, P. Belli, R. Lombardi, G. Franceschini, A. Mulè, and L. Bonomo, "Characterization of solid breast masses: Use of the sonographic breast imaging reporting and data system lexicon," *Journal of Ultrasound in Medicine*, vol. 25, no. 5, pp. 649–659, 2006.

[40] C. J. Huberty, "Discriminant Analysis," *Review of Educational Research*, vol. 45, no. 4, pp. 543–598, 1975.

[41] J. C. Rice, "Logistic regression: An introduction," in *Advances in social science methodology*, vol. 3, pp. 191–245, 1994.

[42] M. Caixinha, M. Santos, and J. Santos, "Automatic Cataract Hardness Classification Ex Vivo by Ultrasound Techniques," *Ultrasound in Medicine & Biology*, vol. 42, no. 4, pp. 989–998, 2016.

[43] S. Milutinovic, G. Radunovic, K. Veljkovic et al., "Development of ultrasound enthesitis score to identify patients with enthesitis having spondyloarthritis: Prospective, double-blinded, controlled study," *Clinical and Experimental Rheumatology*, vol. 33, no. 6, pp. 812–817, 2015.

[44] Q. Zhang, C. Li, H. Han, L. Yang, Y. Wang, and W. Wang, "Computer-aided quantification of contrast agent spatial distribution within atherosclerotic plaque in contrast-enhanced ultrasound image sequences," *Biomedical Signal Processing and Control*, vol. 13, no. 1, pp. 50–61, 2014.

[45] J. Ding, H. D. Cheng, J. Huang, J. Liu, and Y. Zhang, "Breast ultrasound image classification based on multiple-instance learning," *Journal of Digital Imaging*, vol. 25, no. 5, pp. 620–627, 2012.

[46] N. Cristianini and J. Shawe-Taylor, *An Introduction to Support Vector Machines*, Cambridge University Press, Cambridge,UK, 2000.

[47] L. Cai, X. Wang, Y. Wang, Y. Guo, J. Yu, and Y. Wang, "Robust phase-based texture descriptor for classification of breast ultrasound images," *Biomedical Engineering Online*, vol. 14, no. 1, article no. 26, p. 1, 2015.

[48] P.-L. Yen, H.-K. Wu, H.-S. Tseng et al., "Vascular morphologic information of three-dimensional power Doppler ultrasound is valuable in the classification of breast lesions," *Clinical Imaging*, vol. 36, no. 4, pp. 267–271, 2012.

[49] Q. Zhang, J. Suo, W. Chang, J. Shi, and M. Chen, "Dual-modal computer-assisted evaluation of axillary lymph node metastasis in breast cancer patients on both real-time elastography and B-mode ultrasound," *European Journal of Radiology*, vol. 95, pp. 66–74, 2017.

[50] U. R. Acharya, S. V. Sree, M. M. Rama Krishnan et al., "Computer-aided diagnostic system for detection of Hashimoto thyroiditis on ultrasound images from a Polish population," *Journal of Ultrasound in Medicine*, vol. 33, no. 2, pp. 245–253, 2014.

[51] T. Subba Rao, "Classification, parameter estimation and state estimation - an engineering approach using MATLAB," *Journal of Time Series Analysis*, vol. 32, no. 2, 194 pages, 2011.

[52] Y. Hirose, K. Yamashita, and S. Hijiya, "Back-propagation algorithm which varies the number of hidden units," *Neural Networks*, vol. 4, no. 1, pp. 61–66, 1991.

[53] W. K. Moon, J. W. Choi, N. Cho et al., "Computer-aided analysis of ultrasound elasticity images for classification of benign and malignant breast masses," *American Journal of Roentgenology*, vol. 195, no. 6, pp. 1460–1465, 2010.

[54] X.-F. Diao, X.-Y. Zhang, T.-F. Wang, S.-P. Chen, Y. Yang, and L. Zhong, "Highly sensitive computer aided diagnosis system for breast tumor based on color Doppler flow images," *Journal of Medical Systems*, vol. 35, no. 5, pp. 801–809, 2011.

[55] Y.-H. Huang, J.-H. Chen, Y.-C. Chang et al., "Diagnosis of solid breast tumors using vessel analysis in three-dimensional power Doppler ultrasound images," *Journal of Digital Imaging*, vol. 26, no. 4, pp. 731–739, 2013.

[56] G. E. Hinton and R. R. Salakhutdinov, "Reducing the dimensionality of data with neural networks," *American Association for the Advancement of Science: Science*, vol. 313, no. 5786, pp. 504–507, 2006.

[57] Q. Huang, F. Yang, L. Liu, and X. Li, "Automatic segmentation of breast lesions for interaction in ultrasonic computer-aided diagnosis," *Information Sciences*, vol. 314, pp. 293–310, 2015.

[58] X. Feng, X. Guo, and Q. Huang, "Systematic evaluation on speckle suppression methods in examination of ultrasound breast images," *Applied Sciences*, vol. 7, no. 1, p. 37, 2017.

[59] H. Chen, Q. Dou, D. Ni et al., "Automatic fetal ultrasound standard plane detection using knowledge transferred recurrent neural networks," *Lecture Notes in Computer Science (including subseries Lecture Notes in Artificial Intelligence and Lecture Notes in Bioinformatics): Preface*, vol. 9349, pp. 507–514, 2015.

[60] L. Wu, J.-Z. Cheng, S. Li, B. Lei, T. Wang, and D. Ni, "FUIQA: Fetal ultrasound image quality assessment with deep convolutional networks," *IEEE Transactions on Cybernetics*, vol. 47, no. 5, pp. 1336–1349, 2017.

[61] Z. Yu, E.-L. Tan, D. Ni et al., "A Deep Convolutional Neural Network Based Framework for Automatic Fetal Facial Standard Plane Recognition," *IEEE Journal of Biomedical & Health Informatics*, vol. 99, no. 1, 2017.

[62] H. Chen, L. Wu, Q. Dou et al., "Ultrasound Standard Plane Detection Using a Composite Neural Network Framework," *IEEE Transactions on Cybernetics*, vol. 47, no. 6, pp. 1576–1586, 2017.

[63] M. Yaqub, B. Kelly, A. T. Papageorghiou, and J. A. Noble, "A Deep Learning Solution for Automatic Fetal Neurosonographic Diagnostic Plane Verification Using Clinical Standard Constraints," *Ultrasound in Medicine & Biology*, 2017.

[64] Y. Jia, E. Shelhamer, J. Donahue et al., "Caffe: convolutional architecture for fast feature embedding," in *Proceedings of the ACM International Conference on Multimedia*, pp. 675–678, ACM, Orlando, Fla, USA, November 2014.

[65] R.-M. Menchón-Lara, J.-L. Sancho-Gómez, and A. Bueno-Crespo, "Early-stage atherosclerosis detection using deep learning over carotid ultrasound images," *Applied Soft Computing*, vol. 49, pp. 616–628, 2016.

[66] K. Lekadir, A. Galimzianova, A. Betriu et al., "A Convolutional Neural Network for Automatic Characterization of Plaque Composition in Carotid Ultrasound," *IEEE Journal of Biomedical and Health Informatics*, vol. 21, no. 1, pp. 48–55, 2017.

[67] P. Burlina, S. Billings, N. Joshi, and J. Albayda, "Automated diagnosis of myositis from muscle ultrasound: Exploring the use of machine learning and deep learning methods," *PLoS ONE*, vol. 12, no. 8, Article ID e0184059, 2017.

[68] J. Hetherington, V. Lessoway, V. Gunka, P. Abolmaesumi, and R. Rohling, "SLIDE: automatic spine level identification system using a deep convolutional neural network," *International Journal for Computer Assisted Radiology and Surgery*, vol. 2, no. 7, pp. 1–10, 2017.

[69] P. M. Cheng and H. S. Malhi, "Transfer Learning with Convolutional Neural Networks for Classification of Abdominal Ultrasound Images," *Journal of Digital Imaging*, vol. 30, no. 2, pp. 234–243, 2017.

Research Article

A Normalized Shear Deformation Indicator for Ultrasound Strain Elastography in Breast Tissues: An *In Vivo* Feasibility Study

Jingfeng Jiang [1,2] **and Bo Peng**[3]

[1]*Department of Biomedical Engineering, Michigan Technological University, 1400 Townsend Drive, Houghton, MI 49931, USA*
[2]*Department of Medical Physics, University of Wisconsin-Madison, Madison, WI 53705, USA*
[3]*School of Computer Science, Southwest Petroleum University, Chengdu 610500, China*

Correspondence should be addressed to Jingfeng Jiang; jjiang1@mtu.edu

The shear deformation under loads contains useful information for distinguishing benign breast lesions from malignant ones. In this study, we proposed a normalized shear deformation indicator (NSDI) that was derived from the concept of principal strains. Since the NSDI requires both high-quality axial and lateral (parallel and perpendicular to the beam, resp.) displacement estimates, a strategy combining high-quality speckle tracking with signal "denoising" was employed. Both techniques were previously published by our group. Finite element (FE) models were used to identify possible causes for elevated NSDI values in and around breast lesions, followed by an analysis of ultrasound data acquired from 26 biopsy-confirmed *in vivo* breast lesions. We found that, theoretically, the elevated NSDI values could be attributed to two factors: significantly hardened tissue stiffness and increasing heterogeneity. The analysis of *in vivo* data showed that the proposed NSDI values were higher ($p < 0.05$) among malignant cancers as compared to those measured from benign ones. In conclusion, our preliminary results demonstrated that the calculation of NSDI value is feasible and NSDI could add value to breast lesion differentiation with current clinical equipment as a postprocessing tool.

1. Introduction

According to the US National Institute of Cancer, an estimated 252,710 new cases of invasive breast cancer are expected to be diagnosed in 2017. In light of the widespread use of the ultrasound, American College of Radiology has developed a BI-RADS lexicon to standardize the characterization of breast lesions under ultrasound [1]. Through analyzing BIRADS 3–5 lesions, Hille et al. reported that the sensitivity and specificity were 92% and 85%, respectively [2]. Their result suggested that ultrasound probably should not be used alone as the first line of imaging.

In the last two decades, a lot of efforts have been devoted to ultrasound strain elastography (SE) [3]. In Ultrasound SE, tissue displacements are first tracked by correlating radio frequency (RF) signals before and after compression. Then, axial (parallel to the acoustic beam direction) strain defined by the change in length divided by the length before compression can be used as a surrogate for relative tissue elasticity. Ultrasound SE has been successfully applied to noninvasive differentiation of breast tumors [4–7] with several identified metrics: area ratio, elasticity score, strain ratio, and length ratio. The first metric is known as the area ratio which was defined as the ratio between the tumor area measured from the axial strain elastogram and the tumor area appearing on the B-mode image [4, 5, 7]. Typically, a large area ratio (e.g., >1.0) is correlated to an increasing possibility of malignancy. The second metric used a scoring system [6], in which the overall tumor appearance on the axial strain elastogram was rated between 1 and 5 based on a set of graphic criteria. The strain ratio between the tumor and a selected region containing background tissue was also adopted by numerous studies [4, 8, 9]. The fourth metric is the length ratio. The length ratio is defined as the lesion length measured from the

axial strain elastogram over that which appeared on the B-mode image. Based on several published meta-analyses [10–12], the sensitivity of these four metrics often varied from 80% to 98%, while the specificity typically ranged from 85% to 95%. Considerable inter- and intraobserver variability was also reported [13].

Continued research efforts have been devoted to improving the efficacy of ultrasound SE. Excellent work was done by Dr. Thittai and colleagues [14, 15] to use shear information (i.e., the shape change) for the breast lesion differentiation. Recall that previously discussed four metrics were derived from the axial strains only reflecting the dimensional changes under the external compression. The shear strain is defined as follows [16]:

$$\tau_{xy} = \frac{1}{2}\left(\frac{\partial u}{\partial x} + \frac{\partial v}{\partial y}\right), \qquad (1)$$

where u, v, x, and y are the axial and lateral displacements and lateral and axial spatial coordinates, respectively. In the literature, studies [9, 15] stipulated that shear strains could be useful in terms of characterization of the lesion mobility. Because of the poor quality among lateral displacements v, only the first component on the right-hand side of (1) was used. Thittai and colleagues named this technology axial-shear strain elastography. Although feasibility studies [9, 15] have demonstrated its usefulness, the axial-shear strain alone, theoretically, cannot be used as an indicator of shear deformation because it contains rigid-body rotation.

Normalization of axial-shear strain data has been attempted by others [17]. However, their approach was an ad hoc approach and only attempted to scale the axial-shear strain with the fitted local axial strain. Toward this end, the primary objective of this study was to develop an alternative but more rigorous method to assess the shear deformation based on the continuum mechanics. More specifically, the proposed normalized shear deformation indicator (NSDI) leverages the well-established concept of principle strain [16], requiring all three components of the 2D strain tensor: axial strain, lateral strain, and (full) shear strain. Consequently, the proposed NSDI metric requires both high-quality axial and lateral displacement estimates.

In order to improve lateral displacement quality, a published image denoising approach that enforces tissue incompressibility [18] was adopted for our convenience. Our denoising approach is conceptually similar to the work of Lubinski et al. [19] because both methods attempt to enforce the tissue incompressibility. However, main difference does exist. In the work of Lubinski et al., a laterally fixed central line within the tissue being imaged was required and such a laterally fixed line would be difficult to find from data acquired from *in vivo* tissues. In contrast, our denoising approach has no special requirement other than a two-dimensional ultrasonically estimated displacement vector field.

Toward this end, the primary objectives of this study are to (1) understand factors that influence the calculation of the NSDI metric through simplified finite element (FE)

models and (2) demonstrate the feasibility of quantifying NSDI *in vivo*. The second objective was evaluated using *in vivo* breast ultrasound data acquired from biopsy-confirmed breast lesions [5].

2. Materials and Methods

2.1. Definition of Normalized Shear Deformation Indicator (NSDI). Given the lateral strain ϵ_{xx}, axial strain ϵ_{yy}, and shear strain ϵ_{xy}, θ_p below is an angle between the first principle strain ϵ_1 and the positive direction of the lateral direction and can be evaluated as follows [16]:

$$\theta_p = \frac{1}{2}atan\left(\frac{2\epsilon_{xy}}{\epsilon_{xx} - \epsilon_{yy}}\right). \qquad (2)$$

When there is no presence of shear strain (i.e., $\epsilon_{xy} = 0$), θ_p is equal to zero. With the increase of the shear strain ϵ_{xy}, the absolute value of θ_p increases, indicating that the shear strain ϵ_{xy} plays a more prominent role. Eventually, under certain conditions (e.g., the pure shear condition $\epsilon_{xx} = \epsilon_{yy} = 0$), θ_p becomes $\pi/4$. Since the absolute value of θ_p ranges from 0 to $\pi/4$, θ_p can be normalized (hereafter referred to as normalized shear deformation indicator (NSDI)) as follows:

$$NSDI = \frac{|\theta_p|}{\pi/4}. \qquad (3)$$

Consequently, the NSDI metric represents a relative measure of the local shear deformation.

2.2. Implementation. There are three major steps in the proposed NSDI assessment; as stated before, methods from two of our previous publications [18, 20] were adopted for our convenience. In the first step, tracking *in vivo* tissue deformation was achieved through accumulations of smaller deformation as a multistep process [20, 21]. More formally, given a sequence of N ultrasound echo fields under a monotonic compression, sequential motion tracking was first performed between two adjacent frames using a published speckle tracking algorithm [20]. The tracking kernel size is approximately 1.5 mm (lateral; approximately one beam width) × 1.8 mm (axial; approximately 6 wavelength long at 7.5 MHz). Once all $(N - 1)$ frame-to-frame displacement fields were obtained, all displacements were mapped to the coordinate system of the first ultrasound echo frame using B-spline interpolations [20] and then all spatially registered frame-to-frame displacements were summed to obtain the accumulated displacement estimates $(\tilde{u}, \tilde{v})$ from the first frame to the Nth frame. More details of this speckle tracking method can be found elsewhere [20]. Leveraging the availability of graphic processing units (GPUs), this algorithm has been implemented using a parallel computing platform CUDA (NVIDIA Inc., CA, USA).

In the second step, given a 2D displacement vector field $(\tilde{u}, \tilde{v})$ from a rectilinear domain Ω, obtaining a "regularized"

displacement vector field (u, v) on Ω is equivalent to minimize the following energy function [18]:

$$F(u, v) = \int_\Omega \left(\frac{\partial u}{\partial x} + \frac{\partial v}{\partial y} \right)^2 d\Omega + \lambda_1 \int_\Omega (\tilde{u} - u)^2 d\Omega + \lambda_2 \int_\Omega (\tilde{v} - v)^2 d\Omega, \tag{4}$$

where λ_1 and λ_2 are two positive parameters and are also known as the regularization constants. On the right-hand side of (4), the first item is the calculated incompressibility from the regularized displacement field (u, v), while the second and third items are two individual fidelity terms of the ultrasonically measured axial ($\tilde{u}$) and lateral ($\tilde{v}$) displacements, respectively. λ_1 and λ_2 control the trade-offs between the fidelity and the degree of tissue incompressibility. Details regarding solving (4) by the Euler-Lagrange variation of $F(u, v)$ can be found in [18].

In the third step, the regularized displacement vector field (u, v) was used to estimate local strains, that is, ϵ_{xx} (lateral strain), ϵ_{yy} (axial strain), and ϵ_{xy} (shear strain). All three local strains were estimated using a low-pass-filter-based method [23] and windows used for axial and lateral strain estimation were both 1.8 mm. Finally, the proposed NSDI values were calculated and were used to form an image.

2.3. Finite Element Analysis.

The 2D finite element analysis (FEA) was done using a commercial FEA package (ADPL version 17.0, ANSYS, Inc., Canonsburg, PA). Five different cases simulated along with their rationales are described below.

Case 1 (varying deformation level). Typically, the tissue deformation under the freehand scanning from frame to frame varies [5]. In this study, varied levels of deformation occurring *in vivo* (0.25%–5%) were investigated.

Case 2 (heterogeneity within the inclusion). A recent study [24] found that mechanical properties in and around breast cancers are more heterogeneous as compared to benign ones. This is consistent with cancer biology because cancer's microenvironment and the spatial distribution of the desmoplastic reaction are usually complex. Hence, the influence of these heterogeneities was investigated.

Case 3 (varying the modulus ratio between the inclusion and the background). It is well known that pathological evolution of breast lesions influences their mechanical properties [25]. Measurements from 10 *in vivo* breast lesions indicated that the (initial) shear modulus ratios between the lesion and the background approximately varied between 4 and 30 [26]. Thus, the modulus ratio was varied accordingly in a comparable range to investigate how this modulus ratio may influence the calculation of NSDI.

Case 4 (varying inclusion size). Based on breast ultrasound, the size of breast lesions varies [27]. Thus, we decided to vary the diameter of the inclusion from 4 to 12 mm to understand how the size of the inclusion would affect the calculation of NSDI.

Case 5 (varying connectivity between the inclusion and the background). Typically, clinical studies using axial-shear strain elastography found that axial-shear patterns among malignant cancers were different as compared to benign breast lesions [9, 15]. Prior studies have attributed the difference to the fact that benign breast tumors are often more loosely connected to the background and were felt by physicians as "bouncy." Similar to the study conducted by Thitaikumar et al. [14], the friction coefficient was varied to quantify how the varying connectivity would affect the NSDI.

In Cases 1 and 3–5, we simulated a circular hard inclusion embedded into a homogeneous background (40 mm by 40 mm) and this geometry was similar to the model used in [14]. In all 5 cases, displacement boundary conditions were applied. More specifically, all FEA models were compressed from the top for a fixed percentage and free to move on the sides (i.e., no lateral confinement). In the bottom boundary, the geometry was free to move along the lateral direction as well. Poisson's ratio value was set to 0.495 for both the background and inclusion. Contact elements were used to model the interface between the background and the inclusion. In the ANSYS software, friction coefficients of the inclusion and the background interface can be adjusted so that different degrees of bonding between the inclusion and the background can be achieved. In this study, friction coefficients of 0.1 and 1000 were used to represent a slipping boundary and a tightly connected/bonded condition, respectively. The friction coefficient of infinite corresponds to a fully bonded inclusion. In Case 2, five randomly positioned secondary inclusions (1.5 mm diameter and twice harder than the large 10 mm inclusion) were included as shown in Figure 1(a). More detailed descriptions of Cases 1–5 are summarized in Table 1.

3D FEA analysis was also performed using a complex numerical breast phantom (i.e., lesion 2 phantom in a previous publication [22]). Boundary conditions and material properties of the lesion 2 phantom were identical to those presented in the previous publication [22]. In order to keep the current study concise, interested readers are referred to that prior publication for details. Based on FEA-simulated displacements, NSDI values were also calculated for an "image" plane of the lesion 2 phantom (see Figure 1(b)).

2.4. Experimental Design.

In vivo data with pathologically confirmed breast lesions were used to demonstrate the feasibility of utility of the NSDI metric in a clinical workflow. From an archived database of ultrasound scans of human breast lesions, 26 RF echo data sets were arbitrarily chosen. Among them, there were 13 cases of fibroadenoma (FA) and 13 cases of cancers (9 cases of invasive ductal carcinomas [IDC] and 4 cases of unspecified cancers). Once the motion tracking in a sequence was done, the accumulative strains approximately ranged from 0.5% to 15% (mean ± one standard deviation; 3.2% ± 3.0%) in those 26 cases. The detailed protocol for data acquisition was previously reported [5].

All data acquisition was approved by appropriate oversighting institutional review boards (IRBs) and patient consents were obtained. The IRB at the Michigan Technological

TABLE 1: Descriptions of 5 simulated cases. The modulus ratio is the shear modulus ratio between the inclusion and background.

Case number	Modulus ratio	Inclusion size	Background-inclusion interface	Deformation level	Other information
1	4	10 mm	Bonded and slipping (friction coefficient = 0.1)	0.25%–5%	Plane strain
2	5	10 mm	Bonded	1%	Smaller targets within the inclusion
3	2–20	10 mm	Bonded and slipping (friction coefficient = 0.1)	1%	Plane strain
4	4	4–12 mm	Bonded and slipping (friction coefficient = 0.1)	1%	Plane strain
5	4	10 mm	Varying slipping condition (friction coefficient = [0.1 1000])	1%	Plane strain
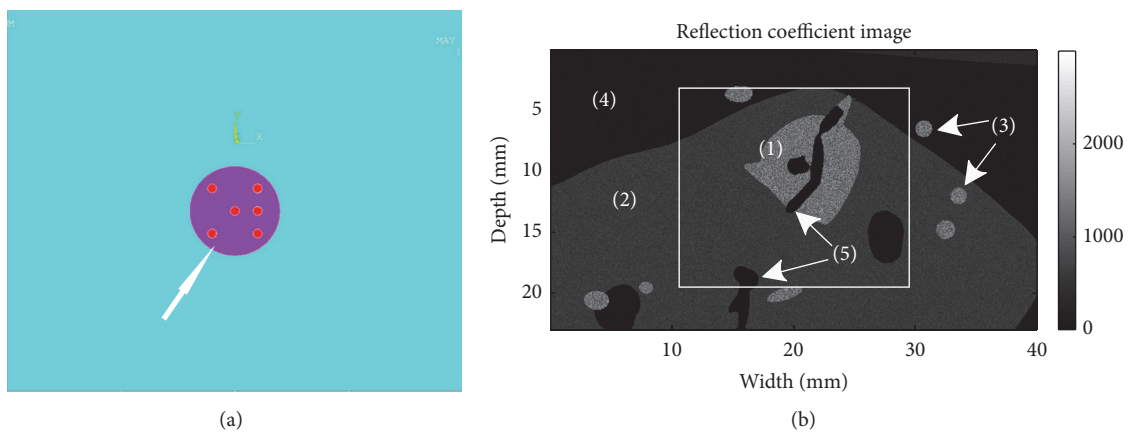
FIGURE 1: Illustrations of two FEA models: (a) a 2D heterogeneous inclusion model and (b) the middle "image" plane of a complex numerical breast phantom (i.e., lesion 2 phantom in a previous publication [22]). In (a), the arrow points to smaller harder inclusions inside the large inclusion. In (b), (1)–(5) denote lesion, fibroglandular tissue, Cooper's ligaments, breast fat, and necrotic zone, respectively.

University approved a secondary analysis of existing data. All *in vivo* data analyses including the manual lesion segmentation were done by a biomedical engineer who has approximately 15-year experience in strain elastography including algorithm development, data acquisition, and image analysis.

During the manual segmentation of a breast lesion, the operator first read a sequence of B-mode and strain images to decide the approximate location and contour of the breast lesion. The approximate location and contour of the lesion were used to set expectations of the lesion size and location. Then, B-mode and (axial and shear) strain images selected from that breast lesion were displayed side-by-side in MATLAB (MathWorks, Inc., MA, USA). Using image contrast provided by B-mode and strain images, the operator manually delineated the respective contours of the breast lesion. If there was little or no image contrast around a part of the lesion boundary, the operator would use a smooth curve to connect the gap(s) that existed around the lesion boundary. The final contours made sure that lesion locations in strain images should have good correspondence to these in B-mode images. However, achieving similar lesion morphology between the B-mode and strain images was attempted by the operator. It is worth noting that improved delineation of breast masses could be obtained with a board-certified radiologist.

3. Results

3.1. FEA Results. Figures 2(a) and 2(b) present images of the NDSI obtained around a fully connected and a loosely connected (friction coefficient of 0.1) inclusion. Regardless of the simulated connectivity, the high concentration of NSDI was observed around the interface between the inclusion and the background. Comparing Figure 2(a) with Figure 2(b), we found that the estimated NSDI was higher around the interface in the case of the loosely bonded inclusion and the high NDSI values spread both inward and outward from the interface. In the case of the fully bonded inclusion, the high NSDI values only spread outward from the interface. The overall pattern of the NDSI distribution in Figures 2(a) and 2(b) was symmetric given the circular inclusion. When the tissue heterogeneity (Figure 2(c)) was included, "packets" of high NSDI values occurred within the inclusion (Figure 2(a) versus Figure 2(c)) on the NSDI image, thereby suggesting
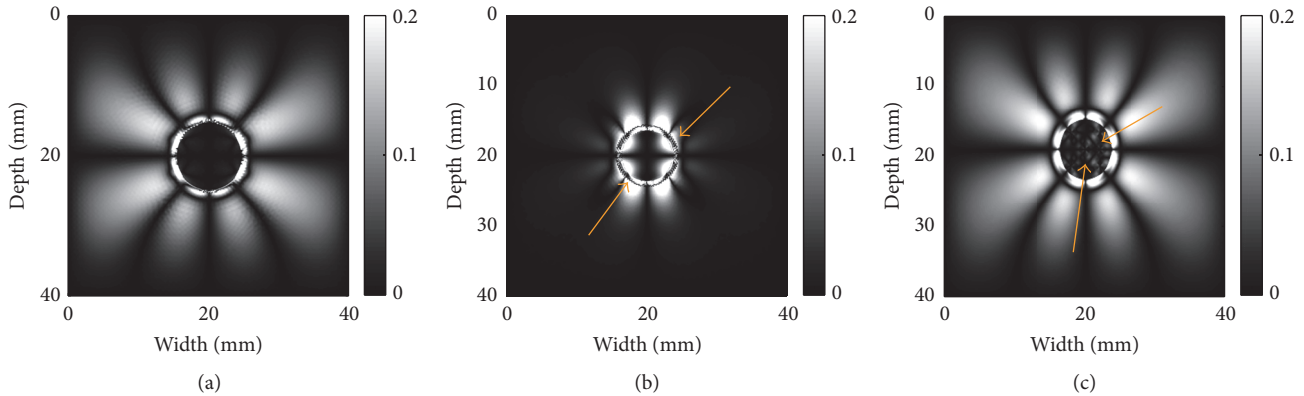
FIGURE 2: Images of calculated NSDI: (a) a 10 mm inclusion bonded to the background (Case 1), (b) a 10 mm inclusion loosely connected to the background (Case 1), and (c) an 8 mm inclusion bonded to the background (Case 2). Arrows in (b) point to high NSDI values around the slipping interface between the inclusion and the background, while the arrow in (c) points to the high NSDI values inside the inclusion.

that the NDSI could be a tool for visualization of breast lesion heterogeneity.

Mean values of the NDSI were calculated within the shaded region of interest (ROI; see Figure 3(a)) around the inclusion for 4 cases investigated (Cases 1 and 3–5). Of note, the shaded ROI had the same size as the size of the inclusion. Figure 3(b) shows that the mean NSDI values at different values of applied compression remained stable. However, the calculated mean NSDI values considerably increased with the increase of the modulus ratio as shown in Figure 3(c). This increasing trend was more obvious in the fully bonded condition. The estimated mean NSDI values were plotted out when the inclusion size increased from 4 mm to 12 mm in Figure 3(d). The calculated NSDI only slightly changed with different levels of compression (3% or less) and with the increase of inclusion size (approximately 12–15%). Also, this trend was not dependent on the connectivity between the inclusion and the background. We also found that the change of the friction coefficient (as an indicator of the connectivity between the inclusion and the background) had little (10% or less) influence over the mean NSDI values (Figure 3(e)). In Figure 3(e), the small fluctuation that occurred when the friction coefficient was around 1 was largely due to the fact that the finite element solution of contact mechanics is a high nonlinear process [28].

In the 3D complex breast phantom (see Figure 1(b)), the boundary of the simulated tumor was clearly visible in both the axial strain image (Figure 4(b)) and the NSDI image (Figure 4(c)). We also found that areas with high NSDI values located close to these tissue interfaces (see the tumor-glandular tissue boundary and the glandular-fat interface in Figure 1(b)). In Figure 4(c), the simulated ductal structure was visible in the NSDI images.

3.2. In Vivo Results. NSDI values were calculated within the corresponding segmented lesions and outside the respective lesions (i.e., an area outside the lesion whose size was equal to the corresponding lesion size; see Figure 3(a)). Of note, the lesion segmentation was conducted on respective axial strain elastograms. Hereafter, we differentiate NDSI values calculated from inside and outside the lesion. They are referred to as the inside NDSI value and outside NDSI value, respectively. A scatter plot displaying the outside NSDI against the inside NSDI is shown in Figure 5(a). As consistent with the scatter plot, based on the Wilcoxon rank-sum test, both the outside and inside NSDI values were significantly lower among benign breast tumors as compared to these among malignant breast cancers ($p < 0.001$ and $p = 0.025$, resp.). Furthermore, the other scatter plot showing the outside NSDI with respect to the size ratio (defined as the lesion size measured from the axial strain elastogram over the lesion size obtained from the corresponding B-mode image) is shown in Figure 5(b). Visually, combining the outside NSDI and the size ratio [4, 5] can separate breast lesions into two clusters, showing good promise.

Three representative examples (one fibroadenoma [FA], one invasive ductal carcinoma [IDC], and one unspecified cancer) were provided in Figures 6–8, respectively. Notably, the outside NSDI values around the FA were considerably lower than these seen around the IDC (Figure 6(b) versus Figures 7(b) and 8(b)). It is also interesting to note that, in 3 out 9 IDC cases, the duct-like structure was visible in the NSDI image (see Figure 7(b)). In the IDC case, the lesion boundary in the shear strain image (Figure 7(c)) was better visualized, whereas the lesion boundary in the axial strain elastogram (Figure 7(d)) was barely visible. In the case of the unspecified breast cancer (i.e., Figure 8), the oscillation of high and low values of NSDI can be seen in Figure 8(b). We stipulate that this is likely due to the tissue heterogeneity as demonstrated by the simplified finite element model (see Figure 2(c)).

4. Discussions

Typically, host stromal responses to the aggressive invasion of carcinomas stimulate the pervasive growth of dense fibrous tissue around the tumor (also known as desmoplastic reaction [29]), probably causing a spatial distribution of heterogeneous and significantly hardened stroma. A recent elastography study conducted by Liu et al. [24] demonstrated
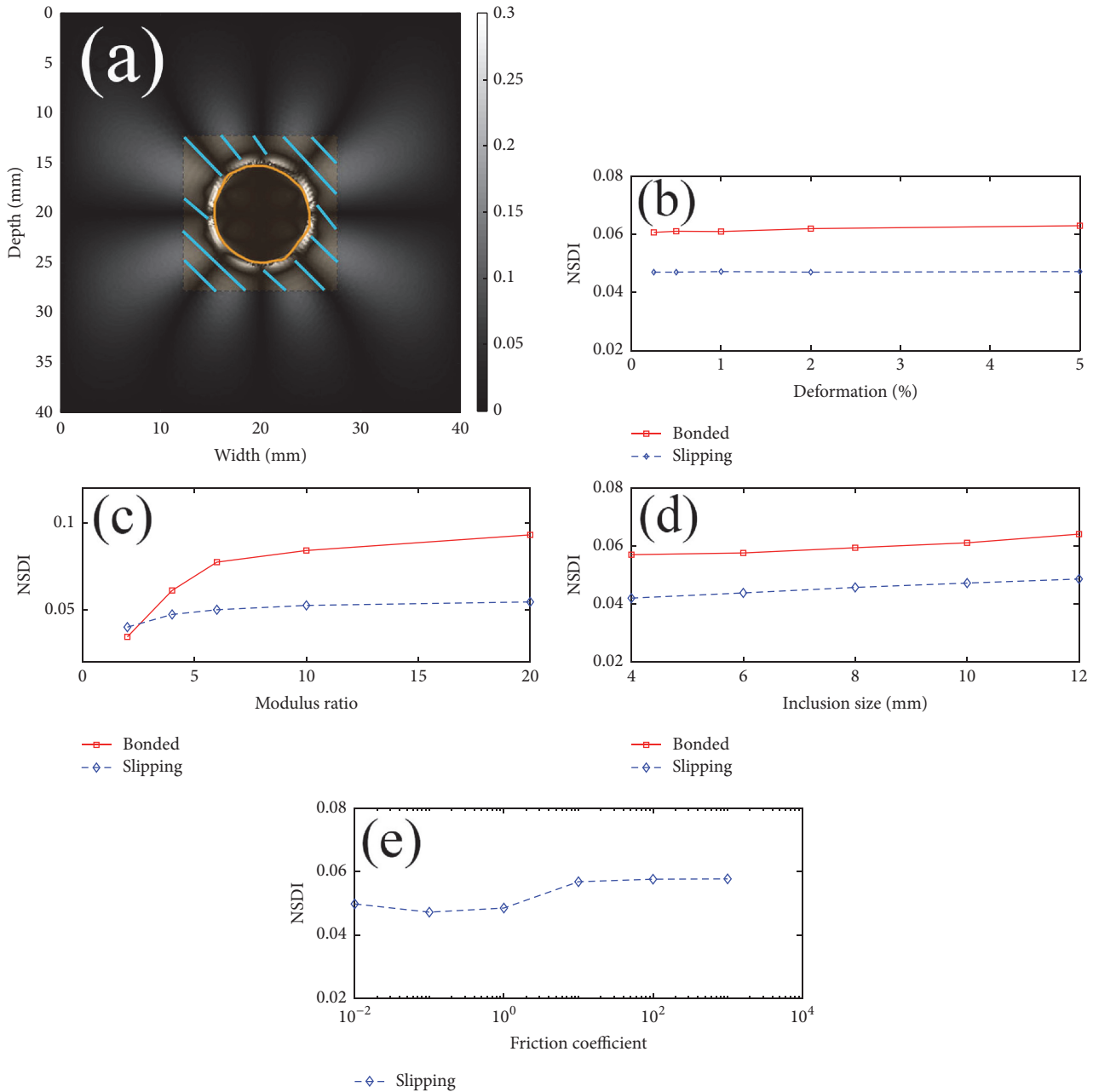
FIGURE 3: (a) An image illustrating how NSDI was calculated around a 10 mm inclusion (Case 1: modulus ratio of 4, bonded interface, and 1% deformation). The inclusion was delineated by the manually segmented contour in orange color, while the rectangular shaded region centered around the inclusion was calculated by a computer program. The rectangular shaded area outside the inclusion had the same area as that of the inclusion. Four NSDI plots are calculated for (b) Case 1, (c) Case 3, (d) Case 4, and (e) Case 5.

that malignant masses have more heterogeneous distributions of tissue modulus, as compared to benign ones. Also, the invasion of cancerous cells tends to follow "specific" low resistance directions around the cancer-stromal interface, and this pattern of growth leads to "stellate" appearance [30], probably causing malignant cancers to firmly connect to their surrounding tissues [31]. This firm connection could cause malignant tumors to be less mobile as compared to benign ones. Consequently, these biological implications could be used to justify the existence of firm connectivity and stiffness

heterogeneity among malignant breast cancers. As we learned from the FEA experiment (see the summary in Table 2), these two factors led to high outside and inside NSDI values.

Many clinical studies in breast SE [6, 7] have been often performed using axial strain elastogram data. Our result suggested that additional information such as shear strain elastogram and the NSDI image may provide useful information. For instance, both our FEA simulation and *in vivo* experiment indicated that the NSDI could depict the duct-like structure, which could be an indication of IDC.
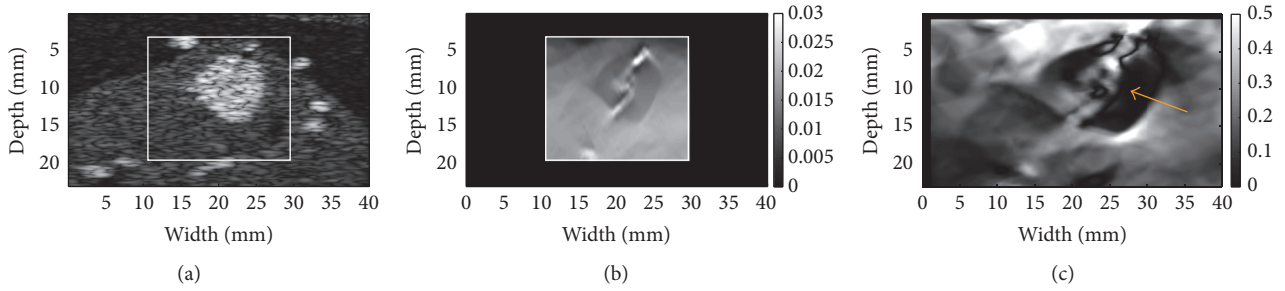
FIGURE 4: Results from a complex numerical breast phantom (i.e., lesion 2 phantom in a previous publication [22]): (a) a B-mode image simulated by Field II where a rectangular box depicts a ROI, (b) an FE-simulated axial strain image, and (c) an NSDI image within the ROI. In (c), arrow points to the suspected artifact due to the presence of the duct structure.
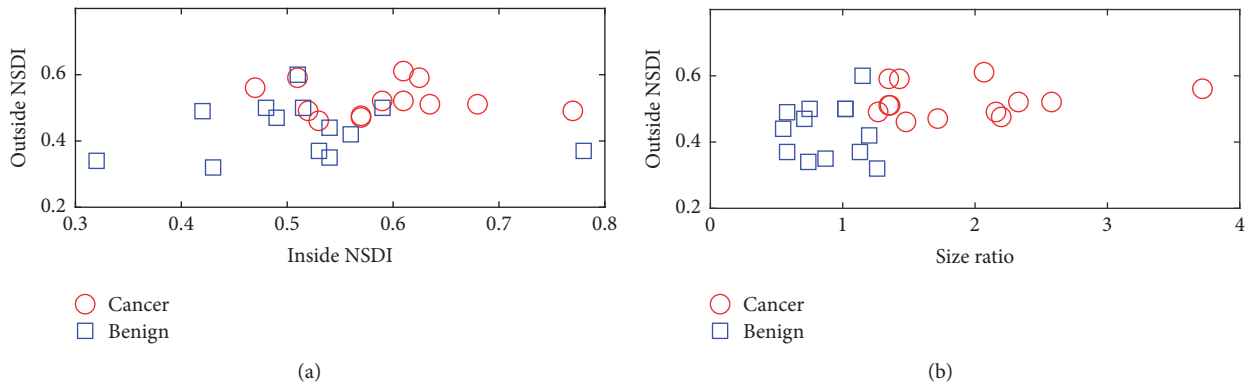
FIGURE 5: Scatter plots: (a) inside NSDI versus outside NSDI and (b) size ratio versus outside NSDI from 26 *in vivo* breast lesions. The size ratio is the lesion size measured from the axial strain elastogram over the lesion size measured from the corresponding B-mode image.
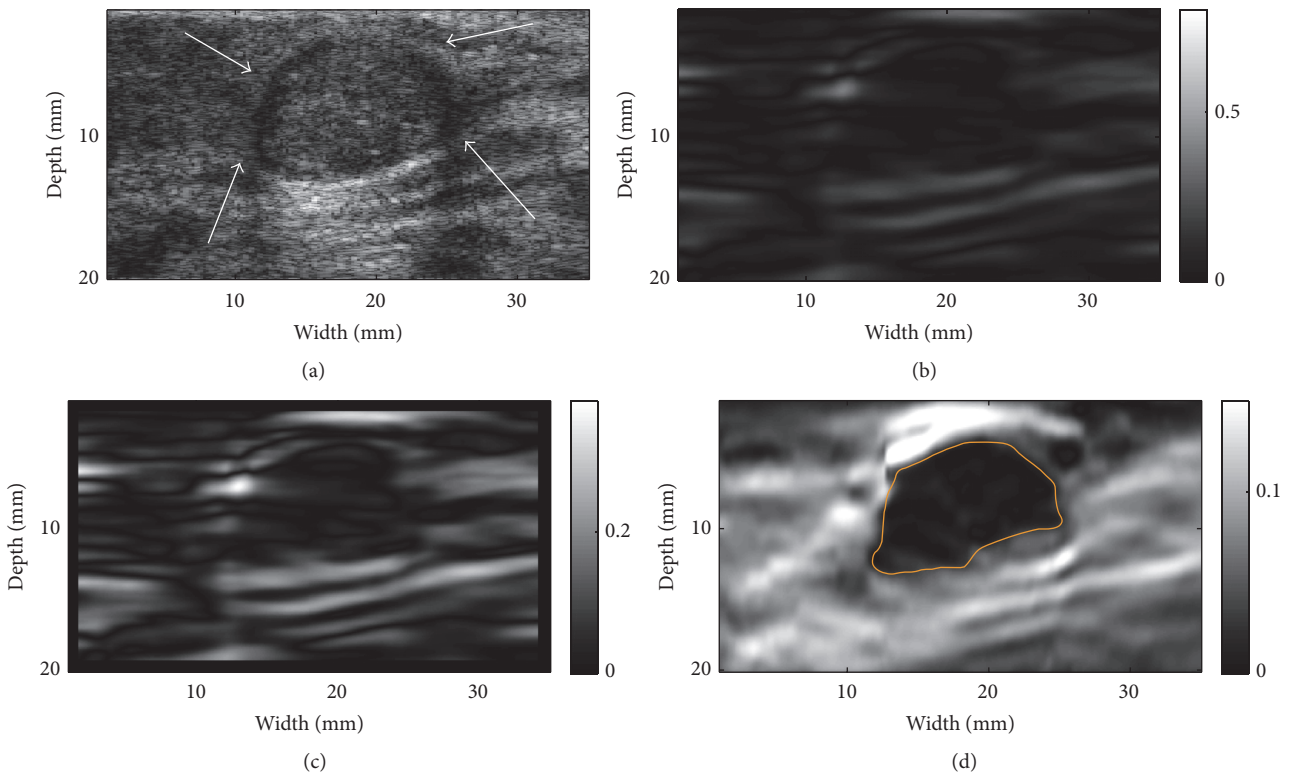
FIGURE 6: Resultant images of a fibroadenoma (FA): (a) A B-mode image indicating the lesion (see arrows), (b) an NSDI image, (c) a shear strain elastogram, and (d) an axial strain elastogram. The contour on (d) is the segmented target boundary and was used for calculations of NSDI for this case.

(a)

(b)

(c)

(d)
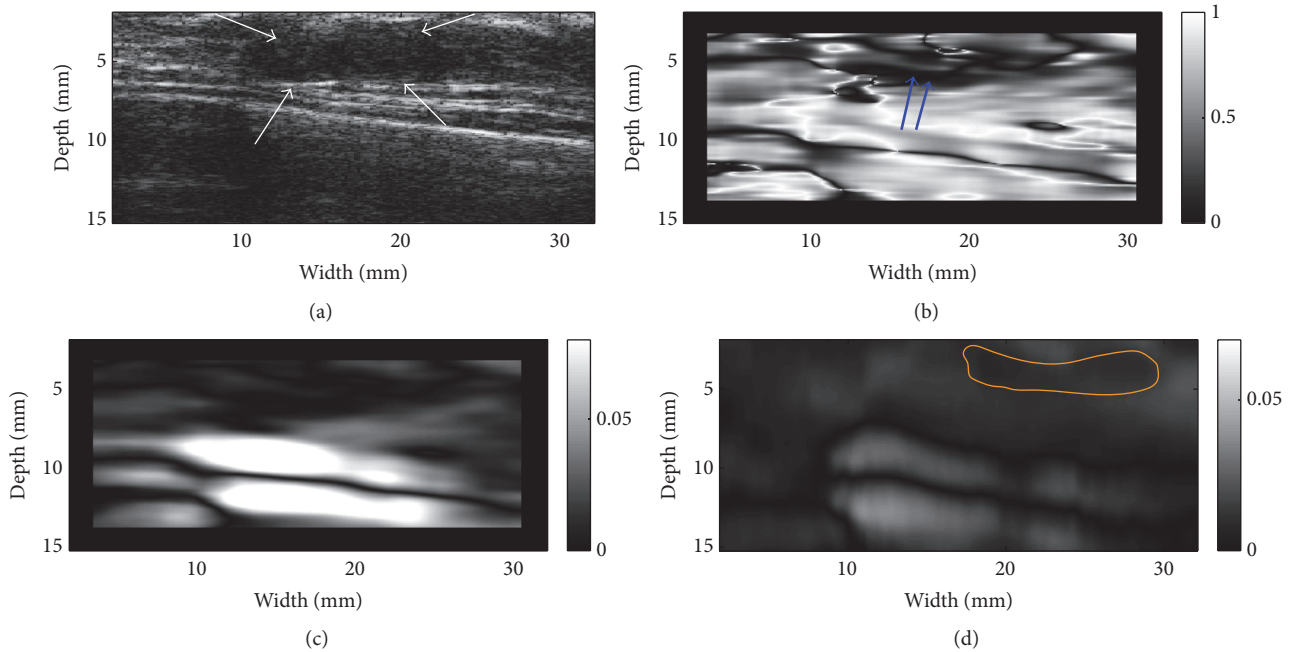
FIGURE 7: Resultant images of an invasive ductal carcinoma (IDC): (a) A B-mode image indicating the lesion (see arrows), (b) an NSDI image, (c) a shear strain elastogram, and (d) an axial strain elastogram. The contour on (d) is the segmented target boundary and was used for calculations of NSDI for this case. Double arrows in (b) point to the suspected ductal-like structure.

(a)

(b)

(c)

(d)
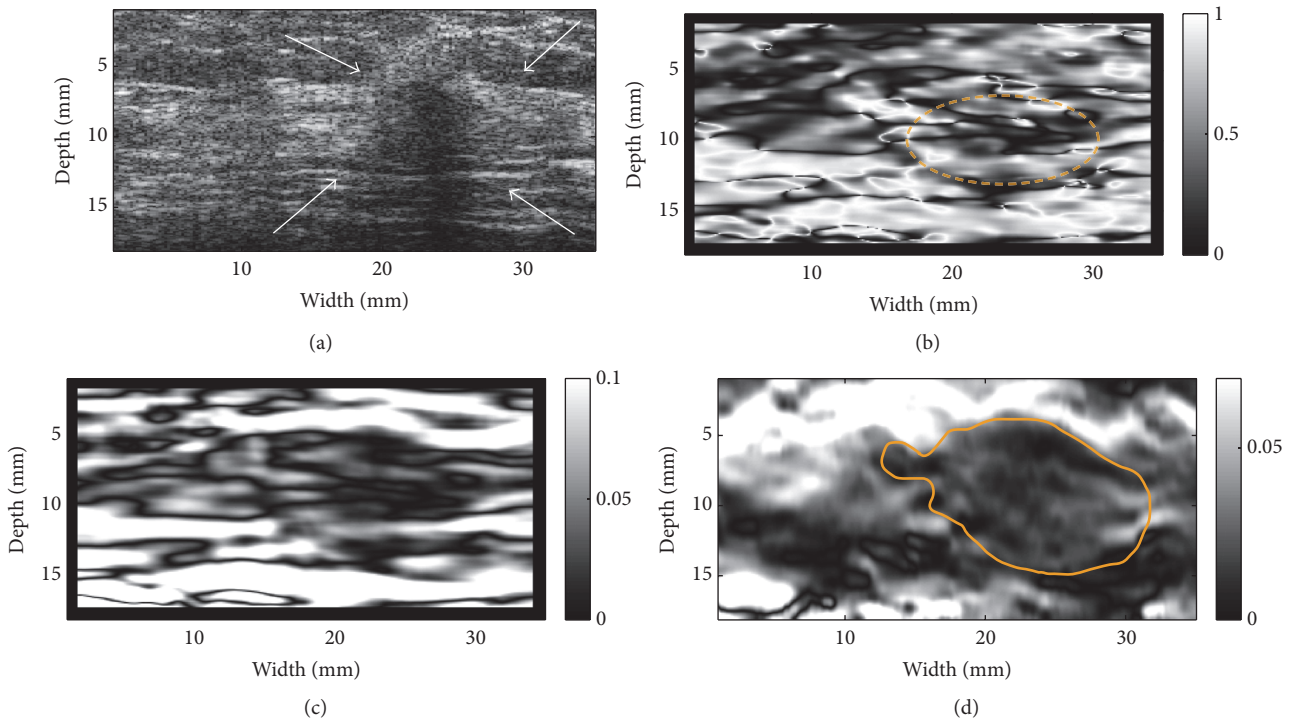
FIGURE 8: Resultant images of a (unspecified) breast cancer: (a) A B-mode image indicating the lesion (see arrows), (b) an NSDI image, (c) a shear strain elastogram, and (d) an axial strain elastogram. The contour on (d) is the segmented target boundary and was used for calculations of NSDI for this case. The elliptic contour in (b) depicts complex NSDI patterns likely induced due to the heterogeneity.

Furthermore, the shear strain elastogram (see Figure 7(c)) may depict the tumor boundary better as compared to the axial strain elastogram. The axial strain elastogram showed the low contrast between the IDC lesion and its background and this could be attributed to the nonlinear tissue elasticity [5, 26], though the exact reason is not known.

Several factors could potentially confound local shear deformation. In addition to the nonlinear elasticity [32], the

TABLE 2: A summary of observations through the FEA study.

Condition	Description	Observation
1	High modulus ratio between the inclusion and the background	High mean outside NSDI
2	Heterogeneity within the inclusion	High inside NSDI
3	Slipping boundary between the inclusion and the background	High NSDI values around the inclusion-background interface

slipping boundary in the tumor-background interface could be another confounding factor because it could cause high NSDI values around the tumor boundary (see Figure 2(b)). Tissue-dependent viscosity could also play a role in the change of strain contrast, thereby affecting the shear deformation. In this preliminary study, our FEA simulations were mainly limited to linearly elastic materials and we consider this as a limitation. We noticed that the complex breast model provided more realistic NSDI images as compared to those simplistic models (i.e., Cases 1–5). Hence, the available open-source elastography simulator [22] will be used to study above-identified confounding factors in future numerical studies. Advanced imaging simulations are ideally suited because they are readily available and the cost is low.

Another limitation is the small number of cases investigated. Given the fact that only 26 *in vivo* breast tumors were studied, more sophisticated statistical analyses were left for future studies. Outcomes of our future studies could be further improved because we are planning on using an optimal frame selection technique [33, 34] to optimize data selection. It is also worth noting that locations of all 26 biopsy-confirmed breast lesions were identified by an experienced biomedical engineer. Although these lesion boundaries were largely consistent with these delineated by board-certified radiologists in an early study [7], the exact tumor boundaries registered with respective pathology were not available for this study.

As shown in Figure 5(a), we also want to note that both the inside and outside NSDI values were elevated in the majority of breast cancers. This observation could be useful for breast lesion differentiation. However, this study was not designed to demonstrate the clinical utility of NSDI for two reasons. First, the quality of lateral displacement estimates after the denoising was relatively poor as compared to these axial displacement estimates. Because of that, the estimation uncertainty of NSDI is still relatively high. In the future, the utility of novel beamforming-based techniques [35–37] may significantly improve the quality of lateral displacement estimation. Thus, we are optimistic that the combination of our denoising approach with one of these beamforming methods should significantly improve the estimation of local shear deformation. Second, in order to accurately estimate local shear deformation, displacements in all three dimensions are needed. Certainly, the definition of NSDI should be modified accordingly. With the availability of whole breast ultrasound scanning systems, obtaining *in vivo* 3D ultrasonically measured displacement estimates becomes feasible [38].

Therefore, a large clinical study of the NSDI is still in the planning stage. Nevertheless, we still feel it appropriate to make one intriguing, albeit subjective, observation regarding the feasibility of the proposed NSDI metric.

In this work, we described the options we have chosen and gave justifications for those choices. While we believe that they are good choices, combining a high-quality subsample estimation method with denoising represents, however, only a feasible path to calculate the proposed NSDI metric. Other paths are also possible. For instance, the above-mentioned novel beamforming methods [35–37] alone may be able to provide high-quality lateral displacement estimates that can be used to calculate the NSDI metric.

5. Conclusions

The proposed NSDI metric was evaluated using FEA models and *in vivo* ultrasound data. This feasibility study showed that the elevated NSDI values should theoretically be correlated to two factors accompanying malignant breast cancers: firm connectivity and stiffness heterogeneity. Initial results also suggest that statistically significant differences in the inside and outside NSDI values were found between the benign and malignant breast tumors. In summary, our preliminary results demonstrated that this conceptually and computationally simple method could be used to improve ultrasound SE with current clinical equipment. Further studies, particularly in conjunction with the 3D ultrasound data, are being planned to explore the clinical utility of the proposed method.

Conflicts of Interest

The authors declare that there are no conflicts of interest.

Acknowledgments

References

[1] N. Abdullah, B. Mesurolle, M. El-Khoury, and E. Kao, "Breast imaging reporting and data system lexicon for US: Interobserver agreement for assessment of breast masses," *Radiology*, vol. 252, no. 3, pp. 665–672, 2009.

[2] H. Hille, M. Vetter, and B. J. Hackelöer, "The accuracy of BI-RADS classification of breast ultrasound as a first-line imaging method," *Ultraschall in der Medizin / European Journal of Ultrasound (UiM/EJU)*, vol. 33, no. 2, pp. 160–163, 2012.

[3] J. Ophir, I. Céspedes, H. Ponnekanti, Y. Yazdi, and X. Li, "Elastography: a quantitative method for imaging the elasticity of biological tissues," *Ultrasonic Imaging*, vol. 13, no. 2, pp. 111–134, 1991.

[4] B. S. Garra, E. I. Cespedes, J. Ophir et al., "Elastography of breast lesions: initial clinical results," *Radiology*, vol. 202, no. 1, pp. 79–86, 1997.

[5] T. J. Hall, Y. Zhu, and C. S. Spalding, "In vivo real-time freehand palpation imaging," *Ultrasound in Medicine & Biology*, vol. 29, no. 3, pp. 427–435, 2003.

[6] A. Itoh, E. Ueno, E. Tohno et al., "Breast disease: clinical application of US elastography for diagnosis," *Radiology*, vol. 239, no. 2, pp. 341–350, 2006.

[7] E. S. Burnside, T. J. Hall, A. M. Sommer et al., "Differentiating benign from malignant solid breast masses with US strain imaging," *Radiology*, vol. 245, no. 2, pp. 401–410, 2007.

[8] A. Thomas, F. Degenhardt, A. Farrokh, S. Wojcinski, T. Slowinski, and T. Fischer, "Significant Differentiation of Focal Breast Lesions. Calculation of Strain Ratio in Breast Sonoelastography," *Academic Radiology*, vol. 17, no. 5, pp. 558–563, 2010.

[9] H. Xu, T. Varghese, J. Jiang, and J. A. Zagzebski, "In vivo classification of breast masses using features derived from axial-strain and axial-shear images," *Ultrasonic Imaging*, vol. 34, no. 4, pp. 222–236, 2012.

[10] X. Gong, Q. Xu, Z. Xu, P. Xiong, W. Yan, and Y. Chen, "Real-time elastography for the differentiation of benign and malignant breast lesions: A meta-analysis," *Breast Cancer Research and Treatment*, vol. 130, no. 1, pp. 11–18, 2011.

[11] G. Sadigh, R. C. Carlos, C. H. Neal, and B. A. Dwamena, "Accuracy of quantitative ultrasound elastography for differentiation of malignant and benign breast abnormalities: A meta-analysis," *Breast Cancer Research and Treatment*, vol. 134, no. 3, pp. 923–931, 2012.

[12] D. Li, L. Guo, H. Xu et al., "Acoustic radiation force impulse elastography for differentiation of malignant and benign breast lesions: a meta-analysis," *International Journal of Clinical and Experimental Medicine*, vol. 8, no. 4, pp. 4753–4761, 2015.

[13] J. H. Yoon, M. H. Kim, E.-K. Kim, H. J. Moon, J. Y. Kwak, and M. J. Kim, "Interobserver variability of ultrasound elastography: How it affects the diagnosis of breast lesions," *American Journal of Roentgenology*, vol. 196, no. 3, pp. 730–736, 2011.

[14] A. Thitaikumar, T. A. Krouskop, B. S. Garra, and J. Ophir, "Visualization of bonding at an inclusion boundary using axial-shear strain elastography: A feasibility study," *Physics in Medicine and Biology*, vol. 52, no. 9, article no. 019, pp. 2615–2633, 2007.

[15] A. K. Thittai, J.-M. Yamal, L. M. Mobbs et al., "Axial-Shear Strain Elastography for Breast Lesion Classification: Further Results From In Vivo Data," *Ultrasound in Medicine & Biology*, vol. 37, no. 2, pp. 189–197, 2011.

[16] R. G. Budynas, *Advanced strength and applied stress analysis*, McGraw-Hill, NY, USA, 1 edition, 1977.

[17] L. Chen, R. J. Housden, G. M. Treece, A. H. Gee, and R. W. Prager, "A normalization method for axial-shear strain elastography," *IEEE Transactions on Ultrasonics, Ferroelectrics and Frequency Control*, vol. 57, no. 12, pp. 2833–2838, 2010.

[18] L. Guo, Y. Xu, Z. Xu, and J. Jiang, "A PDE-based regularization algorithm toward reducing speckle tracking noise: A feasibility study for ultrasound breast elastography," *Ultrasonic Imaging*, vol. 37, no. 4, pp. 277–293, 2015.

[19] M. Lubinski, S. Emelianov, K. Raghavan, A. Yagle, A. Skovoroda, and M. O'Donnell, "Lateral displacement estimation using tissue incompressibility," *IEEE Transactions on Ultrasonics, Ferroelectrics and Frequency Control*, vol. 43, no. 2, pp. 247–256, 1996.

[20] J. Jiang and T. J. Hall, "A coupled subsample displacement estimation method for ultrasound-based strain elastography," *Physics in Medicine and Biology*, vol. 60, no. 21, pp. 8347–8364, 2015.

[21] H. Du, J. Liu, and C. Pellot-Barakat, "Optimizing multicompression approaches to elasticity imaging," *IEEE Transactions on Ultrasonics, Ferroelectrics and Frequency Control*, vol. 53, no. 1, pp. 90–98, 2006.

[22] Y. Wang, E. Helminen, and J. Jiang, "Building a virtual simulation platform for quasistatic breast ultrasound elastography using open source software: A preliminary investigation," *Medical Physics*, vol. 42, no. 9, pp. 5453–5466, 2015.

[23] J. Luo, K. Ying, and J. Bai, "Savitzky-Golay smoothing and differentiation filter for even number data," *Signal Processing*, vol. 85, no. 7, pp. 1429–1434, 2005.

[24] T. Liu, O. A. Babaniyi, T. J. Hall, P. E. Barbone, and A. A. Oberai, "Noninvasive in-vivo quantification of mechanical Heterogeneity of invasive breast carcinomas," *PLoS ONE*, vol. 10, no. 7, Article ID e0130258, 2015.

[25] Y. Fung, *Biomechanics: mechanical properties of living tissues*, Springer-Verlag, NY, USA, 2 edition, 1993.

[26] S. Goenezen, J.-F. Dord, Z. Sink et al., "Linear and nonlinear elastic modulus imaging: An application to breast cancer diagnosis," *IEEE Transactions on Medical Imaging*, vol. 31, no. 8, pp. 1628–1637, 2012.

[27] M. Golshan, B. B. Fung, E. Wiley, J. Wolfman, A. Rademaker, and M. Morrow, "Prediction of breast cancer size by ultrasound, mammography and core biopsy," *The Breast*, vol. 13, no. 4, pp. 265–271, 2004.

[28] P. Wriggers, *Computational contact mechanics*, Springer-Verlag, Heidelberg, Berlin, Germany, 2006.

[29] R. Cotran, V. Kumar, T. Collins, and S. R. Richard, *Robbins pathologic basis of disease*, Saunders, Philadelphia, USA, 6 edition, 1993.

[30] S. Schnitt and L. Collins, *Biopsy interpretation of the breast*, Wolters Kluwer Health/Lippincott Williams & Wilkins, Philadelphia, USA, 2nd edition, 2013.

[31] P. P. Provenzano, K. W. Eliceiri, J. M. Campbell, D. R. Inman, J. G. White, and P. J. Keely, "Collagen reorganization at the tumor-stromal interface facilitates local invasion," *BMC Medicine*, vol. 4, article 38, 2006.

[32] T. Hall, A. Oberait, P. Barbone et al., "Elastic nonlinearity imaging," in *Proceedings of the 2009 Annual International Conference of the IEEE Engineering in Medicine and Biology Society*, pp. 1967–1970, Minneapolis, MN, September 2009.

[33] J. Jiang, T. J. Hall, and A. M. Sommer, "A novel performance descriptor for ultrasonic strain imaging: A preliminary study," *IEEE Transactions on Ultrasonics, Ferroelectrics and Frequency Control*, vol. 53, no. 6, pp. 1088–1102, 2006.

[34] B. R. Chintada, A. V. Subramani, B. Raghavan, and A. K. Thittai, "A Novel Elastographic Frame Quality Indicator and its use in Automatic Representative-Frame Selection from a Cine Loop," *Ultrasound in Medicine & Biology*, vol. 43, no. 1, pp. 258–272, 2017.

[35] M. E. Andcrson, "Multi-dimensional velocity estimation with ultrasound using spatial quadrature," *IEEE Transactions on Ultrasonics, Ferroelectrics and Frequency Control*, vol. 45, no. 3, pp. 852–861, 1998.

[36] S. J. Huntzicker and M. M. Doyley, "Can quantitative synthetic aperture vascular elastography predict the stress distribution within the fibrous cap non-invasively," *The Journal of the Acoustical Society of America*, vol. 135, no. 4, pp. 2372-2372, 2014.

[37] B. Lokesh, B. R. Chintada, and A. K. Thittai, "Rotation Elastogram Estimation Using Synthetic Transmit-aperture Technique: A Feasibility Study," *Ultrasonic Imaging*, vol. 39, no. 3, pp. 189–204, 2017.

[38] B. Peng, Y. Wang, T. J. Hall, and J. Jiang, "A GPU-Accelerated 3-D Coupled Subsample Estimation Algorithm for Volumetric Breast Strain Elastography," *IEEE Transactions on Ultrasonics, Ferroelectrics and Frequency Control*, vol. 64, no. 4, pp. 694–705, 2017.

Research Article

Ultrasound in Prenatal Diagnostics and Its Impact on the Epidemiology of Spina Bifida in a National Cohort from Denmark with a Comparison to Sweden

Charlotte Rosenkrantz Bodin ⓘ,[1] **Mikkel Mylius Rasmussen,**[2] **Ann Tabor,**[3] **Lena Westbom,**[4] **Eleonor Tiblad,**[5] **Charlotte Kvist Ekelund,**[3] **Camilla Bernt Wulff,**[3] **Ida Vogel,**[6,7] **and Olav Bjørn Petersen**[1,7]

[1]*Department of Gynecology and Obstetrics, Aarhus University Hospital, Aarhus, Denmark*
[2]*Department of Neurosurgery, Aarhus University Hospital, Aarhus, Denmark*
[3]*Center of Fetal Medicine, Department of Obstetrics, Copenhagen University Hospital, Rigshospitalet, Copenhagen, Denmark*
[4]*Section of Pediatrics, Department of Clinical Sciences Lund, Faculty of Medicine, Skåne University Hospital, Lund University, Lund, Sweden*
[5]*Department of Fetal Medicine, Karolinska University Hospital, Stockholm, Sweden*
[6]*Department of Clinical Genetics, Aarhus University Hospital, Aarhus, Denmark*
[7]*Center for Prenatal Diagnostics, Aarhus University Hospital, Aarhus, Denmark*

Correspondence should be addressed to Charlotte Rosenkrantz Bodin; chbodi@rm.dk

Objectives. The aim of this study was to assess the incidence, the prenatal detection rate by ultrasound, and the pregnancy outcome of spina bifida (SB) in Denmark (DK) in 2008–2015 and to compare results to national data from Sweden. *Methods*. Data were retrieved from the Danish Fetal Medicine Database, which includes International Classification of Diseases- (ICD-) 10 codes for pre- or postnatally diagnoses and pregnancy outcome. Missing data were obtained from the National Patient Register. Livebirth data with myelomeningocele (MMC) in Sweden were obtained from different databases. *Results*. There were 234 cases with SB in DK in 2008–2015. The incidence of SB was 4.9 : 10,000; 89% were detected with ultrasound prior to week 22; 90% of these pregnancies were terminated (ToP); 91% were isolated malformations of which 11% showed abnormal karyotype. The incidence of newborns with MMC was 1.3 : 10,000 in Sweden. *Conclusions*. Ultrasound screening has a major impact on the epidemiology of SB. The prenatal detection rate of SB was high, and most SB cases were isolated and had a normal karyotype. Among women with a prenatal fetal diagnosis of SB, 90% chose to have ToP. The incidence of newborns with SB was higher in Sweden than in DK.

1. Introduction

Since the introduction of new guidelines for prenatal diagnostics in 2004, all pregnant women in Denmark have been offered a prenatal screening program. The program comprises two ultrasound scans during their pregnancy: one in gestational weeks 11–14 (scanning primarily for chromosomal abnormalities) and one in gestational weeks 18–21 (scanning primarily for malformations) as well as midwife consultations between the scans [1]. These guidelines were issued by the

Danish Health Authority in 2004. They were not designed to eradicate disease but to support pregnant women's reproductive autonomy, confirm normality by offering ultrasound and possibly genetic testing, facilitate planning of optimal postnatal care, and give women the possibility of applying for late termination of pregnancy (ToP) in case of severe fetal disease, like spina bifida (SB), within week 22 + 0. The current screening uptake is approximately 97%.

SB is a birth defect in the group of neural tube defects (NTD). It results from failed closure of the neural folds during

the first month of gestation. SB is associated with severe morbidity and mortality, depending on the type, size, and site of the lesion [2, 3]. The incidence of SB differs globally from 1.7 to 19 : 10,000 fetuses [4–12]. SB can be detected in the second trimester using ultrasound which will reveal specific cranial signs of the cerebellum and the skull [13]. Previous studies have shown that intake of folic acid during pregnancy may decrease the risk of SB [6, 7]. This has made some countries use mandatory food fortification to ensure adequate supply of folic acid to pregnant women [6, 14]. In Denmark, folic acid is recommended as a food supplement from the day pregnancy is planned, but it is not added to food as part of a mandatory scheme. Danish folic acid recommendations have shown no impact on the incidence of SB fetuses in western parts of the country due to Danish pregnant women not complying with the guidelines and thus not getting the recommended amount of folic acid [15–17]. Even so, one of these studies showed a decrease in the incidence of infants born with SB after year 2006, that is, at the same time as the above-mentioned prenatal screening program was introduced at all obstetric departments in Denmark [16]. This suggests that the use of ultrasound scans may have an impact on the epidemiology of SB in Denmark.

Different countries have developed various prenatal ultrasound strategies to manage pregnancies complicated by SB. In Sweden, another Scandinavian country with a population approximately twice the size of the Danish population and similar legislation regarding ToP, second-trimester ultrasound scan is also offered to all pregnant women. In Sweden, however, the proportion of women who accept prenatal ultrasound screening varies more across regions than in Denmark.

The objectives of this study were to estimate the true incidence of SB in Denmark, to assess the detection rate at first-trimester and second-trimester ultrasound screening, to identify pregnancy outcomes in years 2008–2015, and to identify similarities as well as differences in incidence of SB between Denmark and Sweden.

Overlapping and sometimes inconsistent terms are used for spinal NTDs [18]. In the present study, the term "spina bifida" includes all open spinal NTDs and meningocele and lipomatous malformations with neurological deficits of the skin-covered SB.

2. Method

2.1. The Danish Fetal Medicine Database. Data for this study were primarily obtained from the Danish Fetal Medicine Database (DFMD), which is a national database that includes data from all obstetric departments in Denmark. The DFMD contains information on all pregnancies in DK with a first-trimester scan from 1 January 2008. With an uptake of more than 90%, this corresponds to 50, -60,000 pregnancies per year. The DFMD receives information regarding maternal and pregnancy characteristics and International Classification of Diseases- (ICD-) 10 codes for any prenatally diagnosed anomaly automatically from the prenatal software system (Astraia GMBH, Munich, Germany) used in all obstetric
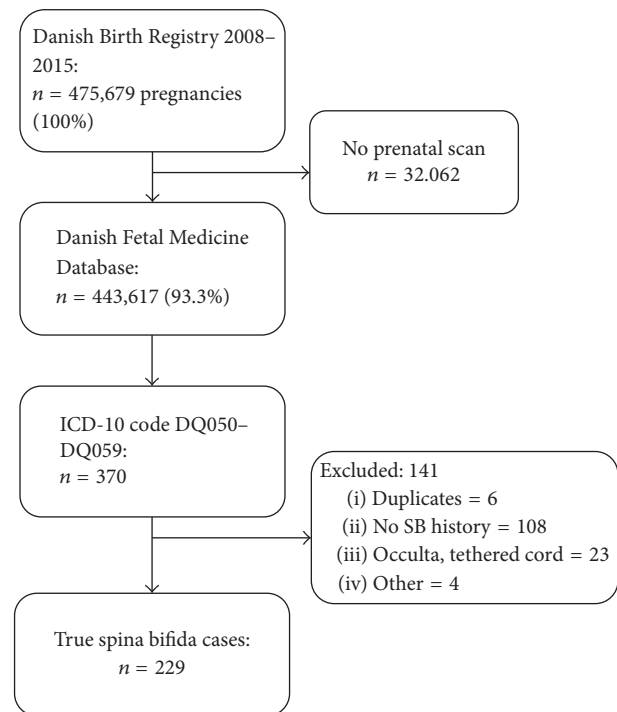
Figure 1: Flowchart of inclusion from the Danish Fetal Medicine Database (DFMD).

departments. Data are linked with pre- and postnatal outcomes from the Danish Cytogenetic Register, the National Patient Register (NPR), and the National Birth Register. The DFMD thus makes it possible to analyze >90% of the entire population of pregnant women with regard to screening results and outcomes [19].

2.2. Data Collection. Data were collected prospectively and analyzed retrospectively. Firstly, we collected data from all pregnancies in Denmark with due date in the period from 1 January 2008 to 31 December 2015 that underwent a second-trimester ultrasound scan and had a pre- or postnatally registered International Classification of Disease- (ICD-) 10 code in the range of Q050–Q059. We performed a search of the Astraia software for cases that had ultrasound indications of SB but lacked an ICD 10-code in the searched range to identify cases that had been given an ICD 10-code not included in our search, for instance, diagnoses in the Q06 group ("other congenital malformations of the spinal cord"). Figure 1 provides an overview of the inclusion parameters. We retrieved data regarding due date, prenatally diagnosed anomaly, anomaly diagnosed at any time postnatally until data extraction, coexistence of other malformations, karyotype, and outcome (live-born, ToP, and adverse pregnancy outcome). No information on size and site of the lesion was obtained.

Secondly, we collected all cases born in the study period with an ICD-10 code for SB from the NPR and included Civil Registration Numbers (CPR, which all citizens in Denmark are given at birth or upon immigration) not already known from the DFMD. In this way, we included SB cases among
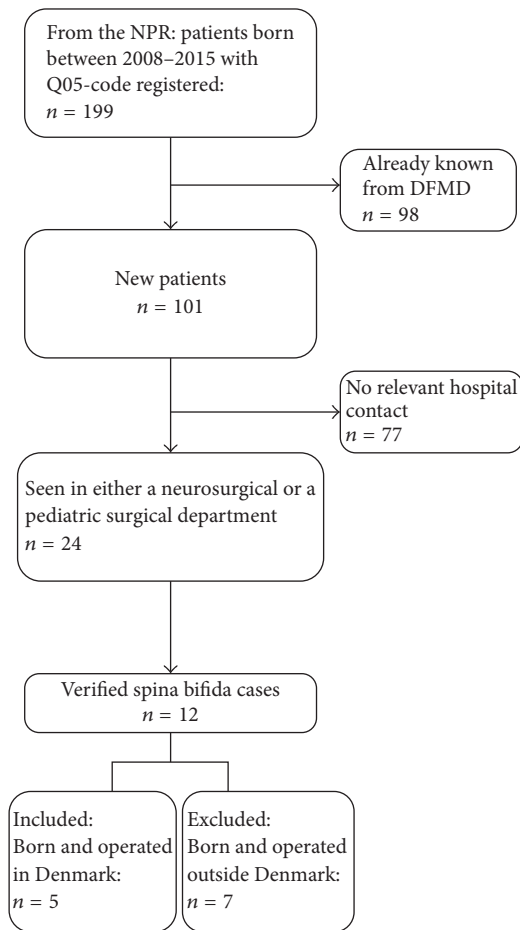
FIGURE 2: Flowchart of inclusion from the National Patient Register (NPR), DFMD: Danish Fetal Medicine Database.

babies to the 7% of mothers who had not been scanned prenatally and therefore had not been registered in the DFMD. We also evaluated patient files for cases with a neurosurgical or pediatric surgical contact, seen in a hospital within the first year of life. See the flowchart in Figure 2.

Medical records on all infants and mothers in whom a ToP was performed (including autopsy results) were evaluated for validation. This made it possible to collect missing data, and cases were included or excluded according to the European Surveillance of Congenital Malformation (EURO-CAT) guidelines [20]. This meant that we excluded all infants with SB occulta, lipomatous malformations, or tethered cord without neurological deficits, as well as all suspected but not confirmed SB cases. Babies born and having had primary surgery outside of Denmark were excluded from further statistical analysis ($n = 7$). Fetal closure of open SB had not been performed on any of these fetuses.

2.3. Statistical Analysis. Data were stored using RedCap software and exported to STATA® 14 for analysis. Student's t-test and Wilcoxon–Mann–Whitney test were used for numerical data, and chi^2-test was used for binominal data. Variation over years was tested by a Poisson regression model, and

ToP rates and detection rates were analyzed using binomial probability tests.

$p < 0.05$ was considered statistically significant; 95% confidence intervals are presented after each result in brackets.

2.4. Sweden. Data from Sweden were collected from the national follow-up program and quality of care registry in spinal dysraphism and hydrocephalus. The SB part of the follow-up program, called the MMCUP, includes a lifelong follow-up of body function/structures, activity, participation, treatment, and self-reported health-related quality of life for all children with SB born between 2007 and 2015 in Sweden [21]. The MMCUP provides information on live born but not unborn fetuses like the Danish registers. Hence, from Sweden, fetuses terminated by ToP or still births were not included. We extracted data from the MMCUP on SB and the prenatal diagnosis for all infants born in Sweden from 1 January 2008 to 31 December 2015.

Data on the total number of births in Sweden were obtained from the Swedish population registry, Statistics Sweden. We received extracted anonymized statistics on infants and abortions coded with Q05 from the Swedish National Board of Health and Welfare and the number of pregnancies for the years 2008–2014 from the following registers: the Medical Birth Register, the Swedish NPR, and the Surveillance Register of Birth Defects. Only patients diagnosed prenatally or within their first year of life were included. Numbers from 2015 were not available at the point of collection. Because of differences in legislation on patient anonymity between the two counties' databases, it was not possible to validate any of the Swedish cases.

2.5. Permissions. Permission to collect and store data was obtained from the Danish Data Protection Agency (reference number: 2012-58-006). Permission to look at the patient files of the babies of mothers who had not been scanned prenatally was granted by the Danish Patient Safety Authority (reference number: 3-3013-1721/1). Ethical approval for the MMCUP was provided in Lund, Sweden (EPN Lund, 241-2009).

3. Results

3.1. Incidence. There were 475,679 pregnancies in Denmark from 2008 to 2015. A total of 234 true SB cases were included in the study population (Figure 1). The incidence of pregnancies complicated by SB was 4.9 : 10,000 [4.3–5.6 : 10,000], and this incidence did not differ over the years 2009–2015 ($p = 0.81$), except in 2008 when there was a significantly lower incidence of pregnancies with SB ($p = 0.03$). The incidence of live-born SB cases was 0.8 : 10.000 [0.6–1.1 : 10,000] with no significant difference between the years ($p = 0.7$).

There were 7 additional cases born and treated outside Denmark but followed in a Danish hospital after immigration.

3.2. Prenatal Diagnosis. Of the 234 cases, 223 had an ultrasound scan done before 22 weeks, whereas 6 did not attend screening until later in pregnancy, and no information on

TABLE 1: Spina bifida cases and detection divided in years; *Poisson regression.

Year	Total SB cases	Prenatal diagnosis	Prenatal diagnosis < week 22
2008	15	14 (93.3%)	13 (86.7%)
2009	32	29 (90.6%)	27 (84.4%)
2010	38	35 (92.1%)	34 (89.4%)
2011	33	30 (90.9%)	28 (84.8%)
2012	28	27 (96.4%)	26 (92.9%)
2013	24	21 (87.5%)	21 (87.5%)
2014	35	34 (97.1%)	31 (88.6%)
2015	29	29 (100%)	27 (93.1%)
Total	234	219 (93.6%)	207 (88.5%)
p value		0.99*	0.99*

TABLE 2: Maternal characteristics from the Danish Fetal Medicine Database; *Wilcoxon–Mann–Whitney test, **Student's t-test, ***chi^2 test; ^Caucasian: European, Middle Eastern, North African, Hispanic; ^^Non-Caucasian: Afro Caribbean, Asian, Oriental.

Characteristic	<week 22 $N = 187$	≥week 22 $N = 16$	p value
Maternal age, years [95% CI]	29.7 [29.0; 30.4]	29.8 [27.4; 32.1]	0.88*
BMI, [95% CI]	25.6 [24.7; 26.5]	28.1 [24.9; 31.3]	0.08**
Smokers, % [95% CI]	3.8 [1.5; 7.6]	6.2 [0.2; 30.2]	0.62***
Ethnicity, % [95% CI]			
(i) Caucasian^	93.2 [88.6; 96.3]	86.7 [59.5; 98.3]	0.35***
(ii) Non-Caucasian^^	6.8 [3.7; 11.4]	13.3 [1.7; 40.5]	
Conception, % [95% CI]			
(i) Spontaneous	90.1 [84.8; 94.0]	93.8 [69.8; 99.8]	0.63***
(ii) Fertility treatment	9.9 [6.0; 15.2]	6.3 [0.2; 30.2]	

screening was available in 5 cases. Prenatal detection at any gestational age was achieved in 93.6% [89.6–96.4%] (219/234) of cases, and 88.5% [83.7–92.5%] had been detected prior to week 22 (207/234) (stratified by years in Table 1).

We divided data on maternal characteristics from DFMD into two subgroups according to gestational age at diagnosis to rule out baseline characteristics as reason for nondetection (Table 2). Complete baseline data were available for 187 out of 207 (<week 22) and for 16 out of 22 (≥week 22), respectively. There was no significant difference between the two groups of mothers regarding age, body mass index (BMI), ethnicity, smoking status, or mode of conception. No information was obtained regarding mothers of the 5 babies with SB who had not been scanned prenatally.

The sensitivity of the Danish screening program was 92.8% [88.6–95.8%], since 207 of the 223 who attended screening were diagnosed before gestational week 22, with 15.5% [10.8–21.1%] in the first (32/207) and 84.5% (78.8–89.2%) in the second trimester (175/207). There was no statistical variation in the prenatal detection rate during the study period ($p = 0.99$).

Information about the type of SB was obtained for 14 of the 16 cases not identified at screening; in 11 of these cases (78.6%), the SB was skin-covered, meaning either meningocele or lipomatous malformations, suggesting that close to all of the opened SB cases were detected.

3.3. Outcome. In cases with a SB diagnosis made by ultrasound prior to week 22 of gestation, 90.3% [86.0–94.5%] (187/207) of the women opted for termination. Of all 234 cases, 190 resulted in ToP, corresponding to 81.6% [76.1–86.4%] of all SB cases in Denmark. The tendency to opt for termination did not change significantly within the study period ($p = 0.99$).

In the database, ethnicity is coded as "Caucasian" (European, Middle Eastern, North African, and Hispanic), Afro Caribbean, Asian, and Oriental. However, as there were very few numbers in the last three groups, we assembled them together in one group, calling it "Non-Caucasian." Among mothers of Non-Caucasian origin, 30.7% chose to continue their pregnancy when SB was diagnosed before week 22. This was higher than the 6.3% in the Caucasian group ($p = 0.0015$). No difference was noted between the two groups regarding mode of conception ($p = 0.13$) or maternal age ($p = 0.08$).

A total of 20 women chose to continue their pregnancy with a SB diagnosis by ultrasound before 22 weeks. 16 of these women had a live-born baby and four miscarried. Of the 27 cases without a prenatal diagnosis before week 22, 22 had a live-born baby, one miscarried, and four opted for termination, and since the fetuses were considered not viable beyond 30 days, ToP was allowed in accordance with Danish legislation.

TABLE 3: Overview of differences between Sweden and Denmark 2008–2015; *2008–2014; **majority in third trimester; p value calculated by Student's t-test.

	Denmark	Sweden	p value
Incidence fetuses	$4.92 : 10,000$	$3.4 : 10,000^*$	0.0001
Incidence live births	$0.8 : 10,000$	$1.3 : 10,000$	0.04
ToP rate	81.2%	$63.0\%^*$	0.02
Prenatal detection RATE among live births	42.1%	$56.3\%^{**}$	0.11

The resulting overall number of live births with SB was 38. Of these, 14 had a skin-covered SB. This is on average 4-5 infants with any kind of SB per year and of these 3 had open SB per year.

Of the 38 infants, 42.1% [25.7–58.6%] (16/38) had a prenatal diagnosis < week 22: that is, 57.9% did not know they were having a baby with SB.

In 91.3% [86.9–94.6%] of cases, SB was an isolated malformation (hydrocephalus and club feet are considered secondary to SB and are not counted as other malformations). A total of 119 (56.9%) of isolated cases had karyotypic or chromosomal information available, and 10.9% [5.9–18.0%] (13/119) were abnormal.

3.4. Results from Sweden. All live-born children with SB in Sweden from 2008 to 2015, in total 121 children, were known. Of these, 72% had an open and 28% had a skin-covered SB. A total of 905,060 babies were born in Sweden during the same period. Hence, the incidence of live-born infants with SB was $1.3 : 10,000$ [1.1–$1.6 : 10,000$], which was higher ($p = 0.04$) than in Denmark. Information on prenatal diagnosis was available for 79% of these infants (96/121) and showed that 56.3% [46.1–66.4%] of the 96 infants had a prenatal diagnosis of SB: that, 43.7% of the mothers had no knowledge that they were expecting a baby with SB. This rate did not change over the years ($p = 0.88$).

In the databases from the National Board of Health and Welfare, which include data from 2008–2014, there were 308 unverified cases coded with SB (Q05) of whom 165 were registered as ToP. According to the MMCUP, only 97 infants born during 2008–2014 fulfilled the criteria for SB, as defined above, compared with 143 infants with a Q05 diagnosis in the national healthcare databases. Provided that all 165 ToP fetuses had SB and that all live-born children with verified SB were known ($n = 97$), the incidence of pregnancies with SB was $3.4 : 10,000$ [3.0–$3.8 : 10,000$] during 2008–2014, and the ToP rate in Sweden based on verified SB was 63% [51.5–76.8] (165/262).

Table 3 provides an overview of the differences in results between Sweden and Denmark.

4. Discussion

This study is the first to cover the impact of prenatal ultrasound screening on the incidence of SB on a national level. In the Danish cohort, we found an incidence of SB of $4.9 : 10,000$. The prenatal detection rate before 22 weeks was high and the majority of these women opted for ToP resulting in very few live births with SB. The rate of live births with SB was higher in Sweden than in Denmark, probably due to fewer women choosing prenatal diagnostics and possibly also a lower prenatal detection rate.

Ultrasound-detectable signs of open SB include "banana sign" of the cerebellum and "lemon sign" of the frontal skull [13]. Closed SB does not have the same impact on cranial structure as open SB and hence lacks the same ultrasound-detectable features [22]. Previous studies have shown that the sensitivity and specificity of ultrasound for open SB are close to 100% [23]. In the Danish study population, we found a sensitivity of 92.8%, and as our data also include some closed SB types, the sensitivity is expected to be lower than 100%.

In Denmark, 88.5% of the total population of SB was diagnosed before gestational week 22 and 93.9% at any gestational age. The EUROCAT society and other studies report prenatal detection rates in the range 81–90% [4, 8, 9, 24, 25]. Our overall prenatal detection rate was significantly higher than the percentage (89.3%) reported by the EUROCAT ($p = 0.03$), suggesting that the Danish prenatal screening program outperforms those of other European countries that pursue different strategies for prenatal screening for anomalies. The superior performance of the Danish program may likely be attributed to high coverage and acceptability. This is corroborated by a recent Dutch study [24] which found the same proportion of pregnant women accepting a second-trimester scan, and where 88% of SB cases are diagnosed in the second trimester.

Among all Danish SB cases, 81.6% resulted in ToP, and of those diagnosed with ultrasound before gestational week 22, 90.3% opted for termination. The ToP rate following prenatal diagnosis was in the same range as for Alsace in France (97%) [4] and the region Emilia-Romagna in Italy (92.4%) [8] (only open SB), but higher than rates reported by the EUROCAT (66%) [26], Atlanta in the US (34%) [12], and the northern parts of the Netherlands (78.6% when diagnosed in the second trimester) [24].

The Danish Spina Bifida Society ("Rygmarvsbrokforeningen af 1988") does not have an official statement regarding ToP, which somehow underlines the liberal attitude towards ToP in Denmark and even among patients and relatives affected by SB. The different attitudes towards ToP evident between different ethnic groups in the present study and geographically may partly explain the varying global incidence of live-born SB cases.

Today, the possibility for prenatal genetic counseling is widely used for known hereditary diseases, and the introduction of prenatal ultrasound has made it possible to offer genetic counseling to parents expecting a child with a malformation, like SB, that has no known hereditary path.

A chromosomal abnormality was found in 10.9% of isolated SB, which is comparable to the rates reported in similar studies [4, 8, 10]. This suggests that there is a high risk of chromosomal anomalies in these pregnancies compared with normal-appearing fetuses [27] and supports the idea that all women with a pregnancy complicated by SB should be offered chromosomal analysis and counseling from a multispecialist team.

It is important to note that previous studies included only open SB [8, 9, 24] or were inconsistent as to whether they included both open and closed SB [10–12, 28]. In our definition of SB, we included open SB and meningocele and lipomatous NTDs with neurological deficits. We did not include information on size and site of the lesion. Our study includes close to 100% of the Danish SB cases which minimizes selection bias and regional differences. The number of SB cases was lower in 2008 than in the other years, possibly due to natural variance over years or missing data in the establishment period in the beginning of 2008. All cases included in the study were validated by clinical audit and patient file review, which eliminates the risk of false-positive cases. A search of the Astraia software for cases that had ultrasound indications but lacked an ICD 10-code for SB was undertaken for the prenatally diagnosed group in an attempt to diminish the risk of underestimation due to noninclusion of false-negative cases. SB cases that died in utero earlier than the second trimester could not be included; thus, this could possibly lead to a small degree of underestimation. For the postnatally diagnosed group, there is a small risk that patients were not given a correct ICD 10-code and hence not reported to the NPR. However, since all SB patients in Denmark are referred to a university hospital, the risk of nonreporting is low. We base this argument on the observation that ICD-10 codes in Denmark serve multiple purposes, including the distribution of funding between healthcare institutions.

The Danish incidence of SB is in line with that of other western developed countries without food fortification [4, 7, 8, 24], whereas studies from other parts of the world where mandatory fortification of grain products exists show a lower total incidence of SB (USA, Canada, and Australia) [6, 12].

Validation of cases that are given ICD-codes for SB (Q05) is absolutely necessary to identify the "true" incidence of SB, as shown in Figures 1 and 2 for the Danish fetal and patient registries. As infants and abortions coded with Q05 were anonymized in the Swedish National Board of Health and Welfare data, validation of these cases could not be undertaken. However, comparison with MMCUP data regarding infants born with SB indicated that 32.2% of the Swedish Q05-coded infants did not have SB, a proportion that is about the same as that in Denmark according to the present study. About two-thirds of the infants with SB had an open, not skin-covered, defect in both countries. The comparison between Denmark and Sweden underlines the difference between using an anonymized and a nonanonymized database. The data from Sweden originate from the MMCUP, which was not anonymized and from the national populations registers, which were anonymized. Hence, 97/143 cases in the national population registers were present in the MMCUP, suggesting that 46 (32.2%) were false

positive in the database. An even higher proportion of false-positives were found in the Danish Patient Registers after full validation of the nonanonymized data, with 108/229 (47.2%) having a wrong diagnosis.

Sweden has the same folic acid recommendations as Denmark [28], and the lower incidence of pregnancies with SB in Sweden than in Denmark (3.4 versus 4.9 : 10,000, $p < 0.001$, Table 3) must therefore be due to other factors. A previous Swedish study found a national incidence of SB of 5.44 : 10,000 during 1999–2002 [28], which is significantly higher than the estimated incidence based on the present 308 pregnancies with unverified SB. So, poor identification of registered pregnancies may have contributed to the low incidence figures for the years 2008–2014 in the present study. Despite the possibly lower incidence of pregnancies with SB, the higher incidence of infants born with SB in Sweden than in Denmark may be explained by a lower percentage of parents choosing prenatal diagnostics, lower detection by ultrasound, and possibly different attitudes towards ToP.

To our knowledge, valid national prevalence figures on SB cases with prenatal ultrasound findings did not exist prior to this study, either in Denmark or in any other country. The present study shows that a full national prenatal ultrasound screening with a high uptake has a major impact on the incidence of SB because of the high detection rate of SB by ultrasound and because a large proportion of women opt for ToP. This study may have implications for the organization of SB prenatal care, surgery, and treatment. Since the patient volume is low with an average of only four new patients per year, patients who need lifelong treatment may be better handled in a few dedicated centers to optimize the expertise of healthcare professionals and to ensure better quality of life for patients.

5. Conclusion

This study includes all fetal SB cases in Denmark during the years 2008–2015. The study shows that, by using ultrasound screening, almost all cases of a SB can be detected. In a country like Denmark where ToP is regulated by law, prenatal ultrasound screening may have an impact on the number of live births of children with ultrasound-detectable malformations, and it may inform healthcare professional and parental decisions with regard to ToP and the planning of postnatal care for the newborn. The difference between Denmark and Sweden, where acceptance of prenatal ultrasound screening is lower, underlines the effect of a nationwide screening program on the epidemiology of SB.

Abbreviations

BMI:	Body mass index
DFMD:	Danish Fetal Medicine Database
EUROCAT:	European Surveillance of Congenital Malformations
GA:	Gestational age
ICD:	International Classification of Diseases
MMC:	Myelomeningocele

NPR: National Patient Registry
("Landspatientregisteret")
NTD: Neural tube defects
SB: Spina bifida
ToP: Termination of pregnancy.

Additional Points

Key Message. In a national cohort from Denmark, >80% of fetal spina bifida cases were detected by prenatal ultrasound with 90% of parents choosing termination of pregnancy in case of open spina bifida, so very few infants with this malformation were born.

Conflicts of Interest

The authors have no conflicts of interest.

Acknowledgments

References

[1] C. K. Ekelund, O. B. Petersen, F. S. Jorgensen et al., "The Danish Fetal Medicine Database: Establishment, organization and quality assessment of the first trimester screening program for trisomy 21 in Denmark 2008-2012," *Acta Obstetricia et Gynecologica Scandinavica*, vol. 94, no. 6, pp. 577–583, 2015.

[2] R. M. Bowman, D. G. McLone, J. A. Grant, T. Tomita, and J. A. Ito, "Spina bifida outcome: a 25-year prospective," *Pediatric Neurosurgery*, vol. 34, no. 3, pp. 114–120, 2001.

[3] P. Oakeshott, G. M. Hunt, A. Poulton, and F. Reid, "Expectation of life and unexpected death in open spina bifida: A 40-year complete, non-selective, longitudinal cohort study," *Developmental Medicine & Child Neurology*, vol. 52, no. 8, pp. 749–753, 2010.

[4] D. Timbolschi, E. Schaefer, B. Monga et al., "Neural tube defects: The experience of the registry of congenital malformations of Alsace, France, 1995-2009," *Fetal Diagnosis and Therapy*, vol. 37, no. 1, pp. 6–17, 2015.

[5] K. S. Au, A. Ashley-Koch, and H. Northrup, "Epidemiologic and genetic aspects of spina bifida and other neural tube defects," *Developmental Disabilities Research Reviews*, vol. 16, no. 1, pp. 6–15, 2010.

[6] C. A. M. Atta, K. M. Fiest, A. D. Frolkis et al., "Global birth prevalence of spina bifida by folic acid fortification status: A systematic review and meta-analysis," *American Journal of Public Health*, vol. 106, no. 1, pp. e24–e34, 2016.

[7] B. Khoshnood, M. Loane, H. De Walle et al., "Long term trends in prevalence of neural tube defects in Europe: Population based study," *BMJ*, vol. 351, Article ID h5949, 2015.

[8] T. Ghi, G. Cocchi, L. Conti et al., "Prenatal diagnosis of open spina bifida in Emilia-Romagna," *Fetal Diagnosis and Therapy*, vol. 37, no. 4, pp. 301–304, 2015.

[9] J. Salvador, M. Arigita, E. Carreras, A. Lladonosa, and A. Borrell, "Evolution of prenatal detection of neural tube defects in the pregnant population of the city of Barcelona from 1992 to 2006," *Prenatal Diagnosis*, vol. 31, no. 12, pp. 1184–1188, 2011.

[10] C. M. Domrose, S. Bremer, C. Buczek et al., "Termination of pregnancy after prenatal diagnosis of spina bifida: a German perspective," *Archives of Gynecology and Obstetrics*, vol. 294, no. 4, pp. 731–737, 2016.

[11] P. Bhide, G. S. Sagoo, S. Moorthie, H. Burton, and A. Kar, "Systematic review of birth prevalence of neural tube defects in India," *Birth Defects Research Part A: Clinical and Molecular Teratology*, vol. 97, no. 7, pp. 437–443, 2013.

[12] L. M. Besser, L. J. Williams, and J. D. Cragan, "Interpreting changes in the epidemiology of anencephaly and spina bifida following folic acid fortification of the U.S. grain supply in the setting of long-term trends, Atlanta, Georgia, 1968-2003," *Birth Defects Research Part A - Clinical and Molecular Teratology*, vol. 79, no. 11, pp. 730–736, 2007.

[13] K. H. Nicolaides, S. Campbell, S. G. Gabbe, and R. Guidetti, "Ultrasound screening for spina bifida: cranial and cerebellar signs," *The Lancet*, vol. 328, no. 8498, pp. 72–74, 1986.

[14] R. Padmanabhan, "Etiology, pathogenesis and prevention of neural tube defects," *Congenital Anomalies*, vol. 46, no. 2, pp. 55–67, 2006.

[15] M. M. Rasmussen and D. Clemmensen, "Folic acid supplementation in pregnant women," *Ugeskr Laeger*, vol. 172, no. 8, p. 613, 2010.

[16] D. Clemmensen, M. Thygesen, M. M. Rasmussen, M. Fenger-Grøn, O. B. Petersen, and C. Mosdal, "Decreased incidence of myelomeningocele at birth: Effect of folic acid recommendations or prenatal diagnostics?" *Child's Nervous System*, vol. 27, no. 11, pp. 1951–1955, 2011.

[17] A. K. Friberg and F. S. Jorgensen, "Few Danish pregnant women follow guidelines on periconceptional use of folic acid," *Danish Medical Journal*, vol. 61, no. 3, 2015.

[18] J. G. McComb, "A practical clinical classification of spinal neural tube defects," *Child's Nervous System*, vol. 31, no. 10, pp. 1641–1657, 2015.

[19] J. A. Hyett, "The Danish Fetal Medicine Database: Revealing the fruits of collaborative research," *Acta Obstetricia et Gynecologica Scandinavica*, vol. 94, no. 6, pp. 561-562, 2015.

[20] EUROCAT. Detailed Congenital Anomaly Coding Guidelines 2013 [cited 2017 December 16], http://www.eurocat-network.eu/content/EUROCAT-Guide-1.4-Section-3.5.pdf.

[21] A. I. Alriksson-Schmidt, M. Arner, L. Westbom et al., "A combined surveillance program and quality register improves management of childhood disability," *Disability and Rehabilitation*, vol. 39, no. 8, pp. 830–836, 2017.

[22] T. Ghi, G. Pilu, P. Falco et al., "Prenatal diagnosis of open and closed spina bifida," *Ultrasound in Obstetrics & Gynecology*, vol. 28, no. 7, pp. 899–903, 2006.

[23] C. A. Lennon and D. L. Gray, "Sensitivity and specificity of ultrasound for the detection of neural tube and ventral wall defects in a high-risk population," *Obstetrics & Gynecology*, vol. 94, no. 4, pp. 562–566, 1999.

[24] J. H. Fleurke-Rozema, T. A. Vogel, B. J. Voskamp et al., "Impact of introduction of mid-trimester scan on pregnancy outcome of open spina bifida in the Netherlands," *Ultrasound in Obstetrics & Gynecology*, vol. 43, no. 5, pp. 553–556, 2014.

[25] EUROCAT. Prenatal Detection Rates 2017 [cited 2017 2 December], http://www.eurocat-network.eu/prenatalscreeninganddiagnosis/prenataldetection(pd)rates.

[26] EUROCAT. Prevalence Tables 2015 [cited 2017 2 December], http://www.eurocat-network.eu/accessprevalencedata/prevalencetables.

[27] J. C. P. Ferreira, F. R. Grati, K. Bajaj et al., "Frequency of fetal karyotype abnormalities in women undergoing invasive testing in the absence of ultrasound and other high-risk indications," *Prenatal Diagnosis*, vol. 36, no. 12, pp. 1146–1155, 2016.

[28] H. Amini, O. Axelsson, B. Ollars, and G. Anneren, "The Swedish Birth Defects Registry: Ascertainment and incidence of spina bifida and cleft lip/palate," *Acta Obstetricia et Gynecologica Scandinavica*, vol. 88, no. 6, pp. 654–659, 2009.

Research Article

Variability in Ultrasound Backscatter Induced by Trabecular Microstructure Deterioration in Cancellous Bone

Xingxing Chou,[1] Feng Xu,[1] Ying Li,[1] Chengcheng Liu [ID],[2]
Dean Ta [ID],[1,3,4] and Lawrence H. Le[5]

[1]*Department of Electronic Engineering, Fudan University, Shanghai 200433, China*
[2]*Institute of Acoustics, Tongji University, No. 1239 Siping Road, Shanghai 200092, China*
[3]*State Key Laboratory of ASIC and System, Fudan University, Shanghai 200433, China*
[4]*Key Laboratory of Medical Imaging Computing and Computer Assisted Intervention (MICCAI) of Shanghai, Shanghai 200032, China*
[5]*Department of Radiology and Diagnostic Imaging, University of Alberta, Edmonton, AB, Canada*

Correspondence should be addressed to Chengcheng Liu; chengchengliu@tongji.edu.cn and Dean Ta; tda@fudan.edu.cn

To determine the relationship between the ultrasonic backscatter parameters and trabecular microstructural variations in cancellous bone, three erosion procedures were performed to simulate various changes in the cancellous bone microstructure. The finite difference time domain (FDTD) method was used to simulate the backscatter signal in cancellous bone. Ultrasonic backscatter properties were derived as functions of the porosity when the ultrasound incident directions were perpendicular and parallel to the major trabeculae direction (MTD), respectively. The variability in the apparent backscatter coefficient (ABC) and apparent integrated backscatter (AIB) due to the trabecular microstructure was revealed. Significant negative correlations between the backscatter parameters (ABC and AIB) and the porosity of the cancellous bone were observed. The simulations showed that the ABC and AIB were influenced by the direction of the trabecular microstructural variations. The linear regressions between the ultrasonic backscatter parameters (ABC and AIB) and the porosity showed significantly different slopes for three erosion procedures when they are ultrasonically perpendicular (for ABC, -1.22 dB, -0.98 dB, and -0.46 dB; for AIB, -0.74 dB, -0.69 dB, and -0.25 dB) and parallel (for ABC, -1.87 dB, -0.69 dB, and -0.51 dB; for AIB, -0.9 dB, -0.5 dB, and -0.34 dB) to the MTD. This paper investigated the relationship between ultrasonic backscatter and cancellous bone microstructure deterioration and indicated that the ultrasonic backscatter could be affected by cancellous bone microstructure deterioration direction.

1. Introduction

Osteoporosis is a multifactorial skeletal disease characterized by decreased bone mass and deteriorated microarchitecture that leads to an increased risk of fracture [1]. Early detection and treatment of osteoporosis are essential for decreasing the risk of fracture. Lots of situations can lead to osteoporosis, such as age-related and microgravity-related situations [2–6]. Both aggravating trend of aging population and the aerospace development indicate the importance of early detection and treatment of osteoporosis.

Ultrasonic backscatter has shown great advantages and potential as a noninvasive tool for cancellous bone assessment [7–15]. Compared with ultrasonic through-transmission measurement, the backscatter measurement can be performed in pulse-echo mode with a single transducer and has easier access to skeletal sites such as the hip and spine. Hosokawa has studied the changes of the ultrasonic through-transmission signal [16]. In theory, the backscatter signal could provide more microstructural information; the backscatter signal is closely related to cancellous bone properties, including the bone mineral density (BMD), bone volume fraction (BV/TV), trabecular separation (Tb.Sp), ultimate strength, and Young's modulus [7–14, 17–25].

Bone is a tissue undergoing continuous construction and degradation; the location of cancellous bone in people's body and different bone loss and growth processes determine the various cancellous bone microstructure. The

trabecular orientation of bone tissue changes in response to mechanical stimuli; the process of bone loss destruction and reconstruction is anisotropic [26, 27]. In age-related osteoporosis, the trabecular elements perpendicular to the major trabecular direction (MTD) are more strongly lost than those parallel to the MTD. Because the weakly oriented trabecular elements to which large loads are not usually applied are the first to disappear, and the porosity of the bone increases (and the state of the osteoporosis progresses) [28, 29]. For spaceflight-induced bone loss, both the weak and strong oriented trabecular elements to which loads are not applied disappear rapidly [1, 4, 5, 28].

The ultrasonic backscattering and propagation are substantially affected by the cancellous bone microstructure [19]; thus the reliability needs to be further improved in ultrasonic backscatter apparatuses, especially assessment of the bone mass changes during bone loss and growth, because the relationship of the ultrasonic backscatter and cancellous bone microstructure parameters is not yet clearly understood. However, a detailed investigation on the relationship between the ultrasonic backscatter and cancellous bone microstructure is difficult because of the various cancellous bone microstructure in the bone loss process. Some image erosion algorithms have been used to simulate the degradation of cancellous bones [16, 29, 30]. Hosokawa realized various cancellous bone microstructure using image erosion methods [16, 29]. Three erosion procedures correspond to age-related, microgravity-related, and other reasons related to bone loss [16, 29]. This paper cited their algorithms to simulate the degradation of cancellous bone in normal bone loss, weightlessness, or microgravity environment bone loss. The ultrasonic backscatter parameters, such as apparent backscatter coefficient (ABC) and apparent integrated backscatter (AIB), are generally measured from fixed region of interest in the ultrasonic backscatter signal [21]. A detailed investigation on the relationship between the ultrasonic backscatter and cancellous bone microstructure is needed.

The objective of this study is to investigate the variability in ultrasonic backscatter induced by different deteriorations of trabecular microstructure. Image erosion methods were used to simulate the deteriorations of trabecular microstructure, and three erosion procedures were performed to realize deteriorations in the cancellous bone microstructure. The FDTD method was used to simulate the backscatter signal in cancellous bone. The variability in the ABC and AIB due to the deteriorations of trabecular microstructure was revealed.

2. Methods

The reconstruction of the 3D microcomputed tomographic (μ-CT) images is useful for the numerical analysis of cancellous bone [32, 33]. The finite difference time domain (FDTD) method is useful for simulating the ultrasound propagation in cancellous bone [29, 34]. The cancellous bone model for the FDTD simulation was realized by the reconstruction of the 3D microcomputed tomographic (μ-CT) images from the cancellous bone [35].

2.1. Cancellous Bone Erosion or Deteriorations. A cancellous bone specimen (approximately $20 \times 20 \times 10$ mm) was sawed
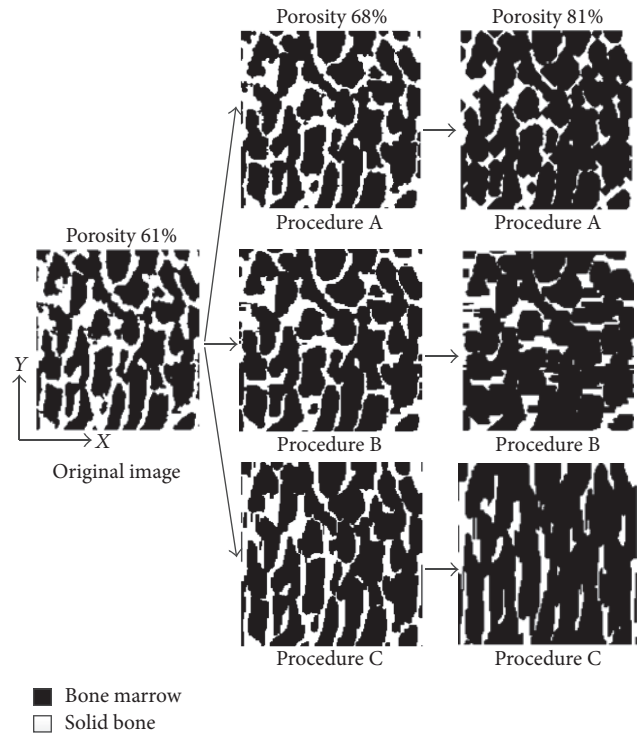
Figure 1: Deteriorations in trabecular microstructure simulated by three erosion procedures.

from a bovine distal tibia, and the trabecular image was provided by a μ-CT system (skyscan1076, Bruker micro-CT, Belgium) with a spatial resolution of $36.4\,\mu$m.

The binary image was obtained from the gray image by the automatic threshold function in the MATLAB to clearly distinguish between the trabeculae and bone marrow. The trabecular structure is with a MTD in most normal cancellous bone [36]. The 2D trabecular structures of the cancellous bone model are defined in x-y plane. As shown in Figure 1, a MTD along the y-direction can be observed.

An image erosion technique was used to erode the edges of the trabeculae in the cancellous bone model and from which to simulate the bone loss process [30, 35]. The erosion procedure was to transform the solid bone into bone marrow [16]. The porosity increased by an increment approximately 2% at the same time. The trabeculae was eroded by three erosion procedures named A, B, and C; each of the erosion procedures was applied in different direction of the trabecular edges, from which to realize distinct changing processes of the trabecular microstructure in different bone loss processes. In erosion procedure A, the erosion was randomly distributed in every direction [16]. In the other two procedures B and C, the erosions were distributed in the y- and x-direction, respectively. Procedure C realized the age-related bone loss, procedure B realized the spaceflight-induced bone loss, and procedure A is for any other reason.

The direction of the erosion distributed was set in the erosion function. To the three erosion procedures, as an example, Figure 1 shows the different changes in trabecular structure induced by them. In Figure 1, the image in the left

TABLE 1: Physical parameter values of cancellous bone [31].

	Trabeculae	Bone Marrow
First Lamé coefficient (GPa)	14.8	2.2
Second Lamé coefficient (GPa)	8.3	0
Density (kg/m^3)	1960	1000
Normal resistance coefficient (s^{-1})	8×10^4	75
Shear resistance coefficient (s^{-1})	8×10^5	0
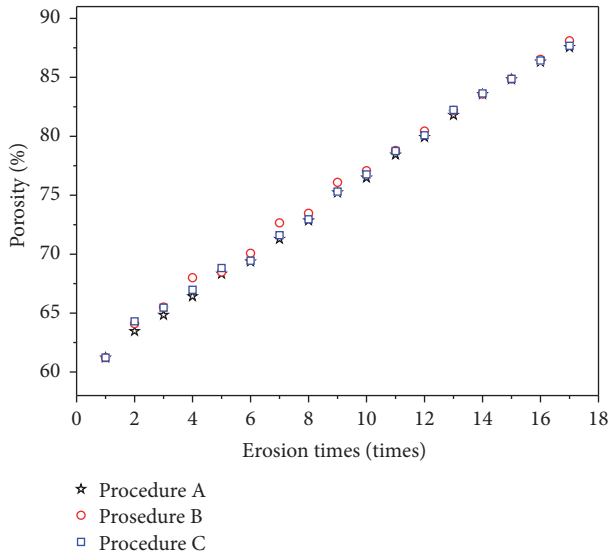
FIGURE 2: Porosity of cancellous bone with respect to erosion times.

FIGURE 3: The geometry of the simulation model.

with a 61% porosity is original image before erosion, and the porosity is increasing with the erosion of original image. As an example, when the porosity is 68%, the images of three procedures are shown in the middle and their porosities are the same; compared with the original image, in the image of procedure A (top), the erosion is randomly distributed in every direction. In the other two procedures B (middle) and C (below), the erosions were distributed in the y- and x-direction, respectively. The solid bones (white) decrease in the corresponding direction. When the porosity is 81% (right), the difference of three erosion procedures is more obvious. It appears that the trabeculae changes of the three erosion procedures are different in directions. Thus, various trabecular microstructures of different causes could be realized by the three erosion procedures, and the trabecular orientation (or the pore orientation) in the y-direction becomes stronger in the cancellous bone model. The porosities of all the cancellous bone models eroded in the three procedures are shown in Figure 2. Each erosion procedure is performed 16 times; porosity of cancellous bone before erosion is 61%, increased by an increment approximately 2% at the same time and increased from 60% to 90% based on the general range.

2.2. Ultrasonic Backscatter Simulations. Figure 3 shows the FDTD simulation model, with a total region of 10.5×7.4 mm, for the ultrasonic backscatter measurement, and a cancellous

bone model (6.0 × 6.0 mm) was placed in the center [21]. The transmitting surfaces were with a diameter of 3.64 mm. The physical parameters of the simulation model are listed in Table 1.

As shown in Figure 3, the ultrasonic propagation was along the x-direction. With the cancellous bone model rotated by 90 degrees, the ultrasonic propagation is perpendicular to the MTD of the cancellous bone when the MTD is in y-direction.

A Gaussian-modulated sinusoidal pulse was used as the ultrasound pressure source [21]:

$$p(t) = -t \cdot \exp\left(-4\beta^2 t^2\right) \sin\left(2\pi f_0 t\right), \tag{1}$$

where β is the bandwidth and f_0 is central frequency. In the simulation, the parameters are defined as follows: β = 0.5 MHz; the central frequency f_0 was set to 1 MHz; the space step was set to 36.4 μm, corresponding to the voxel size of the cancellous bone image; and the time step was 5 ns [37].

2.3. Backscatter Signal Analysis. Figure 4 shows a typical simulated backscatter signal at 1 MHz. The backscattered signal of interest (SOI) was selected by a rectangular window of T in length of the backscatter signal, where T = 2 μs [20].

ABC and AIB were defined as follows [7, 11, 38, 39]:

$$\text{ABC} = 8.68 \ln\left(\frac{S_{\text{SOI}}(f)}{S_r(f)}\right),$$

$$\text{AIB} = \frac{1}{f_{\max} - f_{\min}} \int_{f_{\min}}^{f_{\max}} \text{ABC}(f)\, df, \tag{2}$$

TABLE 2: Linear fitting for the ultrasonic backscatter parameters (ABC and AIB) versus the porosity of the three erosion procedures perpendicular and parallel to MTD[1].

	Perpendicular to MTD			Parallel to MTD		
	Procedure A	Procedure B	Procedure C	Procedure A	Procedure B	Procedure C
ABC						
Intercept (dB)	51.59	31.16	0.02	96.27	13.10	285
Slope (dB)	−1.22	−0.98	−0.46	−1.87	−0.69	−0.51
AIB						
Intercept (dB)	34.23	28.85	0.78	44.82	16.21	5.94
Slope (dB)	−0.74	−0.69	−0.25	−0.90	−0.50	−0.34

[1] All of the p values are below 0.01.
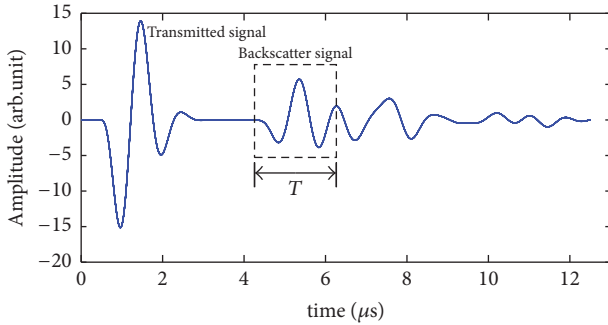
FIGURE 4: Simulated backscatter signals and signal of interest selection.

where $S_{SOI}(f)$ is the amplitude spectrum of the backscatter SOI, $S_r(f)$ is the reference spectrum of the backscatter signal reflected by a standard steel plate, and f_{max} and f_{min} correspond to the −6 dB effective frequency band. The central frequency is used in the calculation of the ABC.

3. Results

3.1. Backscatter Properties for Ultrasonic Propagation Perpendicular to MTD. Figure 5 shows the ABC versus the porosity induced by three different erosion procedures for ultrasonic propagation perpendicular to MTD. The ABC shows significant negative correlations with the porosity of the cancellous bone in all procedures (procedure A: $R = -0.94$; procedure B: $R = -0.97$; procedure C: $R = -0.80$). In the three different erosion procedures, the cancellous bone microstructure undergoes different changes, and the ultrasonic backscatter signals are different. The ABC of procedure B are the smaller than those of the other two procedures, and in procedure B the trabecular microstructural variations are parallel to MTD. The linear fittings for ABC versus the porosity of the three erosion procedures are listed in Table 2. Significant differences are observed between the slopes for the three erosion procedures (procedure A: −1.22 dB; procedure B: −0.98 dB; procedure C: −0.46 dB). The absolute values of the slope for procedure C are the smallest.

The AIB is an important parameter of ultrasonic backscattering. The AIB versus the porosity of the cancellous bone induced by the different erosion procedures

★ Procedure A $R = -0.94$
○ Procedure B $R = -0.97$
□ Procedure C $R = -0.80$
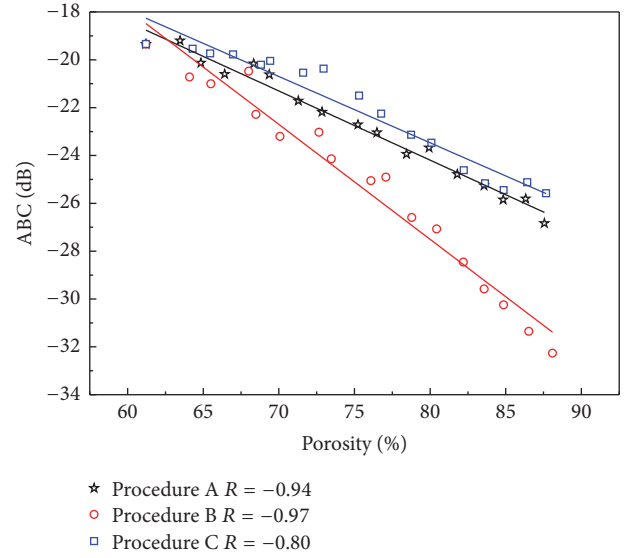
FIGURE 5: Relationships between ABC and cancellous bone porosity induced by different erosions for ultrasonic propagating perpendicular to the MTD.

perpendicular to MTD is shown in Figure 6. Significant negative correlations with the porosity of the cancellous bone are observed in all procedures (procedure A: $R = -0.96$; procedure B: $R = -0.99$; procedure C: $R = -0.91$). The liner regressions between the AIB and porosity showed significant differences in the slopes for the three erosion procedures (procedure A: −0.74 dB; procedure B: −0.69 dB; procedure C: −0.25 dB).

3.2. Backscatter Properties for Ultrasonic Propagation along MTD. The ABC and AIB results versus the porosity of the cancellous bone induced by the different erosion procedures along the MTD are shown in Figures 7 and 8, respectively. Both the ABC and AIB show significant negative correlations with the porosity of the cancellous bone in all procedures (ABC: $R = -0.90, -0.84, -0.71$; AIB: $R = -0.96, -0.90, -0.92$). For the three different erosion procedures, with the increase in the cancellous bone porosity, the cancellous bone microstructure undergoes various changes. The changes in ABC and AIB are different for the same porosity. Based on the regression results listed in Table 2, the slopes for the three
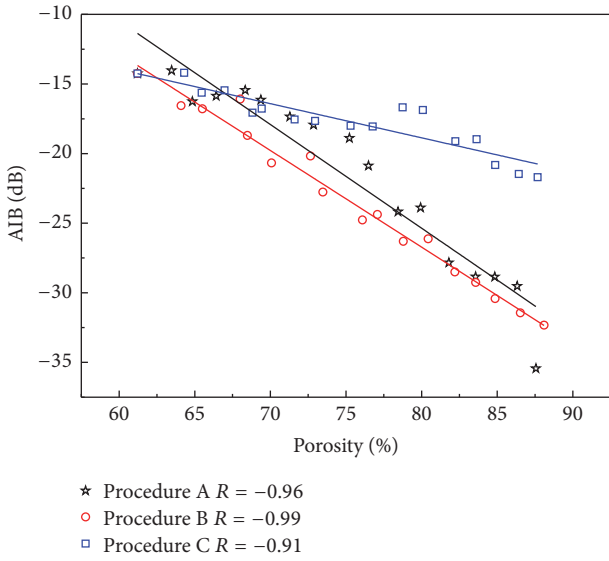
FIGURE 6: Relationships between AIB and cancellous bone porosity induced by different erosions for ultrasonic propagating perpendicular to the MTD.
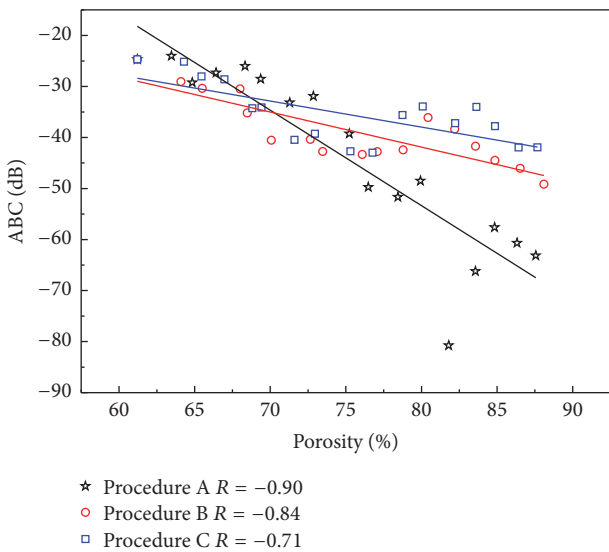
FIGURE 7: Relationships between ABC and cancellous bone porosity induced by different erosions for ultrasonic propagation along the MTD.

erosion procedures are different. Compared with the results perpendicular to the MTD, the values of ABC and AIB are smaller, and the corresponding slopes are different.

4. Discussion

ABC and AIB reflect the frequency-related intensity of the backscatter signal. The signal strength is mainly affected by the scattering cross section and attenuation. The reflected signal energy increases with the scattering cross section. When the ultrasonic incident direction is along the MTD,
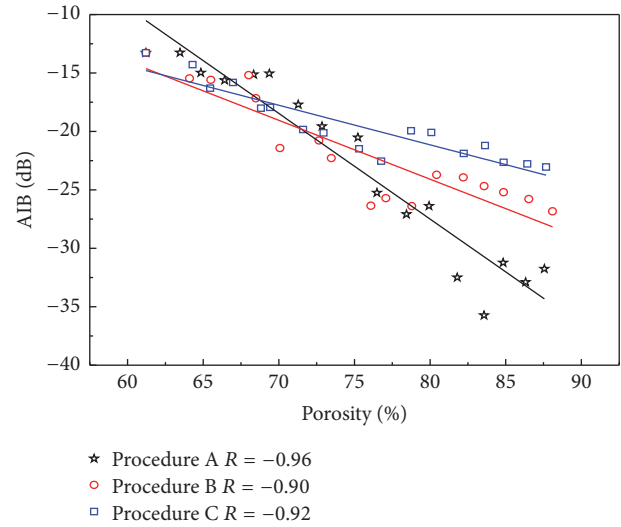
FIGURE 8: Relationships between AIB and cancellous bone porosity induced by different erosions for ultrasonic propagation along the MTD.

the scattering cross section is smaller than that for ultrasonic perpendicular to MTD and the values of ABC are smaller. Besides, the attenuation increases with trabecular bone length in the transmission direction. Thus, the ABC and AIB not only are influenced by bone mass or porosity but also will be influenced by trabecular microstructure of cancellous bone.

The simulations show that ABC and AIB vary differently for the three procedures with the increasing of porosity. With the notations ABC_φ, AIB_φ is used to represent ABC, AIB under procedure φ ($\varphi = A, B, C$), the simulation results show that when the ultrasonic propagation is perpendicular to MTD, both ABC and AIB show significant negative correlations with the porosity of the cancellous bone in all procedures. The slopes of the liner fitting results for the three erosion procedures (ABC: -1.22 dB, -0.98 dB, and -0.46 dB; AIB: -0.74 dB, -0.69 dB, and -0.25 dB) are different. To the same porosity, the ABC_B and AIB_B are smaller than those of the other two procedures. In procedure B, the trabecular microstructure deterioration along the MTD, the length of the trabeculae in the propagation direction, is larger than those of the other procedures, which simulate the spaceflight-induced bone loss. The results indicate that the ABC and AIB may be smallest in the case of the trabecular microstructure deterioration along the MTD when propagation is perpendicular to MTD and with the increasing porosity. The slopes of procedure C are the smallest, which simulates the age-related bone loss. Besides, the difference values of the three procedures also increase for both ABC and AIB.

The ABC_φ and AIB_φ for the three erosion procedures are also different when the propagation is along MTD, but compared to the results of propagation perpendicular to MTD, the values of ABC and AIB are smaller, the corresponding slopes of procedures A, B, and C (perpendicular MTD: ABC: -1.22 dB, -0.98 dB, -0.46 dB; AIB: -0.74 dB, -0.69 dB, -0.25 dB; along MTD: ABC: -1.87 dB, -0.69 dB, -0.51 dB; AIB: -0.9 dB, -0.5 dB, -0.34 dB) are also different, because

there is a major trabecular direction in cancellous bone. The results along MTD further indicate the variability in ABC and AIB induced by the trabecular microstructure in cancellous bone and illustrate that ABC and AIB are sensitive to the trabecular microstructure.

It is the same as the experimental results in the previous study [40]; ABC and AIB both had negative correlations with the porosity. The ABC and AIB are influenced by the trabecular microstructure deterioration direction; the slops of linear fitting between them (ABC and AIB) and porosity indicate that, for the linear evaluation of BV/TV or porosity using ABC or AIB to the age-related and spaceflight-induced bone loss, the deterioration direction maybe should be considered.

In a previous study it was suggested that the ultrasound backscatter was affected by the anisotropic microstructure [19]. And to the same reason induced bone loss, to the trabecular microstructures are various, but the deterioration direction is the same. In the present study, the effect of deterioration direction is investigated. And it is significant that when the deterioration direction is considered, the liner assessment of BV/TV by the ABC or AIB is more accurate.

This study investigated the relationship between ultrasonic backscatter and cancellous bone microstructure deterioration and indicated that the ultrasonic backscatter was affected by cancellous bone microstructure deterioration direction, and we just discussed the parameters of ABC and AIB. Therefore, the study of the trabecular microstructure effect on the different ultrasonic backscatter parameters without the porosity should be elaborated upon in the future.

5. Conclusion

The variabilities of ABC and AIB induced by different direction deteriorations of trabecular microstructure were investigated. ABC and AIB showed significantly negative correlations with the porosity of the cancellous bone. ABC and AIB were sensitive to the trabecular microstructure; they were confined to erosion procedures from which three different direction cancellous bone microstructure changes were revealed. The ABC and AIB are affected by the trabecular microstructure deterioration direction. When using ABC and AIB accurately in the evaluation of cancellous bone mass on different reason related bone loss, the effect of the trabecular microstructure deterioration direction maybe should be considered.

Conflicts of Interest

The authors state that they have no conflicts of interest.

Acknowledgments

References

[1] L. Vico, V. E. Novikov, J. M. Very, and C. Alexandre, "Bone histomorphometric comparison of rat tibial metaphysis after 7-day tail suspension vs. 7-day spaceflight," *Aviation, Space, and Environmental Medicine*, vol. 62, no. 1, pp. 26–31, 1991.

[2] D. Grimm, J. Grosse, M. Wehland et al., "The impact of microgravity on bone in humans," *Bone*, vol. 87, pp. 44–56, 2016.

[3] S. Khosla and B. L. Riggs, "Pathophysiology of age-related bone loss and osteoporosis," *Endocrinology and Metabolism Clinics of North America*, vol. 34, no. 4, pp. 1015–1030, 2005.

[4] R. Y. Lau and X. Guo, "A Review on Current Osteoporosis Research: With Special Focus on Disuse Bone Loss," *Journal of Osteoporosis*, vol. 2011, Article ID 293808, 6 pages, 2011.

[5] M. P. Nagaraja and D. Risin, "The current state of bone loss research: data from spaceflight and microgravity simulators," *Journal of Cellular Biochemistry*, vol. 114, no. 5, pp. 1001–1008, 2013.

[6] J. D. Sibonga, "Spaceflight-induced bone loss: Is there an Osteoporosis Risk?" *Current Osteoporosis Reports*, vol. 11, no. 2, pp. 92–98, 2013.

[7] B. K. Hoffmeister, A. P. Holt, and S. C. Kaste, "Effect of the cortex on ultrasonic backscatter measurements of cancellous bone," *Physics in Medicine and Biology*, vol. 56, no. 19, article no. 006, pp. 6243–6255, 2011.

[8] B. K. Hoffmeister, D. P. Johnson, J. A. Janeski et al., "Ultrasonic characterization of human cancellous bone in vitro using three different apparent backscatter parameters in the frequency range 0.6-15.0 MHz," *IEEE Transactions on Ultrasonics, Ferroelectrics and Frequency Control*, vol. 55, no. 7, pp. 1442–1452, 2008.

[9] K. H. Chong, B. K. Poh, N. A. Jamil, N. A. Kamaruddin, and P. Deurenberg, "Radial quantitative ultrasound and dual energy X-ray absorptiometry: Intermethod agreement for bone status assessment in children," *BioMed Research International*, vol. 2015, Article ID 232876, 7 pages, 2015.

[10] D.-A. Ta, G.-H. Zhou, W.-Q. Wang, and J.-G. Yu, "Measurement of Spectral Maximum Shift of Ultrasonic Backscatter Signals in Cancellous Bone," in *Proceedings of the IEEE Engineering in Medicine and Biology 27th Annual Conference*, pp. 2703–2706, Shanghai, China, January 2006.

[11] D. Ta, W. Wang, K. Huang, Y. Wang, and L. H. Le, "Analysis of frequency dependence of ultrasonic backscatter coefficient in cancellous bone," *The Journal of the Acoustical Society of America*, vol. 124, no. 6, pp. 4083–4090, 2009.

[12] Y. Li, D. Liu, K. Xu, D. Ta, L. H. Le, and W. Wang, "Transverse and Oblique Long Bone Fracture Evaluation by Low Order Ultrasonic Guided Waves: A Simulation Study," *BioMed Research International*, vol. 2017, Article ID 3083141, 10 pages, 2017.

[13] B. K. Hoffmeister, A. R. Wilson, M. J. Gilbert, and M. E. Sellers, "A backscatter difference technique for ultrasonic bone assessment," *The Journal of the Acoustical Society of America*, vol. 132, no. 6, pp. 4069–4076, 2012.

[14] C. C. Liu, D. A. Ta, and W. Q. Wang, "Effect of trabecular bone material properties on ultrasonic backscattering signals," *Chinese Journal of Acoustics*, vol. 38, no. 1, pp. 73–82, 2014.

[15] K. A. Wear, "Ultrasonic scattering from cancellous bone: A review," *IEEE Transactions on Ultrasonics, Ferroelectrics and Frequency Control*, vol. 55, no. 7, pp. 1432–1441, 2008.

[16] A. Hosokawa, "Numerical analysis of variability in ultrasound propagation properties induced by trabecular microstructure

in cancellous bone," *IEEE Transactions on Ultrasonics, Ferroelectrics and Frequency Control*, vol. 56, no. 4, pp. 738–747, 2009.

[17] C. Apostolopoulos and D. Deligianni, "Influence of microarchitecture on cancellous bone ultrasonic backscatter," in *Proceedings of the 8th International Workshop on Mathematical Methods in Scattering Theory and Biomedical Engineering*, pp. 211–217, September 2007.

[18] B. K. Hoffmeister, C. I. Jones III, G. J. Caldwell, and S. C. Kaste, "Ultrasonic characterization of cancellous bone using apparent integrated backscatter," *Physics in Medicine and Biology*, vol. 51, no. 11, article no. 002, pp. 2715–2727, 2006.

[19] C. Liu, D. Ta, F. Fujita et al., "The relationship between ultrasonic backscatter and trabecular anisotropic microstructure in cancellous bone," *Journal of Applied Physics*, vol. 115, no. 6, Article ID 064906, 2014.

[20] C. Liu, T. Tang, F. Xu et al., "Signal of Interest Selection Standard for Ultrasonic Backscatter in Cancellous Bone Evaluation," *Ultrasound in Medicine & Biology*, vol. 41, no. 10, pp. 2714–2721, 2015.

[21] C. Liu, H. Han, D. Ta, and W. Wang, "Effect of selected signals of interest on ultrasonic backscattering measurement in cancellous bones," *Science China Physics, Mechanics & Astronomy*, vol. 56, no. 7, pp. 1310–1316, 2013.

[22] B. K. Hoffmeister, J. A. McPherson, M. R. Smathers, P. L. Spinolo, and M. E. Sellers, "Ultrasonic backscatter from cancellous bone: The apparent backscatter transfer function," *IEEE Transactions on Ultrasonics, Ferroelectrics and Frequency Control*, vol. 62, no. 12, pp. 2115–2125, 2015.

[23] K. A. Wear, "Frequency dependence of ultrasonic backscatter from human trabecular bone: Theory and experiment," *The Journal of the Acoustical Society of America*, vol. 106, no. 6, pp. 3659-2664, 1999.

[24] K. A. Wear, A. P. Stuber, and J. C. Reynolds, "Relationships of ultrasonic backscatter with ultrasonic attenuation, sound speed and bone mineral density in human calcaneus," *Ultrasound in Medicine & Biology*, vol. 26, no. 8, pp. 1311–1316, 2000.

[25] R. Smolíková, M. P. M. P. Wachowiak, and J. M. J. M. Zurada, "An information-theoretic approach to estimating ultrasound backscatter characteristics." *Computers in Biology and Medicine*, vol. 34, no. 4, pp. 355–370, 2004.

[26] J. Wolff, *The Law of Bone Remodelling*, Springer, Berlin, Germany, 1986.

[27] S. Ramtani, J. M. Garcia, and M. Doblare, "Computer simulation of an adaptive damage-bone remodeling law applied to three unit-bone bars structure," *Computers in Biology and Medicine*, vol. 34, no. 4, pp. 259–273, 2004.

[28] H. M. Frost, "Wolff's Law and bone's structural adaptations to mechanical usage: an overview for clinicians," *The Angle Orthodontist*, vol. 64, no. 3, pp. 175–188, 1994.

[29] A. Hosokawa, "Effect of porosity distribution in the propagation direction on ultrasound waves through cancellous bone," *IEEE Transactions on Ultrasonics, Ferroelectrics and Frequency Control*, vol. 57, no. 6, pp. 1320–1328, 2010.

[30] G. Luo, J. J. Kaufman, A. Chiabrera et al., "Computational methods for ultrasonic bone assessment," *Ultrasound in Medicine & Biology*, vol. 25, no. 5, pp. 823–830, 1999.

[31] A. Hosokawa, "Development of a numerical cancellous bone model for finite-difference time-domain simulations of ultrasound propagation," *IEEE Transactions on Ultrasonics, Ferroelectrics and Frequency Control*, vol. 55, no. 6, pp. 1219–1233, 2008.

[32] R. P. Gilbert, P. Guyenne, and J. Li, "Numerical investigation of ultrasonic attenuation through 2D trabecular bone structures reconstructed from CT scans and random realizations," *Computers in Biology and Medicine*, vol. 45, no. 1, pp. 143–156, 2014.

[33] D. Sreenivasan, P. T. Tu, M. Dickinson et al., "Computer modelling integrated with micro-CT and material testing provides additional insight to evaluate bone treatments: Application to a beta-glycan derived whey protein mice model," *Computers in Biology and Medicine*, vol. 68, pp. 9–20, 2016.

[34] J. Litniewski, "Statistics of envelope of high-frequency ultrasonic backscatter from trabecular bone: Simulation study," *Archives of Acoustics*, vol. 35, no. 3, pp. 349–360, 2010.

[35] L. J. Gibson, "The mechanical behaviour of cancellous bone," *Journal of Biomechanics*, vol. 18, no. 5, pp. 317–328, 1985.

[36] G. Haïat, F. Padilla, F. Peyrin, and P. Laugier, "Variation of ultrasonic parameters with microstructure and material properties of trabecular bone: A 3D model simulation," *Journal of Bone and Mineral Research*, vol. 22, no. 5, pp. 665–674, 2007.

[37] J. Virieux, "SH- wave propagation in heterogeneous media: velocity- stress finite-difference method." *Geophysics*, vol. 49, no. 11, pp. 1933–1942, 1984.

[38] S. Chaffaï, F. Peyrin, S. Nuzzo, R. Porcher, G. Berger, and P. Laugier, "Ultrasonic characterization of human cancellous bone using transmission and backscatter measurements: Relationships to density and microstructure," *Bone*, vol. 30, no. 1, pp. 229–237, 2002.

[39] O. Riekkinen, M. A. Hakulinen, J. Töyräs, and J. S. Jurvelin, "Spatial variation of acoustic properties is related with mechanical properties of trabecular bone," *Physics in Medicine and Biology*, vol. 52, no. 23, pp. 6961–6968, 2007.

[40] Y.-Q. Jiang, C.-C. Liu, R.-Y. Li et al., "Analysis of apparent integrated backscatter coefficient and backscattered spectral centroid shift in calcaneus invivo for the ultrasonic evaluation of osteoporosis," *Ultrasound in Medicine & Biology*, vol. 40, no. 6, pp. 1307–1317, 2014.

Review Article

The Use of Ultrasound Imaging in the External Beam Radiotherapy Workflow of Prostate Cancer Patients

Saskia M. Camps ⓘ,[1,2] **Davide Fontanarosa** ⓘ,[3,4,5] **Peter H. N. de With**,[1]
Frank Verhaegen ⓘ,[5] **and Ben G. L. Vanneste** ⓘ[5]

[1]*Faculty of Electrical Engineering, University of Technology Eindhoven, Eindhoven, Netherlands*
[2]*Oncology Solutions Department, Philips Research, Eindhoven, Netherlands*
[3]*School of Clinical Sciences, Queensland University of Technology, Brisbane, QLD, Australia*
[4]*Institute of Health & Biomedical Innovation, Queensland University of Technology, Brisbane, QLD, Australia*
[5]*Department of Radiation Oncology (MAASTRO), GROW School for Oncology and Developmental Biology, Maastricht, Netherlands*

Correspondence should be addressed to Ben G. L. Vanneste; ben.vanneste@maastro.nl

External beam radiotherapy (EBRT) is one of the curative treatment options for prostate cancer patients. The aim of this treatment option is to irradiate tumor tissue, while sparing normal tissue as much as possible. Frequent imaging during the course of the treatment (image guided radiotherapy) allows for determination of the location and shape of the prostate (target) and of the organs at risk. This information is used to increase accuracy in radiation dose delivery resulting in better tumor control and lower toxicity. Ultrasound imaging is harmless for the patient, it is cost-effective, and it allows for real-time volumetric organ tracking. For these reasons, it is an ideal technique for image guidance during EBRT workflows. Review papers have been published in which the use of ultrasound imaging in EBRT workflows for different cancer sites (prostate, breast, etc.) was extensively covered. This new review paper aims at providing the readers with an update on the current status for prostate cancer ultrasound guided EBRT treatments.

1. Introduction

Prostate cancer is the most frequently diagnosed cancer in men worldwide. It accounted for 1.6 million new diagnoses and 366,000 deaths in 2015 [1]. In the next decades, the incidence of prostate cancer might increase due to the possible linkage of this cancer with risk factors associated with economic development (e.g., excess body weight and physical inactivity) [2] and the aging population [3].

One of the curative treatment modalities for prostate cancer is external beam radiotherapy (EBRT) [3]. The aim of this modality is to irradiate tumor tissue using ionizing radiation generated by an X-ray source (e.g., linear accelerator). At the same time, normal tissue must be spared as much as possible to avoid excessive toxicity. EBRT is one of the most common forms of RT treatment and therefore it is often denoted as just radiotherapy (RT) in literature (as will be done in the remainder of this paper).

Prior research using kV radiography has shown [4, 5] that frequent imaging of the patients' anatomical structures of interest during the course of the prostate RT treatment (image guided RT, IGRT) can improve radiation targeting and tumor control. This improved targeting could allow reduction of safety margins, with consequently decreased toxicity. Next to kV radiographs also other imaging modalities have been used for IGRT, such as cone beam CT (CBCT) in combination with fiducial markers [6], magnetic resonance imaging (MRI) [7], implantation of electromagnetic transponders [8], and ultrasound (US) imaging [9].

In this review paper the focus solely lies on the use of US imaging during the IGRT workflow of prostate cancer patients. US imaging typically provides good soft-tissue contrast and therefore it is a modality that allows contouring of structures such as the prostate [10]. It is also a real-time image modality, because the images are reconstructed and visualized directly during the acquisition. Some of the
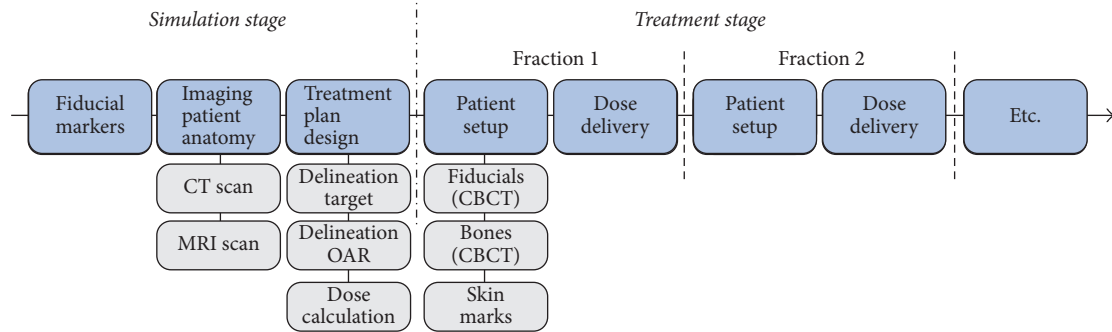
Figure 1: Typical RT workflow for prostate cancer patients. During the simulation stage, fiducial markers are implanted in the prostate, images of the patient's anatomy are acquired, and a treatment plan is designed. Subsequently, the dose is delivered to the patient in several treatment fractions, while ensuring that the patient is set up as accurately as possible.

currently available US systems potentially even allow real-time volumetric imaging and soft-tissue tracking, using a matrix probe (e.g., X6-1 xMatrix array probe, center frequency: 3.2 MHz, Philips Healthcare, Bothell, WA, United States), or a mechanically swept probe (e.g., Clarity Autoscan probe, m4DC7-3/40, center frequency: 5 MHz, Sonix Series; Ultrasonix Medical Corporation, Richmond, BC, Canada).

Some of the limitations and challenges associated with US imaging include the inaccessibility of tissue shielded by bone or air, the proneness for imaging artifacts, and the user dependency [17], due to its mostly manual operation. However, in comparison with other imaging modalities US is cost-effective and it does not deliver ionizing radiation to the patient. The combination of these characteristics with the real-time volumetric tracking ability makes US imaging a suitable image modality for inter- and intrafraction organ motion monitoring during the course of a prostate RT treatment [34]. US imaging could then be used either as standalone system or possibly in combination with other imaging modalities.

In 2015 and 2016 two review articles [11, 12] were published in which the use of US for IGRT of different cancer sites (e.g., prostate, breast, and liver) was extensively covered. The current review article updates this work for prostate cancer. After an introductory summary on US techniques and US systems that can potentially be used during the RT prostate cancer patient workflow, a comprehensive update on the latest developments in this field is presented.

2. EBRT Workflow and US Imaging

2.1. EBRT Workflow. The typical RT workflow of prostate cancer patients consists of several steps, belonging to either the simulation stage (preparatory phase) or the treatment stage (radiation dose delivery phase) (Figure 1). The first step involves the invasive implantation of fiducial markers in the prostate gland. These markers are considered a surrogate for the target and are currently used to monitor its motion between different treatment fractions using X-ray imaging.

Subsequently, a computed tomography (CT) scan and increasingly more often an MRI scan are acquired. The CT scan provides electron-density information allowing for treatment plan preparation, based on prescribed radiation dose and delineations of the anatomical structures of interest (target and organs at risk [OARs]). In case also an MRI is acquired, it is registered with the CT scan based on the fiducial markers [35], which can be visualized with both imaging modalities. Then, the prostate (target) is delineated on the MRI instead of on the CT scan. As the volumes are registered, the delineation can be transferred to the CT scan and used during the treatment plan preparation. MRI-based delineation is preferred as MRI usually allows for a more accurate delineation of the prostate than the CT [36–38].

After finalizing the treatment plan design, the radiation dose will be delivered to the patient in multiple daily treatment fractions (up to 45) during 1-2 months [3]. The setup of the patient prior to each of these treatment fractions is an important step in the RT workflow. This procedure must be as accurate as possible to reproduce the setup at simulation stage, on which the treatment plan was designed.

Nowadays, setting up the patient is typically assisted by the use of skin marks on the patient's body [39], the previously mentioned fiducial markers [40], and CBCT [41]. However, even if the patient seems to be correctly aligned, internal soft-tissue deformations may still occur. The position and shape of the prostate can change, due to a different filling of the bladder and rectum [42]. To account for these deviations from the simulation CT, a safety margin is usually added to the treatment target [18]. Unfortunately, this leads to a larger volume being irradiated, potentially including larger portions of OARs.

Monitoring the position and shape of the prostate during the course of the RT treatment could potentially improve the accuracy of the radiation dose delivery and, in the end, potentially even allow for a margin reduction. In the ideal case, this prostate monitoring would not only include monitoring between different fractions (interfraction), but also during a treatment fraction (intrafraction) [12]. As noted before, US imaging could be a suitable imaging modality for this purpose.

2.2. US Imaging in RT Workflow. US imaging makes use of a probe equipped with piezoelectric elements to create high-frequency sound waves and transmit these into the body. On
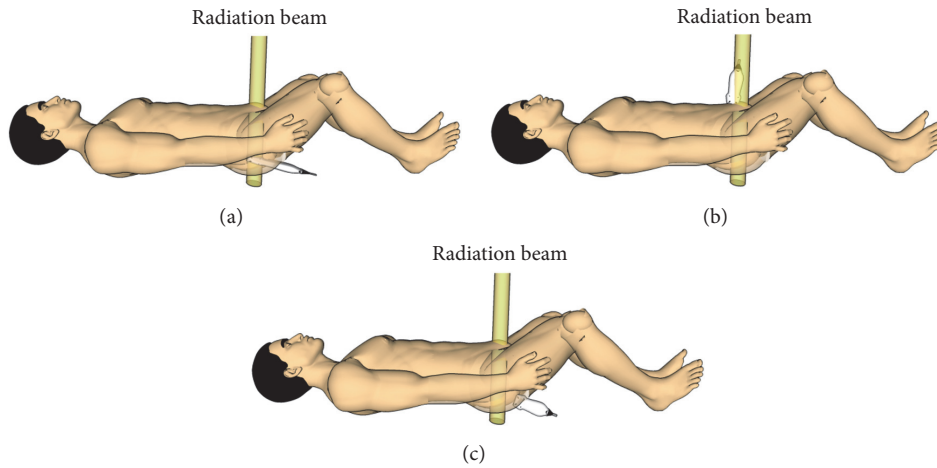
FIGURE 2: US probe setup using three US imaging techniques. (a) TRUS, (b) TAUS, and (c) TPUS with the yellow beam indicating a possible location of a radiation beam during a treatment fraction.
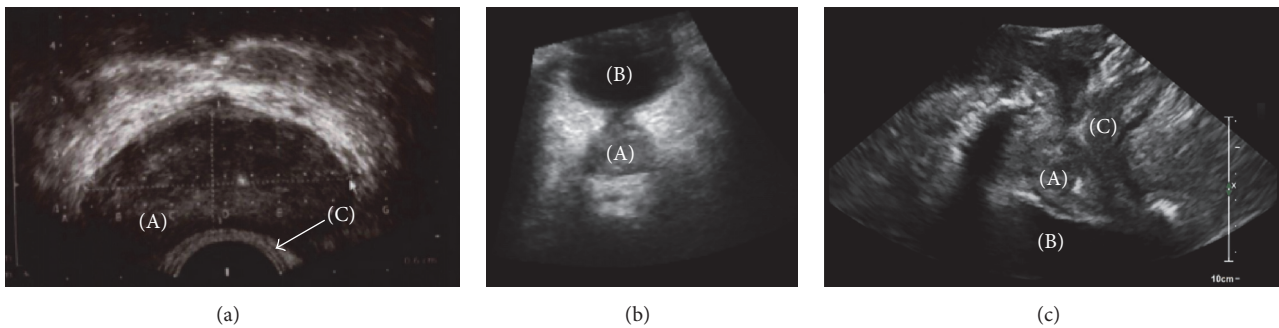
FIGURE 3: Three US techniques suitable for prostate and OARs imaging (a) TRUS, (b) TAUS, and (c) TPUS, with (A) prostate, (B) bladder, and (C) rectum which can partially be seen.

their way through the body, these waves encounter interfaces between different tissues and scattering objects. Due to the difference in acoustic impedance between the tissues at each side of this interface and between the scattering objects and the surrounding tissue, a part of the US waves is reflected, while the remaining waves keep penetrating deeper into the body. The reflected waves are received by the probe, processed, and combined to generate an image.

As air reflects US waves very strongly, the presence of air between the probe and the body of the patient will prevent sufficient penetration of the waves into the body, which significantly degrades the image quality. It is therefore crucial to establish sufficient acoustic coupling between the probe and the body. For this purpose, a coupling medium, such as US gel or water, is typically used.

Several US probes with different shapes and characteristics are commercially available for the different procedures possible with this technology. To image the prostate and OARs during the RT workflow, three US imaging techniques are presently used in clinical practice. These techniques and how they can potentially improve the accuracy of radiation dose delivery are described in the next sections. We refer to the literature (e.g., [43, 44]) for more general details on the physics theory and technology of US imaging.

2.2.1. Transrectal US Imaging.

Transrectal US (TRUS) imaging requires positioning of the probe through the anus inside the rectum (Figure 2(a)) and is therefore a low invasive imaging procedure. As the prostate is located in close proximity of the rectum, TRUS allows imaging of the prostate with a good image quality (Figure 3(a)) [45]. Challenges that can occur while making use of TRUS imaging are rectal filling, which can be removed using an enema [46], and the potential presence of air in the rectum, which results in a poor acoustic coupling between the probe and the body of the patient.

In the EBRT workflow, TRUS imaging is currently used to the guide fiducial marker placement during the simulation stage (Figure 4) [47]. The invasive character of this US modality makes it less suitable for frequent imaging during the course of the treatment. In addition, the presence of the probe inside the rectum being potentially in the path of the radiation treatment beam (Figure 2(a)) raises issues as well. For this reason, no research seems to have been conducted on the use of TRUS for inter- and intrafraction organ motion monitoring during prostate EBRT.

2.2.2. Transabdominal US Imaging.

Transabdominal US (TAUS) imaging involves the positioning of the US probe on the abdomen (Figure 2(b)) and it is therefore a noninvasive
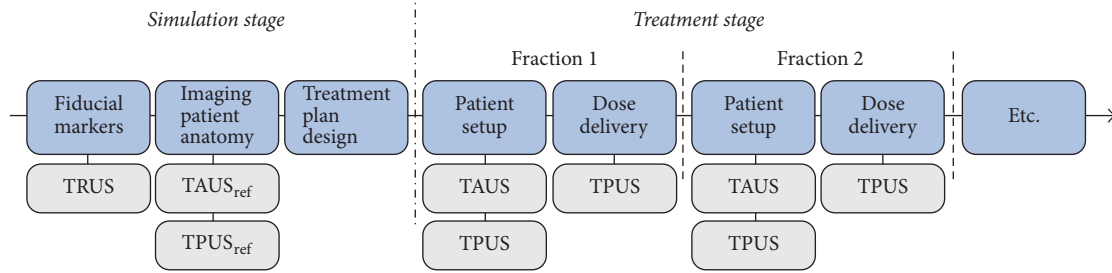
FIGURE 4: RT workflow of prostate cancer patients with US imaging implemented at several steps. The fiducial marker implantation is currently performed under TRUS guidance. The acquisition of the reference TAUS or TPUS images at simulation stage and also the acquisition of TAUS and TPUS prior to dose delivery can provide valuable information for interfraction prostate motion correction. Finally, during dose delivery TPUS imaging could provide information on intrafraction prostate motion.

imaging modality. It is capable of measuring the same prostate volumes as TRUS imaging (considered the standard) [48] and it makes use of the acoustic window of the bladder for prostate visualization (Figure 3(b)). For this reason, TAUS requires a reasonably full bladder, which might lead to discomfort for the patients. However, a filled bladder is often requested during the RT treatment to prevent the whole bladder wall from being irradiated and to push the intestines away from the high dose regions.

During TAUS imaging, the probe is located relatively far from the prostate, which might influence the quality of the acquired images. Particularly the acquisition of TAUS images of obese patients is a challenge [49]. Adipose tissue attenuates the US waves and increases the possibility for imaging artifacts, which can significantly degrade the image quality. Unfortunately, it is a challenge to predict the degree of adipose attenuation and the associated image quality degradation, due to the dependence on patient-specific characteristics, such as fat distribution [50].

The probe setup on the body of the patient during TAUS imaging makes this imaging modality suitable for interfraction monitoring. However, it is more challenging to use TAUS imaging for intrafraction monitoring (Figure 4), as the probe is potentially located in the path of the radiation beam, especially for rotational therapy (Figure 2(b)). Ways to overcome this challenge are currently not available in clinical practice, although they are being investigated. In Section 6 of this paper, the recent developments in this field will be discussed.

In the past 20 years, three systems were commercially available that allowed interfraction monitoring of the prostate during the RT workflow by means of TAUS imaging: SonArray system (Varian Medical Systems, Palo Alto, CA, USA), B-Mode Acquisition and Targeting (BAT) system (Best Nomos, Pittsburgh, PA, USA), and the Clarity system (Elekta, Stockholm, Sweden, formerly called Restitu and commercialized by Resonant Medical, Montreal, QC, Canada). To our knowledge, only the Clarity system is still available on the market and as there have been papers published on this system in the last years, it will be covered in this paper.

The BATCAM system was only used in one study [51] since the publication of the previously mentioned review papers [11, 12]. In this study a comparison was made between

the Clarity system and the BATCAM system, resulting in a good agreement between both. As the BATCAM system was extensively covered in the previous review papers, it will not be discussed further in this work.

In the RT workflow, a freehand sweep using a 2D TAUS probe (C5-2/60, center frequency: 3.5 MHz, Sonix Series; Ultrasonix Medical Corporation, Richmond, BC, Canada) can be acquired by the Clarity system during the simulation stage. Due to the use of a probe localization system, it is possible to reconstruct the sweeps such that a 3D TAUS volume is created. The same procedure is repeated prior to each treatment fraction. The requirement for manual sweep acquisition makes the Clarity system inherently sensitive to uncertainties associated with operator variability and probe pressure. These issues will be covered in more detail in Section 5.

Comparison of the US volumes acquired at treatment stage and the reference US volume acquired at simulation stage allows the calculation and correction of interfractional prostate motion [34]. Besides the fact that the US probe is potentially located in the path of the radiation beam, the need of an operator performing the manual sweep for the 3D TAUS volume reconstruction makes this system not suitable for intrafraction monitoring.

2.2.3. Transperineal US Imaging. Transperineal US (TPUS) imaging is a noninvasive imaging modality, as it involves the positioning of the US probe on the perineum of the patient (Figure 2(c)). Also this imaging modality is capable of measuring the same prostate volumes as TRUS imaging [52]. TPUS imaging does not exploit the acoustic window of the bladder to obtain images of the prostate (Figure 3(c)) and therefore it requires a less strict bladder filling protocol. A semifilled bladder is still beneficial since it yields good imaging contrast distal to the prostate. In addition, as the distance between the prostate and the perineum is smaller, a relatively good image quality can potentially be achieved. However, just like with TAUS imaging, the body composition of the patient can affect the image quality. Finally, due to the fact that the probe setup does not interfere with the radiation beam (Figure 2(c)), TPUS imaging can potentially be used also for intrafraction monitoring of the prostate (Figure 4).

FIGURE 5: Clarity Autoscan system setup with (a) probe and (b) baseplate.

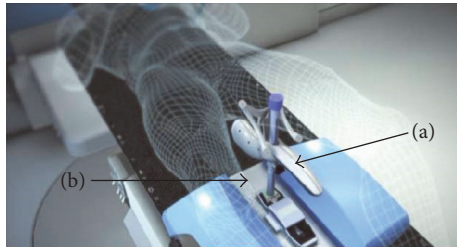Currently there is only one commercial system available that enables the inter- and intrafraction prostate motion monitoring during the RT workflow using TPUS imaging: Clarity Autoscan (Elekta, Stockholm, Sweden) [34]. This system is an extension of the Clarity system as described above. Like the Clarity system it employs a 2D probe (m4DC7-3/40, center frequency: 5 MHz, Sonix Series; Ultrasonix Medical Corporation, Richmond, BC, Canada). However, the Autoscan probe is mounted in a housing which also comprises a motorized control of the sweeping motion. This automation of the sweeping motion makes a manual sweep superfluous.

The Autoscan probe which can be localized in the room by a probe tracking system is attached to a baseplate on the CT or on the linear accelerator (LINAC) couch during the procedure (Figure 5), allowing positioning and locking of the probe for TPUS imaging. The use of the baseplate and the automatically performed sweeping motion potentially reduce the operator dependence. The operator dependence will be covered in more detail in Section 5.

The Clarity Autoscan system follows the TPUS workflow, as represented in Figure 4. First, a 3D TPUS volume is acquired at simulation stage. Then, prior to the dose delivery, a full sweep is acquired and reconstructed. Comparison of this full sweep with the image acquired at simulation allows the calculation of a required couch shift to account for interfraction prostate motion.

During the radiation dose delivery, continuous volumetric imaging using the US probe is performed. This allows position monitoring of the prostate in 3D. The therapist can interrupt the treatment and perform a couch correction, in case the motion in a certain Cartesian direction is exceeded for a certain amount of time. These motion direction and time thresholds can be set by the operator prior to the first treatment delivery [34].

3. Interfraction Monitoring

3.1. Fiducial Markers. As already introduced in Section 2, currently 3-4 fiducial markers are implanted prior to the start of the radiation treatment. The most frequently used markers are made of gold and provide a surrogate for the prostate position. The markers are visible using kV imaging modalities (such as CBCT or 2D X-ray radiographs) but can also cause metal-induced image artifacts [40].

The implantation procedure is often performed under TRUS guidance and involves invasively positioning the markers in the prostate through the perineum or the rectum [53]. The procedure can be considered as well tolerated by the majority of patients [47, 54], but it is definitely not without risks. One study [55] even suggests that the risk associated with the implantation of the markers through the rectum is still underestimated. An overall rate of symptomatic infection with the fiducial marker implantation was reported to be 7.7% with one-third requiring hospital admission.

The use of fiducial markers during the RT workflow is based on the assumption that the marker position inside the prostate will not change during the whole course of the treatment, from the simulation stage until the final treatment fraction. Changes in anatomy and physiology, however, can potentially cause or mimic marker migration [56]. Moreover, studies have shown that the presence of fiducial markers in the prostate can affect the dose deposition [57] and that imaging the fiducial markers using CBCT adds a nonnegligible dose to the patient [58].

Therefore, interfraction motion monitoring should be ideally performed with a noninvasive image modality that does not require the presence of these fiducial markers inside the prostate. In this regard, US imaging is an excellent candidate. In the next section studies are discussed which used TAUS or TPUS imaging for interfraction motion monitoring of the prostate.

3.2. TAUS and TPUS Imaging. In Table 1 the studies are reported that compared the use of TAUS (Clarity system) or TPUS (Clarity Autoscan system) with other imaging modalities for interfraction prostate monitoring. As the work of Tas et al. [59] only includes data from one prostate cancer patient, it is excluded from this table. The studies indicated with an asterisk (∗) were included in the previously mentioned review papers [11, 12]. However, they have been added to this work to provide a complete overview.

The older studies primarily focused on TAUS imaging. In these studies, 2D techniques [13, 15, 17] and volumetric imaging techniques [14, 16, 19, 20] were used for comparison with the TAUS imaging. One study [21] also compared the results of a surface imaging system (AlignRT, VisionRT, London, UK) with TAUS imaging. The four most recent studies [22–25] examined the use of TPUS imaging in comparison with volumetric imaging only, such as CBCT and an additionally acquired planning CT.

All studies (TAUS and TPUS) reported the differences (using mean ± standard deviation (SD) or error notation including mean and systematic and random error [18]) between the US imaging technique and another image modality. The reported mean differences for the anterior-posterior (AP), left-right (LR), and superior-inferior (SI) directions were in 9 out of 11 studies in the absolute range of 0–3 mm. Some studies also reported the Bland-Altman 95% limits of agreement (LoA) [60] and/or the ranges of the measured differences. For the studies that did not report the LoA, the ranges are detailed in the final column of Table 1. The largest range difference was reported by Robinson et al. [16], ranging between 1.3 mm and 61.4 mm.

TABLE 1: Studies comparing TAUS or TPUS with other imaging techniques used for IGRT. The first column details the first author and year of publication. * indicates that the paper was also included in [11, 12]. The second column details the used US technique: TAUS (Clarity) or TPUS (Clarity Autoscan). The third column indicates the parameters varied in the study. The fourth column indicates the image modality used for comparison with FM (fiducial marker) and EPI (electronic portal imaging). The columns five and six detail the number of patients and the number of acquired scans, respectively. Most studies reported the difference using mean ± standard deviation (SD) (column seven); however, one study used the error notation [13]. The square brackets indicate absolute values. The final column details the Bland-Altman Limits of Agreement (LoA) or, if this was not reported, the range of measured differences denoted between [].

First author	US	Parameters	Compared with	# pts	# US scans	Difference: mean ± SD [mm]			Bland-Altman/Range [mm]		
						AP	LR	SI	AP	LR	SI
Cury* (2006) [14]	TAUS	-	CT	10	30	-0.2 ± 1.6	0.2 ± 1.7	0.1 ± 1.4	-	-	-
Johnston* (2008) [15]	TAUS	Assisted segmentation	FM (EPI)	8	255	1.3 ± 6.6	0.9 ± 4.0	1.3 ± 5.1	-11.7–14.3	-7–8.8	-8.8–11.4
		Manual segmentation	FM (EPI)	7	181	2.1 ± 4.6	0.8 ± 3.5	0.2 ± 4.5	-6.8–11.1	-6.0–7.7	-8.7–9.0
Robinson* (2012) [16]	TAUS	(1) All datasets	CT	17	CT: 136 US: 272		10.3 ± 7.9		[1.3–61.4]		
		(2) Remove insufficient data	CT	-	US: 210		8.7 ± 4.9		[1.0–40.0]		
		(3) Review (2) manufacturer	CT	-	US: 153		7.4 ± 3.1		[1.8–17.1]		
Van Der Meer* (2013) [17]	TAUS	-	FM (EPI)	8	244	-2.3 ± 3.6	2.5 ± 4.0	0.6 ± 4.9	-9.3–4.7	-5.4–10.3	-8.9–10.2
Mayyas* (2013) [13]	TAUS	-	Bone (EPI)	27	1100	μ: -0.7 Σ: 2.4 σ: 3.4	μ: -0.5 Σ: 1.6 σ: 3.2	μ: -1.0 Σ: 2.4 σ: 3.6	μ = mean error Σ = systematic error [18] σ = random error		
Li (2015) [19]	TAUS	-	FM (CBCT)	6	78	0.0 ± 3.0	-0.2 ± 2.7	-1.9 ± 2.3	-7.3–7.2	-5.6–6.9	[-10.0–2.9]
Fargier-Voiron (2015) [20]	TAUS	Raw database	CBCT	25	284	2.8 ± 4.1	0.5 ± 3.3	-0.9 ± 4.2	-5.3–10.9	-5.9–6.9	-9.0–7.3
		Data corrected by mean US-CBCT difference of first 3 fractions	CBCT	25	284	-0.5 ± 3.9	0.3 ± 3.0	-1.0 ± 4.2	-8.1–7.1	-5.6–6.2	-7.7–7.3
Krengli (2016) [21]	TAUS	-	3D surface image	40	1318	-1.2 ± 4.9	-0.7 ± 5.0	-2.6 ± 6.4	-25.8–18.0	-48.8–15.9	[-22.5–22.1]
Richter (2016) [22]	TPUS	-	CBCT	10	150	[3.0 ± 2.4]	[2.7 ± 2.3]	[3.2 ± 2.7]	[-7.1–8.2]	-8–5	-9.4–6.5
Fargier-Voiron (2016) [23]	TPUS	With intrafraction motion	CBCT	12	357	1.9 ± 3.2	0.2 ± 2.6	0.7 ± 2.6	-4.3–8.1	-4.4–5.8	4.9–5.3
		No intrafraction motion	CBCT	12	357	2.8 ± 3	-0.1 ± 2.5	-0.3 ± 2.5	-3.2–8.8	-5–4.7	-5.1–4.6
Trivedi (2017) [24]	TPUS	-	FM (CT)	17	30	-0.06 ± 2.86	0.63 ± 3.27	-0.49 ± 3.49	-4.55–7.52	-5.96–7.06	[-6.70–6.78]
Li (2017) [25]	TPUS	-	FM (CBCT)	7	177	0.3 ± 1.7	0.0 ± 1.7	0.2 ± 2.0	-4.2–5.5	-4.8–3.9	[-4.5–5.7]

The Bland-Altman LoA are detailed in the final column of Table 1 and were reported by 5 out of 12 studies. The LoA (bias ± 1.96∗SD) are a measure for the interchangeability of two methods or systems. If the limits are smaller than or equal to an a priori defined tolerance, one method can be used interchangeably with the other. The TPUS studies (min LoA: 3.2 mm; max LoA: 9.4 mm) tend to report slightly lower LoA values than the TAUS studies (min LoA: 5.3 mm; max LoA: 11.7 mm). Considering that the prostate safety margins currently used in clinical practice (using fiducial markers) range from 3 to 10 mm [61], neither TAUS nor TPUS could be considered interchangeable with the imaging techniques they have been compared with. However, this does not automatically imply that the US techniques perform worse than the comparison technique, simply because there is no recognized ground truth. Therefore, potential inaccuracies in the imaging modality that the US is compared with can influence the results and associated conclusions.

The absence of ground truth is also reflected in conflicting conclusions regarding the potential performance of US imaging in the RT workflow. For example, Li et al. [19] concluded that it is feasible to use TAUS imaging for image guidance during the prostate RT workflow and that this image modality appears comparable to CBCT when used for the same purpose. On the other hand, Fargier-Voiron et al. [20] concluded that TAUS imaging cannot replace CBCT without increasing treatment margins. These conclusions seem to differ significantly, while the reported mean differences between the reference imaging modality and TAUS imaging are comparable.

In general, it seems that the studies investigating the use of TPUS imaging are more optimistic about the accuracy, interchangeability, and usability in comparison to the TAUS imaging studies. For example, Trivedi et al. [24] conclude that TPUS imaging provides excellent imaging of the prostate and comparable localization results. Also Li et al. [25] conclude that TPUS is a feasible image modality for IGRT and has a good accuracy.

In conclusion, different opinions exist in the literature regarding the comparability between US (TAUS and TPUS) and other imaging modalities used for image guidance during the RT workflow. For this reason, more research is necessary before final conclusions can be drawn about the usability of US imaging in the prostate IGRT workflow. Also, it is very important that US imaging is standardized to reduce the operator dependency (see Section 5).

4. Intrafraction Monitoring

As discussed in the introduction section, the position and shape of the prostate can change, due to, for example, different bladder or rectum fillings. This phenomenon can occur not only between treatment fractions, but potentially also during a treatment slot. Intrafractional prostate motion has been investigated in several studies using, for example, the Calypso localization system (Calypso Medical Technologies, Inc., Seattle, WA, USA) (e.g., [8, 62]). This system is based on the electromagnetic detection of beacon transponders which need to be implanted in the prostate. Calypso provides continuous, real-time localization of the prostate surrogates and it has been shown to have a submillimeter accuracy in a phantom [63].

These transponders need to be implanted in the prostate and, in addition, can cause image artifacts on MRI that could be used for treatment response assessment. In addition, an antenna which is necessary for the localization of the beacons is present in the path of the radiation beam. Finally, assumptions are needed to determine a relation between the position of the transponders and the shape and location of the prostate, making the Calypso system not a real volumetric tracking system.

As the Clarity Autoscan system (TPUS) does not involve implantation of transponders in the prostate, it allows for real volumetric tracking of the prostate. In addition, during the procedure no equipment is present in the beam path, which potentially makes it a more favorable solution for intrafraction prostate motion tracking in comparison to the Calypso system. Abramowitz et al. [64] found a good agreement between the Clarity Autoscan system and the Calypso system, while examining the ability of both systems to track a prostate-like sphere in a phantom.

The accuracy and precision of the Clarity Autoscan system have been evaluated in a study using a male pelvic phantom [65]. In this study, a latency of 223 ± 45.2 milliseconds was reported between the motion of the phantom and the US tracking. In addition, a mean position error of 0.23 mm (LR) and 0.45 mm (SI) was reported. These positional and timing accuracies were found to be acceptable under the simulated treatment conditions examining, among others, the performance of the system while the radiation beam was on and while the image quality was degraded by the introduction of an air gap between the probe and the surface of the phantom. This was done to assess tracking performance under worse image quality conditions.

In the literature, three papers [26, 27, 66] and one abstract [28] are available in which intrafraction prostate monitoring was clinically investigated using the Clarity Autoscan system. The authors of these publications reported different metrics. For example, Richardson and Jacobs [27] reported the total frequency of intrafraction prostate displacements per direction for different thresholds, while Baker and Behrens [26] reported the percentage of fractions with displacements larger than 2 mm. These differences make it difficult to compare the results directly.

Ballhausen et al. [66] investigated data from 6 prostate cancer patients. This data was used to verify their hypothesis that the intrafraction motion of the prostate can be modeled as a time-dependent "random walk" [67]. It was shown that the prostate tends to move away from the treatment isocenter during a fraction and that this drift away from the isocenter increases over time. These findings imply that a shorter dose delivery time could be favorable. Such a reduction of the treatment time can be achieved by using, for example, volumetric modulated arc therapy (VMAT) or RapidArc® Radiotherapy Technology (see [3] for more details on radiation techniques).

Table 2: Studies reporting on the use of TPUS imaging with the Clarity Autoscan system for intrafraction prostate motion monitoring. The first column details the first author and publication year. The second column details the used system, while the third and fourth column indicate the number of patients and scans examined, respectively. The fifth column contains the examined time intervals in seconds, while the final column details some results and conclusions.

First author	System	# pts	# US scans	Time [sec]	Results and conclusions
Baker (2016) [26]	TPUS	10	51	120–150	(i) Largest displacement (2.8 mm) in posterior direction (ii) Displacement insignificant during treatment time (iii) Displacement increases over time
Richardson (2017) [27]	TPUS	20	526	385	(i) Posterior motion seems most common (ii) 35% of patients displacement > 10 mm (iii) Duration of displacement varies considerably between patients
Guillet (2017) [28]	TPUS	10	330	140 (+120 setup) 290 (+120 setup)	(i) Largest movement in AP direction (ii) Dosimetric impact increases with treatment time duration

Baker and Behrens [26] investigated the prostate intrafraction motion during a time interval corresponding to a beam-on time for RapidArc (120–150 seconds) (see Table 2). A tolerance of 2 mm was considered, as this value is perceived to be clinically irrelevant according to the British Ionization Radiation Medical Exposure Regulations 2000 (IRMER 2000). In the study, maximal intrafractional displacements of -0.2 ± 1.1 mm (AP), -0.2 ± 0.8 mm (LR), and $+0.2 \pm 0.9$ mm (SI) were found. The largest displacement of 2.8 mm was measured in the posterior direction. Also, displacements of larger than 2 mm were measured for 10% (AP), 2% (LR), and 4% (SI) of the examined fractions. The authors concluded that the displacement of the prostate is insignificant during the measured time interval. However, the conclusion was also drawn that the displacement increases over time, which is in line with the findings of Ballhausen et al. [66].

Richardson and Jacobs [27] instead used the Clarity Autoscan system to assess the intrafraction prostate motion during intensity-modulated radiotherapy (IMRT) with static beams from different angles, which consequently has a longer treatment time (reported mean of 385 seconds). In this case, the authors considered three different thresholds: 3 mm (fine tolerance), 7 mm (future planning target volume), and 10 mm (current planning target volume). In addition to a technical overview, also the first clinical experiences of the physicians were captured in a letter [68] and article [69].

Also in this study, the motion of the prostate in the posterior direction seems to be the most common (Table 2). All patients experienced at least one displacement larger than 3 mm and 35% of the patients experienced one displacement larger than 10 mm. These higher rates of motion in comparison with [26] can potentially be explained by the fact that the evaluated time interval was much longer (385 seconds versus 120–150 seconds). In the study of Richardson and Jacobs [27] also the duration of the intrafraction prostate displacement was calculated as a proportion of the total treatment time. This duration varied considerably between patients. For example, for motion larger than 3 mm in the posterior direction, durations from 2% of the treatment time up to 92% of the treatment time were observed for individual patients.

Finally, also one abstract was published by Guillet et al. [28] in which the dosimetric impact of the intrafraction motion was investigated and in which also some prostate movement results were reported. Also in this work, the largest movements were reported in the AP direction (Table 2), with 18% of the short treatment sessions (140 seconds) and 31% of the longer treatment sessions (290 seconds) displaying motions larger than 3 mm. In addition, in this work it was also shown that the dosimetric impact of the intrafractional motion increases with the treatment time duration.

5. Operator Dependence

Currently, the operator who acquires the US images in the clinic (not only in the RT environment) may need to (manually) place the US probe on the body of the patient, interpret the live images, and then decide if the correct anatomical structures are visualized with sufficient image quality. This makes US imaging operator dependent and this dependence may cause significant variability in the quality of the acquired US images and thus influence the ability to locate and track the prostate and OARs.

Section 5.1 discusses the studies that investigated prostate displacement induced by probe pressure in both TAUS and TPUS. Inter- and intraoperator variability is detailed in Section 5.2.

5.1. Probe Pressure Effects. As introduced previously, the Clarity system requires the acquisition of a manual sweep along the abdomen of the patient using the TAUS probe prior to radiation dose delivery. The acquired image can then be used for interfraction motion correction. Subsequently, the probe is removed from the body of the patient and the patient is irradiated. In case the prostate is displaced due to probe pressure, it might move to a different position when the probe is removed from the body. This displacement after the probe removal is not accounted for in the interfraction motion correction, which might lead to a suboptimal radiation dose delivery.

Table 3 details studies that investigated prostate displacement due to probe pressure. Two out of three TAUS studies used a relative method to assess the prostate displacement.

TABLE 3: Studies reporting on prostate displacement induced by probe pressure. The first column details the first author and publication year. Δ indicates that the specific study was mentioned in the previous review paper [11], but these specific results were not discussed. The second column details the used system, while the third column provides the imaging modality with which the prostate displacement was assessed. The fourth and fifth column specify the number of examined patients and the assessed scans, respectively. The prostate displacement in all directions is listed in column 6 with a indicating results per 1 mm probe shift and in the final column the displacement vector can be found.

First author	System	Assessed with	# pts	# US scans	Prostate displacement mean ± SD [mm]			Displacement vector mean ± SD [mm]
					AP	LR	SI	
Van Der Meer$^{\Delta}$ (2013) [17]	TAUS	Relative TAUS	13	376	0.7	−0.5	0.0	3.0
Fargier-Voiron$^{\Delta}$ (2014) [29]	TAUS	Relative TAUS	8	24	-	-	-	2.5 ± 1.2
Baker (2015) [30]	TAUS	TPUS	9	42	−0.1 ± 1.0	0.2 ± 0.7	−0.1 ± 0.8	1.3 ± 0.7
Li (2017) [31]	TPUS	Relative TPUS	10	16 series	0.07 ± 0.11^{a}	0.04 ± 0.11^{a}	0.42 ± 0.09^{a}	2–4

For example, Van Der Meer et al. [17] acquired images at no pressure (reference situation: probe touching the skin) and subsequently acquired images at low pressure, intermediate pressure, and high pressure. To determine the displacement due to probe pressure the location of the prostate was compared to the reference situation.

Baker and Behrens [30] assessed the effect of TAUS probe positioning using TPUS imaging. In this work, a reference image was acquired using just a TPUS probe without the TAUS probe actually being in place on the body of the patient. The average displacement vector of the prostate found by Baker and Behrens [30] was significantly lower than the distance found in the other studies (1.3 mm versus 2.5 mm and 3.0 mm). The studies concluded that even though the prostate displacements are small, a minimal pressure should be used in order to make the probe setup more reproducible.

The effect of probe pressure during TPUS imaging were reported in two studies. Mantel et al. [70] investigated the shift of the penile bulb after positioning the TPUS probe against the perineum. A superior shift of the penile bulb could bring it closer to the prostate and therefore closer to the high dose region. This could lead to an increase of dose delivered to the penile bulb, which has been correlated earlier (e.g., [71]) with the incidence of erectile dysfunction. The authors studied datasets from 10 patients and reported that the penile bulb had a significant median shift of 6.2 mm in the superior direction. In addition, no relevant volume changes of the prostate and planning target volume due to probe pressure were observed and just minor motion of these structures was reported, mainly in the superior direction. No quantitative results on this prostate and planning target volume motion were reported in the paper.

In another study [31] the pressure applied by a TPUS probe was found to have a quantitatively similar impact on prostate displacement as the TAUS probe (Table 3). As this conclusion contradicts the conclusion of Mantel et al. [70], it implies that more research is necessary to understand the impact of TPUS probe pressure on the displacement of the prostate and OARs. Li et al. [31] also detected a systematic intrafraction drift of the prostate. They hypothesized that this drift was caused by the relaxation of the compressed tissue of the perineal area present between the prostate and the probe. As intrafraction motion monitoring is possible using TPUS imaging, this drift can be monitored and, when needed, potentially compensated for.

With TPUS imaging the probe does not need to be removed prior to dose delivery. Therefore, no displacement of the prostate and organs at risk due to probe removal is expected. As long as the pressure is not so high that it produces a shift of the OARs into high dose regions (as reported e.g., for the penile bulb in the previous paragraph) and it is reproducible, the consequences of the pressure in the US guided RT workflow should be minimal. For TAUS imaging, it was reported that it is difficult to reproduce the pressure [29]; however, for TPUS imaging results on this issue are currently not available. If future studies prove that it is feasible to position the TPUS probe with a reproducible probe pressure, it would add another advantage to this imaging modality in comparison to TAUS imaging.

5.2. US Image Interpretation. The variation in US probe pressure applied by different operators may influence the displacement of the prostate and thus result in US image variation. However, also during interpretation of the images inter- and intraoperator variability can occur. This variability seems to be more present in operators with limited US imaging experience. For this reason, the importance of training has been emphasized by the American Association of Physicist in Medicine [72].

The inter- and intraoperator variability for different levels of expertise have been investigated in a few studies (Table 4). In these studies, the operators were asked to match a reference contour of the prostate to a newly acquired US image to determine the required setup shift during interfraction motion monitoring. Subsequently, differences in the performed matches were statistically examined.

The results reported by Fiandra et al. [32] show that the interuser variability decreases with growing TAUS imaging experience. The same holds for the intrauser variability during TPUS imaging, as reported by Pang et al. [33]. The operators that matched the images in the study of Van Der Meer et al. [17] received thorough training and scanning

TABLE 4: Studies reporting on the inter- and intraoperator variability of the Clarity system (TAUS) or the Clarity Autoscan system (TPUS). The first column details the first author and publication year. ∗ indicates that the detailed results were discussed in the review paper [11] as well, while Δ highlights that these specific results were not discussed, but the paper was included in the previous review. The second column specifies the used system, while the third and fourth column provide the number of compared operators and their experience, respectively. In the fifth column the number of examined patients is specified, while in the sixth column the number of matches made by the operators is detailed. The seventh column explains the metric that was used to quantify the intraoperator variability (column eight) and the interoperator variability (column nine).

First author	System	# operators	Experience	# pts	# matches	Metric	Intra AP	Intra LR	Intra SI	Inter AP	Inter LR	Inter SI
Van der Meer∗ (2013) [17]	TAUS	2 (intra) 3 (inter)	-	13	817	SD (mm)	0.7	0.8	1	1.4	1.3	1.8
Fiandra$^\Delta$ (2014) [32]	TAUS	2	Expert (>5 years)	10	60	Mean ± SD of operator Δ (mm)	-	-	-	−0.1 ± 1.4	−0.4 ± 1.2	0.1 ± 1.3
		5	>1 year	10	150	Root mean square error with respect to expert [mm]	-	-	-	2.1 ± 2.1	1.3 ± 1.7	1.7 ± 1.7
		4	<1 year	10	120		-	-	-	3.1 ± 2.7	2.7 ± 2.7	3.2 ± 3.2
		7	All operators	10	70	Δ between operator and total group median [mm] in all directions	≤2 in 93.3% of the time			≤2 in 93.8% of the time		
Pang (2017) [33]	TPUS	5	9–16 months	10	50		≤2 in 96.7% of the time			-		
		2	4–9 months	10	20		≤2 in 60% and 80% of the time			-		

instructions. These operators seem to perform similarly to the operators with more than one year of experience of Fiandra et al. [32].

In Table 1, the results reported by Robinson et al. [16] regarding the differences in prostate localization between TAUS imaging and CT are listed. These results seem to confirm as well that more experience (clinical operator versus manufacturer representative) results in better agreement between the CT and TAUS based prostate locations.

In addition to providing training to the operators, making the system less prone to operator dependence could potentially reduce both inter- and intraoperator variability. In comparison with the Clarity system, the Clarity Autoscan system has already implemented several improvements to potentially reduce operator dependence. In particular, the mechanically swept probe could be attractive, since it minimizes the disadvantages of a manual sweep acquisition, such as the variance in probe pressure and sweeping motion. In addition, the probe is attached to a baseplate avoiding the need to hold it by hand and the operator is assisted to reproduce the earlier used probe pressure and setup by means of visual feedback.

Another approach to reduce operator dependence and potentially even allow less trained operators to acquire good-quality images was proposed by Camps et al. [73, 74]. In this work, the simulation CT scan of prostate cancer patients (currently almost always available for treatment planning purposes) was used to optimize the patient-specific US probe setup that would allow visualization of all the required anatomical structures with sufficient image quality. This helps to reduce the need for image interpretation during the acquisition and the operator variability in probe positioning.

6. Challenges

Some challenges associated with the use of US imaging in the RT workflow have already been described in the previous sections, such as the inter- and intraoperator variability and the displacement of anatomical structures due to probe pressure. In this section, a number of other challenges associated with the implementation of US imaging in the prostate RT workflow are discussed.

6.1. Intrafraction US Imaging. The presence of the US probe in the radiation beam during the treatment can potentially cause dose delivery errors, which might influence the treatment outcome for the patient. Three possible solutions have been proposed in the literature for this problem. One option is to design the treatment plan in such a way that the US probe is completely avoided during the treatment [75]. Second, the radiation can be delivered through the probe, but it requires that the possible dose deviations are taken into account during the treatment planning process, as investigated by, for example, Bazalova-Carter et al. [76]. As a third solution, Schlosser and Hristov [77] designed a 4D radiolucent US probe with significantly less metal components close to the imaging field. This probe should produce a minimal interference with the radiation beam.

Martyn et al. [78] also investigated the effect of an US probe on the surface dose delivered to a phantom using a Monte Carlo study. In this study, a phantom was imaged using an Elekta Autoscan probe parallel to the radiation beam to mimic TAUS imaging, or perpendicular to the beam, to mimic TPUS imaging. It was shown that the presence of the probe in the TPUS configuration produces dose perturbations near the surface of the phantom, when there is overlap between the probe and the radiation field. However, the dose increase was of a similar order of magnitude as the one resulting from interfraction motion. In case no probe-field overlap occurred, the measured dosimetric effect was minimal. In the TAUS probe setup, instead, a dose increase near the surface of the phantom was measured and reported to be smaller than 5%.

Several studies (e.g., [75, 79–81]) also looked into the possibility of replacing a human operator handling the probe at the bedside with a robot. Schlosser et al. [75], for example, built a patient-safe robotic manipulator which could be used to control the pitch and pressure of a TAUS probe. To safely control the robot remotely from outside the LINAC room, a haptic device was added to the design. During the treatment delivery, the beam angles were restricted to prevent collision with the robotic hardware or the probe. The authors showed that the robotic system was able to image the prostate remotely. In addition, both the tracking ability of the US probe and the robot performance were not degraded during radiation beam operation. The use of such a robotic system could not only enable intrafraction TAUS imaging, but also potentially allow for an easier probe pressure and position reproduction using both TAUS and TPUS imaging.

6.2. Speed of Sound and Refraction Effects. Most clinical US systems work in pulse-echo mode, where the time of flight of the US pulses is used to infer the depth of the structures in the scanned tissues. This time of flight is calculated with the speed of sound (SOS) of the tissues traversed by the pulse. Different tissues have a different SOS. For example, adipose tissue typically has an SOS around 1450 m/s, while for connective tissue it is around 1600 m/s [82].

However, the US systems usually assume a fixed average SOS value of 1540 m/s for all human soft tissues [83]. This assumption may produce wrong quantitative estimates of organ boundary positions up to several millimeters. Fontanarosa et al. published multiple studies [84–87] in which CT scans were used to create SOS maps for correcting these aberrations. These corrections are essential to restore quantitative comparability with the reference simulation CT scan.

Not only does the usability of US imaging in the RT workflow rely on the acquisition and interpretation of the US images, but also the precision of the calibration procedure of the localization system and, associated with that, the precision that can be achieved while localizing the US probe in absolute coordinates in the simulation or treatment room are of importance. How well the US probe is localized influences the coregistration between, for example, the simulation CT scan and the reference US image, or two US images acquired at different time points.

The phantoms used in a calibration procedure are typically made of homogeneous tissue equivalents to avoid the SOS effects. In addition, refractions inside the phantom should not affect the calibration procedure. However, in the work of Ballhausen et al. [88] it has been shown that the calibration of a 3D US system can be affected by refraction of the sound waves at the phantom surface. Particularly when the probe was tilted during the calibration procedure this could result in a position difference of more than 0.5 mm.

Van der Meer et al. [89] simulated five different scenarios mimicking the errors that could occur when using the Clarity system for TAUS image guidance. These errors could be due to, for example, the above-mentioned inaccurate calibration, but also due to laser offsets or patient motion between the simulation CT and simulation US image acquisition. It has been shown that it is important to take SOS aberrations into account and to assess the matching of US and CT images. In case these images do not match, a manual correction could be performed, potentially introducing operator variability. In such a case, the authors recommend rescanning the patient to avoid problems during the dose delivery procedure.

Summarizing, it is important to take SOS aberrations into account while registering US images to another image modality. In addition, caution should be used while performing calibration and image acquisition, to avoid image matching issues.

6.3. Hypofractionation and Adaptive Radiotherapy. In current clinical practice, it is common to deliver the radiation dose to prostate cancer patients in multiple treatment fractions (even up to 45). It has been suggested that hypofractionation could result in the same or better outcomes for the prostate patients [90]. In a hypofractionation scheme, a higher dose per fraction is delivered to the patient in less treatment fractions. The treatment is then delivered over a shorter amount of time and with a total lower dose.

As the dose delivered per treatment fraction is higher and there are fewer fractions to potentially perform corrections or compensate for errors performed in the previous fractions, it is even more crucial to deliver the radiation correctly. Ricardi et al. [91] used the Clarity system in the treatment of intermediate risk prostate cancer patients treated with a hypofractionated schedule. It was shown that the hypofractionated schedule under US guidance was a safe and effective treatment approach with consistent biochemical control and a mild toxicity profile.

Patient immobilization during the treatment fraction is also an important aspect of the RT workflow. For this reason, a wide range of immobilization devices is available on the market, ranging from a simple leg immobilizer (Civco Medical Solutions, IA, USA) to vacuum cushions (e.g., Vac-Lok, Civco Medical Solutions, IA, USA) that can adapt to the body composition of the patient. Pang et al. [92] investigated the interfraction setup differences, patient satisfaction, and radiation therapist satisfaction regarding two immobilization devices: the traditionally used leg immobilizer and the Clarity Autoscan immobilization device. The results showed that the setup errors were smaller with the Clarity device and the patients were satisfied with the new device. The radiation

therapist, though, had some issues with the weight and bulkiness of the new device.

ART aims at reducing or compensating for the effects of patient-specific treatment variation measured during the course of a radiotherapy treatment [93, 94] by adaptively modifying the treatment plan of the patient. This approach could be used to further improve the accuracy of radiation dose delivery. However, in current clinical practice, typically CT scans provide the electron-density information necessary for treatment planning and dose calculation. So, in case replanning proves necessary, one or multiple additional CT scans during the course of the treatment must be acquired. Not only does this result in extra radiation dose delivery to the patient, but also high costs are associated with the rather complex CT acquisition procedure.

Van Der Meer et al. [95] and Camps et al. [96] have investigated the feasibility of creating pseudo-CT scans of the pelvic region, based on combinations of rigid and deformable image registrations of TAUS images. These TAUS images acquired at simulation stage and during treatment stage were used to create a deformation field that represented the changes that occurred in tissue distribution between these two time points. The subsequent application of this deformation field on the simulation CT resulted in the creation of a pseudo-CT scan. It was shown that this pseudo-CT scan represents the anatomy of the patient at treatment stage better than the simulation CT. These results are promising and may lead to the ability to replan based on a pseudo-CT scan, instead of on a regular CT scan.

7. Conclusion

In this work, the recent relevant studies regarding the use of US imaging for guidance during the prostate EBRT workflow have been discussed. Several US based guidance systems have been introduced to the market in the last 15 years with varying success. TPUS imaging seems to overcome some of the issues associated with the limitations of TAUS imaging during intrafraction organ motion monitoring, such as displacement of the organs due to probe pressure and the interference with the radiation beam.

The studies that investigated TPUS imaging show promising results and, for this reason, we recommend the use of TPUS imaging during the US guided external beam radiotherapy workflow of prostate cancer patients. However, there are still several challenges to be addressed, which are associated with inter- and intraoperator variability during the acquisition of the images and the interpretation of these images. In addition, technical aspects of the US image modality, such as SOS aberrations and refractions should be investigated further to understand if these cause issues while using TPUS imaging for both inter- and intrafraction monitoring.

If a decrease in user variability and an increase of usability of the US guided EBRT systems can be achieved, this would potentially make the use of this approach more appealing to physicians and medical experts, in the end, resulting in smaller margins with less toxicities for prostate cancer patients undergoing EBRT.

Abbreviations

AP: Anterior-posterior
ART: Adaptive radiotherapy
BAT: B-mode acquisition and targeting
CBCT: Cone beam computed tomography
CT: Computed tomography
EBRT: External beam radiotherapy
EPI: Electronic portal imaging
FM: Fiducial marker
IGRT: Image guided radiotherapy
IMRT: Intensity-modulated radiotherapy
kV: Kilovolt
LINAC: Linear accelerator
LoA: Limits of agreement
LR: Left-right
MRI: Magnetic resonance imaging
OAR: Organ at risk
RT: Radiotherapy
SD: Standard deviation
SI: Superior-inferior
SOS: Speed of sound
TAUS: Transabdominal ultrasound
TPUS: Transperineal ultrasound
TRUS: Transrectal ultrasound
US: Ultrasound
VMAT: Volumetric modulated arc therapy
2D: Two-dimensional
3D: Three-dimensional.

Conflicts of Interest

The authors declare that there are no conflicts of interest regarding the publication of this paper.

References

[1] C. Fitzmaurice, C. Allen, R. M. Barber et al., "Global, regional, and national cancer incidence, mortality, years of life lost, years lived with disability, and disability-adjusted life-years for 32 cancer groups, 1990 to 2015: a systematic analysis for the global burden of disease study," *JAMA Oncology*, vol. 3, no. 4, pp. 524–548, 2017.

[2] L. A. Torre, R. L. Siegel, E. M. Ward, and A. Jemal, "Global cancer incidence and mortality rates and trends—an update," *Cancer Epidemiology, Biomarkers & Prevention*, vol. 25, no. 1, pp. 16–27, 2016.

[3] B. G. L. Vanneste, E. J. Van Limbergen, E. N. Van Lin, J. G. H. Van Roermund, and P. Lambin, "Prostate Cancer Radiation Therapy: What Do Clinicians Have to Know?" *BioMed Research International*, vol. 2016, Article ID 6829875, 2016.

[4] M. J. Zelefsky, M. Kollmeier, B. Cox et al., "Improved clinical outcomes with high-dose image guided radiotherapy compared with non-IGRT for the treatment of clinically localized prostate cancer," *International Journal of Radiation Oncology • Biology • Physics*, vol. 84, no. 1, pp. 125–129, 2012.

[5] J. Sveistrup, P. M. af Rosenschöld, J. O. Deasy et al., "Improvement in toxicity in high risk prostate cancer patients treated with image-guided intensity-modulated radiotherapy compared to 3D conformal radiotherapy without daily image guidance," *Journal of Radiation Oncology*, vol. 9, no. 1, article 44, 2014.

[6] U. A. van der Heide, A. N. T. J. Kotte, H. Dehnad, P. Hofman, J. J. W. Lagenijk, and M. van Vulpen, "Analysis of fiducial marker-based position verification in the external beam radiotherapy of patients with prostate cancer," *Radiotherapy & Oncology*, vol. 82, no. 1, pp. 38–45, 2007.

[7] J. J. W. Lagendijk, B. W. Raaymakers, and M. van Vulpen, "The Magnetic Resonance Imaging-Linac System," *Seminars in Radiation Oncology*, vol. 24, no. 3, pp. 207–209, 2014.

[8] R. D. Foster, T. D. Solberg, H. S. Li et al., "Comparison of transabdominal ultrasound and electromagnetic transponders for prostate localization," *Journal of Applied Clinical Medical Physics*, vol. 11, no. 1, pp. 57–67, 2010.

[9] A. Y. C. Fung, K. M. Ayyangar, D. Djajaputra, R. M. Nehru, and C. A. Enke, "Ultrasound-based guidance of intensity-modulated radiation therapy," *Medical Dosimetry*, vol. 31, no. 1, pp. 20–29, 2006.

[10] D. Shen, Y. Zhan, and C. Davatzikos, "Segmentation of prostate boundaries from ultrasound images using statistical shape model," *IEEE Transactions on Medical Imaging*, vol. 22, no. 4, pp. 539–551, 2003.

[11] D. Fontanarosa, S. Van Der Meer, J. Bamber, E. Harris, T. O'Shea, and F. Verhaegen, "Review of ultrasound image guidance in external beam radiotherapy: I. Treatment planning and inter-fraction motion management," *Physics in Medicine and Biology*, vol. 60, no. 3, pp. R77–R114, 2015.

[12] T. O'Shea, J. Bamber, D. Fontanarosa, S. Van Der Meer, F. Verhaegen, and E. Harris, "Review of ultrasound image guidance in external beam radiotherapy part II: Intra-fraction motion management and novel applications," *Physics in Medicine and Biology*, vol. 61, no. 8, pp. R90–R137, 2016.

[13] E. Mayyas, I. J. Chetty, M. Chetvertkov et al., "Evaluation of multiple image-based modalities for image-guided radiation therapy (IGRT) of prostate carcinoma: A prospective study," *Medical Physics*, vol. 40, no. 4, Article ID 041707, 2013.

[14] F. L. B. Cury, G. Shenouda, L. Souhami et al., "Ultrasound-based image guided radiotherapy for prostate cancer-comparison of cross-modality and intramodality methods for daily localization during external beam radiotherapy," *International Journal of Radiation Oncology • Biology • Physics*, vol. 66, no. 5, pp. 1562–1567, 2006.

[15] H. Johnston, M. Hilts, W. Beckham, and E. Berthelet, "3D ultrasound for prostate localization in radiation therapy: A comparison with implanted fiducial markers," *Medical Physics*, vol. 35, no. 6, pp. 2403–2413, 2008.

[16] D. Robinson, D. Liu, S. Steciw et al., "An evaluation of the clarity 3D ultrasound system for prostate localization," *Journal of Applied Clinical Medical Physics*, vol. 13, no. 4, pp. 100–112, 2012.

[17] S. Van Der Meer, E. Bloemen-Van Gurp, J. Hermans et al., "Critical assessment of intramodality 3D ultrasound imaging for prostate IGRT compared to fiducial markers," *Medical Physics*, vol. 40, no. 7, Article ID 071707, 2013.

[18] M. van Herk, "Errors and margins in radiotherapy," *Seminars in Radiation Oncology*, vol. 14, no. 1, pp. 52–64, 2004.

[19] M. Li, H. Ballhausen, N.-S. Hegemann et al., "A comparative assessment of prostate positioning guided by three-dimensional ultrasound and cone beam CT," *Journal of Radiation Oncology*, vol. 10, no. 1, article no. 82, 2015.

[20] M. Fargier-Voiron, B. Presles, P. Pommier et al., "Ultrasound versus Cone-beam CT image-guided radiotherapy for prostate

and post-prostatectomy pretreatment localization," *Physica Medica*, vol. 31, no. 8, pp. 997–1004, 2015.

[21] M. Krengli, G. Loi, C. Pisani et al., "Three-dimensional surface and ultrasound imaging for daily IGRT of prostate cancer," *Journal of Radiation Oncology*, vol. 11, no. 1, article no. 159, 2016.

[22] A. Richter, B. Polat, I. Lawrenz et al., "Initial results for patient setup verification using transperineal ultrasound and cone beam CT in external beam radiation therapy of prostate cancer," *Journal of Radiation Oncology*, vol. 11, no. 1, article no. 147, 2016.

[23] M. Fargier-Voiron, B. Presles, P. Pommier et al., "Evaluation of a new transperineal ultrasound probe for inter-fraction image-guidance for definitive and post-operative prostate cancer radiotherapy," *Physica Medica*, vol. 32, no. 3, pp. 499–505, 2016.

[24] A. Trivedi, T. Ashikaga, D. Hard et al., "Development of 3-dimensional transperineal ultrasound for image guided radiation therapy of the prostate: Early evaluations of feasibility and use for inter- and intrafractional prostate localization," *Practical Radiation Oncology*, vol. 7, no. 1, pp. e27–e33, 2017.

[25] M. Li, H. Ballhausen, N.-S. Hegemann et al., "Comparison of prostate positioning guided by three-dimensional transperineal ultrasound and cone beam CT," *Strahlentherapie und Onkologie*, vol. 193, no. 3, pp. 221–228, 2017.

[26] M. Baker and C. F. Behrens, "Determining intrafractional prostate motion using four dimensional ultrasound system," *BMC Cancer*, vol. 16, no. 1, article no. 484, 2016.

[27] A. K. Richardson and P. Jacobs, "Intrafraction monitoring of prostate motion during radiotherapy using the Clarity® Autoscan Transperineal Ultrasound (TPUS) system," *Radiography*, vol. 23, no. 4, pp. 310–313, 2017.

[28] L. Guillet, M. Fargier-Voiron, D. Sarrut, and M.-C. Biston, "Evaluation of intrafraction motions with a transperineal ultrasound imaging system: dosimetric impact for prostate cancer," *Physica Medica: European Journal of Medical Physics*, vol. 31, pp. e25–e26, 2015.

[29] M. Fargier-Voiron, B. Presles, P. Pommier et al., "Impact of probe pressure variability on prostate localization for ultrasound-based image-guided radiotherapy," *Radiotherapy & Oncology*, vol. 111, no. 1, pp. 132–137, 2014.

[30] M. Baker and C. F. Behrens, "Prostate displacement during transabdominal ultrasound image-guided radiotherapy assessed by real-time four-dimensional transperineal monitoring," *Acta Oncologica*, vol. 54, no. 9, pp. 1508–1514, 2015.

[31] M. Li, N.-S. Hegemann, F. Manapov et al., "Prefraction displacement and intrafraction drift of the prostate due to perineal ultrasound probe pressure," *Strahlentherapie und Onkologie*, vol. 193, no. 6, pp. 459–465, 2017.

[32] C. Fiandra, A. Guarneri, F. Muñoz et al., "Impact of the observers' experience on daily prostate localization accuracy in ultrasound-based IGRT with the Clarity platform," *Journal of Applied Clinical Medical Physics*, vol. 15, no. 4, pp. 168–173, 2014.

[33] E. P. P. Pang, K. Knight, M. Baird, and J. K. L. Tuan, "Inter-and intra-observer variation of patient setup shifts derived using the 4D TPUS Clarity system for prostate radiotherapy," *Biomedical Physics & Engineering Express*, vol. 3, no. 2, p. 25014, 2017.

[34] M. Lachaine and T. Falco, "Intrafractional prostate motion management with the Clarity Autoscan system," *Medical Physics International*, vol. 1, 2013.

[35] C. C. Parker, A. Damyanovich, T. Haycocks, M. Haider, A. Bayley, and C. N. Catton, "Magnetic resonance imaging in the radiation treatment planning of localized prostate cancer using

intra-prostatic fiducial markers for computed tomography co-registration," *Radiotherapy & Oncology*, vol. 66, no. 2, pp. 217–224, 2003.

[36] M. Milosevic, S. Voruganti, R. Blend et al., "Magnetic resonance imaging (MRI) for localization of the prostatic apex: comparison to computed tomography (CT) and urethrography," *Radiotherapy & Oncology*, vol. 47, no. 3, pp. 277–284, 1998.

[37] C. Rasch, I. Barillot, P. Remeijer, A. Touw, M. van Herk, and J. V. Lebesque, "Definition of the prostate in CT and MRI: a multi-observer study," *International Journal of Radiation Oncology • Biology • Physics*, vol. 43, no. 1, pp. 57–66, 1999.

[38] P. J. Horsley, N. J. Aherne, G. V. Edwards et al., "Planning magnetic resonance imaging for prostate cancer intensity-modulated radiation therapy: impact on target volumes, radiotherapy dose and androgen deprivation administration," *Asia-Pacific Journal of Clinical Oncology*, vol. 11, no. 1, pp. 15–21, 2015.

[39] G. Bentel, *Patient Positioning and Immobilization in Radiation Oncology*, McGraw-Hill, New York, NY, USA, 1999.

[40] A. G. M. O'neill, S. Jain, A. R. Hounsell, and J. M. O'sullivan, "Fiducial marker guided prostate radiotherapy: A review," *British Journal of Radiology*, vol. 89, no. 1068, article no. 0296, 2016.

[41] M. Oldham, D. Létourneau, L. Watt et al., "Cone-beam-CT guided radiation therapy: a model for on-line application," *Radiotherapy & Oncology*, vol. 75, no. 3, pp. 271.e1–271.e8, 2005.

[42] K. M. Langen and D. T. L. Jones, "Organ motion and its management," *International Journal of Radiation Oncology • Biology • Physics*, vol. 50, no. 1, pp. 265–278, 2001.

[43] C. R. Hill, J. C. Bamber, and G. R. ter Haar, "Preface," *Physical Principles of Medical Ultrasonics*, pp. xiii–xv, 2005.

[44] J. T. Bushberg, *The Essential Physics of Medical Imaging*, Lippincott Williams & Wilkins, 2002.

[45] R. G. Aarnink, H. P. Beerlage, J. J. M. C. H. De La Rosette, F. M. J. Debruyne, and H. Wijkstra, "Transrectal ultrasound of the prostate: Innovations and future applications," *The Journal of Urology*, vol. 159, no. 5, pp. 1568–1579, 1998.

[46] S. Gill, J. Li, J. Thomas et al., "Patient-reported complications from fiducial marker implantation for prostate image-guided radiotherapy," *British Journal of Radiology*, vol. 85, no. 1015, pp. 1011–1017, 2012.

[47] J. F. Langenhuijsen, E. N. J. T. van Lin, L. A. Kiemeney et al., "Ultrasound-guided transrectal implantation of gold markers for prostate localization during external beam radiotherapy: complication rate and risk factors," *International Journal of Radiation Oncology • Biology • Physics*, vol. 69, no. 3, pp. 671–676, 2007.

[48] J. W. N. C. Huang Foen Chung, S. H. De Vries, R. Raaijmakers, R. Postma, J. L. H. R. Bosch, and R. Van Mastrigt, "Prostate volume ultrasonography: The influence of transabdominal versus transrectal approach, device type and operator," *European Urology*, vol. 46, no. 3, pp. 352–356, 2004.

[49] R. N. Uppot, D. V. Sahani, P. F. Hahn, M. K. Kalra, S. S. Saini, and P. R. Mueller, "Effect of obesity on image quality: Fifteen-year longitudinal study for evaluation of dictated radiology reports," *Radiology*, vol. 240, no. 2, pp. 435–439, 2006.

[50] R. N. Uppot, "Impact of Obesity on Radiology," *Radiologic Clinics of North America*, vol. 45, no. 2, pp. 231–246, 2007.

[51] B. J. Salter, M. Szegedi, C. Boehm et al., "Comparison of 2 transabdominal ultrasound image guidance techniques for prostate and prostatic fossa radiation therapy," *Practical Radiation Oncology*, vol. 7, no. 2, pp. e99–e107, 2017.

[52] K. A. Griffiths, L. P. Ly, B. Jin, L. Chan, and D. J. Handelsman, "Transperineal Ultrasound for Measurement of Prostate Volume: Validation Against Transrectal Ultrasound," *The Journal of Urology*, vol. 178, no. 4, pp. 1375–1380, 2007.

[53] K. Shinohara and M. Roach III, "Technique for Implantation of Fiducial Markers in the Prostate," *Urology*, vol. 71, no. 2, pp. 196–200, 2008.

[54] Ş. Iğdem, H. Akpinar, G. Alço, F. Ağaçayak, S. Turkan, and S. Okkan, "Implantation of fiducial markers for image guidance in prostate radiotherapy: Patient-reported toxicity," *British Journal of Radiology*, vol. 82, no. 983, pp. 941–945, 2009.

[55] J. Loh, K. Baker, S. Sridharan et al., "Infections after fiducial marker implantation for prostate radiotherapy: Are we underestimating the risks?" *Journal of Radiation Oncology*, vol. 10, no. 1, article no. 38, 2015.

[56] P. A. Kupelian, T. R. Willoughby, S. L. Meeks et al., "Intraprostatic fiducials for localization of the prostate gland: Monitoring intermarker distances during radiation therapy to test for marker stability," *International Journal of Radiation Oncology • Biology • Physics*, vol. 62, no. 5, pp. 1291–1296, 2005.

[57] J. C. L. Chow and G. N. Grigorov, "Dose measurements near a non-radioactive gold seed using radiographic film," *Physics in Medicine and Biology*, vol. 50, no. 18, pp. N227–N234, 2005.

[58] J. R. Perks, J. Lehmann, A. M. Chen, C. C. Yang, R. L. Stern, and J. A. Purdy, "Comparison of peripheral dose from image-guided radiation therapy (IGRT) using kV cone beam CT to intensity-modulated radiation therapy (IMRT)," *Radiotherapy & Oncology*, vol. 89, no. 3, pp. 304–310, 2008.

[59] B. Tas, I. F. Durmus, and S. T. Ozturk, "Image guided radiotherapy (igrt) comparison between cone beam ct and ultrasound system for prostate cancer," *Universal Journal of Physics and Application*, vol. 10, no. 4, pp. 110–114, 2016.

[60] J. Martin Bland and D. Altman, "Statistical methods for assessing agreement between two methods of clinical measurement," *The Lancet*, vol. 327, no. 8476, pp. 307–310, 1986.

[61] G. J. Meijer, J. de Klerk, K. Bzdusek et al., "What CTV-to-PTV Margins Should Be Applied for Prostate Irradiation? Four-Dimensional Quantitative Assessment Using Model-Based Deformable Image Registration Techniques," *International Journal of Radiation Oncology • Biology • Physics*, vol. 72, no. 5, pp. 1416–1425, 2008.

[62] P. Kupelian, T. Willoughby, A. Mahadevan et al., "Multi-institutional clinical experience with the Calypso System in localization and continuous, real-time monitoring of the prostate gland during external radiotherapy," *International Journal of Radiation Oncology • Biology • Physics*, vol. 67, no. 4, pp. 1088–1098, 2007.

[63] J. M. Balter, J. N. Wright, L. J. Newell et al., "Accuracy of a wireless localization system for radiotherapy," *International Journal of Radiation Oncology • Biology • Physics*, vol. 61, no. 3, pp. 933–937, 2005.

[64] M. C. Abramowitz, E. Bossart, R. Flook et al., "Noninvasive real-time prostate tracking using a transperineal ultrasound approach," *International Journal of Radiation Oncology, Biology, Physics*, vol. 84, no. 3, p. S133, 2012.

[65] A. S. Yu, M. Najafi, D. H. Hristov, and T. Phillips, "Intrafractional tracking accuracy of a transperineal ultrasound image guidance system for prostate radiotherapy," *Technology in Cancer Research & Treatment*, Article ID 1533034617728643, 2017.

[66] H. Ballhausen, M. Li, N.-S. Hegemann, U. Ganswindt, and C. Belka, "Intra-fraction motion of the prostate is a random walk," *Physics in Medicine and Biology*, vol. 60, no. 2, pp. 549–563, 2015.

[67] H. Ballhausen, M. Reiner, S. Kantz, C. Belka, and M. Söhn, "The random walk model of intrafraction movement," *Physics in Medicine and Biology*, vol. 58, no. 7, pp. 2413–2427, 2013.

[68] S. Hilman, R. Smith, S. Masson et al., "Implementation of a daily transperineal ultrasound system as image-guided radiotherapy for prostate cancer," *Clinical Oncology*, vol. 29, no. 1, p. e49, 2017.

[69] S. Hilman and P. Jacobs, "Image-guided radiotherapy for prostate cancer using transperineal ultrasound," *RAD Magazine*, pp. 29-30, 2017.

[70] F. Mantel, A. Richter, C. Groh et al., "Changes in penile bulb dose when using the Clarity transperineal ultrasound probe: A planning study," *Practical Radiation Oncology*, vol. 6, no. 6, pp. e337–e344, 2016.

[71] S. A. Mangar, M. R. Sydes, H. L. Tucker et al., "Evaluating the relationship between erectile dysfunction and dose received by the penile bulb: Using data from a randomised controlled trial of conformal radiotherapy in prostate cancer (MRC RT01, ISRCTN47772397)," *Radiotherapy & Oncology*, vol. 80, no. 3, pp. 355–362, 2006.

[72] J. A. Molloy, G. Chan, A. Markovic et al., "Quality assurance of U.S.-guided external beam radiotherapy for prostate cancer: Report of AAPM Task Group 154," *Medical Physics*, vol. 38, no. 2, pp. 857–871, 2011.

[73] S. M. Camps, F. Verhaegen, G. Paiva Fonseca, P. H. N. De With, and D. Fontanarosa, "Automatic transperineal ultrasound probe positioning based on CT scan for image guided radiotherapy," in *Proceedings of the Medical Imaging 2017: Image-Guided Procedures, Robotic Interventions, and Modeling*, USA, February 2017.

[74] S. Camps, F. Verhaegen, P. H. N. de With, and D. Fontanarosa, "CT Scan Based Prostate Cancer Patient-Specific Transperineal Ultrasound Probe Setups for Image Guided Radiotherapy," in *Proceedings of the IEEE International Ultrasonics Symposium*, IEEE, Washington, DC, USA, 2017.

[75] J. Schlosser, K. Salisbury, and D. Hristov, "Telerobotic system concept for real-time soft-tissue imaging during radiotherapy beam delivery," *Medical Physics*, vol. 37, no. 12, pp. 6357–6367, 2010.

[76] M. Bazalova-Carter, J. Schlosser, J. Chen, and D. Hristov, "Monte Carlo modeling of ultrasound probes for image guided radiotherapy," *Medical Physics*, vol. 42, no. 10, pp. 5745–5756, 2015.

[77] J. Schlosser and D. Hristov, "Radiolucent 4D Ultrasound Imaging: System Design and Application to Radiotherapy Guidance," *IEEE Transactions on Medical Imaging*, vol. 35, no. 10, pp. 2292–2300, 2016.

[78] M. Martyn, T. P. O'Shea, E. Harris, J. Bamber, S. Gilroy, and M. J. Foley, "A Monte Carlo study of the effect of an ultrasound transducer on surface dose during intrafraction motion imaging for external beam radiation therapy," *Medical Physics*, vol. 44, no. 10, pp. 5020–5033, 2017.

[79] M. A. L. Bell, H. T. Sen, I. Iordachita, P. Kazanzides, and J. Wong, "In vivo reproducibility of robotic probe placement for a novel ultrasound-guided radiation therapy system," *Journal of Medical Imaging*, vol. 1, no. 2, p. 25001, 2014.

[80] H. T. Şen, M. A. L. Bell, Y. Zhang et al., "System integration and preliminary in-vivo experiments of a robot for ultrasound guidance and monitoring during radiotherapy," in *Proceedings of the 17th International Conference on Advanced Robotics, ICAR 2015*, pp. 53–59, Turkey, July 2015.

[81] S. Gerlach, I. Kuhlemann, P. Jauer et al., "Robotic ultrasound-guided SBRT of the prostate: feasibility with respect to plan

quality," *International Journal for Computer Assisted Radiology and Surgery*, vol. 12, no. 1, pp. 149–159, 2017.

[82] T. D. Mast, "Empirical relationships between acoustic parameters in human soft tissues," *Acoustic Research Letters Online*, vol. 1, pp. 37–42, 2000.

[83] P. N. T. Wells, Biomedical ultrasonics, Academic Pr, 1977.

[84] D. Fontanarosa, S. Van Der Meer, E. Harris, and F. Verhaegen, "A CT based correction method for speed of sound aberration for ultrasound based image guided radiotherapy," *Medical Physics*, vol. 38, no. 5, pp. 2665–2673, 2011.

[85] D. Fontanarosa, S. Van Der Meer, E. Bloemen-Van Gurp, G. Stroian, and F. Verhaegen, "Magnitude of speed of sound aberration corrections for ultrasound image guided radiotherapy for prostate and other anatomical sites," *Medical Physics*, vol. 39, no. 8, pp. 5286–5292, 2012.

[86] D. Fontanarosa, S. Van Der Meer, and F. Verhaegen, "On the significance of density-induced speed of sound variations on US-guided radiotherapy," *Medical Physics*, vol. 39, no. 10, pp. 6316–6323, 2012.

[87] D. Fontanarosa, S. Pesente, F. Pascoli, D. Ermacora, I. A. Rumeileh, and F. Verhaegen, "A speed of sound aberration correction algorithm for curvilinear ultrasound transducers in ultrasound-based image-guided radiotherapy.," *Physics in Medicine and Biology*, vol. 58, no. 5, pp. 1341–1360, 2013.

[88] H. Ballhausen, B. D. Ballhausen, M. Lachaine et al., "Surface refraction of sound waves affects calibration of three-dimensional ultrasound," *Journal of Radiation Oncology*, vol. 10, no. 1, article no. 119, 2015.

[89] S. van der Meer, E. Seravalli, D. Fontanarosa, E. J. Bloemen-van Gurp, and F. Verhaegen, "Consequences of Intermodality Registration Errors for Intramodality 3D Ultrasound IGRT," *Technology in Cancer Research & Treatment*, vol. 15, no. 4, pp. 632–638, 2016.

[90] D. Dearnaley, I. Syndikus, H. Mossop et al., "Conventional versus hypofractionated high-dose intensity-modulated radiotherapy for prostate cancer: 5-year outcomes of the randomised, non-inferiority, phase 3 CHHiP trial," *The Lancet Oncology*, vol. 17, no. 8, pp. 1047–1060, 2016.

[91] U. Ricardi, P. Franco, F. Munoz et al., "Three-dimensional ultrasound-based image-guided hypofractionated radiotherapy for intermediate-risk prostate cancer: Results of a consecutive case series," *Cancer Investigation*, vol. 33, no. 2, pp. 23–28, 2015.

[92] E. P. P. Pang, K. Knight, M. Baird, J. M. Q. Loh, A. H. S. Boo, and J. K. L. Tuan, "A comparison of interfraction setup error, patient comfort, and therapist acceptance for 2 different prostate radiation therapy immobilization devices," *Advances in Radiation Oncology*, vol. 2, no. 2, pp. 125–131, 2017.

[93] D. Yan, F. Vicini, J. Wong, and A. Martinez, "Adaptive radiation therapy," *Physics in Medicine and Biology*, vol. 42, no. 1, pp. 123–132, 1997.

[94] M. Ghilezan, D. Yan, and A. Martinez, "Adaptive Radiation Therapy for Prostate Cancer," *Seminars in Radiation Oncology*, vol. 20, no. 2, pp. 130–137, 2010.

[95] S. Van Der Meer, S. M. Camps, W. J. C. Van Elmpt et al., "Simulation of pseudo-CT images based on deformable image registration of ultrasound images: A proof of concept for transabdominal ultrasound imaging of the prostate during radiotherapy," *Medical Physics*, vol. 43, no. 4, pp. 1913–1920, 2016.

[96] S. Camps, S. van der, F. Meer, and D. Fontanarosa, "Various approaches for pseudo-CT scan creation based on ultrasound to ultrasound deformable image registration between different treatment time points for radiotherapy treatment plan adaptation in prostate cancer patients," *Biomedical Physics & Engineering Express*, vol. 2, no. 3, p. 35018, 2016.

Research Article

Contrast-Enhanced Ultrasound Improves the Pathological Outcomes of US-Guided Core Needle Biopsy That Targets the Viable Area of Anterior Mediastinal Masses

Jian-hua Zhou,[1] Hong-bo Shan,[2] Wei Ou,[3,4] Yun-xian Mo,[5] Jin Xiang,[6] Yu Wang,[7] Jian Li [1], and Si-yu Wang[3,4]

[1]*Department of Diagnostic & Interventional Ultrasound, Sun Yat-Sen University Cancer Center,*
 State Key Laboratory of Oncology in South China, Collaborative Innovation Center for Cancer Medicine, Guangzhou, China
[2]*Department of Endoscopy, Sun Yat-Sen University Cancer Center, State Key Laboratory of Oncology in South China,*
 Collaborative Innovation Center for Cancer Medicine, Guangzhou, China
[3]*Department of Thoracic Surgery, Sun Yat-Sen University Cancer Center, State Key Laboratory of Oncology in South China,*
 Collaborative Innovation Center for Cancer Medicine, Guangzhou, China
[4]*Guangdong Association Study of Thoracic Oncology, Guangzhou, China*
[5]*Department of Radiology, Sun Yat-Sen University Cancer Center, State Key Laboratory of Oncology in South China,*
 Collaborative Innovation Center for Cancer Medicine, Guangzhou, China
[6]*Department of Pathology, Sun Yat-Sen University Cancer Center, State Key Laboratory of Oncology in South China,*
 Collaborative Innovation Center for Cancer Medicine, Guangzhou, China
[7]*Department of Internal Medicine, Sun Yat-Sen University Cancer Center, State Key Laboratory of Oncology in South China,*
 Collaborative Innovation Center for Cancer Medicine, Guangzhou, China

Correspondence should be addressed to Jian Li; lijian@sysucc.org.cn

Based on the option that ultrasound-guided core needle biopsy (US-CNB) of the enhanced portion of anterior mediastinal masses (AMMs) identified by contrast-enhanced ultrasound (CEUS) would harvest viable tissue and benefit the histological diagnoses, a retrospective study was performed to elucidate the correlation between the prebiopsy CEUS and diagnostic yield of AMMs and found that CEUS potentially improved the diagnostic yield of AMMs compared with conventional US with a significant increase in the cellularity of samples. Furthermore, the marginal blood flow signals and absence of necrosis can predict the diagnostic yield of AMM. It was concluded that US-CNB of the viable part of AMMs, as verified by CEUS, was able to harvest sufficient tissue with more cellularity that could be used for ancillary studies and improve the diagnostic yield. And CEUS was recommended to those patients with AMMs undergoing repeated US-CNB, with the absence of marginal blood signals or presence of necrosis.

1. Introduction

Anterior mediastinal masses (AMMs) may appear in a wide variety of diseases from benign lesions to extremely malignant diseases. Masses in this area are more likely to be malignant than those in other compartments of the mediastinum. Lymphomas and thymic epithelial tumors are the two most common etiologies of AMMs [1]. Treatment strategies for AMMs are diverse and are based on a conclusive histological diagnosis with subclassification (such as medical treatment for lymphoma and neoadjuvant radiochemotherapy with surgery for advanced thymic epithelial tumors). Since it is the era of personalized medicine, strategies may also be based on genetic information (such as targeted therapy for non-small cell lung cancer based on testing for epidermal growth factor mutations and anaplastic lymphoma kinase rearrangement) [2].

Available approaches for the histological diagnosis of AMMs include the following: image-guided fine needle aspiration or core needle biopsy, endobronchial ultrasound-guided transbronchial or endoscopic ultrasound-guided transesophageal needle aspiration biopsy, and surgical procedures such as parasternal anterior mediastinotomy, cervical mediastinoscopy, video-assisted thoracoscopic surgery, and thoracotomy. In general, AMMs that are suspected to be malignant without upfront surgical resection are recommended for imaging-guided core needle biopsy [3, 4]. Related studies have demonstrated that satisfactory specimens can be obtained by core needle for a more accurate histological diagnosis with subclassification and genetic information for personalized therapy and prognosis [5–8].

The image guidance of computer tomography (CT) involves the use of radiation, is expensive, and lacks real-time monitoring, which means that it is an alternative approach for AMMs that cannot be adequately imaged by ultrasound (US) [9]. Evidence of the AMM by B-mode US is the first step for ultrasound-guided core needle biopsy (US-CNB). Vascular information can be obtained by color Doppler ultrasound, which helps to extend the diagnostic potential and safety of this minimally invasive procedure. The advantages of US guidance include real-time needle movement control, real-time blood flow imaging, minimal invasiveness, cost-effectiveness, and the ability to perform the biopsy procedure at the bedside when critically ill patients are in a semiupright position. Considering these advantages, US-CNB is the most efficient first-line approach for the biopsy of AMMs if the target is adequately imaged [10]. According to previous studies, the diagnostic yield of US-guided biopsy of AMMs varies from 70 to 90% [11–13]. The occasional failure of the diagnosis is primarily due to necrosis or fibrosis of the lesion, low cellularity, or sampling error [14]. Since it is difficult to identify these situations by conventional US, multiple punctures or repeated biopsies are performed to avoid a false-negative diagnosis and to increase the diagnostic yield, which increase the cost and delay therapy [15]. Fortunately, with the use of contrast agents, contrast-enhanced ultrasound (CEUS) offers an effective way to image tumor vascularity in both animal and clinical studies [16, 17]. CEUS patterns and features in the differentiation of malignant and benign diseases of the chest are controversial [18–21]. CEUS is not routinely performed for AMMs but is used on demand to address specific questions raised in an individual patient. In CEUS, the depiction of nonperfused areas (potentially necrotic, liquid, or fibrotic areas) might be relevant information prior to any US-guided biopsy [22]. This study is based on the hypothesis that the prebiopsy CEUS of AMMs will improve the delineation of viable from nonviable tissue and hence allow the targeting of the viable area of AMMs and the harvest of biopsy samples with more cellularity. This would ultimately lead to a conclusive histological diagnosis, which will benefit therapeutic decision-making.

This retrospective study aimed to compare the usefulness between conventional US and CEUS in their ability to identify the target area of AMMs and to plan the core needle biopsy route. Another study aim was to assess possible prebiopsy ultrasonic characteristics that may predict the patients with the highest probability of achieving conclusive histological diagnoses.

2. Patients and Methods

2.1. Study Population.
The present study was approved by the Research and Ethics committee of Sun Yat-Sen University Cancer Center (SYSUCC), and written informed consent was obtained from each patient before CEUS and US-CNB were performed.

Masses located in the precardiac vascular region of the mediastinum were diagnosed as AMMs by the radiologist [23]. A total of 92 patients with AMMs suspected to be malignant that were detected by chest CT from July 2006 to June 2016 at our institution underwent initial US-CNB. The inclusion criteria for referral for US-CNB were based on the CT findings of a suspected AMM located adjacent to the chest wall and confirmed by conventional US evaluation. Since it is considered the shortest distance from the cutting system, solid content in the AMM should be at least 15 mm thick. Patients were able to control their breathing during the procedure. The International Normalized Ratio was not greater than 1.6 and the platelet count was greater than 10^5/L.

The patients' demographic data, ultrasonic characteristics, diagnostic procedures, cost and duration between the initial US-CNB and treatment, hospitalization, pathological results, and clinical treatment records were reviewed using the Panoramic Patients Information System from the Department of Information.

2.2. Prebiopsy US and CEUS Evaluation.
The conventional US evaluation of the AMMs included the B-mode of grey scale US and the C-mode of color Doppler blood flow. Grey scale US was used in the initial evaluation of the AMMs of patients who were recommended to undergo US-CNB. Location, size, ultrasonic pattern, and presence of necrosis were recorded. The color Doppler window was focused on the AMM to detect blood flow signals. The blood flow signals within the tumor were then categorized as "marked flow signals" or "not marked" including no, minimal, or moderate blood flow signals, or no-due to interference by the heart-beat, with reference to Adler's method [24]. The Doppler filter was adjusted on an individual basis to eliminate the influence from the heart-beat. Necrosis was determined if B-mode showed an echoic area with a clear boundary within the AMMs where the CDFI detected the absence of blood flow signals.

CEUS was performed with an Acuson Sequoia 512 (Siemens Medical Solutions, Mountain View, CA, USA) coupled to a 4C1 convex array probe using a low mechanical index (0.18) to avoid disruption of microbubbles. A 2.4 ml bolus of a US blood pool contrast agent (SonoVue, Bracco, Milan, Italy) was injected into the antecubital vein, followed by a 5-ml saline flush. Next, the AMM was scanned continuously for up to 4 minutes. The dynamic image was recorded on the hard-drive of the ultrasound system. Necrosis was determined if CEUS showed the complete absence of enhancement during all phases.

At the end of conventional US evaluation, or after supplement with CEUS, an appropriate approach to achieve a suitable acoustic window for the biopsy path and target was determined. The operator of the US-CNB should be involved in the evaluation of the CEUS procedure.

2.3. US-CNB. An ultrasonography system (Avius, Hitachi, Tokyo, Japan) with a 2.0–5.0 MHz ultrasound interventional probe (EUP-B512, Hitachi, Tokyo, Japan) was used for the biopsy, and color Doppler imaging was routinely used to delineate large vessels, such as the internal thoracic artery, that were in close proximity to the AMMs to avoid puncturing them during the biopsy. The information obtained from the diagnostic chest CT and prebiopsy US or CEUS was used to optimize and plan the biopsy route and target. An 18-gauge core biopsy needle (Magnum; Bard, Covington, GA, USA) was used for the transthoracic CNB. Children under 16 years of age were recommended to undergo this procedure in the operation theater with nonintubation general anesthesia; adults underwent this procedure after routine sterilization and local anesthesia (3–5 ml 1% lidocaine). A free hand approach was used for the CNB procedure. The probe was fixed and the core needle was inserted into the chest wall in the intercostal muscles. The core needle was fired until the tip of the needle reached the margin of the AMM. The whole procedure was monitored by real-time US. The number of puncture attempts was decided by the volume and quality of the specimen obtained. The specimens were fixed in 10% formalin and were sent to the pathology department for evaluation by 2 experienced pathologists. In some cases, half the specimen that was harvested was promptly collected in a sterile tube for molecular studies. The patients stayed in the recovery room for at least 30 minutes so that possible morbidities such as active bleeding or other complications could be observed.

2.4. Pathological Evaluation and Cellularity. Core needle biopsy specimens were stained with routine hematoxylin and eosin (H&E). All results that described staining patterns or morphologic features of the specimens were evaluated under the guidance of 2 experienced pathologists who specialized in cancer pathology. The ancillary study, which included immunohistochemistry (IHC), in situ hybridization (ISH), and fluorescence in situ hybridization (FISH) was performed for the requirements of the pathologist. Lung tissue found in the sample was noted. Diagnoses of lymphoma, thymoma, and carcinoma without accurate subclassification or origin were regarded as nonconclusive histological diagnoses. A histological diagnosis of normal, hyperplasia with fibrosis, necrotic tissue, low cellularity, or insufficient tissue was defined as a failed diagnosis. Failure and nonconclusive diagnoses were both regarded as nonconclusive histological diagnoses. A conclusive histological diagnosis was achieved by a pathologist with H&E staining and the required ancillary studies based on the CNB samples that were used in treatment decisions. The final diagnoses based on the definitive histological diagnoses obtained by the biopsy were confirmed by surgical pathology or response to medical treatment.

The cancer pathologist also selected the photomicrographs (magnification 40x) for the computer-assisted image analysis of cellularity (Axio Imager, Zeiss Imaging System, Germany). The percentage of tumor cells was evaluated in each biopsy sample. The primary endpoint was the maximum percentage of tumor cells across the different samples.

2.5. Statistics. SPSS software version 23.0 (IBM, Armonk, NY, USA) was used for all statistical analyses. The Mann–Whitney U test was used for numerical data, while the Pearson Chi-square test was used for categorical data. Binary logistic regression analysis was used to determine possible factors that could predict a conclusive histological diagnosis by US-CNB. Statistical significance was set at $p < 0.05$.

3. Results

3.1. General. Out of all patients, 64 were men and 28 were women, who had a mean age of 34.5 years (range: 5.0–68.0 years). All patients underwent evaluation by US ($n = 75$) or CEUS ($n = 17$) before the initial US-CNB. Eighteen of those 20 patients who were undiagnosed as a result of the initial US-CNB with prebiopsy US underwent US ($n = 11$) or CEUS ($n = 7$) evaluation before the repeated US-CNB. Two undiagnosed patients who underwent repeated US-CNB with prebiopsy US underwent multiple US-CNB procedures. In all, 308 punctures were performed (range: 2–5, mean: 2.8 punctures per patient). Seven patients who had undergone US-CNB and failed to receive a conclusive histological diagnosis were referred to other alternative procedures such as CT-guided biopsy, EBUS-TBNA, or a surgical procedure such as parasternal mini-mediastinotomy, cervical mediastinoscopy, VATS, or thoracotomy, as shown in Figure 1. The diagnostic yields of US-CNB according to the final diagnosis were as follows: 96.0% (24/25) for thymic epithelial tumors; 90.0% (9/10) for thymomas; 100.0% (15/15) for thymic carcinomas; 92.9% (39/42) for lymphomas; 60.0% (3/5) for Hodgkin's lymphomas; 97.3% (36/37) for non-Hodgkin's lymphomas that originated form T cells ($n = 18$) and B cells ($n = 19$); 90.0% (9/10) for germ cell tumors; 100% (2/2) for teratomas; 100.0% (1/1) for seminomas; 85.7% (6/7) for nonseminomatous or mixed germ cell tumors; 83.3% (10/12) for other malignancies; 66.7% (2/3) for metastases; 100% (3/3) for sarcomas; 75.0% (3/4) for lung cancers; 100.0% (2/2) for neuroendocrine tumors; and 100% (1/1) for tuberculosis.

3.2. Initial US-CNB for Histological Diagnoses of AMMs. No significant differences were observed in the demographic or ultrasonic characteristics including age, gender, cancer history, location, size, and CDFI category of AMMs between the US and CEUS groups. Prebiopsy CEUS detected more marginal blood flow signals and necrosis than conventional US ($p < 0.05$). Although no significant difference was observed in the number of punctures of the core needle between these two groups, the initial US-CNB with prebiopsy CEUS potentially improved the yield of conclusive histological diagnoses with increasing cellularity of the samples

Table 1: Baseline characteristics, prebiopsy ultrasonographic features, and outcomes of 92 patients with AMMs who underwent initial US-CNB with prebiopsy conventional US or CEUS evaluation.

	US ($n = 75$)	CEUS ($n = 17$)	p value
Age (years), mean ± SD	34.0 ± 15.6	36.4 ± 17.1	0.763
Gender, male/female	50/25	14/3	0.207
Cancer history yes/no	3/75	2/17	0.205
Location of AMMs (both/left/right)	8/40/27	0/10/7	0.408
Size of AMMs (mm), mean ± SD	66.0 ± 29.3	70.1 ± 33.9	0.721
CDFI category (marked/not marked)	29/46	3/14	0.074
Marginal blood flow signals (presence/absence)	47/28	15/2	0.043
Necrosis (presence/absence)	8/67	5/12	0.046
Punctures of core needle (mean ± SD)	2.5 ± 0.8	2.9 ± 0.9	0.333
Repeated US-guided CNB (no/yes)	17/58	0/17	0.031
Conclusive histological diagnoses (no/yes)	20/55	1/16	0.067
Cellularity (mean ± SD)	0.64 ± 0.25	0.83 ± 0.18	0.001
Lung tissue in the sample (presence/absence)	6/69	0/17	0.144
Duration between initial CNB and treatment decision (days mean ± SD)	8.5 ± 4.2	5.9 ± 3.6	<0.001

US, ultrasound; US-CNB, ultrasound-guided core needle biopsy; AMM, anterior mediastinal mass; CEUS, contrast-enhanced ultrasound; SD, standard deviation.

Table 2: Results of the univariate analysis to establish confounding factors related to the ability to obtain a conclusive histological diagnosis of anterior mediastinal masses by US-CNB.

	Conclusive diagnoses ($n = 83$)	Nonconclusive diagnoses ($n = 9$)	p value
Age (years), mean ± SD	34.29 ± 16.36	36.00 ± 9.80	0.051
Gender, male/female	60/23	4/5	0.085
Cancer history (yes/no)	5/78	1/8	0.557
Location (both/left/right)	8/46/29	0/4/5	0.371
Size (mm), mean ± SD	81.6 ± 35.9	90.11 ± 29.78	0.819
CDFI category (marked/not marked)	58/25	2/7	0.004
Marginal blood flow signals (presence/absence)	60/23	2/7	0.002
Necrosis (presence/absence)	9/24	4/5	0.021
Punctures of core needle (mean ± SD)	3.3 ± 2.5	4.1 ± 2.0	<0.001
Repeated US-CNB (with/without)	12/71	5/4	0.003
Cellularity mean ± SD	0.7 ± 0.2	0.4 ± 0.3	0.009

US-CNB: ultrasound-guided core needle biopsy; CDFI: color Doppler flow imaging; SD: standard deviation.

($p = 0.001$); this helped to avoid repeated US-CNB compared with conventional US ($p = 0.031$), as shown in Table 1. The diagnostic yield of the initial US-CNB of AMMs was 77.2% (71/92).

3.3. Repeated US-CNB for the Histological Diagnoses of AMMs.
Prebiopsy CEUS potentially improved the yield of conclusive histological diagnoses (5/6, 83.3%) compared with US (7/11, 63.6%) in individuals who underwent repeated US-CNB of AMMs ($p = 0.395$), as increased cellularity was observed in the samples ($p = 0.001$), as shown in Figure 2. Repeated US-CNB resulted in a diagnostic yield of 70.6% (12/17) and contributed to significant improvements in the diagnostic yield of those patients who underwent initial US-CNB with prebiopsy US from 73.3% (55/75) to 87.3% (67/75) ($p < 0.001$). Overall, the diagnostic yield of US-CNB increased from 77.2% (71/92) to 90.2% (83/92)

with supplementation of repeated US-CNB in this study population ($p < 0.001$).

3.4. CEUS Improved the Diagnostic Yield of US-CNB.
Taken together, prebiopsy CEUS improved the diagnostic yield (21/23, 91.3%) of US-CNB compared with prebiopsy US (62/86, 72.1%) ($p = 0.043$, odds ratio: 4.065, and 95% confidence interval: lower 0.885, upper 18.677) and decreased the need for repeated US-CNB in cases with a failed diagnosis (CEUS 0.0%, 0/2 versus US 75.0%, 18/24) and potentially avoided multiple US-CNB procedures (CEUS 0.0%, 0/1 versus US 40% 2/5).

3.5. Prebiopsy Ultrasonic Characteristics and Their Correlation with Histological Yield.
A univariate analysis revealed that prebiopsy ultrasonic characteristics including marked blood flow signals ($p = 0.004$), the presence of marginal blood
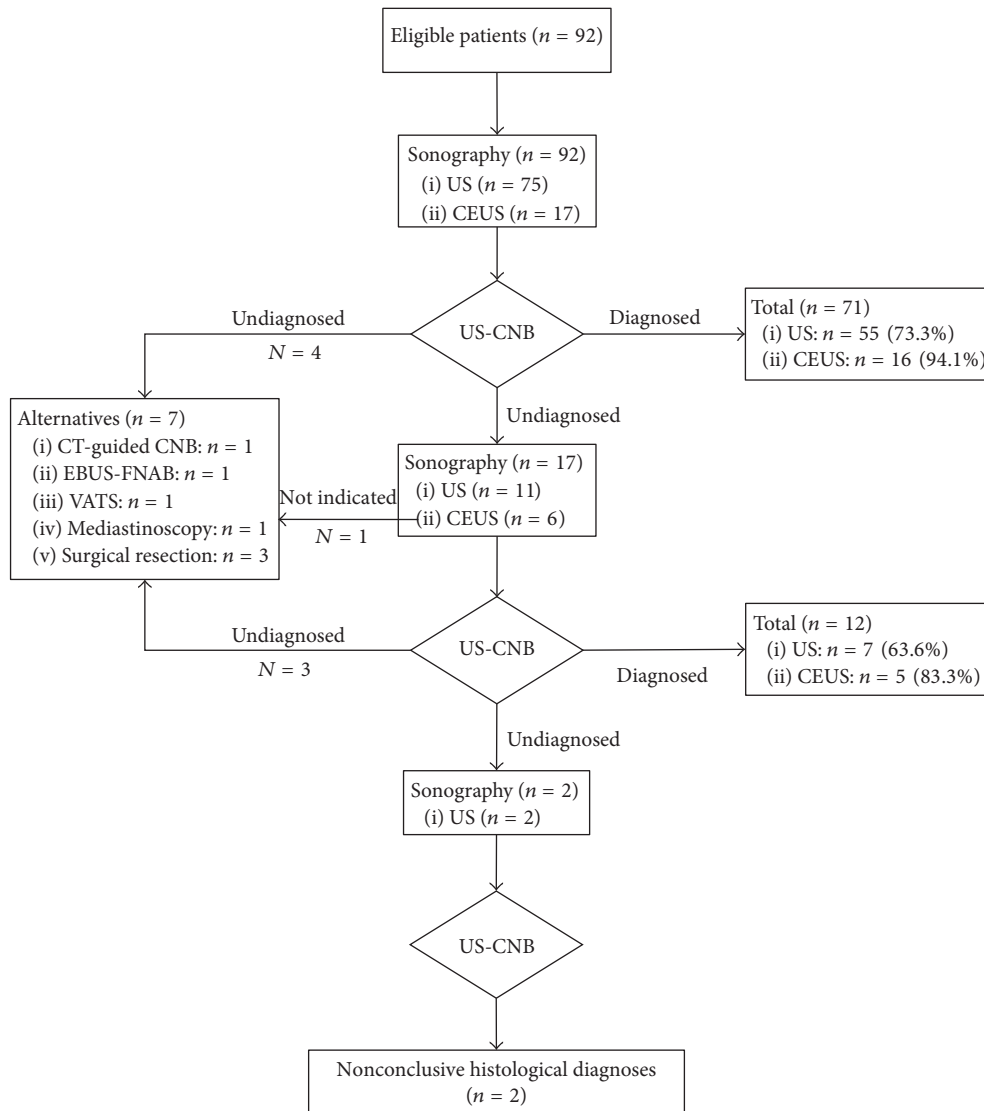
FIGURE 1: The flow chart of the 92 patients with anterior mediastinal masses who underwent initial ultrasound-guided core needle biopsy with prebiopsy ultrasound or contrast-enhanced ultrasound evaluation. CEUS: contrast-enhanced ultrasound; US: ultrasound; AMMs: anterior mediastinal masses; US-CNB: ultrasound-guided core needle biopsy.

flow signals in close proximity to the probe ($p = 0.002$), and the absence of necrosis ($p = 0.021$) in the AMMs led to a higher conclusive histological diagnostic yield of US-CNB. Although more punctures ($p < 0.001$) and repeated procedures ($p = 0.003$) were performed, samples obtained from the patients with nonconclusive histological diagnoses were of low cellularity ($p = 0.009$), as shown in Table 2.

Logistic regression using the Enter method showed that prebiopsy ultrasonic characteristics including the presence of marginal blood flow signals (Exp(B) 0.116, 95.0% CI lower 0.021, upper 0.634) and the absence of necrosis (Exp(B) 5.986, 95.0% CI lower 1.185, upper 30.246) in AMMs can precisely predict the diagnostic yield (negative predictive value, 44.4%; positive predictive value, 97.6%; and overall predicative value, 92.4%).

3.6. Complications. Three patients complained of minor pain after completion of the procedure. No morbidities such as hemorrhage and pneumothorax were observed during or after the US-guided CNB procedure.

3.7. Treatment Based on the Conclusive Histological Diagnoses. The duration between the initial US-CNB and the treatment decision was shortened to a greater extent in those patients who underwent initial US-CNB with prebiopsy CEUS compared with those who underwent US ($p < 0.001$) because more repeated biopsies were needed in the conventional US group, which delayed the start of therapy. Of those 71 patients (71/92, 77.2%) who received conclusive histological diagnoses from the initial US-CNB, the results contributed to the best and prompt management decisions including those related to palliative care ($n = 9$), surgery-centered treatment ($n = 6$),
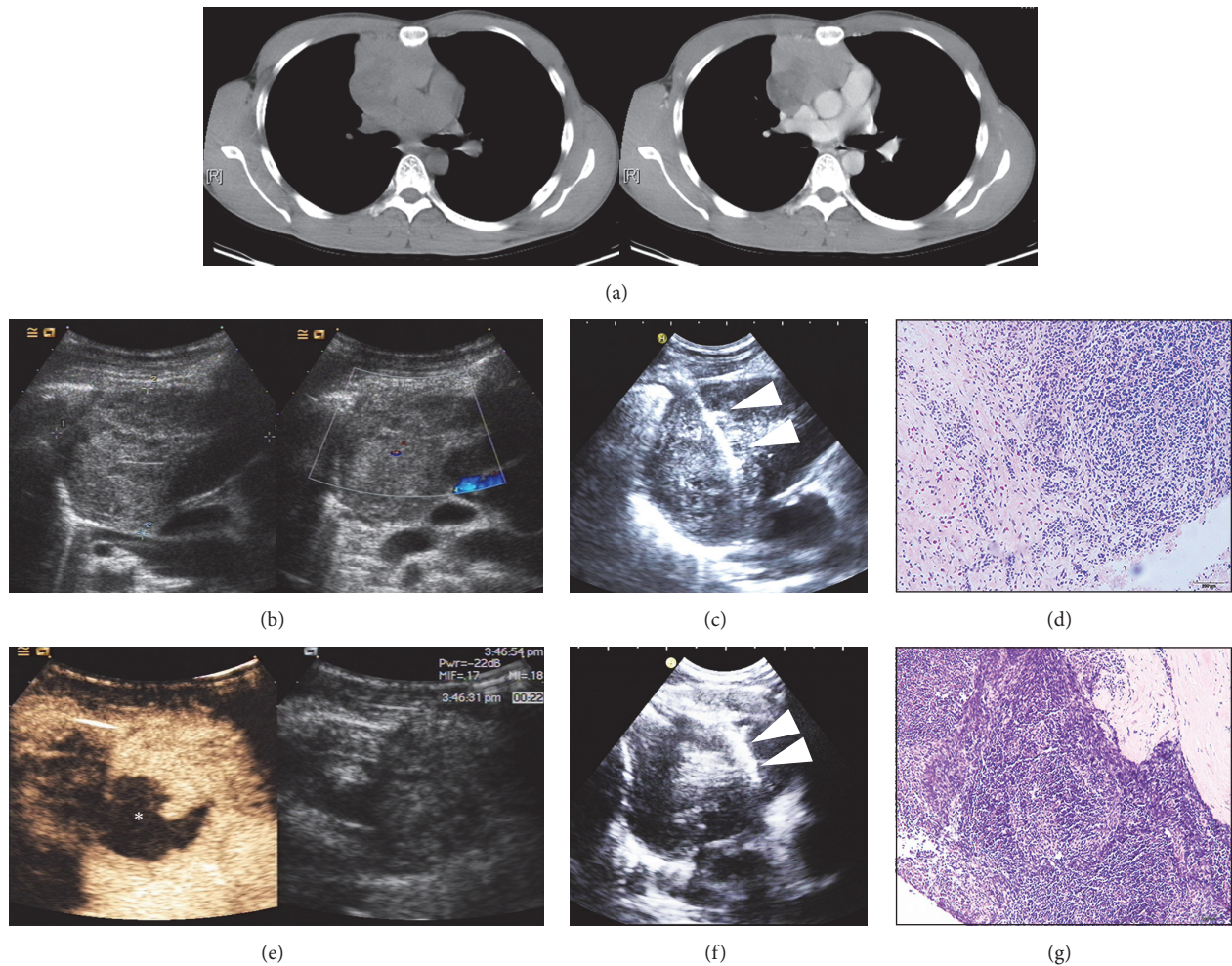
(a)

(b)

(c)

(d)

(e)

(f)

(g)

FIGURE 2: Twenty-nine-year-old man with thymoma. (a) Plain computed tomography revealed an irregular mass in the right anterior mediastinum. Contrast-enhanced computed tomography revealed that the mass was compressing the superior vena cava and aorta. (b) B-mode ultrasound showed an inhomogeneous mass visible in the right anterior mediastinum. Color Doppler ultrasound showed dot-like flow signals in the center of mass. (c) US-CNB of the mass with prebiopsy conventional US evaluation. White triangles indicate the needle. (d) H&E staining (magnification 100x) of the core needle biopsy sample showed major necrosis and a small number of enlarged nuclear cells with a nest-like arrangement, suspected tumor, and an insufficiency for immunohistochemistry staining. (e) Contrast-enhanced ultrasound revealed intensive inhomogeneous enhancement of the left anterior part of the AMM (22 seconds after the injection of 2.4 ml SonoVue); the left posterior part of the AMM was not enhanced throughout. The white flower-shaped dot indicates the necrosis with great confidence. (f) US-CNB of the mass with prebiopsy contrast-enhanced ultrasound targeted the left anterior enhanced portion of the AMM, which was confirmed by CEUS. (g) H&E staining (magnification 100x) of the core needle biopsy sample revealed karyomegaly within lymphocytes and a diagnosis of thymoma B1 with immunohistochemical staining, which was confirmed by surgical pathology. The approach of all ultrasonography procedures involved a right parasternal scan of the 3rd intercostal space.

chemotherapy-centered treatment ($n = 55$), and targeted therapy ($n = 1$) with crizotinib due to positive ALK gene translocation of lung cancer.

4. Discussion

AMMs were more likely to be malignant compared with masses in other parts of the mediastinum [1]. Successful biopsy of AMMs and the achievement of a conclusive histological diagnosis with subclassification or genetic information are crucial for prompt treatment decisions in the era of personalized therapy [25]. The present and previous studies

showed high diagnostic yields and low morbidity in the group that underwent US-CNB for AMMs [14, 15, 19, 26, 27]. All of these studies approved US as a standard guidance for biopsy procedures if AMMs can be imaged well by US. We found that the therapeutic strategies based on the conclusive histological diagnoses after the initial US-CNB of AMMs were selected more promptly than in failed cases. Although repeated US-CNB increased the diagnostic yield, this procedure should be avoided due to high cost and time consumption, risk of complications, delayed therapy, and deterioration of the patients' faith in medicine and because repeated procedure is associated with increased anxiety and depression in patients [10].
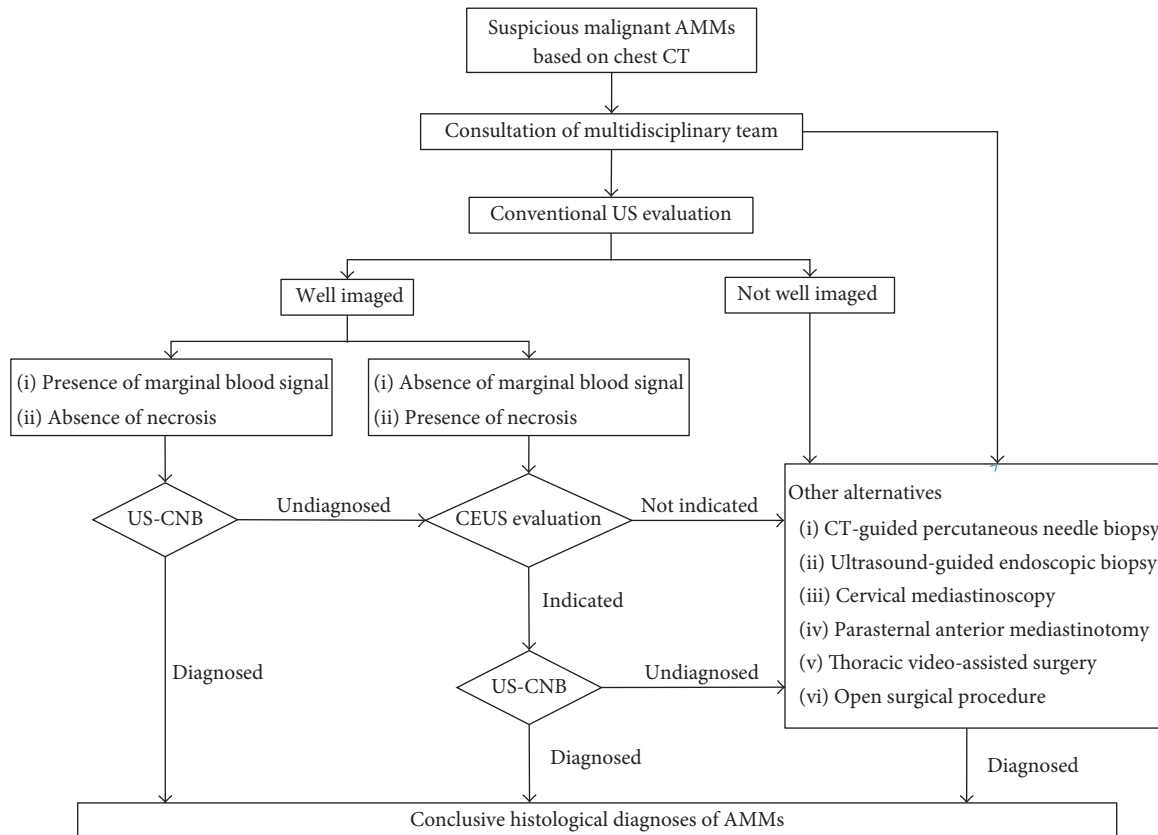
FIGURE 3: Suggested proposal for the integration of contrast-enhanced ultrasound into ultrasound management of suspicious malignant anterior mediastinal masses detected on chest computerized tomography. CEUS: contrast-enhanced ultrasound; US: ultrasound; AMMs: anterior mediastinal masses; US-CNB: ultrasound-guided core needle biopsy.

Several studies have shown that CEUS can differentiate necrosis or nonviable tissue from viable tumor tissue with great confidence and that prebiopsy CEUS definitely improves the diagnostic yield of US-CNB of mediastinal masses. A prospective study with a small number of patients (15 patients) showed that B-mode US associated with CEUS and US-guided biopsy reached an elevated accuracy (91.66%, 11/12) for the diagnosis of mediastinal masses [19]. Most recently, several high-volume studies have demonstrated that, compared with conventional US, CEUS can improve the diagnostic accuracy of AMMs [26, 27]. The present study found that prebiopsy CEUS improved the diagnostic yield as a result of the pronounced ability of CEUS to distinguish viable tissue from necrotic or nonviable tissue. This was confirmed by the higher detection rate of nonenhancement area and higher cellularity in the CNB samples of those patients who underwent prebiopsy CEUS compared with those who underwent conventional US.

CEUS does not discriminate between benign and malignant tissue in pleural-based lesions or lung disease [18, 28]; the present study showed that CEUS contributes to the management of AMMs by US. CEUS plays a role in the exclusion of fully cystic lesions and in the selection of target areas in patients who are suitable for US-guided CNB. More patients (75.0%, 16/24) with failed diagnoses

after US-CNB with prebiopsy conventional US underwent repeated US-guided CNB compared with those (0.0%, 0/2) with prebiopsy CEUS. Other biopsy alternatives but not repeated US-CNB should be recommended for those cases that failed to reach a conclusive diagnosis by US-CNB with prebiopsy CEUS, which means that CEUS even plays a role in the prevention of repeated US-CNB. No lung tissues were found in the CNB samples with prebiopsy CEUS without statistical significance; this may imply that prebiopsy CEUS could distinguish AMMs from surrounding atelectasis and avoid transpleural puncture, which is recommended for the diagnosis of thymic epithelial tumors according to the NCCN or ESMO guidelines [4, 29].

In the present study, the final diagnoses confirmed that the most common malignancies were lymphoma and thymic epithelial tumors. The diagnostic yield of US-CNB was higher in thymic epithelial tumors, but the diagnostic yield for Hodgkin's disease (60%, 3/5) was lower than that for non-Hodgkin's lymphoma (97.3%, 36/37). The present study also confirmed that an 18-gauge core needle biopsy for AMMs achieved a satisfactory yield for NHL (36/37, 97.3%) but not for HL (3/5, 60%). For the diagnosis of lymphoma, the recommendation is excisional biopsy, but core needle biopsy may be adequate if it is diagnostic [30, 31]. The diagnosis of Hodgkin's lymphoma depends on the presence of typical

R-S cells and histological structure, which are always deficient in CNB samples. If Hodgkin's lymphoma is suspected, excisional biopsy is recommended [31]. Considering that non-Hodgkin's lymphoma is the main etiology of AMMs, core needle biopsy of the viable part of AMMs would contribute to the satisfactory pathological outcome and flow cytometry for the therapeutic strategy.

Conventional US evaluation and guided CNB can achieve a diagnostic yield as high as 70–90% [14, 26, 32]. Prebiopsy CEUS should not be routinely recommended for all patients with AMMs according to the cost-effectiveness principle. The present study found that prebiopsy ultrasonic characteristics of AMMs including the presence of marginal blood flow signals and the absence of necrosis can precisely predict the diagnostic yield. In addition, these 2 parameters could be used to triage the patients who underwent prebiopsy conventional US who may require further CEUS. Prebiopsy CEUS should be used selectively for AMMs with an absence of marginal blood flow signals or AMMs with necrosis or in those patients who undergo repeated CNB, just as the suggested proposal for integration of CEUS into the management of AMMs by US, as shown in Figure 3.

The present study is a retrospective review, and the low volume of prebiopsy CEUS procedures was not performed randomly, but on demand by the specialist. The study population included patients with AMMs that were suspected to be malignancies detected on chest CT; therefore, few patients with benign diseases were included. The dominant deficiency of the technique used in this study is that CEUS was not used directly for imaging guidance. It was used as part of a prebiopsy evaluation and supplied the operator with effective information to distinguish AMMs from the surrounding anatomical structures and to target the puncture area. Although the operators of US-guided CNB were involved in the CEUS evaluation, no precise spatial correlation was maintained between CEUS and CNB. The supposed proposal for integration of CEUS into the management of AMMs by US based on this study should be confirmed by random controlled trials that require multicenter cooperation for these scarce diseases of the anterior mediastinum.

5. Conclusion

US-CNB of the viable part of anterior mediastinal masses verified by prebiopsy CEUS supplies sufficient tissue with increased cellularity for underlying ancillary studies and increases pathologic yield. Further CEUS should be recommended for those AMMs with an absence of marginal blood flow signals close to the probe, those that are mostly necrotic, and patients who undergo repeated US-CNB.

Conflicts of Interest

The authors declare that they have no conflicts of interest.

Authors' Contributions

Jian-hua Zhou and Hong-bo Shan contributed equally to the present study.

References

[1] B. V. Duwe, D. H. Sterman, and A. I. Musani, "Tumors of the mediastinum," *CHEST*, vol. 128, no. 4, pp. 2893–2909, 2005.

[2] M. Saito, K. Shiraishi, H. Kunitoh, S. Takenoshita, J. Yokota, and T. Kohno, "Gene aberrations for precision medicine against lung adenocarcinoma," *Cancer Science*, vol. 107, no. 6, pp. 713–720, 2016.

[3] A. Marchevsky, A. Marx, P. Ströbel et al., "Policies and reporting guidelines for small biopsy specimens of mediastinal masses," *Journal of Thoracic Oncology*, vol. 6, no. 7, pp. S1724–S1729, 2011.

[4] N. Girard, E. Ruffini, A. Marx, C. Faivre-Finn, and S. Peters, "Thymic epithelial tumours: ESMO Clinical Practice Guidelines for diagnosis, treatment and follow-up," *Annals of Oncology*, vol. 26, Article ID mdv277, pp. v40–v55, 2015.

[5] C.-M. Chen, J. W.-C. Chang, Y.-C. Cheung et al., "Computed tomography-guided core-needle biopsy specimens demonstrate epidermal growth factor receptor mutations in patients with non-small-cell lung cancer," *Acta Radiologica*, vol. 49, no. 9, pp. 991–994, 2008.

[6] D. M. DiBardino, A. Saqi, J. A. Elvin et al., "Yield and clinical utility of next-generation sequencing in selected patients with lung adenocarcinoma," *Clinical Lung Cancer*, vol. 17, no. 6, pp. 517–522.e3, 2016.

[7] J. K. Frederiksen, M. Sharma, C. Casulo, and W. R. Burack, "Systematic review of the effectiveness of fine-needle aspiration and/or core needle biopsy for subclassifying lymphoma," *Archives of Pathology & Laboratory Medicine*, vol. 139, no. 2, pp. 245–251, 2015.

[8] C. Amador-Ortiz, L. Chen, A. Hassan et al., "Combined core needle biopsy and fine-needle aspiration with ancillary studies correlate highly with traditional techniques in the diagnosis of nodal-based lymphoma," *American Journal of Clinical Pathology*, vol. 135, no. 4, pp. 516–524, 2011.

[9] M. Petranovic, M. D. Gilman, A. Muniappan et al., "Diagnostic yield of CT-guided percutaneous transthoracic needle biopsy for diagnosis of anterior mediastinal masses," *American Journal of Roentgenology*, vol. 205, no. 4, pp. 774–779, 2015.

[10] T. Azrumelashvili, M. Mizandari, D. Magalashvili, and T. Dundua, "Imaging guided mediastinal percutaneal core biopsy–technique and complications," *Georgian Medical News*, no. 242, pp. 24–34, 2015.

[11] C.-J. Yu, P.-C. Yang, D.-B. Chang et al., "Evaluation of ultrasonically guided biopsies of mediastinal masses," *CHEST*, vol. 100, no. 2, pp. 399–405, 1991.

[12] B. Morrissey, H. Adams, A. R. Gibbs, and M. D. Crane, "Percutaneous needle biopsy of the mediastinum: Review of 94 procedures," *Thorax*, vol. 48, no. 6, pp. 632–637, 1993.

[13] D. J. Rubens, J. G. Strang, P. J. Fultz, and R. H. Gottlieb, "Sonographic guidance of mediastinal biopsy: an effective alternative to ct guidance," *American Journal of Roentgenology*, vol. 169, no. 6, pp. 1605–1610, 1997.

[14] H.-J. Chen, W.-C. Liao, S.-J. Liang, C.-H. Li, C.-Y. Tu, and W.-H. Hsu, "Diagnostic impact of color doppler ultrasound-guided core biopsy on fine-needle aspiration of anterior mediastinal masses," *Ultrasound in Medicine & Biology*, vol. 40, no. 12, pp. 2768–2776, 2014.

[15] C. F. N. Koegelenberg, A. H. Diacon, E. M. Irusen et al., "The diagnostic yield and safety of ultrasound-assisted transthoracic biopsy of mediastinal masses," *Respiration*, vol. 81, no. 2, pp. 134–141, 2011.

[16] J. Han, Y. Liu, F. Han et al., "The degree of contrast washout on contrast-enhanced ultrasound in distinguishing intrahepatic cholangiocarcinoma from hepatocellular carcinoma," *Ultrasound in Medicine & Biology*, vol. 41, no. 12, pp. 3088–3095, 2015.

[17] J. H. Zhou, W. Zheng, L. H. Cao et al., "Quantitative evaluation of viable tissue perfusion changes with contrast-enhanced greyscale ultrasound in a mouse hepatoma model following treatment with different doses of thalidomide," *British Journal of Radiology*, vol. 84, no. 1005, pp. 826–832, 2011.

[18] C. Görg, T. Bert, R. Kring, and A. Dempfle, "Transcutaneous contrast enhanced sonography of the chest for evaluation of pleural based pulmonary lesions: experience in 137 patients," *Ultraschall in der Medizin / European Journal of Ultrasound (UiM/EJU)*, vol. 27, no. 5, pp. 437–444, 2006.

[19] M. Caremani, A. Benci, D. Tacconi, U. Occhini, L. Lapini, and A. Caremani, "Sonographic management of mediastinal syndrome," *Journal of Ultrasound*, vol. 12, no. 2, pp. 61–68, 2009.

[20] M. Hocke, M. Menges, T. Topalidis, C. F. Dietrich, and A. Stallmach, "Contrast-enhanced endoscopic ultrasound in discrimination between benign and malignant mediastinal and abdominal lymph nodes," *Journal of Cancer Research and Clinical Oncology*, vol. 134, no. 4, pp. 473–480, 2008.

[21] M. Sperandeo, G. Rea, M. A. Grimaldi, F. Trovato, L. M. C. Dimitri, and V. Carnevale, "Contrast-enhanced ultrasound does not discriminate between community acquired pneumonia and lung cancer," *Thorax*, vol. 72, no. 2, pp. 178–180, 2017.

[22] F. Piscaglia, C. Nolsøe, C. F. Dietrich et al., "The EFSUMB guidelines and recommendations on the clinical practice of contrast enhanced ultrasound (CEUS): update 2011 on non-hepatic applications," *Ultraschall in der Medizin / European Journal of Ultrasound (UiM/EJU)*, vol. 33, no. 1, pp. 33–59, 2012.

[23] K. Fujimoto, M. Hara, N. Tomiyama, M. Kusumoto, F. Sakai, and Y. Fujii, "Proposal for a new mediastinal compartment classification of transverse plane images according to the Japanese Association for Research on the Thymus (JART) general rules for the study of mediastinal tumors," *Oncology Reports*, vol. 31, no. 2, pp. 565–572, 2014.

[24] D. D. Adler, P. L. Carson, J. M. Rubin, and D. Quinn-Reid, "Doppler ultrasound color flow imaging in the study of breast cancer: preliminary findings," *Ultrasound in Medicine & Biology*, vol. 16, no. 6, pp. 553–559, 1990.

[25] G. H. Lyman and H. L. Moses, "Biomarker tests for molecularly targeted therapies - The key to unlocking precision medicine," *The New England Journal of Medicine*, vol. 375, no. 1, pp. 4–6, 2016.

[26] D. Yi, M. Feng, W. Wen-Ping, J. Zheng-Biao, and P.-L. Fan, "Contrast-enhanced US-guided percutaneous biopsy of anterior mediastinal lesions," *Diagnostic and Interventional Radiology*, vol. 23, no. 1, pp. 43–48, 2017.

[27] J. Fu, W. Yang, S. Wang et al., "Clinical value of contrast-enhanced ultrasound in improving diagnostic accuracy rate of transthoracic biopsy of anteriormedial mediastinal lesions," *Chinese Journal of Cancer Research*, vol. 28, no. 6, pp. 617–625, 2016.

[28] G. Trovato and M. Sperandeo, "Lung ultrasound in pneumothorax: the continuing need for radiology," *The Journal of Emergency Medicine*, vol. 51, no. 2, pp. 189–191, 2016.

[29] D. S. Ettinger, G. J. Riely, W. Akerley et al., "Thymomas and thymic carcinomas," *Journal of the National Comprehensive Cancer Network*, vol. 11, no. 5, pp. 562–576, 2013.

[30] AD. Zelenetz, WG. Wierda, JS. Abramson, RH. Advani, CB. Andreadis, and N. Bartlett, "Non-hodgkins lymphomas," *Journal of the National Comprehensive Cancer Network: JNCCN*, vol. 11, no. 3, pp. 257-72, 2013.

[31] R. T. Hoppe, R. H. Advani, W. Z. Ai et al., "Hodgkin lymphoma, version 2.2012 featured updates to the nccn guidelines," *Journal of the National Comprehensive Cancer Network*, vol. 10, no. 5, pp. 589–597, 2012.

[32] K. Wernecke, "Percutaneous biopsy of mediastinal tumours under sonographic guidance," *Thorax*, vol. 46, no. 3, pp. 157–159, 1991.

Research Article

Correlation between Pathological Characteristics and Young's Modulus Value of Spastic Gastrocnemius in a Spinal Cord Injury Rat Model

Li Jiang,[1] Yu-jue Wang,[1] Qiao-yuan Wang,[2] Qing Wang,[3] Xiao-mei Wei,[1] Na Li,[1] Wei-ping Guo,[4] and Zu-lin Dou[1]

[1]*Department of Rehabilitation, The 3rd Affiliated Hospital of Sun Yat-sen University, Guangzhou, China*
[2]*Department of Ultrasound, The 3rd Affiliated Hospital of Sun Yat-sen University, Guangzhou, China*
[3]*Institute of Medical Information, School of Biomedical Engineering, Southern Medical University, Guangzhou, China*
[4]*Department of Gastroenterology Surgery, The 3rd Affiliated Hospital of Sun Yat-sen University, Guangzhou, China*

Correspondence should be addressed to Wei-ping Guo; gwping856@126.com and Zu-lin Dou; douzul@163.com

The goal of the present study were (1) to investigate the pathological characteristics of gastrocnemius muscle (GM) and quantitatively assess GM tissue stiffness in rat models with spinal cord injury (SCI) and (2) to explore the correlation between pathological characteristics changes and Young's modulus value of GM. 24 Sprague Dawley male rats were allocated into normal control groups and SCI model subgroups, respectively. GM stiffness was assessed with shear wave sonoelastography technology. All GMs were further analyzed by pathological examinations. GM weights were decreased, the ratio of type I fibers was decreased, and the ratio of type II fibers was increased in the GM in the model group. MyHC-I was decreased, while MyHC-II was increased according to the electrophoretic analysis in model subgroups. The elastic modulus value of GM was increased in the model group. A significant negative correlation was found between Young's modulus value of GM and the ratio of type I fibers of GM in model subgroup. Our studies showed that the stiffness of GM is correlated with pathological characteristics during the initial stages of SCI in rats. We also identified shear wave sonoelastography technology as a useful tool to assess GM stiffness in SCI rat models.

1. Introduction

Spasticity is a common disorder in patients with injury of the brain and spinal cord. Severe spasticity impacts patient limb function and subsequently their daily life. Previous studies have shown that spastic skeletal muscle secondary structures changes (such as shortening of muscle fibers, increased connective tissue, and adipose tissue) can modify certain biomechanical properties, such as increased stiffness levels [1, 2]. Understanding the pathophysiology of spasticity may provide important clues to its treatment. According to studies on the pathophysiology of spasticity, exaggerated reflexes and secondary changes in mechanical muscle fibers properties have a major role in spastic movement disorder [3]. Clinically, spasticity is associated with increased muscle tone, stiffness,

and eventual joint contractures [4]. Spastic muscle stiffness can reflect the level of spasticity. The assessment of spastic muscle stiffness is conductive to the development of personalized spasticity treatment strategy but also helpful to study the effectiveness of the therapeutic intervention.

Clinicians often judge the changes in muscle hardness by passively pulling the spastic limbs and touching the spastic muscle, and the assessment results are greatly influenced by the subjective factors from the examiner. It is essential to have an objective, quantifiable method of measuring spasticity muscle stiffness. Sonoelastography can directly detect Young's modulus value of biological tissue to determine its elasticity. On sonoelastographic images, a relaxed muscle structure will appear mostly soft (green blue), while contracted or degenerated muscle fiber will appear

hard (red) [5]. This imaging method further promotes the comparison of elastic properties under various physiological conditions [6]. Despite its known advantages, this technique has been applied for the evaluation of spastic muscles stiffness following UMN injury [5, 7].

Muscle biopsy is the most prevalent type of analysis of spastic muscle tissue. Sectioned muscles from patients with spasticity show abnormalities such as increased variability in fiber size. Variability in fiber size (i.e., large and small fibers within the same muscle) is characteristic of numerous neuromuscular disorders and not specific to spasticity [2]. Some biopsy studies report an increased percentage of type I fiber in muscle from patients with spasticity and fewer report an increased percentage of Type II fiber. There is no general agreement on muscles issue which must be due, in part, to the sampling problems. Animal models of spasticity have allowed for the elucidation of possible mechanisms and the evaluation of potential therapeutic interventions for these serious clinical problems. Only complete spinal transection at the thoracic level in animal models would duplicate completely and permanently what is seen in humans after SCI. The rat models with SCI have been used as experimental subjects for spasticity muscles in most laboratories [8, 9].

In a previous study [10], we reported changes in the pathological characteristics and Young's modulus values of GM in rats with completed spinal cord injury (SCI). This brought up the question of whether there is a correlation between these pathological GM characteristics and Young's modulus value in SCI model rats. Therefore, in this study, we used SCI rat models to explore the pathological changes and Young's modulus values of GM in rats with SCI at different time points, and the correlation analysis was used to determine whether the pathological characteristics were correlated with Young's modulus value. The results of the study will reveal the relevant factors of spastic muscles and help to find the treatment strategies to reduce muscle stiffness.

2. Materials and Methods

2.1. Materials. Forty-two Sprague Dawley male rats (260–280 g) were divided into the control group (6 rats) and the SCI model group (36 rats). The rats in the SCI model group were randomly divided into the 2 w, 4 w, and 12 w subgroups (12 rats per group). This study was approved by the Sun Yat-sen University Center for Ethical Review (approval number: IACUC-20140201).

2.2. Methods

2.2.1. Model Preparation. The rats were anesthetized by the abdominal injection of 10% chloral hydrate solution at a dose of 0.35 ml/100 g body weight [8, 9]. Following anesthetization, the rats were fastened to a sterile operating table and the spinal cord was completely severed at the T10 level before a gelatin sponge was placed in severed space ($3 \times 2 \times 2$ mm). We then sutured the muscle, fascia, and skin of the rats. Following principles from a previous study, we took measures to prevent postoperative infection and used an artificial extruding bladder to assist with micturition [8].

2.2.2. Muscle Tone and Mobility Behavioral Assessment. Plantar flexor muscle tone was assessed using the Modified Ashworth Scale (MAS). Mobility behavior was assessed using the Basso, Beattie, and Bresnahan Locomotor Rating Scale (BBB Scale) [11]. The assessors were double-blinded to the groups.

2.2.3. Supersonic Sonoelastography. An AixPlorer ultrasonic scanner (Supersonic Imagine, Aix en Provence, France), coupled with a linear transducer array (4–15 MHz, SuperLinear 15-4, Vermon, Tours, France), was used in the present study. The scanner was set at the supersonic shear imaging (SSI) mode (musculoskeletal preset). SSI operates on a transient elastography principle. It produces elastography images based on the combination of a radiation force and an ultrafast ultrasound acquisition imaging system capable of capturing in real time the propagation of the resulting shear waves. The elastic modulus can be calculated from the velocity of the propagating wave when a faster velocity indicates a greater elastic modulus. Therefore, the elastic modulus can be calculated by measuring the propagation of shear waves. A light touch on the skin with the ultrasound probe is suggested by the manufacturer and a quantitative elasticity map can be computed from the system within a few milliseconds [12].

Measurement positions included ankle flexion (0°) and extension (−90°). Rat calf skin hair was removed, and each rat was laid on its left side with the right lower limb placed on a platform (hip and knee 90° flexion). Next, the probe was lightly placed on the skin above the GM, ensuring that the long axis of the probe was perpendicular to the tibia. The ROI was set to 10×10 mm, and the depth was set to approximately 0.5–1.0 cm. The probe was then rotated 90° to make the long axis parallel to the tibia. The two-dimensional gray-scale and elastic images were simultaneously observed with double real-time imaging. The elasticity imaging mode was then employed, followed by the application of the acoustic radiation pulse and detection of shear wave after the muscle elasticity image was stable. The image was then captured when the Q-BOX function measuring Young's modulus value (kPa) was initiated (Figure 1). Each image was captured five times for each plane measurement and all plane measurements were averaged.

2.2.4. Type of Muscle Fiber and Myosin Heavy Chain Isoform Quantification. In order to obtain the GM subsistence values, Type I, Type IIa, and Type IIb muscle fibers were counted in ATPase stain by Image J. Next, the GM Type I, IIa, IIb, and IIx myosin heavy chain (MyHC) data was analyzed with electrophoresis. The percentage proportions of MHC isoforms in the analyzed muscles were estimated by comparing the degree of staining intensity with Coomassie brilliant blue [13]. Quantity one software was applied for data analysis.

2.2.5. Statistical Analysis by SPSS 19.0 Software. Measurement data were described as the difference in means. One-way analysis of variance (ANOVA) was used to analyze differences among groups. The least significant difference t-test was used to analyze data with constant variances. Dunnett's $T3$ test was used to analyze data without constant variances. Pearson's
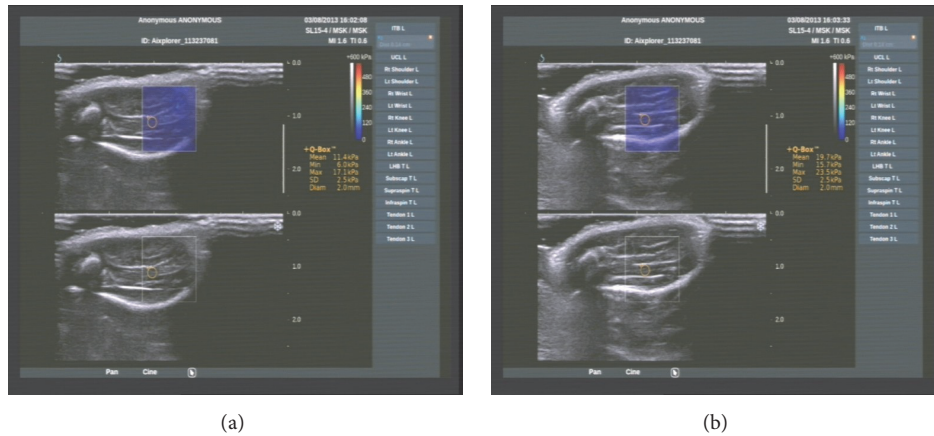
(a)

(b)

FIGURE 1: Image of sonoelastography ((a) ankle flexion; (b) ankle extension).

TABLE 1: Results of the general assessment in different groups.

Group	Body weight (g)	GM weight (g)	BBB (score)	MAS (score)
SCI				
2 w	275.33 ± 6.42	0.93 ± 0.18	3.17 ± 0.98	1.50 ± 0.48
4 w	287.33 ± 10.65	0.98 ± 0.45	4.83 ± 0.97	1.33 ± 1.03
12 w	290.33 ± 16.21	1.24 ± 0.11	7.17 ± 1.33	0.83 ± 0.41
Control	285.50 ± 7.42	1.62 ± 0.07	21.00	0
F	2.11	9.70	429.72	4.67
P	0.13	<0.01	<0.01	0.01

TABLE 2: Results of Young's modulus value in different groups.

Group	Ankle flexion	Ankle extension	t	P
SCI				
2 w	8.27 ± 1.03	25.08 ± 2.40	−14.69	<0.01
4 w	8.94 ± 0.62	31.13 ± 3.71	−13.71	<0.01
12 w	8.33 ± 2.54	37.38 ± 5.54	−13.29	<0.01
Control	11.17 ± 0.71	18.14 ± 2.10	−7.93	<0.01
F	5.29	29.78	—	—
P	0.01	<0.01	—	—

correlation analysis was applied to the correlation between Young's modulus value and the type ration. $P < 0.05$ was considered to indicate a statistically significant difference.

3. Results

After removing the overweight and underweight rats, six rats were included in each subgroup.

3.1. General Assessment. The overall weight of the SCI rats in the 2 w subgroup was lower than those of the control and 12 w subgroups ($P < 0.05$). However, the difference between the weight of the SCI rats in the 2 w and 4 w subgroups was not significant. The weights of the SCI rats in the 4 w and 12 w subgroups were higher than those of the control group, but the difference was not statistically significant. The GM weight of the rats in the 2 w subgroup was the lightest. The weights of the GMs were higher in the 4 w and 12 w subgroups compared to the control group ($P < 0.05$). The BBB scores of the rats in the 2 w subgroup were the lowest. Interestingly, the BBB scores of the rats in the 2 w and 4 w subgroups were significantly lower than in the 12 w subgroup ($P < 0.05$). The MAS scores of the three subgroups were higher than that of the control group ($P < 0.05$) (Table 1).

3.2. Young's Modulus Value. All of the sonoelastography images were acquired from the right GM of rats. Measurement positions included ankle flexion (0°) and extension

(−90°). In the control group, Young's modulus value of the ankle flexion was higher than the ankle extension ($t = 1.93$, $P = 0.00$). In each SCI subgroup, Young's modulus value of the ankle flexion was higher than the ankle extension ($P < 0.05$).

Compared with the control group, Young's modulus value gradually increased with time in the area under the ankle flexion position ($F = 29.78$, $P < 0.01$) in the subgroups. Young's modulus value for the 2 w subgroup was significantly lower than that for the 4 w and 12 w subgroups, and the 4 w subgroup value was significantly lower than the 12 w subgroup. In the ankle extension position, Young's modulus value of three SCI subgroups was significantly lower than that of the control group ($P < 0.05$). However, the results of the three SCI subgroups reached statistical significance when compared with each other (Table 2).

3.3. ATPase Stain. The proportion of Type I fiber in the three SCI subgroups was significantly lower than in the control group ($F = 9.99$, $P < 0.01$). The proportion of Type IIa muscle fiber in the three SCI subgroups was significantly higher than that of the control group ($F = 5.96$, $P < 0.01$). However, the results of Type I and Type IIa fiber in the three SCI subgroups were not statistically different when compared to each other. The difference in the proportion of the Type IIb fiber from the three SCI subgroups was not statistically significant when compared to the control group ($F = 2.63$, $P = 0.08$) (Table 3).

Table 3: The proportion of each type of muscle fiber in different groups.

Group	Type I	Type IIa	Type IIb
SCI			
2 w	0.25 ± 0.12	0.42 ± 0.24	0.34 ± 0.12
4 w	0.19 ± 0.12	0.49 ± 0.19	0.33 ± 0.07
12 w	0.18 ± 0.10	0.61 ± 0.20	0.21 ± 0.13
Control	0.46 ± 0.10	0.15 ± 0.12	0.38 ± 0.09
F	9.99	5.96	2.63
P	<0.01	<0.01	0.08

Table 4: The proportion of MyHC electrophoresis results in SCI rats.

Group	MyHC-I	MyHC-IIa	MyHC-IIx	MyHC-IIb
SCI				
2 w	8.80 ± 1.45	3.68 ± 1.61	43.50 ± 3.46	44.01 ± 5.18
4 w	4.58 ± 2.26	3.38 ± 0.93	44.22 ± 3.45	47.81 ± 3.33
12 w	0.44 ± 0.25	4.25 ± 1.50	45.60 ± 2.91	49.71 ± 3.66
Control	9.91 ± 1.26	5.55 ± 0.18	39.20 ± 1.47	45.34 ± 1.95
F	50.49	3.85	5.31	2.81
P	<0.01	0.03	0.01	0.07

The rat GMs included four types of MyHC, namely, MyHC-I, MyHC-IIa, MyHC-IIb, and MyHC-IIx, according to the electrophoretic analysis (Figure 2). In the control group, the proportions of MyHC-I, MyHC-IIa, MyHC-IIb, and MyHC-IIx were $9.91 \pm 1.26\%$, $5.55 \pm 0.18\%$, $45.34 \pm 1.95\%$, and $39.20 \pm 1.47\%$, respectively. In the SCI group, the proportion of MyHC-I decreased significantly compared with the control group ($F = 50.49$, $P < 0.01$) and, in the 4 w and 12 w subgroups, was significantly lower than that observed in the 2 w subgroup ($P < 0.05$). Furthermore, the proportion of MyHC-I in the 12 w subgroup was significantly lower than that in the 4 w subgroup ($P < 0.05$). The proportions of MyHC-IIa in all three SCI subgroups were higher than the control group. However, the three SCI subgroups were statistically significantly different in the proportion of MyHC-IIa when compared to each other ($P < 0.05$). The proportions of MyHC-IIx in all of the SCI subgroups were higher than that observed in the control group; however, there was no statistically significant difference when compared with each other ($P > 0.05$). Nevertheless, the proportion of MyHC-IIb in the three SCI subgroups was not significantly different when compared with the control group ($P > 0.05$) (Table 4).

3.4. Correlation Analysis. In the control group, when the rats were in the ankle flexion state, Young's modulus value was positively correlated with body weight ($r = 0.89$, $P = 0.02$; Figure 2(a)) and negatively correlated with the proportion of MyHC-I ($r = -0.83$, $P = 0.04$; Figure 2(b)). In the 2 w subgroup, Young's modulus value was negatively correlated with the proportion of MyHC-I ($r = -0.85$, $P = 0.03$; Figure 3(a)). In the control group, when the rats were in the ankle extension state, Young's modulus value was negatively correlated with the proportion of Type I fiber ($r = -0.91$,

$P = 0.01$; Figure 2(c)). In the 4 w subgroup, Young's modulus value was found to be negatively correlated with body weight ($r = -0.92$, $P = 0.01$, Figure 3(b)).

4. Discussion

The results of the comparative analysis in this study showed that each subgroup displayed a significant decrease in body weight and GM weight, which was similar to the results from previous investigations [14, 15]. The main reason for this could be a combination of the denervation, atrophy, and paralysis of the muscle below the injury site. Furthermore, reports show that a decline in muscle mass following injury was associated with poor appetite during the acute stage, after surgery [14]. As time progressed in the present study, the general condition of the muscle in the SCI group became more stable, the SCI was gradually restored to normal conditions, and animal weight increased. In addition, the function of the lower limb movement gradually recovered with time. The peak MAS appeared in the 2 w subgroup rats. A decrease in MAS, however, was apparent in the 4 w subgroup. In the 12 w subgroup, the MAS value was lower than was observed in the 2 w and 4 w subgroups but higher when compared to the control group. The BBB score was lowest in the 2 w subgroup. This group exhibited incomplete combined movement in the hip and knee joint. Incomplete flexion and extension movement of the ankle joint appeared in rats of the 4-w subgroup. At 12 weeks after injury, the BBB score increased to approximately 7-8 scores [15]. The recovery of rats in each subgroup displayed individual differences, with the 2 w subgroup being the worst and the 12 w subgroup being the best of the SCI rats. In this respect, the results are similar to previous studies. In this study, the SCI completely debilitated the rats, which were never able to fully recover to normal conditions.

The GM of rats includes four types of muscle fibers: Type I, Type IIa, Type IIb, and Type IIx. Muscle fiber Type I, Type IIa, and Type IIb can be distinguished by ATPase staining [15]. The proportion of Type I muscle fiber significantly decreased following injury. In contrast, the proportion of Type II muscle fiber significantly increased following injury. The observed trend of change is similar to those reported in previous studies [16]. Electrophoresis showed that the proportion of MyHC-I, MyHC-IIa, and MyHC-IIx were significantly modified, similar to previous studies [17]. Among these changes, the increased Type IIa muscle fiber was the most obvious change. At 12 weeks, we observed a 60% Type IIa increase, which was significantly higher than the proportion of Type I muscle fibers (20%). The proportion of Type IIb muscle fiber showed a decreasing trend but did not reach statistical significance when compared with the control group. These changes appear to be strongly related to SCI and reduced movement. Moreover, the transition to a different type of muscle fiber has been shown to be caused by the ability of mutual transformation between different types of skeletal muscle fiber, namely, plasticity. Studies have confirmed that electrical stimulation and weightlessness can induce the transformation and its plasticity is related to the state of the muscle fibers [18]. Previous studies on SCI
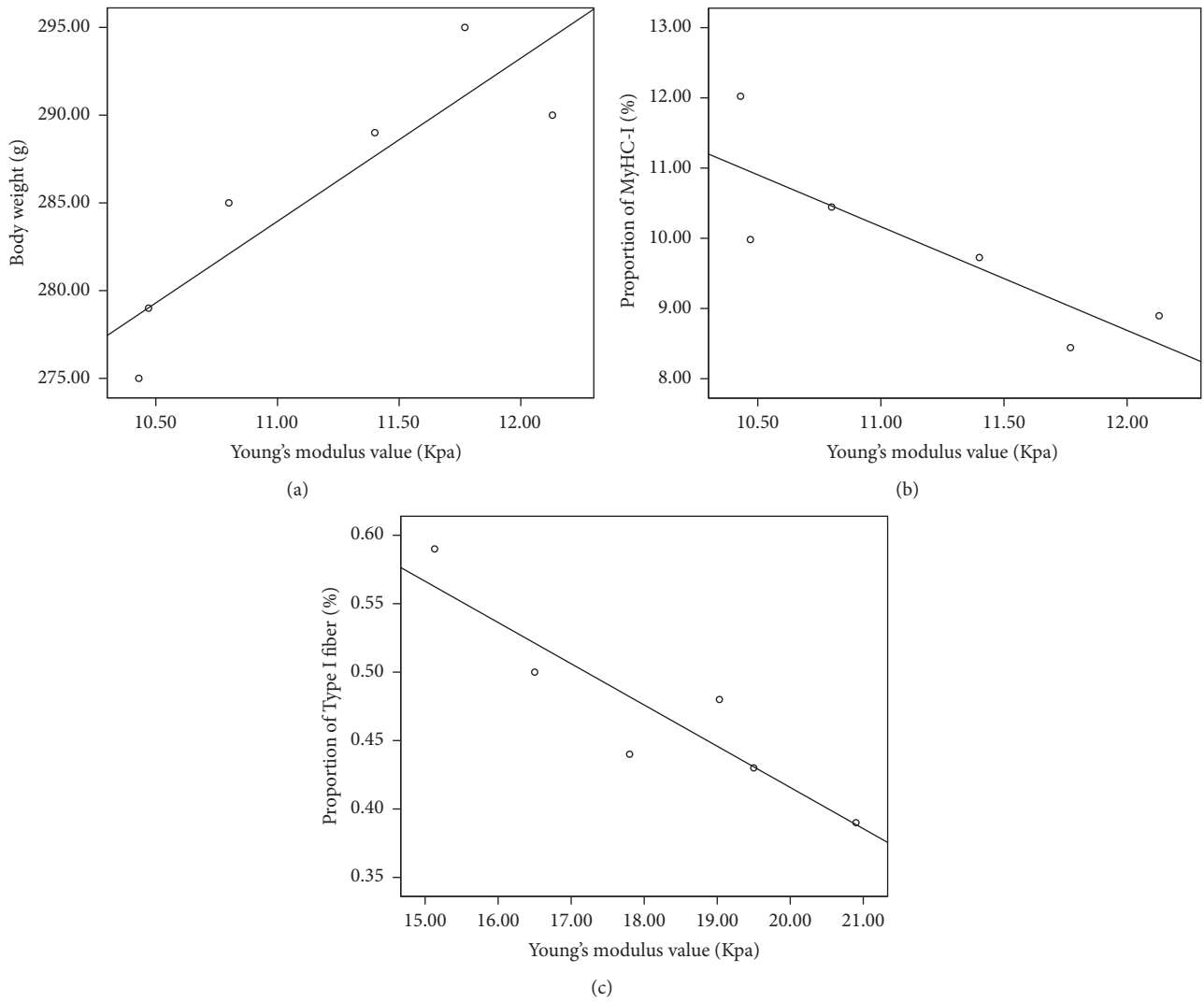
(a)

(b)

(c)

FIGURE 2: The correlation between Young's modulus value and weight (a), proportion of MyHC-I (b), and proportion of Type I muscle fiber (c) in rats model. (a), (b) Ankle flexion; (c) ankle extension.
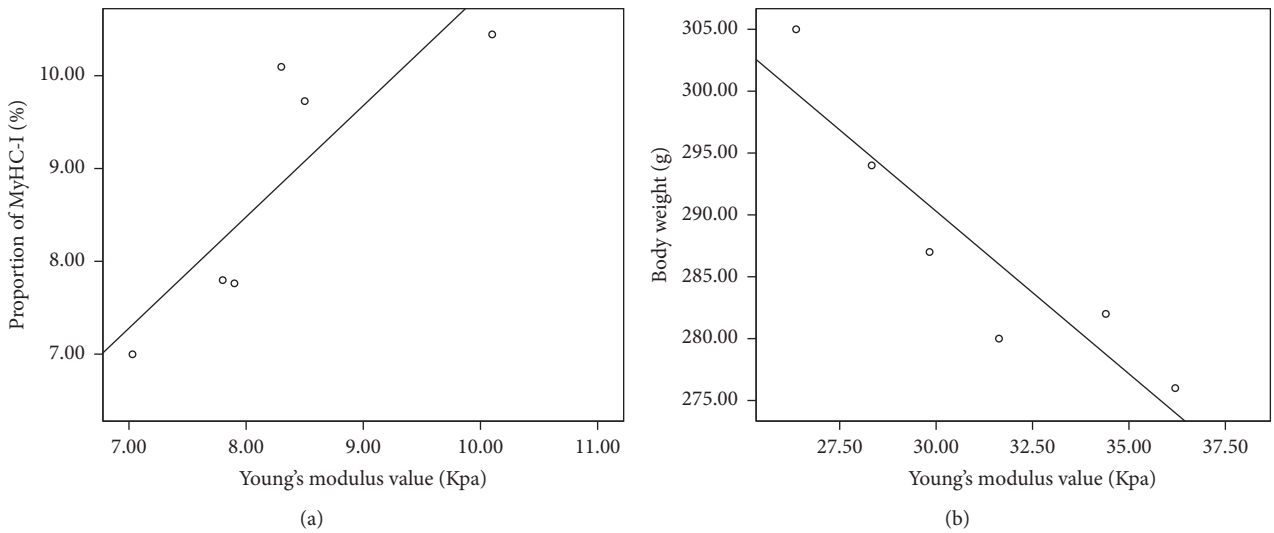

(a)

(b)

FIGURE 3: The correlation between Young's modulus value and the proportion of MyHC-I (a) and weight (b). (a) Two-week subgroup, ankle flexion. (b) Four-week subgroup, ankle extension.

rats found that Type I GM muscle fibers can transform into Type II muscle fibers [10, 19]. Nevertheless, the shift between muscle fiber types can be reversed through the correct amount of electrical stimulation. It is widely known that the physiological function of each muscle fiber is different. Type I muscle fibers produce small, extended tension. However, Type II muscle fibers produce long fibers with a short tension time. Skeletal muscle constitutes different fibers and produces different types of tension [18]. Modifications to muscle fiber types influence the physiological function and biomechanical characteristics of skeletal muscle, such as shortened relaxation time and fatigue, also influencing the normal muscle contraction function.

Clinical studies have confirmed that the elastic modulus value is greater when muscles are in contraction compared to their state in relaxation. Thus, the elastic modulus value can tell the state of the muscle [6]. At different ankle positions, the contractive condition of GM was found to also be different. For the more comprehensive evaluation of the hardness characteristics of GM spasm in SCI rats, this study included two measuring positions: ankle extension ($-90°$) and flexion ($0°$). In the ankle extension position, Young's modulus value for the GM in each subgroup of SCI rats was less than that in the control group. The minimum value appeared at the 2nd week and was improved at the 12th week. A reason for this result may be that the muscle had undergone paralysis. At the 2nd week, the muscle paralysis was at its most severe. Paralysis recovers over time; therefore, by the 12th week, GM had regained the initiative movement. In the ankle flexion position, Young's modulus value of SCI rats in each subgroup was significantly higher than that of the control rats. Previous studies showed that the hardness of spasmodic muscle is significantly higher than normal controls [6, 7]. In addition, we found that Young's modulus value in the state of ankle flexion was significantly higher than the value in the state of ankle extension for each SCI subgroup. We believed that the difference observed between the two conditions was caused by the abnormal state of joints after SCI. After lower limb paralysis, the ankle state changes from extension to flexion, and this change remains until normal movement is restored. Moreover, the GM stays in a tension-free condition when the ankle is in the extension state. In turn, the GM becomes tense when the ankle flexes. Therefore, the elastic modulus value increases, causing Young's modulus value to also increase. Additional causes of the degree of GM spasm include weight, fiber classification, and muscle structure change. Another factor to consider is the assessment of the hardness of the ankle flexion as a suitable position to measure the hardness of GM spasms, as found in the present study.

Based on the above results, we know that the pathological characteristics and elastic modulus dynamically change after SCI. Therefore, we posed the question of whether GM hardness is correlated with pathological change. The results of our correlative analysis showed that, for normal rats, Young's modulus value was positively correlated with the body weight observed in the control group and was negatively correlated with the proportion of MyHC-I in the ankle flexion state. Young's modulus value was negatively correlated with the proportion of Type I muscle fibers when the ankle was in the extension state. In this study, the normal rats with higher level weight own bigger mass GM than rats with lower weight and bigger mass GM appeared to be stiffer than smaller mass GM. As we know, Type I muscle fiber produces small, sustained tension, and Type II muscle fiber produces large, short-term tension. The different muscle fibers constituents result in different tension levels [18]. In addition, GM with higher proportion of MyHC-I showed lower tension and stiffness in either flexion or extension state. Furthermore, for the SCI rats, Young's modulus value was negatively correlated with the proportion of MyHC-I in the 2 w subgroup and was negatively correlated with body weight in the 4 w subgroup. We considered the change of the pathological features of GM in rats with SCI was complicated. Body weight, ration of muscle fibers, and proportion of MyHC all varied following the injury course. However, for the different time point subgroup, the influence of SCI was different. Young's modulus value is lowest in 2 w subgroups. Like 2 w rats model, we thought the increased proportion of MyHC-I is one of the causes that resulted in decreased Young's modulus value during ankle flexion in the study. For 4 w rats model, weight mass increased following rats condition improvement. GM showed more tension at flexion state in rats with lower weight, resulting in a higher Young's modulus value. During recovery, for 12 w subgroup, rats model got better and better condition, and proportion of MyHC and ratio of muscle fibers got normal; however, GM stiffness did not show any decrease. We will make more efforts to make the issue clear in the future.

Also, skeletal muscle includes an inner and outer membrane and perimysium. These compositions are the foundation of muscle elasticity. Previous studies found that rats with SCI have extracellular connective tissue modifications during recovery [2, 17]. Due to limited experimental methods, this study did not include quantitative measurements for changes in muscle composition. Future experiments will determine whether Young's modulus value is related to these pathological changes.

5. Conclusions

The present study used sonoelastography to evaluate GM in rats after SCI. From these studies, we found that this imaging technique can be used in the evaluation of modifications to GM hardness in rats following SCI. We observed a series of GM dynamic changes in rats at 2, 4, and 12 weeks following complete SCI. Such a decrease in muscle weight and the change of muscle fiber composition led to the conclusion that the effects of SCI are not limited to pathological changes, but also to changes in the hardness of the GM (Young's modulus value) area affected by SCI. Modifications to the hardness of the GM in SCI rats were related to pathological changes (weight, the type of MyHC, and muscle fiber type of GM) that took place during the earlier phase following SCI. Moreover, Young's modulus value observed at the later times may be related to modifications in the extracellular connective tissue.

Conflicts of Interest

The authors have no conflicts of interest regarding the publication of this manuscript.

Acknowledgments

References

[1] J.-M. Gracies, "Pathophysiology of spastic paresis. I: paresis and soft tissue changes," *Muscle & Nerve*, vol. 31, no. 5, pp. 535–551, 2005.

[2] J. R. H. Foran, S. Steinman, I. Barash, H. G. Chambers, and R. L. Lieber, "Structural and mechanical alterations in spastic skeletal muscle," *Developmental Medicine & Child Neurology*, vol. 47, no. 10, pp. 713–717, 2005.

[3] C. Trompetto, L. Marinelli, L. Mori et al., "Pathophysiology of spasticity: Implications for neurorehabilitation," *BioMed Research International*, vol. 2014, Article ID 354906, 2014.

[4] G. Sheean, "The pathophysiology of spasticity," *European Journal of Neurology*, vol. 9, supplement 1, pp. 3–9, 2002.

[5] D. Vasilescu, D. Vasilescu, S. Dudea, C. Botar-Jid, S. Sfrângeu, and D. Cosma, "Sonoelastography contribution in cerebral palsy spasticity treatment assessment, preliminary report: a systematic review of the literature apropos of seven patients.," *Medical Ultrasonography*, vol. 12, no. 4, pp. 306–310, 2010.

[6] A. Nordez and F. Hug, "Muscle shear elastic modulus measured using supersonic shear imaging is highly related to muscle activity level," *Journal of Applied Physiology*, vol. 108, no. 5, pp. 1389–1394, 2010.

[7] E. Yaşar, E. Adigüzel, S. Kesikburun et al., "Assessment of forearm muscle spasticity with sonoelastography in patients with stroke," *British Journal of Radiology*, vol. 89, no. 1068, article no. 0603, 2016.

[8] J. B. G. Ramsey, L. M. Ramer, J. A. Inskip, N. Alan, M. S. Ramer, and A. V. Krassioukov, "Care of rats with complete high-thoracic spinal cord injury," *Journal of Neurotrauma*, vol. 27, no. 9, pp. 1709–1722, 2010.

[9] F. F. Santos-Benito, C. Muñoz-Quiles, and A. Ramón-Cueto, "Long-term care of paraplegic laboratory mammals," *Journal of Neurotrauma*, vol. 23, no. 3-4, pp. 521–536, 2006.

[10] L. Jiang, X. Wei, Q. Wang et al., "Study based on sonoelastography technology for spastic gastrocnemius in rat with spinal cord injure," *Zhonghua Yi Xue Za Zhi*, vol. 96, no. 5, pp. 364–369, 2016.

[11] D. M. Basso, M. S. Beattie, and J. C. Bresnahan, "A sensitive and reliable locomotor rating scale for open field testing in rats," *Journal of Neurotrauma*, vol. 12, no. 1, pp. 1–21, 1995.

[12] L. Lacourpaille, F. Hug, K. Bouillard, J.-Y. Hogrel, and A. Nordez, "Supersonic shear imaging provides a reliable measurement of resting muscle shear elastic modulus," *Physiological Measurement*, vol. 33, no. 3, pp. N19–N28, 2012.

[13] D. Łochyński, D. Kaczmarek, M. J. Redowicz, J. Celichowski, and P. Krutki, "Long-term effects of whole-body vibration on motor unit contractile function and myosin heavy chain composition in the rat medial gastrocnemius," *Journal of Musculoskeletal and Neuronal Interactions*, vol. 13, no. 4, pp. 430–441, 2013.

[14] D. Durozard, C. Gabrielle, and G. Baverel, "Metabolism of rat skeletal muscle after spinal cord transection," *Muscle & Nerve*, vol. 23, no. 10, pp. 1561–1568, 2000.

[15] E. Landry, J. Frenette, and P. A. Guertin, "Body weight, limb size, and muscular properties of early paraplegic mice," *Journal of Neurotrauma*, vol. 21, no. 8, pp. 1008–1016, 2004.

[16] R. J. Talmadge, N. D. Garcia, R. R. Roy, and V. R. Edgerton, "Myosin heavy chain isoform mRNA and protein levels after long-term paralysis," *Biochemical and Biophysical Research Communications*, vol. 325, no. 1, pp. 296–301, 2004.

[17] Z. Daoli, X. Ping, X. Feng, and X. Shouyong, "Function of histochemical type of skeletal muscle fiber in rat and myosin heavy chain," *Acta Anatomica Sinica*, vol. 38, no. 1, pp. 93–97, 2007.

[18] M. Nordin and V. H. Frankel, "Basic biomechanics of the musculoskeletal system," *Lippincott Williams & Wilkins*, vol. 4, 2001.

[19] J. Fridén and R. L. Lieber, "Spastic muscle cells are shorter and stiffer than normal cells," *Muscle & Nerve*, vol. 27, no. 2, pp. 157–164, 2003.

Research Article
A Modified 2D Multiresolution Hybrid Algorithm for Ultrasound Strain Imaging

Jibing Wu,[1,2] Yang Jiao,[1] Zhile Han,[1] Jie Xu,[1] and Yaoyao Cui[1]

[1]*Suzhou Institute of Biomedical Engineering and Technology, Chinese Academy of Sciences, Suzhou, Jiangsu 215163, China*
[2]*University of Chinese Academy of Sciences, Beijing 100049, China*

Correspondence should be addressed to Yaoyao Cui; cuiyy@sibet.ac.cn

Ultrasound elastography is an imaging modality to evaluate elastic properties of soft tissue. Recently, 1D quasi-static elastography method has been commercialized by some companies. However, its performance is still limited on high strain level. In order to improve the precision of estimation during high compression, some algorithms have been proposed to expand the 1D window to a 2D window for avoiding the side-slipping. But they are usually more computationally expensive. In this paper, we proposed a modified 2D multiresolution hybrid method for displacement estimation, which can offer an efficient strain imaging with stable and accurate results. A FEM phantom with a stiffer circular inclusion is simulated for testing the algorithm. The elastographic contrast-to-noise rate (CNRe) is calculated for quantitatively comparing the performance of the proposed algorithm with conventional 1D elastography using phase zero estimation and the 1D elastography using downsampled (d-s) baseband signals. Results show that the proposed method is robust and performs similarly as other algorithms in low strain but is superior when high level strain is applied. Particularly, the CNRe of our algorithm is 15 times higher than original method under 4% strain level. Furthermore, the execution time of our algorithm is five times faster than other algorithms.

1. Introduction

Mechanical properties of soft tissue have been used as an important indicator of several diseases, such as breast [1, 2], liver, and prostate cancer [3, 4]. Generally, the carcinoma tissue is stiffer than the surrounding normal tissues. Palpation, as the standard procedure during physical examination, is used to touch and feel tissue below the surface of the body, while its accuracy is limited by the depth of measurement [5]. Ultrasound elastography is a relative new imaging modality for the clinical evaluation of elastic properties of soft tissue using ultrasound. It was first referred to as elastography by Ophir et al. in 1991 [6]. It became a very hot research focus of medical ultrasound in the last two decades [7, 8]. Major medical imaging device companies have launched their ultrasound products with elastography or shear wave imaging modalities [7–10]. Clinical trials have been conducted for various clinical applications with promising results.

Ultrasound elastography has been developing into an effective method in cancer diagnosis due to its capability and simple implementation [11]. The basic steps of the technique are as follows: (1) the biological tissue is compressed by contact or noncontact way; (2) backscattered radio frequency (RF) signals before and after tissue compression are collected, respectively, by ultrasonic transducer; (3) the tissue displacement estimation algorithm is applied to estimate the displacement field from the RF signals; and (4) the strain field is reconstructed from the displacement field by strain estimation algorithm.

Accurate estimation of tissue displacement is a very important step in ultrasound elastography. Different methods were proposed in the last two decades. Majority of these methods use correlation technique in time domain or the phase domain for displacement estimation [6, 12–14]. In time domain, several matching operators like correlation coefficients, the sum of squared differences (SSD), and the sum of absolute differences (SAD) are employed to finding the optimal matching in the pre- and postcompression RF signals [15, 16]. Since the computational cost of the matching operators in time domain is large, phase-based methods like phase zero

estimation, which have higher computational efficiency than time-domain methods, have been implemented in clinical ultrasound system for real-time strain imaging [13, 17]. Both 1D and 2D elastography methods can obtain displacements field, but the 1D estimation algorithms only consider axial displacements in tissue. They have difficulty in obtaining precise results in complex tissue environment, especially under high compression conditions. In general, the RF data sequence will be shifted laterally because of the lateral displacement in tissue. In order to reduce the errors due to lateral motion in 1D elastography, 2D elastography algorithms like hybrid displacement estimation method and a modified block matching method have been proposed [18, 19]. These methods consider both axial and lateral displacement; they expand the 1D window to a 2D window to avoid the side-slipping of the 1D window, which can greatly improve the precision of estimation result in high compression situation, but 2D elastography is usually more computational expensive than 1D elastography.

In this paper, we proposed a modified 2D multiresolution hybrid method for displacement estimation, which can offer an efficient strain imaging with stable and accurate results. To test the algorithm, a heterogeneous computational phantom is simulated using finite element model (FEM), with a rectangle background containing a stiffer circular inclusion. The synthetic RF data are generated from Filed II software [20]. We compare the result with three different algorithms and show a great improvement of our method in ultrasound elastography.

2. Methods

In order to make a tradeoff between speed and accuracy, we proposed a method using modified 2D multiresolution hybrid elastography. Preprocessing procedure is first applied to the raw RF data to obtain envelopes and baseline signals at different resolutions. Chen et al. proposed a hybrid displacement estimation method, which applied 3-level estimation based on cross-correlation and weighted phase separation (WPS) [18]. We suggest processing coarse estimation also on 3-level cross-correlation on sampled RF data by different sampling rate. And then a fine estimation is carried out on the whole frame RF date by phase zero-crossing method [15], which uses the results of the coarse estimation as the input to improve the resolution and accuracy.

2.1. Preprocessing. The analytic signals of predeformation and postdeformation radio frequency (RF) signals are obtained by applying Hilbert transformation to the raw RF data. The baseband signals can be calculated by demodulating the analytic signals with a carrier wave $\exp(jw_0 t)$, where w_0 denotes the modulation frequency. The modulation frequency w_0 should be chosen close to the transducer's center frequency.

The baseband signals are downsampled at different downsample rates. The downsample rates should satisfy the Nyquist sampling condition. The downsampled baseband signals are then converted into amplitude and phase data using FFT. The amplitude data at different scales are used in corresponding coarse to fine estimation, but the phase data are only used for fine estimation.
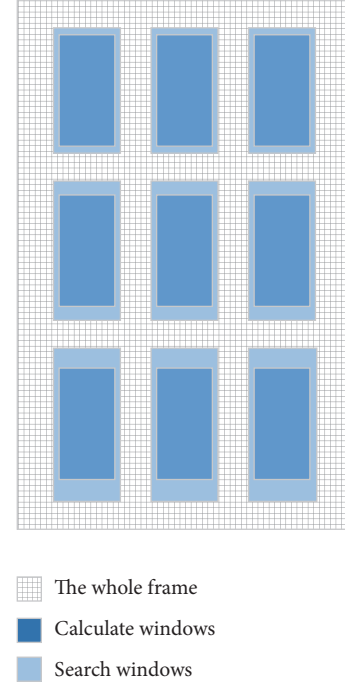

⊞ The whole frame

■ Calculate windows

■ Search windows

Figure 1: Over of the level 1 search, the calculate windows and search windows are equally distributed.

2.2. Coarse Estimation

2.2.1. Level 1 Search. Nine evenly distributed windows have been selected in the coarsest scale of the predeformation frame (see Figure 1). Displacements are calculated in these 9 windows by finding the highest correlation coefficient between predeformation and postdeformation frames in a search window [19, 21]. The correlation coefficient can be expressed as

$$R\left(d_x, d_y\right)$$
$$= \frac{\sum_{(x,y)\in T}\left[A\left(x,y\right)-\overline{A}\right]\left[B\left(x+d_x, y+d_y\right)-\overline{B}\right]}{\sqrt{\sum_{(x,y)\in T}\left[A\left(x,y\right)-\overline{A}\right]^2\sum_{(x,y)\in T}\left[B\left(x+d_x, y+d_y\right)-\overline{B}\right]^2}}, \quad (1)$$

where d_x is the lateral displacement, d_y is the axial displacement, A and B denote the envelope data from predeformation and postdeformation frame, $\overline{A}$ and $\overline{B}$ are the averages of A and B, and T is the window size. Since computational cost at this level is relatively cheap, the size of search windows can be set large enough, and in order to reduce the errors in this level, we do not use multiresolution search method mentioned by Chen in this level. In addition, the size of the search windows in the lower rows is selected bigger than in the upper row since displacement will be accumulated with respect to depth. The output of level 1 search is nine axial-lateral displacement estimations within the nine search windows.

2.2.2. Level 2 Search. Level 2 search is performed at a finer scale than level 1 search. Seven by 11 evenly distributed calculate windows are selected on the predeformation frame. The size of the calculate windows is 1/3 of the size at level 1
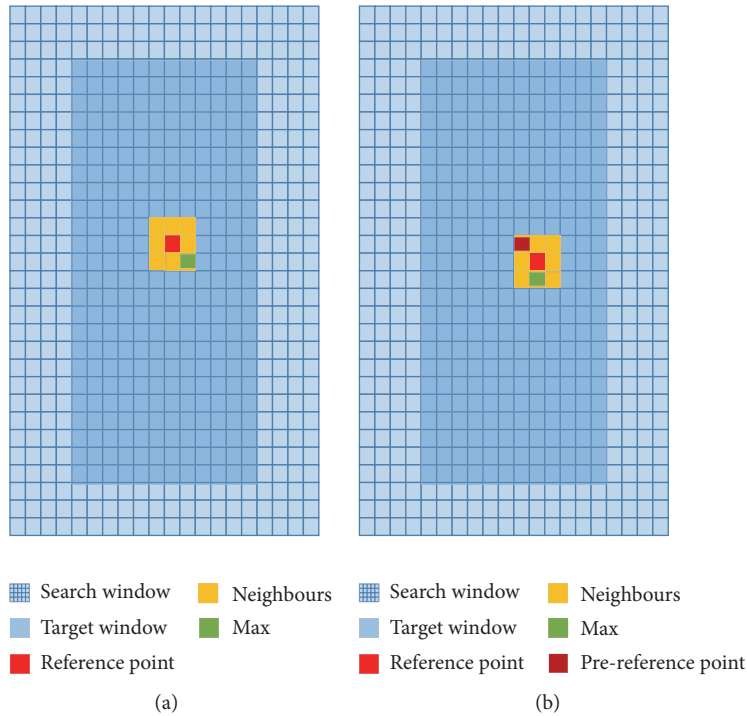
FIGURE 2: Level 2 search strategy. (a) Set the initial center point of search window to be a reference point and then find the max in its neighbours according to the correlation coefficient. (b) Propagate the reference and its neighbours and then continue to calculate the correlation coefficient.

and the size of the search windows is bigger than that at level 1, which is selected according to the deformation degree. The initial axial and lateral displacement estimates of level 2 are inherited from the output of level 1 and bilinear interpolated to the finer scale. The search windows located at the point according to the output and the center of calculate windows.

The so-called "following tracking" strategy (see Figure 2) is used to decide the search direction at each window [22]. First, set the initial center point of search window to be a reference point, and then set the reference point's immediate neighbours to be the search points; after that we need to calculate the correlation coefficient of calculate windows and search windows at each search point. The point which has the highest correlation coefficient will be the next reference point; the search points then propagate to the current reference point's neighbours, and so on. When the reference point occurs at a fixed position or out the range of search window, the calculation in this window is completed, and the axial and lateral displacement estimation is according to the position of the final reference point. Chen et al. used a multiresolution search method in this level; we removed it and increased the numbers of the reference point's neighbours to obtain a more accurate result. We suggested that the increment of computational complexity in this level is meaningful.

However, this time the searches are not independent; there is another delivering strategy that is used to deliver displacement estimations from one window to the next window which on the same column. The next window's initial reference point is no longer the center point of search window, but the position according to the output of the current window.

The advantage of the searching strategy above is that we can find the point which matches the highest correlation coefficient quickly with lower computational complexity. Moreover, the strategy has a good error-correction mechanism to ensure displacement continuity in both axial and lateral direction.

2.2.3. Level 3 Search. The calculate windows and search windows are the smallest in coarse search and this process should finish the whole frame search. The size of calculate windows should be 1/2 of the size at level 2, and level 3 search stops when the calculate windows cover the whole frame. Similar as in level 2, we also need to interpolate the displacement results in level 2 to level 3 with finer scale. And we use the same search strategy to obtain the axial and lateral displacement in level 3 [22]. Since we do not need further refinement of the lateral displacement, and in order to avoid shifting the signals laterally too much, we extract the significant part of the lateral displacement and only shift the RF signal within that region. The lateral displacement should be smoothed and be considered as the final lateral displacement. There are many kinds of the smooth method; we suggest using the Savitzky-Golay filtering method.

2.3. Fine Estimation

2.3.1. Displacement Estimation. The initial axial and lateral displacement estimation over the whole RF data can be

bilinear interpolated from the coarse estimation from level 3 search. A modified phase zero algorithm is proposed for the fine displacement estimation [13].

Let us denote x_1 and x_2 to be the 1D windowed RF signals before and after compression of the tissue. In elastography, the postdeformation RF data is considered to be a compressed and time-shifted vision of the predeformation signals, and the signal compression can be neglected. Thus, x_2 can be expressed as

$$x_2(t) = x_1(t + \tau). \tag{2}$$

In general, the correlation between two signals can be calculated from the cross-correlation function as follows:

$$\langle a, b \rangle \langle t \rangle = \int_{-\infty}^{\infty} a^*(t') b(t' + t) dt'. \tag{3}$$

Consequently, the signal's autocorrelation function can be a time-shifted modification of the cross-correlation function

$$\langle x_1, x_2 \rangle \langle t \rangle = \int_{-\infty}^{\infty} x_1^*(t') x_2(t' + t) dt'$$

$$= \int_{-\infty}^{\infty} x_1^*(t') x_1(t' + t + \tau) dt',$$

$$\int_{-\infty}^{\infty} x_1^*(t') x_1(t' + t + \tau) dt' \tag{4}$$

$$= \int_{-\infty}^{\infty} x_1^*(t') x_1(t' + t + \tau) dt'$$

$$= \langle x_1, x_1 \rangle \langle t + \tau \rangle,$$

$$\langle x_1, x_2 \rangle \langle t \rangle = \langle x_1, x_1 \rangle \langle t + \tau \rangle.$$

Since the maximum of the autocorrelation equals the maximum of the cross-correlation, the conventional cross-correlation determines this maximum to estimate the time shift. When we return the baseband signals to analytic signals, the phase $\varphi(t)$ of the correlation function of the analytic signals $x_{1+}(t)$ and $x_{2+}(t)$ has an identical root

$$\varphi(-\tau) = 0,$$

$$\varphi(t) = \arg(\langle x_{1+}, x_{2+} \rangle(t)),$$

$$x_{1+}(t) = \exp(j\omega_0 t) x_1(t), \tag{5}$$

$$x_{2+}(t) = \exp(j\omega_0 t) x_2(t).$$

Using the Newton iteration, we can figure out the root of $\varphi(t)$ to find the time shift estimation

$$\tau_{0,0} = 0,$$

$$\tau_{k,0} = \tau_{k-1,N}$$

$$\tau_{k,l} = \tau_{k,l-1} - \frac{\varphi(t_n)}{\varphi'(t_n)} \approx \tau_{k,l-1} - \frac{\varphi(t_n)}{\omega_0} \tag{6}$$

$$= \tau_{k,l-1} - \frac{\arg(\langle x_{1+}, x_{2+} \rangle(\tau_{k,l-1}))}{\omega_0}.$$

Then replace it by a sum of oversampled signals

$$\tau_{k,l} = \tau_{k,l-1} - \frac{1}{w_0} \arg \Bigg(\exp(j\omega_0 \tau_{k,l-1})$$

$$\cdot \sum_{\tau_{k,l-1}-T/2}^{\tau_{k,l-1}+T/2} x_1^*(t) x_2(t - \tau_{k,l-1}) \Bigg), \tag{7}$$

where $\tau_{k,l}$ denotes the displacement estimation in the kth window after iterating for l times and T denotes the calculation window size.

In original phase zero-crossing estimation, the displacement estimation of the previous window will be used as the initial value for the next window [13]. The error of one window will propagate to the remaining windows along the RF line. This can cause large accumulated errors in the whole frame. On the other hand, this algorithm is based on the assumption that the lateral displacement in the tissue is negligible. However, tissue will be deformed in both the axial and the lateral directions when freehand compression is applied [21]. Lateral displacement should be considered when estimating the whole displacement field.

We propose a modified algorithm to solve the problems described above. We get the coarse estimation including axial and lateral displacement in the previous coarse calculation, so the iteration between the neighbouring windows can be simplified comparing with 1D elastography method. And the lateral deviation will be applied to the computational process. The calculation is independent of each window, so it makes it easier to take this algorithm to be executed based upon CUDA (Compute Unified Device Architecture)

$$\tau_{0,0} = 0,$$

$$\tau_{k,0} = \tau'_{k,\text{coarse}},$$

$$\tau_{k,l} = \tau_{k,l-1} - \frac{1}{w_0} \arg \Bigg(\exp(j\omega_0 \tau_{k,l-1}) \tag{8}$$

$$\cdot \sum_{\tau_{k,l-1}-T/2}^{\tau_{k,l-1}+T/2} x_1^*(t) x_{2,\text{shift}}(t - \tau_{k,l-1}) \Bigg).$$

The initial value of each window is replaced by the coarse axial displacement $\tau'_{k,\text{coarse}}$ on current window. And take the lateral shift on $x_2(t)$ to be $x_{2,\text{shift}}(t)$.

2.3.2. Strain Estimation. Strain is defined as the gradient of the displacement. Here we only calculate the axial strain and the least-squares strain estimator (LSQSE) is used, which employs a piecewise linear curve fitting [23]. After the axial displacement field is obtained, the strain map may be modeled as

$$u(i) = az(i) + b, \tag{9}$$

where u denotes the axial displacement and z is the tissue depth. The constants a and b are the coefficients to be
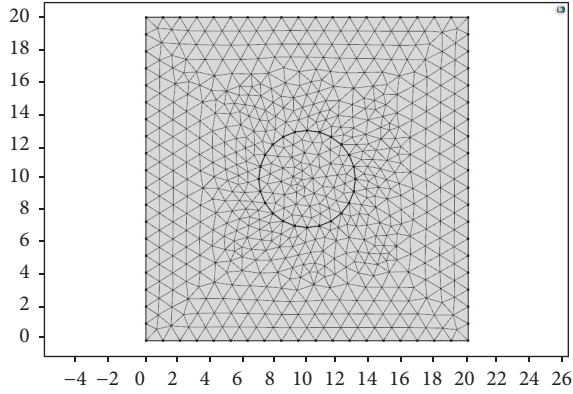
FIGURE 3: Heterogeneous finite element model simulates the stiffer circular inclusion.

FIGURE 4: Strain map simulated by COMSOL as the ground truth.

estimated, and a represents the local strain. Transform the z to matrix form

$$
\underline{u} = A \begin{bmatrix} a \\ b \end{bmatrix} = \begin{bmatrix} z(1) & 1 \\ z(2) & 1 \\ \cdots & 1 \\ \cdots & 1 \\ z(N) & 1 \end{bmatrix} \bullet \begin{bmatrix} a \\ b \end{bmatrix}. \tag{10}
$$

The least square solution is given by

$$
\begin{bmatrix} \widehat{a} \\ \widehat{b} \end{bmatrix} = A^T \left[AA^T \right]^{-1} \widehat{u}, \tag{11}
$$

where $\widehat{a}$ and $\widehat{b}$ denote the estimation of a and b, respectively.

2.4. Simulation. A FEM (finite element model) phantom is simulated using Commercial FEM software COMSOL Multiphysics 5.0 (COMSOL USA). FIELD II software is used for ultrasound simulations. The size of rectangle background of the 2D model is 20 mm × 20 mm, with a stiffer circular inclusion in the center. The radius of the inclusion is 3 mm. Triangular mesh was generated and refined automatically by COMSOL (see Figure 3). Smooth displacement and strain field can be obtained for further RF signal simulation. The inclusion and its background have same density of 1000 kg/m3 and Poisson's ratio of 0.495. Young's modulus of the inclusion is 100 kPa, which is multiple times stiffer than the background. In this study, we set strain contrast between lesion and background to be 5, so that there will be a clear boundary and CNRe can be easily used for performance comparison. The phantom is compressed by uniaxial compression with axial displacement set to 0.3 mm–0.8 mm (i.e., the axial strain is 1.5%–4.0%). The bottom of the phantom is fixed.

A 192-element linear array transducer (64 active elements) with a center frequency of 7.5 Mhz is simulated. The transducer has a pitch of 0.255 mm and an element height of 5 mm. The element width is equal to the wavelength. The number of scan-lines is 128 and the distance between adjacent lines is equal to the pitch. 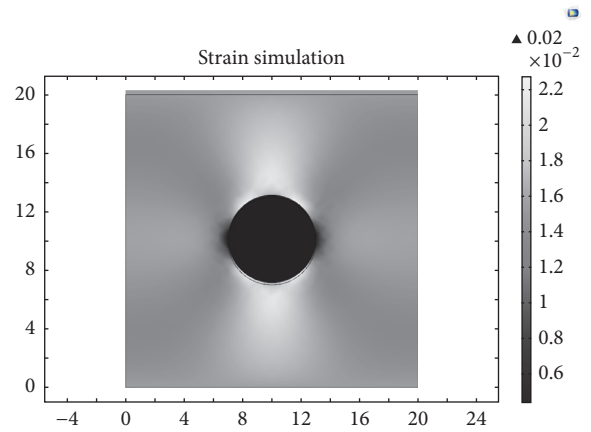The transmitting focus is at 30 mm and dynamic focusing with focal zones step by 1 mm is used for receiving focus. The image zone has a width of 20 mm and a depth of 20 mm. The speed of sound is assumed to be 1540 m/s and the sampling frequency of the RF signals is 120 Mhz. The original scatters are randomly distributed in the image zone with random scattering amplitude. The predeformation RF signals are simulated with FIELD II using the parameters described above [20, 24]. The new scatters positions after compression are calculated according to COMSOL simulation. The postdeformation RF signals are then simulated with FIELD II using the new scatterer distribution.

3. Results and Discussion

Ultrasound RF data was generated using computer simulation. With the synthetic RF data, the displacement and strain distribution were calculated using the modified 2D multiresolution hybrid elastography. Comparison was made between the proposed method, the original 1D elastography and the 1D elastography using downsampled (d-s) baseband signals. Since the modified method has a downsampled step, we make a downsampled version of 1D elastography to compare with the proposed method. To achieve that, we use the same processes as the 1D elastography method to get envelop signals, and the envelop signals will be then downsampled and further 1D elastography calculations will be performed on the downsampled envelop signals.

Figure 4 shows the theoretical strain maps using finite element analysis in COMSOL as the ground truth. Figure 5 presents the estimated strains obtained by three algorithms for the computational phantom under different applied strain. The direct viewing of the result shows that 1D elastography is slightly better under low strain level; the reason is that the 1D method build on the whole RF data and the iterative calculation is more complete and precise under low strain level. The performance of the algorithm we proposed is similar to 1D algorithm when low strain is applied but much better under higher strain level. As we can see in the first two columns, some error appeared in the center of the
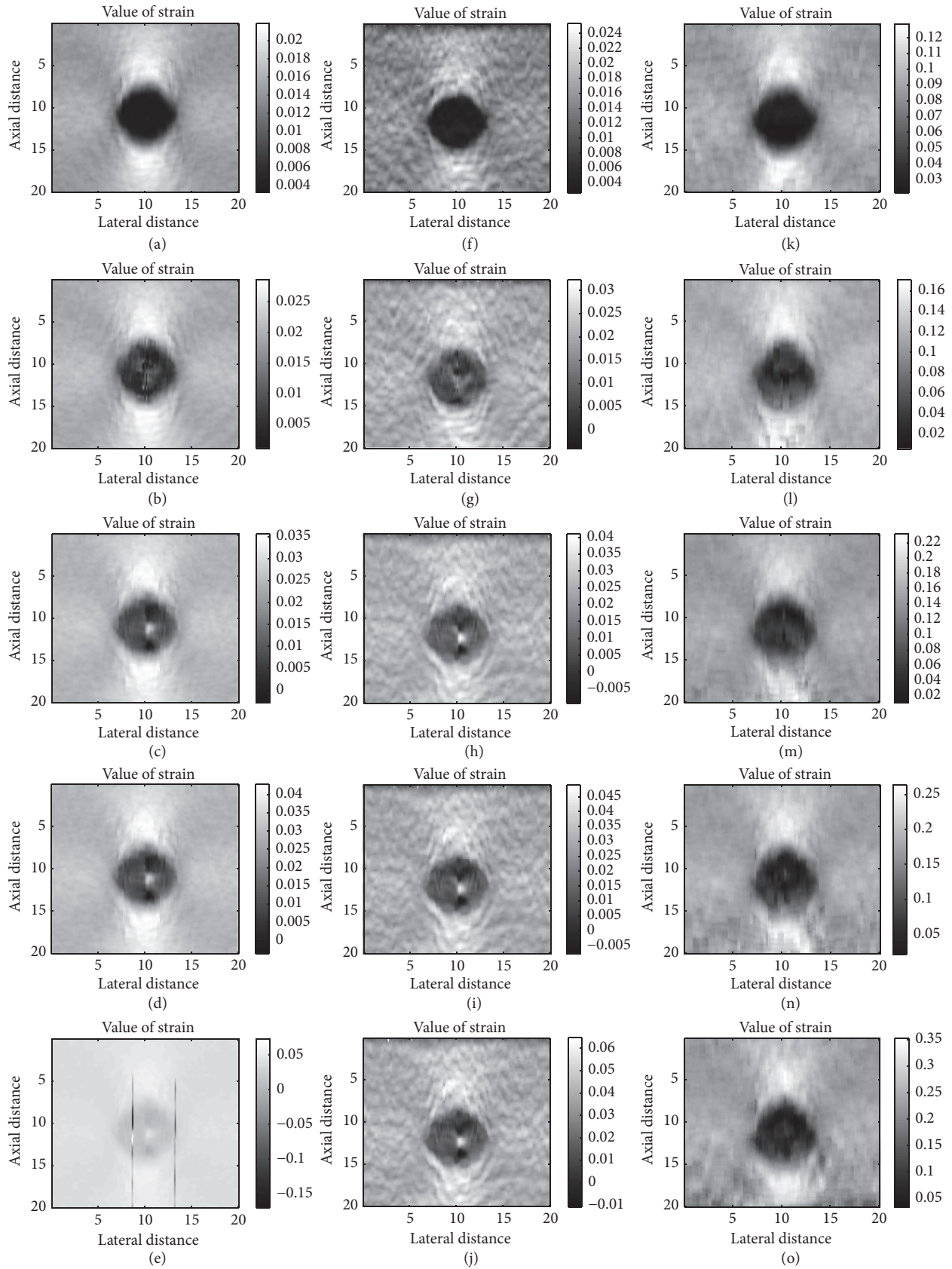
FIGURE 5: Strain maps of three different algorithms. Different strain levels as 1.5%, 2.0%, 3.0%, 3.5%, and 4.0% are applied at each row. The first column ((a)–(e)), the second column ((f)–(j)), and the third column ((k)–(o)) show, respectively, the strain map obtained by original 1D elastography and original 1D elastography with downsampled and modified 2D multiresolution hybrid elastography.
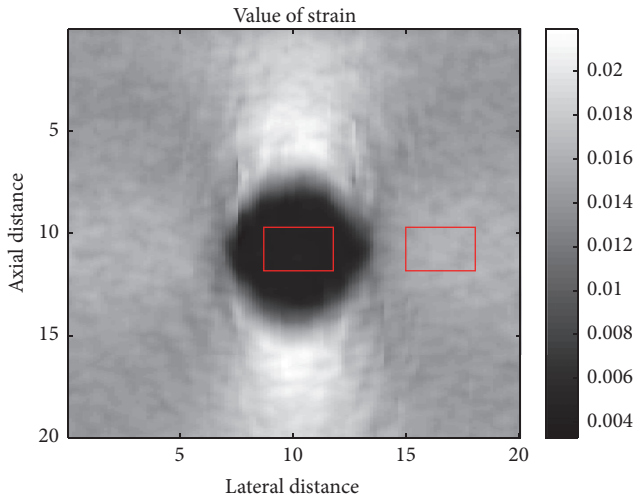
FIGURE 6: The extra area of inclusion and background for the calculation of CNRe and the average estimated strain rate.

result when strain level increased, and there are two error lines in 1D elastography (Figure 5(e)) because of the lacking consideration of lateral displacement and iterative calculation between two windows.

To quantify the performance of different algorithms, CNRe is calculated at each strain level and we use the binary strain image to measure the accuracy of each algorithm [25]. The definition of the CNRe is provided in the following:

$$\text{CNR}_e = \frac{2(s_1 - s_2)^2}{\sigma_{s_1}^2 + \sigma_{s_2}^2}, \tag{12}$$

where s_1 and $\sigma_{s_1}^2$ denote the mean and the variance of strain estimation in the inclusion and s_2 and $\sigma_{s_2}^2$ are the mean and the variance of strain estimation in the background (see Figure 6). The larger the CNRe value, the better the clarity of the results.

We have made a record of the average estimated strain rate for both inclusion and background for comparison purpose. The ratio of s_1 and s_2 previously mentioned is shown directly in Figure 7. We can see that the three different algorithms have shown similar average strain ratio between lesion and background in different strain level.

We make a complete test with three algorithms under different strain level range 0.2% to 4%. Same as 1D algorithms, the CNRe of our algorithms is too low to distinguish between the lesion and background when strain level is lower than 0.8%, which means the noise on strain estimation will blur the boundary between lesion and background. And the CNRe of the modified 2D multiresolution hybrid elastography algorithm is much higher than the other two algorithms at high strain level (see Figure 8). We can see that the original 1D elastography has a slight better result in low strain level; the reason is that the 1D method build on the whole RF data and the iterative calculation is more complete and precise under low strain level. The performance of the algorithm we proposed is similar to 1D algorithm when low strain is applied but better under higher strain level.
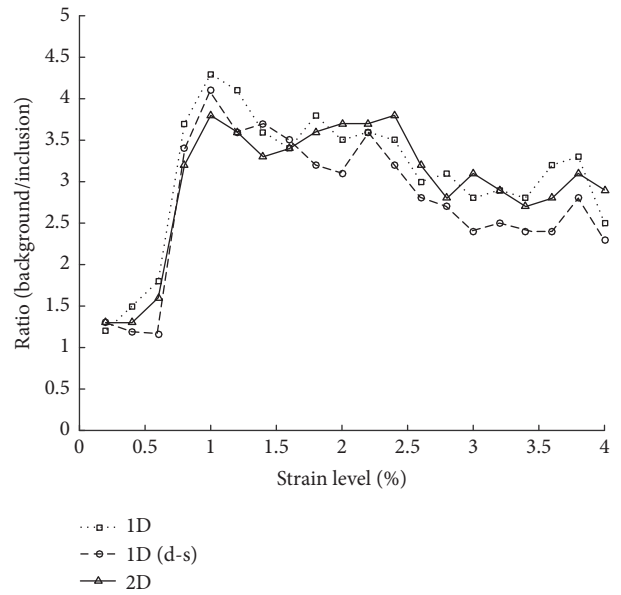

FIGURE 7: The ratio of average estimated strain rates of the inclusion and the background.
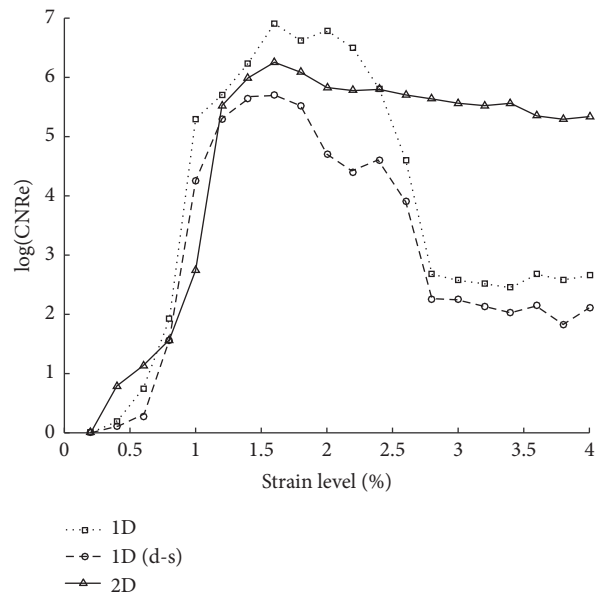

FIGURE 8: The CNRe results of three different algorithms.

The strain binary images (see Figure 9) are obtained by thresholding the strain map. We set the threshold at the same level and plot the binary images, respectively. It is an immediate way to see the accuracy of each strain image. We set the average estimated strain rate for whole phantom as the threshold of the binary images. Additionally, the inclusion area ratios are calculated and compared with the ground truth of FEA result. Then we calculate the inclusion area ratio as the numbers of black pixels and all pixels in the image. The standard denotes the inclusion area ratio in FEA model and results of calculated strain ratio from three methods
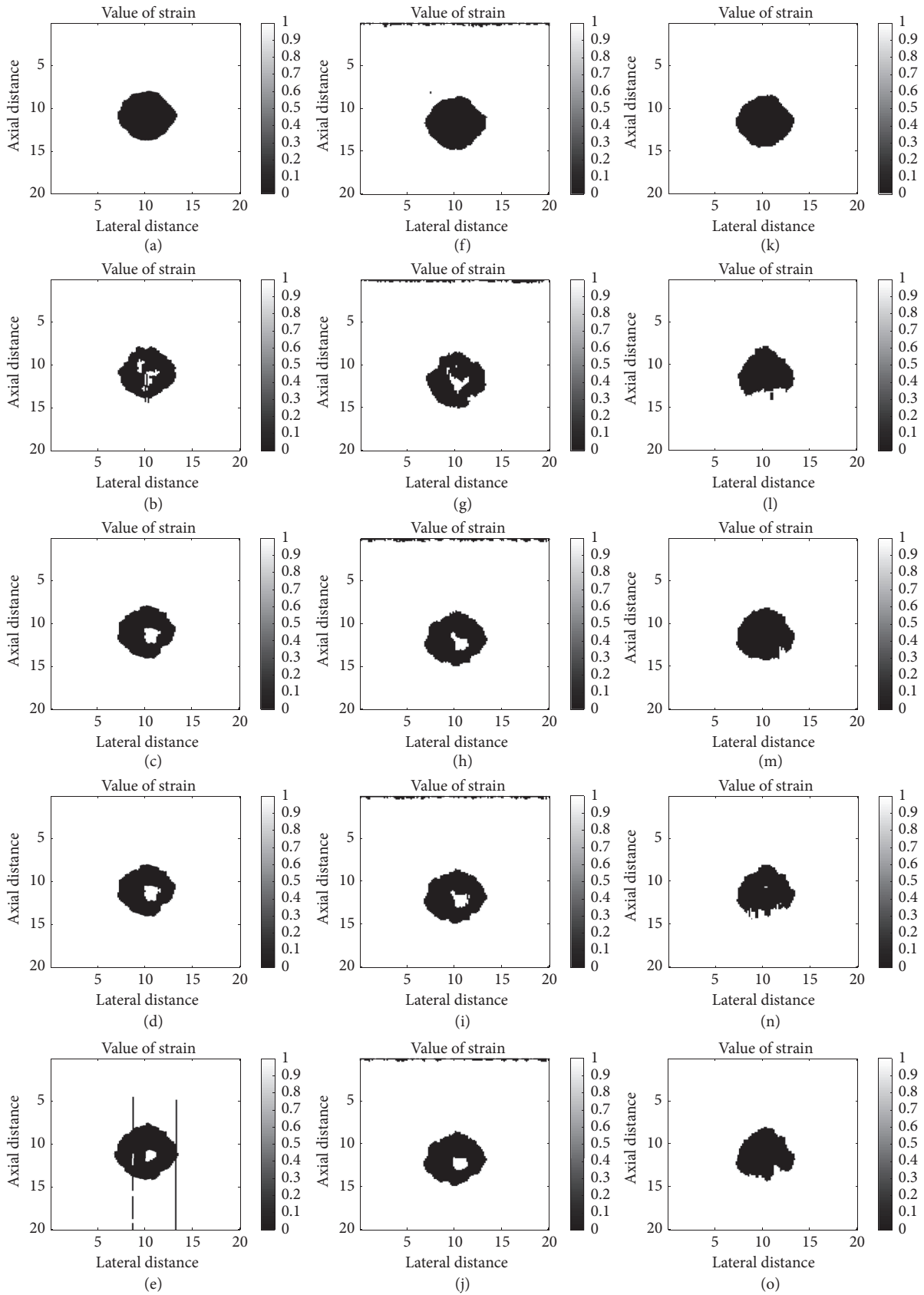
FIGURE 9: Strain binary images of three different algorithms. Different strain levels as 1.5%, 2.0%, 3.0%, 3.5%, and 4.0% are applied at each column. The first column ((a)–(e)), the second column ((f)–(j)), and the third column ((k)–(o)) show, respectively, the strain binary map obtained by the corresponding strain map using 1D elastography, downsampled 1D elastography, and the proposed 2D elastography method.
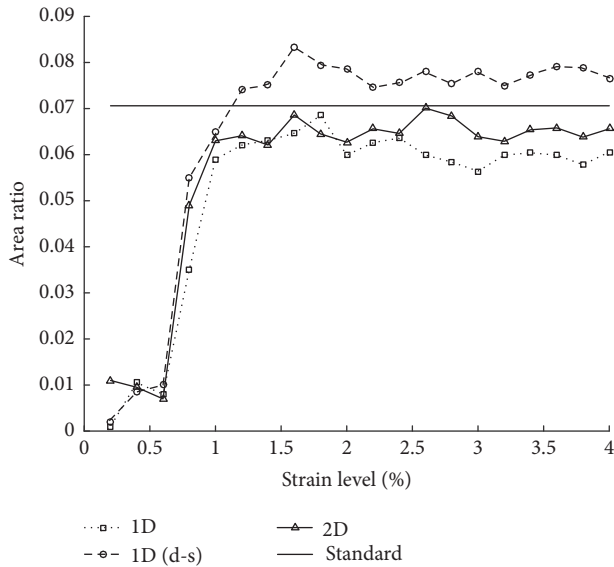
FIGURE 10: The inclusion area ratios results of three different algorithms, where the standard denotes the inclusion area ratio in FEA model.

TABLE 1: Execution times of three different algorithms.

Method	1D	1D with downsampled	Modified 2D
Times (s)	10.2	2.3	1.8

are shown in Figure 10. The inclusion area ratio of the new method is closer to the standard than other methods.

In the algorithm we proposed, the lateral resolution depends on the amount of the windows in level 3 search. The lateral resolution increased with the increasing of the amount until the resolution is equal to the sampling frequency of the RF data. The axial resolution is determined by the physical size of transducer such as the kerf of the array element. The purpose of the consideration of lateral displacement in our algorithm is not to improve the later resolution but to compensate for the interference of lateral offset and get higher accuracy in axial strain image.

All the algorithms were executed with an Intel(R) Core(TM) i7-4790K CPU @2.40 GHz 8.00 GB RAM, and MATLAB 2014b was used for implementing and testing them on Windows operation system. The execution times of the different methods are shown in Table 1. The modified 2D multiresolution hybrid elastography algorithm has a shorter time than the other algorithms.

4. Conclusion

A modified 2D multiresolution hybrid method has been proposed in this paper. Using finite element model phantom under different strain levels, we have shown that the new algorithm can achieve better CNRe comparing with different methods including original 1D elastography method and original 1D elastography method with downsampled (d-s). These results demonstrate that the method we suggested is robust and accurate when high level strain is applied. The result of execution time has shown that the new framework has a higher efficiency that it may well be more suitable for real-time application in clinical practice. The limitation of our algorithm is that, to a great extent, the accuracy of the final result is determined by the output of coarse estimation. The strain image calculated by our algorithm is slightly worse than original 1D elastography under low strain level. In this study, we use simulated data to compare the performance of the proposed method with other methods in different strain level, since ground truth of strain map can be easily obtained. In our next study, we will test our method using phantom and in vivo data.

Conflicts of Interest

The authors declare that there are no conflicts of interest regarding the publication of this paper.

Acknowledgments

References

[1] B. S. Garra, E. I. Cespedes, J. Ophir et al., "Elastography of breast lesions: initial clinical results," *Radiology*, vol. 202, no. 1, pp. 79–86, 1997.

[2] A. Itoh, "Review of the techniques and diagnostic criteria of breast ultrasound elastography," *Medix Hitachi Supplement*, vol. 8, 2007.

[3] M. Friedrich-Rust, M. F. Ong, E. Herrmann et al., "Real-time elastography for noninvasive assessment of liver fibrosis in chronic viral hepatitis," *American Journal of Roentgenology*, vol. 188, no. 3, pp. 758–764, 2007.

[4] K. König, U. Scheipers, A. Pesavento, A. Lorenz, H. Ermert, and T. Senge, "Initial experiences with real-time elastography guided biopsies of the prostate," *The Journal of Urology*, vol. 174, no. 1, pp. 115–117, 2005.

[5] J.-L. Gennisson, T. Deffieux, M. Fink, and M. Tanter, "Ultrasound elastography: Principles and techniques," *Diagnostic and Interventional Imaging*, vol. 94, no. 5, pp. 487–495, 2013.

[6] J. Ophir, I. Céspedes, H. Ponnekanti, Y. Yazdi, and X. Li, "Elastography: a quantitative method for imaging the elasticity of biological tissues," *Ultrasonic Imaging*, vol. 13, no. 2, pp. 111–134, 1991.

[7] J. Ophir, S. Srinivasan, R. Righetti, and A. Thittai, "Elastography: A decade of progress (2000-2010)," *Current Medical Imaging Reviews*, vol. 7, no. 4, pp. 292–312, 2011.

[8] K. J. Parker, M. M. Doyley, and D. J. Rubens, "Imaging the elastic properties of tissue: the 20 year perspective." *Physics in Medicine and Biology*, vol. 56, no. 1, p. -R29, 2011.

[9] J. Ophir, S. K. Alam, B. S. Garra et al., "Elastography: Imaging the elastic properties of soft tissues with ultrasound," *Journal of Medical Ultrasonics*, vol. 29, no. WINTER, pp. 155–171, 2002.

[10] A. P. Sarvazyan, O. V. Rudenko, S. D. Swanson, J. B. Fowlkes, and S. Y. Emelianov, "Shear wave elasticity imaging: a new ultrasonic technology of medical diagnostics," *Ultrasound in Medicine & Biology*, vol. 24, no. 9, pp. 1419–1435, 1998.

[11] M. M. Doyley, "Model-based elastography: a survey of approaches to the inverse elasticity problem," *Physics in Medicine and Biology*, vol. 57, no. 3, pp. R35–R73, 2012.

[12] R. Zahiri-Azar and S. E. Salcudean, "Motion estimation in ultrasound images using time domain cross correlation with prior estimates," *IEEE Transactions on Biomedical Engineering*, vol. 53, no. 10, pp. 1990–2000, 2006.

[13] A. Pesavento, "A time-efficient and accurate strain estimation concept for ultrasonic elastography using iterative phase zero estimation," *IEEE Transactions on Ultrasonics, Ferroelectrics and Frequency Control*, vol. 46, no. 5, pp. 1057–1067, 1999.

[14] M. O'Donnell, A. Skovorada, and B. Shapo, "Measurement of arterial wall motion using Fourier based speckle tracking algorithms," in *Proceedings of the IEEE 1991 Ultrasonics Symposium*, pp. 1101–1104, Orlando, Fla, USA.

[15] F. Viola and W. F. Walker, "A comparison of the performance of time-delay estimators in medical ultrasound," *IEEE Transactions on Ultrasonics, Ferroelectrics and Frequency Control*, vol. 50, no. 4, pp. 392–401, 2003.

[16] S. Langeland, J. D'Hooge, H. Torp, B. Bijnens, and P. Suetens, "Comparison of time-domain displacement estimators for two-dimensional RF tracking," *Ultrasound in Medicine & Biology*, vol. 29, no. 8, pp. 1177–1186, 2003.

[17] J. E. Lindop, G. M. Treece, A. H. Gee, and R. W. Prager, "Phase-based ultrasonic deformation estimation," *IEEE Transactions on Ultrasonics, Ferroelectrics and Frequency Control*, vol. 55, no. 1, pp. 94–111, 2008.

[18] L. Chen, R. J. Housden, G. M. Treece, A. H. Gee, and R. W. Prager, "A hybrid displacement estimation method for ultrasonic elasticity imaging," *IEEE Transactions on Ultrasonics, Ferroelectrics and Frequency Control*, vol. 57, no. 4, pp. 866–882, 2010.

[19] Y. Zhu and T. J. Hall, "A modified block matching method for real-time freehand strain imaging," *Ultrasonic Imaging*, vol. 24, no. 3, pp. 161–176, 2002.

[20] A. Jensen J and Field., "A program for simulating ultrasound systems," in *Proceedings of the 10th Nordicbaltic Conference on Biomedical Imaging*, vol. 4, Supplement 1, pp. 351–353, 1996.

[21] H. Shi and T. Varghese, "Two-dimensional multi-level strain estimation for discontinuous tissue," *Physics in Medicine and Biology*, vol. 52, no. 2, article no. 006, pp. 389–401, 2007.

[22] L. Chen, G. M. Treece, J. E. Lindop, A. H. Gee, and R. W. Prager, "A quality-guided displacement tracking algorithm for ultrasonic elasticity imaging," *Medical Image Analysis*, vol. 13, no. 2, pp. 286–296, 2009.

[23] F. Kallel and J. Ophir, "A least-squares strain estimator for elastography," *Ultrasonic Imaging*, vol. 19, no. 3, pp. 195–208, 1997.

[24] J. A. Jensen and P. Munk, "Computer phantoms for simulating ultrasound B-Mode and CFM Images," in *Acoustical Imaging*, vol. 23, pp. 75–80, 1997.

[25] T. Varghese and J. Ophir, "An analysis of elastographic contrast-to-noise ratio," *Ultrasound in Medicine & Biology*, vol. 24, no. 6, pp. 915–924, 1998.

Research Article

Differentiation of the Follicular Neoplasm on the Gray-Scale US by Image Selection Subsampling along with the Marginal Outline Using Convolutional Neural Network

Jeong-Kweon Seo,[1] Young Jae Kim,[1] Kwang Gi Kim,[1] Ilah Shin,[2] Jung Hee Shin,[3] and Jin Young Kwak[2]

[1]*Department of Biomedical Engineering, College of Medicine, Gachon University, Gyeonggi-do, Republic of Korea*
[2]*Department of Radiology, Severance Hospital, Research Institute of Radiological Science, Yonsei University, College of Medicine, Seoul, Republic of Korea*
[3]*Department of Radiology and Center for Imaging Science, Samsung Medical Center, Sungkyunkwan University School of Medicine, Seoul, Republic of Korea*

Correspondence should be addressed to Kwang Gi Kim; kimkg@gachon.ac.kr and Jin Young Kwak; docjin@yuhs.ac

We conducted differentiations between thyroid follicular adenoma and carcinoma for 8-bit bitmap ultrasonography (US) images utilizing a deep-learning approach. For the data sets, we gathered small-boxed selected images adjacent to the marginal outline of nodules and applied a convolutional neural network (CNN) to have differentiation, based on a statistical aggregation, that is, a decision by majority. From the implementation of the method, introducing a newly devised, scalable, parameterized normalization treatment, we observed meaningful aspects in various experiments, collecting evidence regarding the existence of features retained on the margin of thyroid nodules, such as 89.51% of the overall differentiation accuracy for the test data, with 93.19% of accuracy for benign adenoma and 71.05% for carcinoma, from 230 benign adenoma and 77 carcinoma US images, where we used only 39 benign adenomas and 39 carcinomas to train the CNN model, and, with these extremely small training data sets and their model, we tested 191 benign adenomas and 38 carcinomas. We present numerical results including area under receiver operating characteristic (AUROC).

1. Introduction

Thyroid cancer has been one of the most diagnosed forms of cancers worldwide over the past few decades [1]. Follicular thyroid cancer is the second most common thyroid cancer after papillary thyroid cancer, comprising 10–20% of thyroid cancer. It is noted that follicular thyroid cancer has a higher incidence of distant metastasis and thus has prognosis worse than the more common papillary thyroid carcinoma [2–4]. Therefore, it is important to preoperatively notice this entity for prompt management.

Follicular neoplasm of the thyroid gland comprises follicular adenoma and carcinoma. It is challenging to preoperatively differentiate these two entities, and much clinical effort has been made up to this point. Overlapping clinical presentations, ultrasound (US) features, and molecular biology resulted in a limited value of diagnostic power through preoperative evaluation with US, fine-needle aspiration cytology, and immunohistochemistry [5–8]. Therefore, a differential diagnosis of these two entities is currently obtained by identifying capsular or vascular invasion at the periphery of the lesion among pathologic examination following diagnostic thyroidectomy [9].

In CAD (computer-aided diagnosis), many scientists and researchers have developed methods to detect thyroid nodules or automated diagnosis assistance systems, mainly to differentiate between benignancy and malignancy of thyroid nodules and break through those difficulties in definitive diagnoses of nodule lesions and assist radiologists with developing a plan of action [10–12].

Recently, the rapidly progressing industries in artificial intelligence technologies reached numerous markets and

countries in various fields of our life, even in the area of medical sciences [13–16]. In this article, we develop and demonstrate newly conducted techniques and observe some meaningful aspects seen in various experiments, such as scaling a parameterized normalization to draw reasonable evidence of the existence of features retained on the margin of thyroid follicular neoplasms, which could be helpful in identifying capsular or vascular invasion occurring at the margin of the lesion, or inspirational to the invention of an efficient numerical method to differentiate malignant from benign follicular neoplasms on US images, in view of a CNN (convolutional neural network) [17].

In this paper, after reviewing other machine-learning type methodologies in Section 2, we introduce our model training schemes, presented in Section 3, focused on a technique that disregards features of intro area of thyroid nodule images; that is, we concentrate our image recognition model on capturing the features characterized in the boundary region of thyroid follicular neoplasms, in virtue of the fact that the previously mentioned differential diagnosis based on the pathologic examination taken after diagnostic thyroidectomy depended considerably on the properties of the boundary region of the nodules. In Section 4, we present numerical results, developing a newly devised parameterized normalization treatment, including AUROC (area under receiver operating characteristic) and those curves, as well as overall differentiation accuracy, and so on. In Section 5, finally, we discuss the existence of features on the boundary of US thyroid follicular neoplasms that could possibly be trained by our proposed CNN based inference model and its efficiency, including our future works.

2. Technical Issues in US Classification Experiments Using Artificial Neural Network

In view of machine learning or artificial intelligent techniques for differentiation of malignant from benign thyroid nodules, there are lots of methods or treatments with sample data sets to extract efficient features for application in a training model of a given machine learning or ANN training tools [10, 11, 18–20]. For support vector machine (SVM), some remarkable ways of feature extracting techniques and imagery subsampling treatments are conducted to efficiently train classification models such as those found in [10, 20–23], and, for ANN type of methods, the methodologies found in [10, 19, 24–27] mostly use some ways of preprocessed training with feature extraction techniques including pathological reports or information on patients such as age, sex, health condition, and the results of various medical tests or cytological data. In other words, most of ANN methods found in there actually demonstrate training with nondirect US images but with some kinds of nonimagery input data sets extracted from original US image information.

In our implementation of CNN model training for differentiating between thyroid follicular adenoma and carcinoma for US thyroid images, we engage US images in a fixed size of pixels in resolution on input nodes directly without extracting

Table 1: Configuration of the list of the numbers of our sample collection of ultrasonography thyroid nodule images without sex identification.

	Hospital A	Hospital B	Total
Follicular adenoma	190	60	250
Follicular carcinoma	40	43	83

any preprocessed statistical features. For a training object of a CNN model, from the reported diagnostic US determining features in the differentiation of thyroid follicular adenoma and carcinoma, we focus on a way of training which magnifies training efficiency of imagery and morphologic features of US found in the adjacent region of the boundary of lesion. For a method of SVM applied in [21] to differentiate risky hypoechoic thyroid nodules, although they try to take the features found in boundary region of thyroid nodules by setting up the data set comprising 131 medium-risk hypoechoic nodules characterized by regular boundaries and 42 high-risk hypoechoic nodules characterized by irregular boundaries, since the morphological shapes of boundary regions are so distinctive that even human eyes may easily recognize the risky nodules, one may not be sure that its model would be a good fit to work for any ambiguously shaped general cases of thyroid follicular adenoma and carcinoma (refer to Figure 1).

Exhibited here are renderings of our own sample gatherings of thyroid nodule images to deal with our classification models of convolutional neural network, and, afterward, we introduce and define the type of training methodology in Section 2.

For our own collection of sample thyroid images, we have 250 cases of follicular adenoma, as well as 83 cases of follicular carcinoma, visualized in gray-scale 8-bit bitmap US thyroid nodule images, and the data sets were obtained from 2 different US clinics which identified as Hospital A (= H_A) and Hospital B (= H_B) (refer to Table 1). For the data denoted by clinic HA, in total, 230 patients with 230 thyroid nodules were included in this study. Of the 230 patients, 51 (22.174%) were men, and 179 (77.826%) were women. Mean age of the 230 patients included was 48.72 years. Mean size of the 230 thyroid nodules was 29.84 mm, and the mean of the pixel intensity of the grey-scale 8-bit bitmap US images is 63.819, where the mean value of the max intensity is 176.1475, and the mean of the minimum intensity is 7.1230. For the data of HB, totally, 103 patients with 103 thyroid nodules were included in this study, where 22 (21.359%) were men, 71 (68.933%) were women, and 10(9.708%) were the missed sex identification, and the mean age was 43.90 years. Mean size of the 103 thyroid nodules was 32.81 mm, and the mean of the pixel intensity of the grey-scale 8-bit bitmap US images is 82.07 where the mean value of the max intensity is 192.1154, and the mean of the minimum intensity is 6.6827. These data sets are given from both institutional databases which was reviewed after from January 2003, for patients diagnosed with follicular adenoma and follicular carcinoma after surgical excision. In Table 1, we present the list of the numbers of our sample cases of US thyroid images.
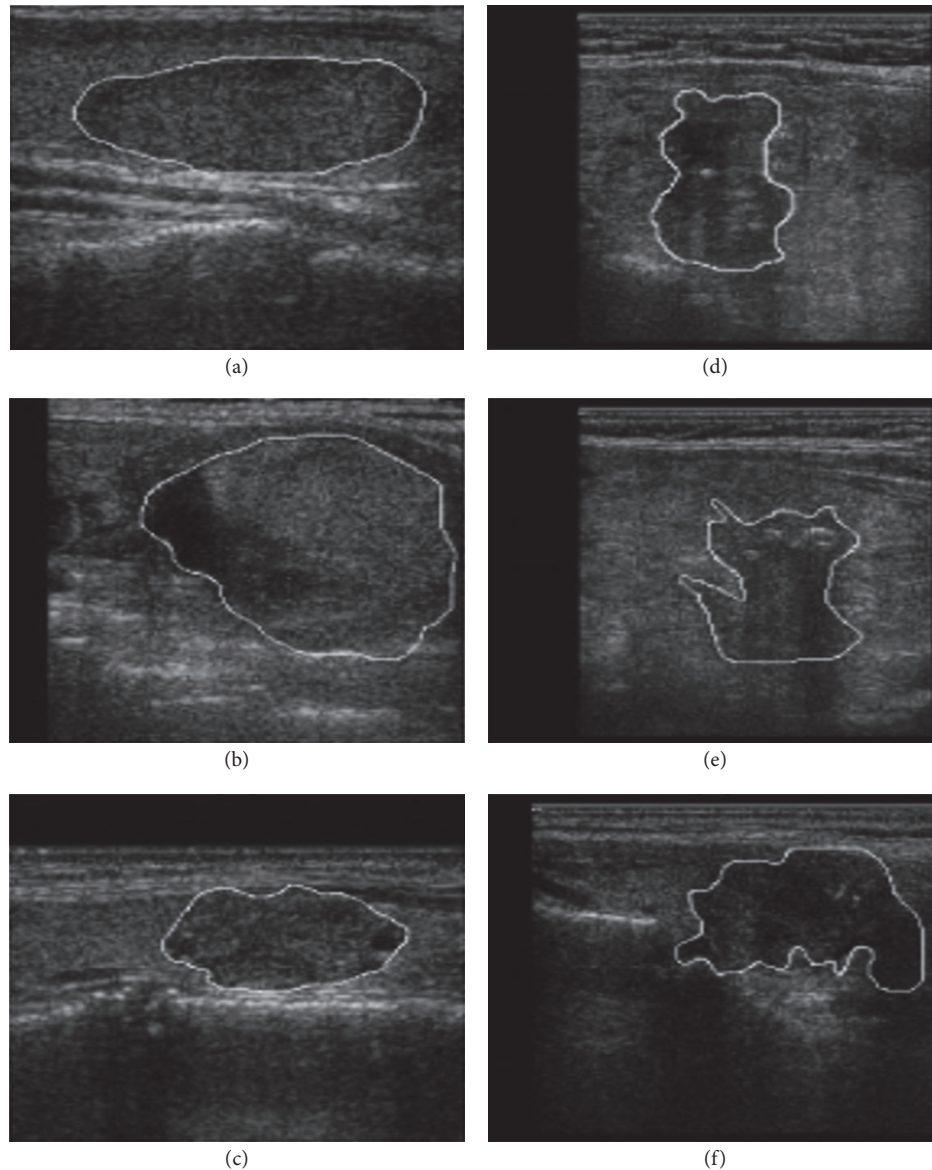
FIGURE 1: Thyroid US images with delineated nodules: (a–c) nodules of regular boundaries; (d–f) nodules of irregular boundaries, belonging to the data set in [21].

3. US Differentiation Applying CNN

We make use of CNN to differentiate US images of follicular neoplasms between the adenoma and the carcinoma. We demonstrate experiments with the data set given in Table 1 to train a CNN model to infer the differentiation.

3.1. Data Setup

3.1.1. Making Subsets. Here, aiming to derive a data invariant numerical result related to the characteristics of the fine imagery features captured by our CNN model retained on the margin of thyroid follicular neoplasms, delivered from various examinations as far as possible, we organize 6 kinds of disjoint subsets from the data set given in Table 1, into Set_a, Set_b, Set_c, Set_d, Set_e, and Set_f (see Table 2).

After removing some US contaminated images tainted at some marginal area with an extraneous substance, such as diagnostic marking signs of the radiologist, we reduced the data sets shown in Table 2 into those refined sets listed in Table 3, in which Set_a^* corresponds to Set_a, and Set_b to Set_b^*, and so on.

3.1.2. Training Data and Test Data. To implement the training of our model, we use Set_a^* as training data and the other subsets for each as test data, based on the data sets given in Table 3; that is, this organization of training and test data is set to be an extremely small training set for small test set architecture to demonstrate various examinations and to deduce the existence of data invariant characteristics of fine common features captured by our nodule's boundary based CNN modeling. To set up the practical training and test data
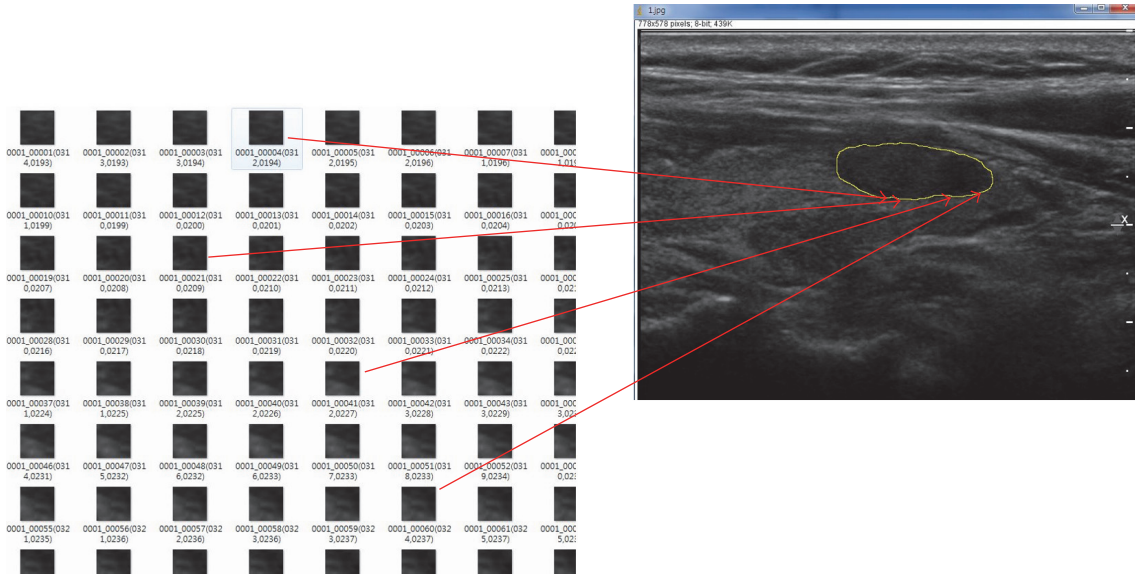
FIGURE 2: Selection of images (here we set 50×50 pixels in size) aligned on the contour of each thyroid follicular neoplasm's margin.

TABLE 2: Configuration of the list of the numbers of our sample collection of US thyroid nodule images in 6 disjoint subsets.

	Set_a	Set_b	Set_c	Set_d	Set_e	Set_f	Total
Follicular adenoma	H_A				H_B		250
	40	30	60	60	30	30	
Follicular carcinoma	H_A				H_B		83
	40	0	0	0	13	30	

TABLE 3: Refined configuration of the list of the numbers of our sample collection of US thyroid nodule images in 6 disjoint subsets.

	Set_a*	Set_b*	Set_c*	Set_d*	Set_e*	Set_f*	Total
Follicular adenoma	H_A				H_B		230
	39	30	59	59	20	23	
Follicular carcinoma	H_A				H_B		77
	39	0	0	0	12	26	

sets based on each boundary of nodule, we select small 2D box images (here we set 50×50 pixels in size) aligned on the contour of each thyroid follicular neoplasms' margin (see Figure 2).

To have this selection of marginal box images for the training data, following the contour of the nodule's margin, we chose somewhat distinctive images judged manually, while for test data we select box images centered at every point of pixels on the manually drawn, closed virtual contour margin line of the thyroid nodule, and afterward we have the training and test data sets given in Table 4, in which Set_$a°$ corresponds to Set_$a*$, and Set_$b°$ to Set_$b*$, and so on.

3.2. Differentiation via the Rule of Decision by Majority. From the nodule information given in Table 3 and the training and test data organization given in Table 4, we examine the

TABLE 4: The number of selected partial box images along with the contour of margins of thyroid follicular neoplasms used to organize training and test data sets.

		Follicular adenoma	Follicular carcinoma	Total
Training_data	Set_$a°$	625	859	1484
Test_data	Set_$b°$	18170	0	18170
	Set_$c°$	43669	0	43669
	Set_$d°$	50061	0	50061
	Set_$e°$	12537	8939	21476
	Set_$f°$	18740	16648	35388

differentiation, applying a decision by majority to judge the differentiation for each follicular neoplasm by those subsampled data sets taken from each own boundary region. For a simple representation of our CNN based statistical inference applying the decision by majority, let us assume that there exist 500 selected subsampled images given from the boundary of a nodule so that our trained CNN model determines each selected subsampled image to be carcinoma in 255 counts and adenoma in 245 counts, and then we determine that the nodule is carcinoma, owing to the fact that the counts to be carcinoma exceed those for adenoma (see Figure 3).

3.2.1. The Structure of Convolutional Neural Network as a CNN Model. We apply an AlexNet type of CNN structure [28] to train data sets, which comprises 5 convolutional layers and 2 pooling layers, the details of which are described in Table 5 and Figure 4. (In Table 5, characters m and n represent the size of the convolution kernel for each input channel and the number of total kernels applied to each layer, resp.)

3.3. Overview. In view of the setup, the data set is organized from an assumption that every margin of thyroid follicular

TABLE 5: Training structure of the convolutional neural net (5-conv, 2-pool, 2-fully-conn structure).

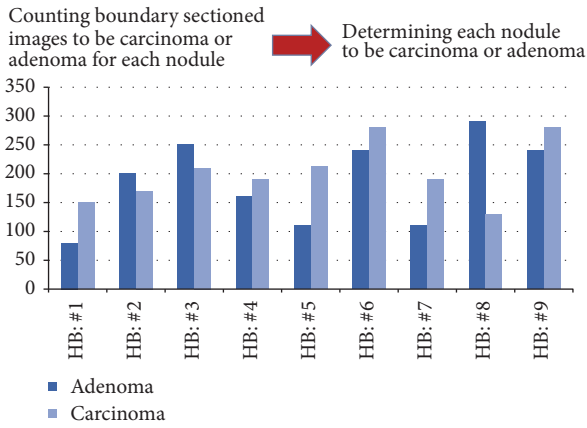| Layer	$(m \times m) \times n$	Activation	
Conv.	$(3 \times 3) \times 16$	ReLu	
Conv.	$(3 \times 3) \times 256$	ReLu	
Max-Pooling	kernel size: (2×2)		Strides: 2
Conv.	$(3 \times 3) \times 512$	ReLu	
Conv.	$(3 \times 3) \times 2048$	ReLu	
Conv.	$(3 \times 3) \times 4096$	ReLu	
Max-Pooling	kernel size: (2×2)		Strides: 2
Fully-Conn.	512	ReLu	
Fully-Conn.	256	ReLu	(Dropout rate: 50%)
Fully-Conn.		Softmax	Output units: 2

FIGURE 3: An illustration to determine differentiation of nodules by counting CNN model based semijudged selection images taken from boundary regions for each nodule.

neoplasms may contain certain obvious features that help differentiate between adenoma and carcinoma and that those features would well be detected and trained, even with the small number of images of thyroid nodules [9]. Our standard of outlining of the contour of each thyroid follicular is drawn from the official medical specialist from both clinic, Samsung Medical Centre, and Yonsei University Medical Centre in Seoul, South Korea, the coauthors of this article.

4. Numerical Results

In this section, we present numerical results related to differentiating thyroid follicular neoplasms between adenoma and carcinoma and some observable aspects in the feature recognition of CNN in view of a newly developed data normalization method by devising a parameterized scaling treatment. For the numerical results in this section, we train the CNN model described in Table 5 and Figure 4, with 380 of epochs of training, 400 of batch size, 0.0001 for learning rate, and 0.5 for dropout rate, with a standard backpropagation algorithm [17, 28, 29]. We customized the popular TensorFlow (version

1.0.0) library in Python3.x for our main programs of the experiments. It took several minutes to train each experimental model where it took a few seconds to infer the results for test data sets, on two Ndvia Pacal TitanX 12 GB GPUs.

4.1. Training Aspects of the Parameterized Scaling Treatment in Data Normalization. Here, we give training results of CNN with regard to the data normalization, applying a parameterized scaling treatment. For the normalization of training data in our experiments, we apply a mean-zero based min-max normalization of training input data, which transforms all the scores of input data into a common range $[0, 1]$ and then minus the mean of the input data set. We let a pair of indices (i, j) represent the pixel point located in the ith position in the x-axis and the j-th position in the y-axis in each input image and the corresponding pixel value is denoted by u_{ij}; then the mean-zero based min-max normalization v_{ij} for training data is given as

$$v_{ij} = \frac{u_{ij} - E\left[u_{ij}\right] - \min_{(i,j)} u_{ij}}{\max_{(i,j)} u_{ij} - \min_{(i,j)} u_{ij}}, \tag{1}$$

where $E[u_{ij}]$ denotes the mean value of u_{ij} in the position (i, j).

While the test data is normalized applying a scaling parameter α, it is performed as

$$q_{ij} = \frac{p_{ij} + \alpha \cdot E\left[p_{ij}\right] - \min_{(i,j)} p_{ij}}{\max_{(i,j)} p_{ij} - \min_{(i,j)} p_{ij}}, \tag{2}$$

where $E[p_{ij}]$ denotes the mean value of p_{ij}, the pixel value of test data is at position (i, j), and q_{ij} denotes the parameterized normalization of p_{ij}. Here, note that if $\alpha = 0$ in (2), it is the min-max normalization [30].

Here we are examining the CNN model for the test data. We have the parameter α in (2) range $[-1.5, 1.5]$ for every 0.3 increase. For the results obtained by test data from Set_$b°$ to Set_$f°$ listed in Table 4, we present the accuracy of differentiation in percentage (%), and for each test set we draw the plots given from Figures 5(a)–5(g), where we draw plots of true benignancy of adenoma for Set_$b°$, Set_$c°$, Set_$d°$, Set_$e°$, and Set_$f°$ and the false benignancy of carcinoma for Set_$e°$, and Set_$f°$, respectively. In Figure 5, each curve represents the tendency of differentiation for a corresponding single follicular nodule; for example, for Set_$b°$, there are 30 kinds of nodules (refer to Table 3), and then there are 30 lines of curve in Figure 5(a), and for a given α each plot lying in the vertical line indicates the percentage (%) to be classified as benign, one for each nodule, respectively.

Now, summarizing the plots given in Figure 5, we draw the plots in mean cumulative percentage (%) versus α for true benignancy of adenoma test data and for false benignancy of carcinoma data, observing the slopes of plots in the mean cumulative percentage (%) proportional to α, which represents the tendency of differentiation to be classified as benign adenoma. We provide the plots to compare those slopes in Figure 6.

Seeing the plots in Figure 6, the slopes of mean cumulative percentage (%) versus α, where $\alpha \geq -0.5$, have a positive

TABLE 6: Result of the CNN inference conducted on test data Set_$f°$, applying $\alpha = 0.15$.

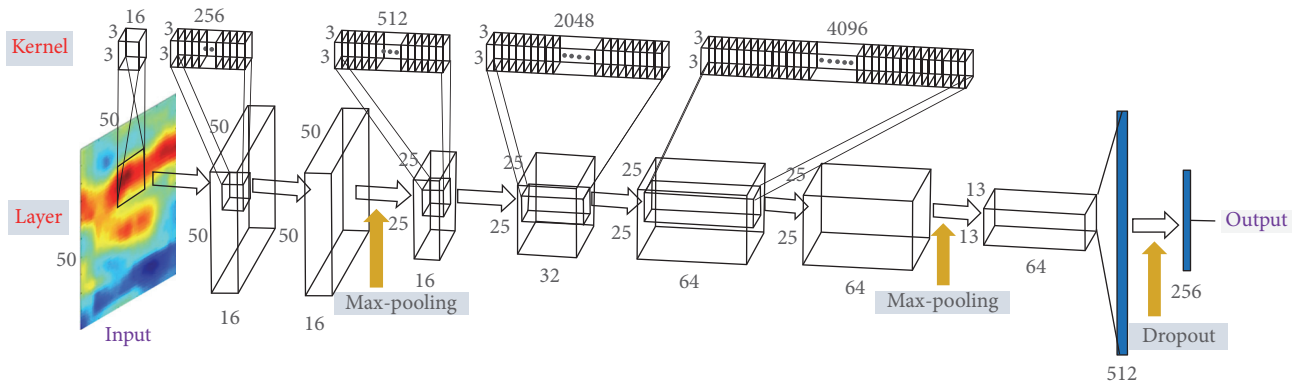|	Predicted_Adenoma	Predicted_Carcinoma	
	True_Adenoma	*False_Carcinoma*	Accuracy (True negative rate)
	17	6	73.91%
	False_Adenoma	*True_Carcinoma*	Accuracy (True positive rate)
	7	19	73.07%
Set_$f°$			$F_{0.5}$-score: 0.7540
	False omission rate	Positive predictive value	F_1-score: 0.7451
	0.29	*0.76*	F_2-score: 0.7364
			G-mean: 0.7452

FIGURE 4: CNN training architecture with 5-conv, 2-pool, and 2-fully-conn. network corresponding to the structure in Table 5.

sign for all the plots, and these behaviors of slopes could promote the increase of differentiation accuracy in total for true benign data, but the behavior could also cause a decrease for carcinoma data, which gives us a sense of fine-tuning through the control of α.

4.2. Fine-Tuning Effect of the Parameterized Data Normalization. Along with the fact that the control of α could give an increase in total differentiation accuracy, the result of a demonstration of differentiation for a set of test data reveals the possibility that a nice choice of α gives us a highly recommendable CNN differentiation model as a model of fine-tuning. Here, a result of the demonstration conducted on test data Set_$f°$ is given in Table 6, for which we choose $\alpha = 0.15$.

In Figure 7, we give the plots of differentiation in percentage (%) versus α for false benignancy and true benignancy for test data Set_$f°$. Seeing Figure 7(a), we know that around $\alpha = 0.15$ the plots lying in vertical line with values less than 50% counts about 19, and, seeing Figure 7(b), we know that around $\alpha = 0.15$ the plots lying in vertical line with values greater than 50% count 17 approximately.

Furthermore, to represent the efficiency of our training model and the comparison result given from different values of α, in Figure 8, we give the receiver operating characteristic (ROC) [31] curve drawn by the differentiation result from the test on the test data set Set_$f°$ by scaling α in the interval

of $[-0.6, 0.6]$, where the corresponding area under the curve (AUC) is 0.8088.

On the other hand, seeing that test data sets Set_$b°$, Set_$c°$, and Set_$d°$ are derived from the data set H_A and Set_$e°$ and Set_$f°$ from H_B, respectively, we apply a different normalizing parameter α in (2) for the sets from H_A and for those from HB such that $\alpha = 1.5$ for H_A and $\alpha = 0.15$ for H_B. The differentiation results for both H_A and H_B are given in Table 7.

5. Discussion

In our experiments of CNN inference modeling to differentiate thyroid follicular neoplasms between follicular adenoma and carcinoma of gray-scale 8-bit bitmap US thyroid images, we implemented the mean-zero based min-max normalization method defined in (1) for input data to be trained by CNN architecture and rescaled it with a parameter denoted as α in (2) for test data. In our numerical simulation of training of model, referring to Table 3, the readers may see that our acquisition of the training data and test data sets is taken from two different clinic centres, the total amounts of samples for the use of training data set are very limited, the whole samples of follicular carcinoma images from clinic H_A are used to be training data, and the sample images from H_B are used to be test data set, so that we naturally determined the fixed partitioning scheme. As a result of the experiments of scaling the normalization parameter α chosen in a real number

(a) True benignancy in percentage (%) for range [−1.5, 1.5] defined in (2), for Set_b° denoted in Table 4

(b) True benignancy in percentage (%) for range [−1.5, 1.5] defined in (2), for Set_c° denoted in Table 4

(c) True benignancy in percentage (%) for range [−1.5, 1.5] defined in (2), for Set_d° denoted in Table 4

(d) True benignancy in percentage (%) for range [−1.5, 1.5] defined in (2), for Set_e° denoted in Table 4

(e) False benignancy in percentage (%) for range [−1.5, 1.5] defined in (2), for Set_e° denoted in Table 4

(f) True benignancy in percentage (%) for range [−1.5, 1.5] defined in (2), for Set_f° denoted in Table 4

(g) False benignancy in percentage (%) for range [−1.5, 1.5] defined in (2), for Set_f° denoted in Table 4
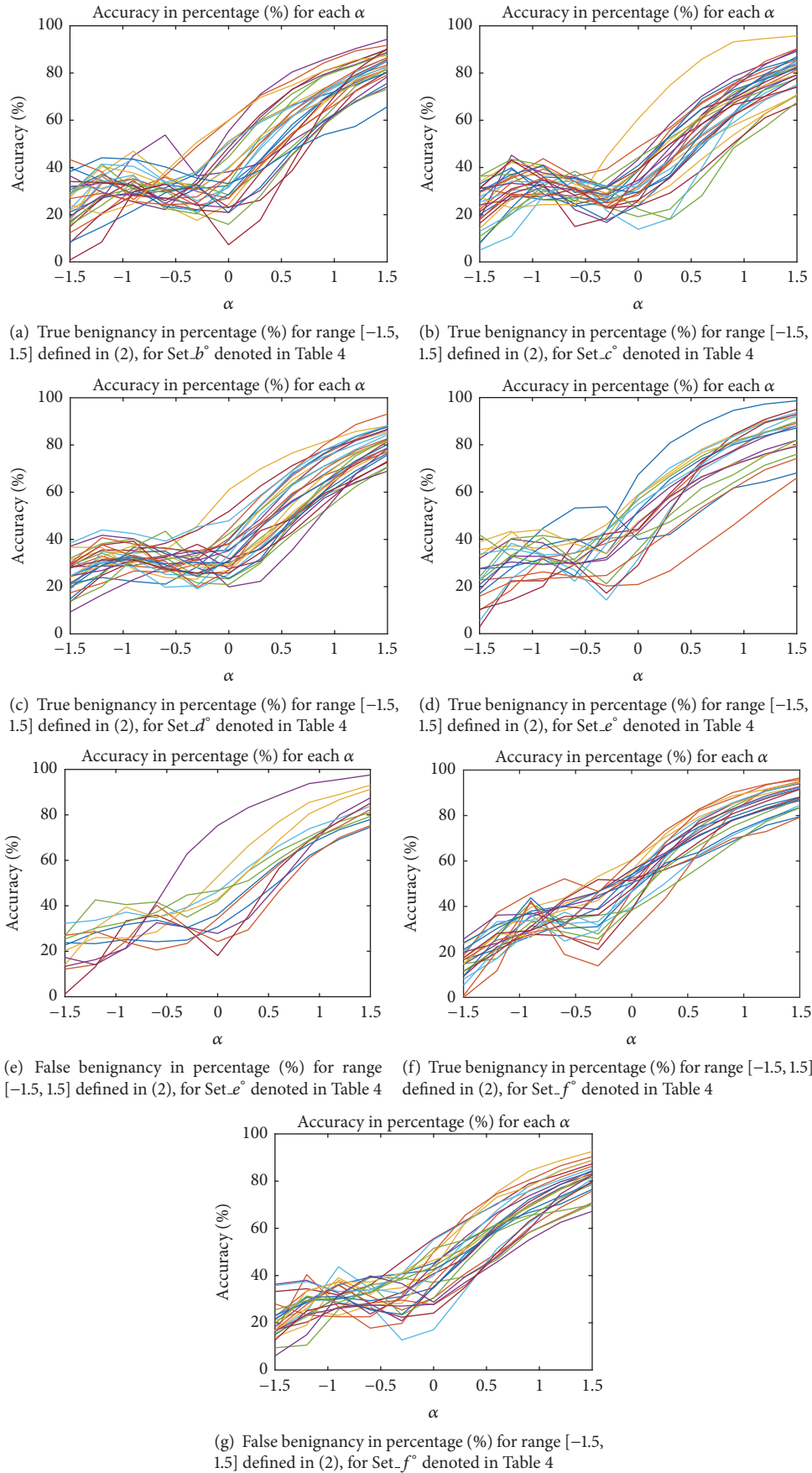
FIGURE 5: Plots of differentiation in percentage (%) versus α for false benignancy of carcinoma and true benignancy of adenoma for each of the test data sets.

TABLE 7: Result of the CNN inference conducted on the test data groups, both H_A and H_B.

	Predicted_Adenoma	Predicted_Carcinoma		Overall accuracy
	True_Adenoma	*False_Carcinoma*	True negative rate	
	100%	*0.00%*	1.0	
	False_Adenoma	*True_Carcinoma*	True positive rate	
H_A	-	-	-	*100%*
			$F_{0.5}$-score: -	
	False omission rate	Positive predictive value	F_1-score: -	
	-	-	F_2-score: -	
			G-mean: -	
	True_Adenoma	*False_Carcinoma*	True negative rate	
	69.76%	*30.24%*	0.6976	
	False_Adenoma	*True_Carcinoma*	True positive rate	
H_B	*28.95%*	*71.05%*	0.7105	*70.37%*
			$F_{0.5}$-score: 0.6818	
	False omission rate	Positive predictive value	F_1-score: 0.6923	
	0.2683	0.6749	F_2-score: 0.7031	
			G-mean: 0.6925	
	True_Adenoma	*False_Carcinoma*	True negative rate	
	93.19%	*6.81%*	0.9319	
	False_Adenoma	*True_Carcinoma*	True positive rate	
Total	*28.95%*	*71.05%*	0.7105	*89.52%*
			$F_{0.5}$-score: 0.6818	
	False omission rate	Positive predictive value	F_1-score: 0.6923	
	0.0582	0.6750	F_2-score: 0.7031	
			G-mean: 0.6925	

FIGURE 6: Plots of true benignancy of adenoma for Set_$b°$, Set_$c°$, Set_$d°$, Set_$e°$, and Set_$f°$ and false benignancy of carcinoma for Set_$e°$ and Set_$f°$, in cumulative percentage (%) for α ranging [−1.5, 1.5] defined in (2).

interval [−1.5, 1.5], we found out that the slopes of mean cumulative percentage (%) versus α, where $\alpha \geq -0.5$, have a positive sign for all the plots, and these behaviors of slopes increased the differentiation accuracy in total for true adenoma data but promoted a decrease for carcinoma data, providing a sense of fine-tuning through the control of α. Although the training data is chosen among the subsets of H_A by adjusting the normalizing parameter α chosen differently from each other between the two hospital data sets, H_A

and H_B, respectively, we could differentiate the images in H_B, of which the test result of differentiation over 89% in overall accuracy supports the availability of our inference model. Furthermore, from the test results shown in Figure 6, we see that there is no pairing of data sets, of which plots have to cross over themselves where $\alpha \geq 0$, of which the original hospital databases are different from each other, and these plot behaviors in the results might somewhat weakly suggest that the two different hospital databases have their own distinctive imagery characteristics for each of them so that it makes sense to apply a different normalizing parameter α for each hospital data set, respectively. For this, one may suggest that the configuration of the pixel intensities which differs along both data sets, HA and HB, affects that. (Refer to the fact that, for HA, the mean of the pixel intensity of the grey-scale 8-bit bitmap US images is 63.819, the mean value of the max intensity is 176.1475, and the mean of the minimum intensity is 7.1230, whereas, for HB, the mean of the pixel intensity is 82.07, the mean value of the max intensity is 192.1154, and the mean of the minimum intensity is 6.6827, as denoted before.)

On the other hand, with regard to the data set, our shortage of data sets seldom makes someone imagine a good performance to infer disease diagnostic determination, comparing to that of such a relatively plentiful of data sets of MNIST and ILSVRC [32]. Hence, to tackle our small data set problem, we mainly seek to develop inference methodologies and overcome the extremely harsh task of our inference model with small data set via seeking a kind of ensemble-like neural-network method. Moreover, for the performance of our proposed model, basically like other machine learning based technology, we may not be sure about the robust

(a) False benignancy in percentage (%) for range [−1.5, 1.5] defined in (2), for Set_b° denoted in Table 4

(b) True benignancy in percentage (%) for range [−1.5, 1.5] defined in (2), for Set_c° denoted in Table 4
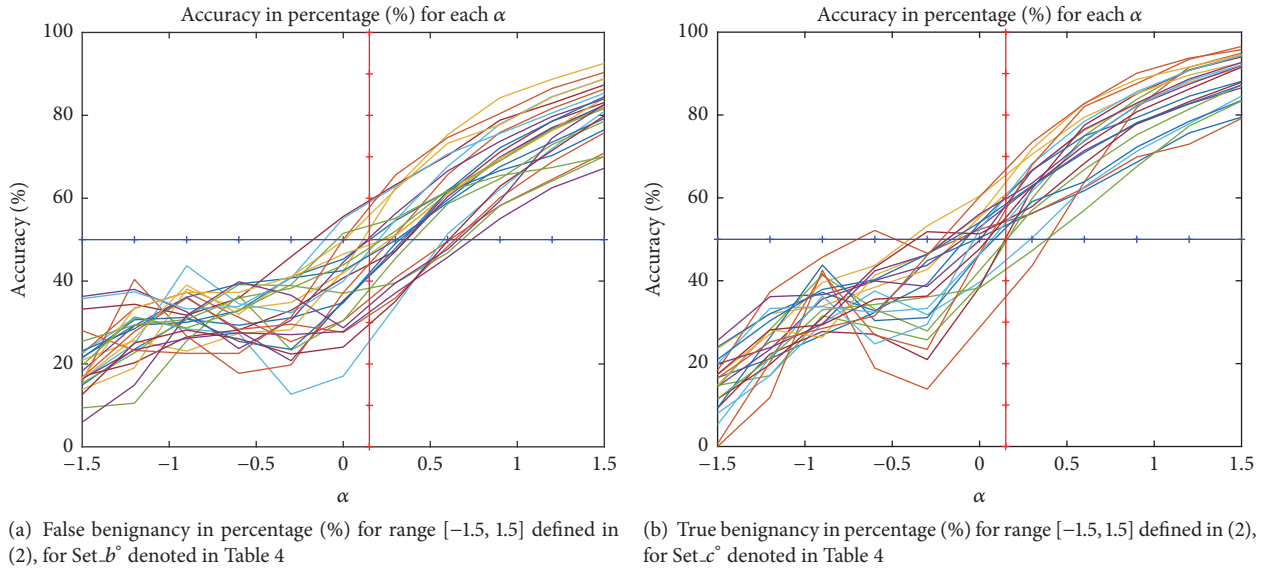
FIGURE 7: Plots of differentiation in percentage (%) versus α for false benignancy of carcinoma and true benignancy of adenoma for test data Set_f°.
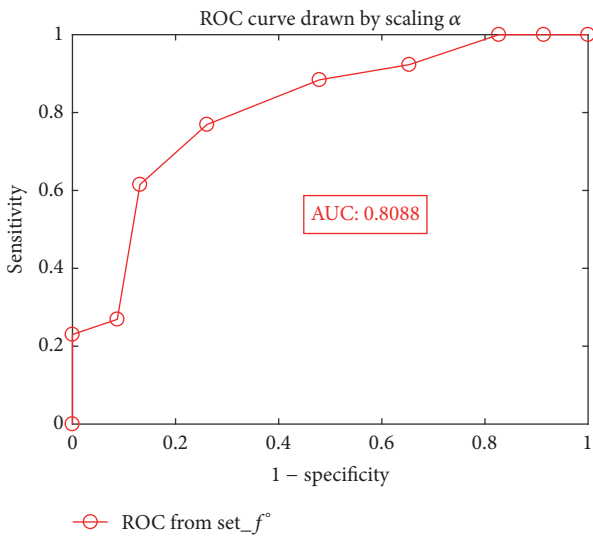

FIGURE 8: ROC curves given by differentiation test on Set_f°, for α ranging [−0.6, 0.6] defined in (2).

functioning of our methodology yet, since like most of other vision based deep-learning architectures severely it suffers from the types of organizations or the amount of sample data sets to be applied to do specific inference, so that the proposed methodology may or may not suffer from those kinds of problems. In our research article, we have not suggested any mathematical proof of theoretical issues related to our presented numerical results rather than given experimental conviction for the possibility of the utility. From the experiments in [5], also we see that although the amounts of samples are so rare, they conclude some reasonable researching insights into the diagnostic differentiation for follicular neoplasm lesion of thyroid. Now we hope that we open the chances of the successful application similar to our proposed method to the readers with much plentiful sets of sample data.

For the sample data acquisition, both health centres, here Hospital A (= H_A) and Hospital B (= H_B), referring to Table 1, have different protocol for the acquisition of the ultrasound images, based on the apparatus to take the ultrasound image pictures; that is, the machines to take the ultrasound images and the related mechanical conditions are different. In this case, we have the difficulty to adjust the data sets to have the same depth of intensity of ultrasound wave and resolutions for both clinics' data sets, and we thought that the differences in those parameters influence the inference model results, and it is expressed in the classification results where the classification results for data sets included either side of clinic have the similar up-and-down slopes of differentiation, that is, for data from same clinic have the tendency of near distance of plots themselves relatively compared to the other clinic's data sets, referring to Figure 6.

For the sample data organization, referring to both clinics' data sets, the critical point to determine how many data sets to be set as training data and test data is largely dependent on the number of follicular carcinoma images, since, to balance the number of sample data for training the model, we set prior data from either clinic (here H_A, referring to Table 3) having much ample number of samples compared to the other clinic (here H_B, referring to Table 3) to be used as training data, without loss of generality. And the total amount of follicular carcinoma sample images are be used in developing our inference model inferior to that of follicular adenoma images so that we determine having training data set from the sample images of H_A which owns further sample data compared to H_B, especially for follicular carcinoma images. Actually, considering the data confusion in training the inference model occurred from the mixed data given from different environment of protocol in data acquisition from the two different clinic centres and, to avoid that ill-conditioned data organization and the following training results, we mainly separated the training data set given from either clinic and the

test data set from the other clinic. And lastly, we determined organizing the training data and the test data as given in Table 3.

Now, here we give an overall answer to handle our choice of hyperparameters for our proposed neural network. Referring to Figures 5 and 6, we found out that the tendency of the slopes in those plots in Figures 5 and 6 gives us that as the proposed normalization parameter α moves the differentiation results change, and those kinds of differentiation trends are revealed to be coherent to each model with some variances of the neural network's parameters such as batch size and learning rate. Consequently, our proposed values of the neural network's parameters are one of the good choices which enabled us to get the numerical results which are persuasive to readers to convince them of the effectiveness of our proposed methodology to infer the differentiation depending on our organization of data sets. In our experiments, we experienced some overfittings or underfittings for the validation sets for training epochs over just several hundreds of epochs, and the similar phenomenon often happened for some variances of learning rates, and so on. For dropout rate, (the recently introduced technique, called "dropout" [29], consists of setting to zero the output of each hidden neuron with probability 0.5. The neurons which are "dropped out" in this way do not contribute to the forward pass and do not participate in backpropagation), we refer to the dropout rate given in [32] which deals with the AlexNet. For the structure of CNN, in our experiments, there is no prominent dominance for many heavy layers of CNN rather than popular AlexNet type of CNN architecture. For the 2D box image of size 50×50 pixels, as we see the illustration given in Figure 9, the raw contour ROI of US images taken from both clinic centres has the resolution size about 200~600 ± ε pixels, and we thought that the resampling 2D box image, which is represented as the red square in Figure 9, (to be inferred for the full US image's differentiation based on our ensemble-like voting system of CNN) should be not too small or too large to have the inference model not to lose the critical morphological vision based features which may reside in the region of boundary of thyroid lesion. And of course, even our choice of the 2D-boxing size is not absolutely given someone to ensure it is the best choice, since the size may be the one of good choice to infer the model. Unfortunately, like most of other deep-learning models, especially for vision based models like CNN, there are still behaviors of each model's distinctive inference performances, and someone may say it is just black-box to analyze it in the sense of mathematical inspirations.

On the other hand, out of loss of generality, the choice of our neural network's parameters does not guarantee the absolute superiority for our applied AlexNet types of neural network; it is only dependent on one's own data sets and the experimental experiences and, here in our proposed method and the corresponding numerical results, only made to give the readers sorts of insight about the possibility or the effectiveness of our proposed inference model.

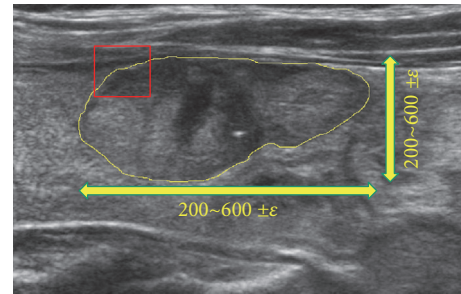For the experimental experiences, we have ever applied various kinds of examinations with SVM, K-NN, simple

FIGURE 9: An example of a raw contour ROI of US thyroid image with resolution size ranging 200~600 ± ε pixels. The red square represents an example of 2D box image we have selected to set up the data sets for the use in developing our deep-learning inference model, which is described in Section 3.1.

ANN, and so on. Unfortunately, with these activities of experiments, we did not find any acknowledgeable results of inference models, yet. Finally, as we apply our proposed methodology, we observed breakthrough results, although still one may be doubtful of the real big data based performance of it. These results of our proposed method to infer the diagnoses to determine the alternative choice of classification problem, showing a possible superior task ability of ensemble-like methods to normal classical inference methodologies generally known.

5.1. Comparison with the Benchmark Thyroid Follicular Neoplasm US Images

5.1.1. Preliminary Experiments by SVM, KNN, ANN, and CNN. As mentioned above, we have applied various kinds of basic examinations with SVM, KNN, Normal Bayes Classifier, and Feed-Forward-Perceptron network (ANN) to have similar types of differentiation of thyroid follicular neoplasm US images, based on the sense of full size image and not resampling from the contour region of nodules. The preliminary results of SVM, KNN, Normal Bayes Classifier, and ANN which applies with some well-known feature selection such as Mean, Skewness, Energy, Entropy, Compactness, Solidity, GLCM_contrast, GLCM_homogeneity, GLCM_energy, GLCM_entrophy, and Gabor_O2S1 are given in Table 8 [33, 34]. The readers may well compare the results to those in Table 7.

And even from the preliminary experiments taken with the full US image based (not resampled along contour) CNN inference, we have found the total accuracy ~75%, but there are still many follicular carcinoma images that failed to be differentiated.

5.1.2. Comparison with USFNA Based Differentiation for a Follicular Thyroid Neoplasm US Images. For the comparison performance of our differentiation method for US images follicular thyroid neoplasm, we have found the USFNA (ultrasound-guided fine-needle aspiration) and the experimental results in [5] where the FNA performance ranges 51~67% in accuracy, which gives inferior results compared to our proposed methodology, as given in Table 9.

TABLE 8: Result of various typical inference model.

	Predicted_Adenoma	Predicted_Carcinoma		Overall Accuracy
	True_Adenoma 18.30%	*False_Carcinoma* 81.70%	True negative rate 0.183	
	False_Adenoma 22.92%	*True_Carcinoma* 77.08%	True positive rate 0.7708	
SVM			$F_{0.5}$-score: 0.4148	*40.96%*
	False omission rate 0.4400	Positive predictive value 0.3718	F_1-score: 0.5017	
			F_2-score: 0.6346	
			G-mean: 0.5354	
	True_Adenoma 91.50%	*False_Carcinoma* 8.50%	True negative rate 0.9150	
	False_Adenoma 81.25%	*True_Carcinoma* 18.75%	True positive rate 0.1875	
KNN			$F_{0.5}$-score: 0.4091	*63.45%*
	False omission rate 0.3578	Positive predictive value 0.5806	F_1-score: 0.2835	
			F_2-score: 0.2169	
			G-mean: 0.3299	
	True_Adenoma 79.08%	*False_Carcinoma* 20.92%	True negative rate 0.7908	
	False_Adenoma 43.75%	*True_Carcinoma* 56.25%	True positive rate 0.5625	
ANN			$F_{0.5}$-score: 0.6136	*70.28%*
	False omission rate 0.2577	Positive predictive value 0.6279	F_1-score: 0.5934	
			F_2-score: 0.5745	
			G-mean: 0.5943	
	True_Adenoma 38.56%	*False_Carcinoma* 61.44%	True negative rate 0.3856	
	False_Adenoma 13.54%	*True_Carcinoma* 86.46%	True positive rate 0.8646	
Normal Bayes Classifier			$F_{0.5}$-score: 0.5162	*57.03%*
	False omission rate 0.1805	Positive predictive value 0.4689	F_1-score: 0.6081	
			F_2-score: 0.7398	
			G-mean: 0.6367	

TABLE 9: Comparison result of diagnostic performance with other USFNA method [5] for follicular thyroid neoplasm.

(%)	FS (Frozen Section)	USFNA	Our proposed
Sensitivity	80.0 (24/30)	84.2 (48/57)	71.05 (27/38)
Specificity	96.3 (77/80)	52.2 (36/69)	93.19 (178/191)
PPV	88.9 (24/27)	59.3 (48/81)	67.49 (27/40)
NPV	92.8 (77/83)	80.0 (36/45)	89.89 (178/189)
Accuracy	91.8 (101/110)	66.7 (84/126)	89.52 (205/229)

On the other hand, we found our general types of benchmark computer-aided systems listed in [35] where the author collected sample images from the open database proposed by Pedraza et. al. [36]. They applied a pretrained model transferring model which is initialized from the pretrained GoogLeNet network achieving excellent classification performance attaining 98.29% classification accuracy, 99.10% sensitivity, and 93.90% specificity. Although the types of

US thyroid images of various computer-aided differentiation systems found in [21–23, 35] present excellent performances, their models are mostly treated with papillary thyroid carcinoma. And there are lots of reports that even USFNA is widely used in discriminating between benign and malignancy in various lesions of the thyroid showing excellent performances (sensitivity 65%–98% and specificity 72%–100%) for papillary thyroid carcinoma [5].

6. Conclusion

Although the amount of data sets relatively is not so plentiful compared to some well-known big data based machine-learning models, by the concurrent research works in the reference's authors where the follicular thyroid neoplasm US images are still not well studied for deep-learning based inference technology, we conclude that our proposed methods of CNN with data sets given by image selection subsampling along with the boundary of thyroid follicular neoplasms may

detect some morphological features reflected in the region of boundary of nodules, which make sense to be supported by the background knowledge related to the known US image features indicating the criteria for diagnosing the carcinoma of thyroid follicular neoplasms in the general sense of clinical reports, especially concerning the characteristics of the marginal contour region of thyroid follicular neoplasms.

7. Future Works

Meanwhile, these results also reveal a suggestion that some imagery features, which could be recognized as scaling α, exist on the boundary of nodules so that a CNN inference model recognizes them and learns. These conjectures of the existence of learnable imagery features adjacent of the boundary of nodules for our CNN model need to be proven by a variety of fine-tuning techniques, including Standardization (Z-score normalization), tanh-Estimators, and other data normalizing techniques [37], as well as adjusting batch training modes, learning rate, convolution layers, and so on. Moreover, although we fixed the pixel resolution in this article to 50 $\times$ 50 for the subsampling image selection near the boundary of nodules, one may have other flexible choices of subsampling image size to train CNN and compare the efficiencies.

Conflicts of Interest

The authors declare that there are no conflicts of interest regarding the publication of this paper.

Authors' Contributions

Authors Kwang Gi Kim and Jin Young Kwak contributed equally to this work.

Acknowledgments

References

[1] N. Howlader et al., *SEER Cancer Statistics Review*, Populations, National Cancer Institute, 1975.

[2] M. Podda, A. Saba, F. Porru, I. Reccia, and A. Pisanu, "Follicular thyroid carcinoma: Differences in clinical relevance between minimally invasive and widely invasive tumors," *World Journal of Surgical Oncology*, vol. 13, no. 1, article no. 193, 2015.

[3] M. D. Brennan, E. J. Bergstralh, J. A. Van Heerden, and W. M. McConahey, "Follicular thyroid cancer treated at the Mayo Clinic, 1946 through 1970: Initial manifestations, pathologic findings, therapy, and outcome," *Mayo Clinic Proceedings*, vol. 66, no. 1, pp. 11–22, 1991.

[4] S. A. Hundahl, I. D. Fleming, A. M. Fremgen, and H. R. Menck, "A National Cancer Data Base report on 53,856 cases of thyroid carcinoma treated in the U.S., 1985–1995," *Cancer*, vol. 83, no. 12, pp. 2638–2648, 1998.

[5] J. H. Yoon, E.-K. Kim, J. H. Youk, H. J. Moon, and J. Y. Kwak, "Better understanding in the differentiation of thyroid follicular adenoma, follicular carcinoma, and follicular variant of papillary carcinoma: a retrospective study," *International Journal of Endocrinology*, vol. 2014, Article ID 321595, 9 pages, 2014.

[6] E.-K. Kim, C. S. Park, and W. Y. Chung, "New sonographic criteria for recommending fine-needle aspiration biopsy of nonpalpable solid nodules of the thyroid," *American Journal of Roentgenology*, vol. 178, no. 3, pp. 687–691, 2002.

[7] Z. W. Baloch, S. Fleisher, V. A. LiVolsi, and P. K. Gupta, "Diagnosis of "follicular neoplasm": A gray zone in thyroid fine-needle aspiration cytology," *Diagnostic Cytopathology*, vol. 26, no. 1, pp. 41–44, 2002.

[8] M. Sobrinho-Simões, C. Eloy, J. Magalhes, C. Lobo, and T. Amaro, "Follicular thyroid carcinoma," *Modern Pathology*, vol. 24, pp. S10–S18, 2011.

[9] C. R. McHenry and R. Phitayakorn, "Follicular adenoma and carcinoma of the thyroid gland," *The Oncologist*, vol. 16, no. 5, pp. 585–593, 2011.

[10] D. Koundal, S. Gupta, and S. Savita, "Computer-Aided Diagnosis of Thyroid Nodule: A Review," *International Journal of Computer Science & Engineering Survey (IJCSES)*, vol. 3, 2012.

[11] K. K. Delibasis, P. A. Asvestas, G. K. Matsopoulos, E. Zoulias, and S. Tseleni-Balafouta, "Computer-aided diagnosis of thyroid malignancy using an artificial immune system classification algorithm," *IEEE Transactions on Information Technology in Biomedicine*, vol. 13, no. 5, pp. 680–686, 2009.

[12] D. E. Maroulis, M. A. Savelonas, S. A. Karkanis, D. K. Iakovidis, and N. Dimitropoulos, "Computer-aided thyroid nodule detection in ultrasound images," in *Proceedings of the 18th IEEE Symposium on Computer-Based Medical Systems*, pp. 271–276, June 2005.

[13] L. M. Clements and K. M. Kockelman, "Economic Effects of Automated Vehicles," *Transportation Research Record*, vol. 2606, pp. 106–114, 2017.

[14] D. Gerhardus, "Robot-assisted surgery: The future is here," *Journal of Healthcare Management*, vol. 48, no. 4, pp. 242–251, 2003.

[15] D. Silver, A. Huang, C. J. Maddison et al., "Mastering the game of Go with deep neural networks and tree search," *Nature*, vol. 529, no. 7587, pp. 484–489, 2016.

[16] S. Yu and L. Guan, "A CAD system for the automatic detection of clustered microcalcifications in digitized mammogram films," *IEEE Transactions on Medical Imaging*, vol. 19, no. 2, pp. 115–126, 2000.

[17] Y. A. LeCun, L. Bottou, G. B. Orr, and K.-R. Müller, "Efficient backprop," *Lecture Notes in Computer Science*, vol. 1524, pp. 9–50, 1998.

[18] H. Wu, Z. Deng, B. Zhang, Q. Liu, and J. Chen, "Classifer model based on machine learning algorithms: Application to differential diagnosis of suspicious thyroid nodules via sonography," *American Journal of Roentgenology*, vol. 207, no. 4, pp. 859–864, 2016.

[19] K. J. Lim, C. S. Choi, D. Y. Yoon et al., "Computer-Aided Diagnosis for the Differentiation of Malignant from Benign Thyroid Nodules on Ultrasonography," *Academic Radiology*, vol. 15, no. 7, pp. 853–858, 2008.

[20] S. Tsantis, D. Cavouras, I. Kalatzis, N. Piliouras, N. Dimitropoulos, and G. Nikiforidis, "Development of a support vector machine-based image analysis system for assessing the thyroid

nodule malignancy risk on ultrasound," *Ultrasound in Medicine & Biology*, vol. 31, no. 11, pp. 1451–1459, 2005.

[21] M. A. Savelonas, D. E. Maroulis, D. K. Iakovidis, and N. Dimitropoulos, "Computer-aided malignancy risk assessment of nodules in thyroid US images utilizing boundary descriptors," in *Proceedings of the 12th Pan-Hellenic Conference on Informatics, PCI 2008*, pp. 157–160, Greece, August 2008.

[22] M. Savelonas, D. Maroulis, and M. Sangriotis, "A computer-aided system for malignancy risk assessment of nodules in thyroid US images based on boundary features," *Computer Methods and Programs in Biomedicine*, vol. 96, no. 1, pp. 25–32, 2009.

[23] I. Legakis, M. A. Savelonas, D. Maroulis, and D. K. Iakovidis, "Computer-based nodule malignancy risk assessment in thyroid ultrasound imageS," *International Journal of Computers and Applications*, vol. 33, no. 1, pp. 29–35, 2011.

[24] J. Salim, "Attia, Cytological Detection of Thyroid Cancer by Optical Image Analysis," *Journal of Natural Sciences Research*, vol. 5, no. 18, 2015.

[25] G. Zhang and V. L. Berardi, "An investigation of neural networks in thyroid function diagnosis," *Health Care Management Science*, vol. 1, no. 1, pp. 29–37, 1998.

[26] M. Malathi and S. Srinivasan, "Classification of Ultrasoud Thyroid Nodule Using Feed Forward Neural Network," *World Engineering Applied Sciences Journal*, vol. 8, no. 1, pp. 12–17, 2017.

[27] V. Vikram Hegde and N. Deepamala, "Automated Prediction of Thyroid Disease using," *ANN, IJIRSET*, vol. 5, no. Special Issue, May 2016.

[28] Y. LeCun, L. Bottou, Y. Bengio, and P. Haffner, "Gradient-based learning applied to document recognition," *Proceedings of the IEEE*, vol. 86, no. 11, pp. 2278–2323, 1998.

[29] N. Srivastava, G. Hinton, A. Krizhevsky, I. Sutskever, and R. Salakhutdinov, "Dropout: a simple way to prevent neural networks from overfitting," *Journal of Machine Learning Research*, vol. 15, no. 1, pp. 1929–1958, 2014.

[30] S. Aksoy and R. M. Haralick, "Feature normalization and likelihood-based similarity measures for image retrieval," *Pattern Recognition Letters*, vol. 22, no. 5, pp. 563–582, 2001.

[31] "Book Reviews : Signal Detection Theory and ROC Analysis in Psychology and Diagnostics : Collected Papers. By JOHN A. SWETS. Mahwah, NJ: Lawrence Erlbaum Associates, 1996, 308 pages, $54.95, hardbound," *Medical Decision Making*, vol. 19, no. 2, pp. 217-217, 2016.

[32] A. Krizhevsky, I. Sutskever, and G. E. Hinton, "Imagenet classification with deep convolutional neural networks," in *Proceedings of the 26th Annual Conference on Neural Information Processing Systems (NIPS '12)*, pp. 1097–1105, Lake Tahoe, Nev, USA, December 2012.

[33] R. M. Haralick, I. Dinstein, and K. Shanmugam, "Textural Features for Image Classification," *IEEE Transactions on Systems, Man, and Cybernetics*, vol. 3, no. 6, pp. 610–621, 1973.

[34] S. W. Zucker and D. Terzopoulos, "Finding structure in Co-occurrence matrices for texture analysis," *Computer Graphics and Image Processing*, vol. 12, no. 3, pp. 286–308, 1980.

[35] J. Chi, E. Walia, P. Babyn, J. Wang, G. Groot, and M. Eramian, "Thyroid Nodule Classification in Ultrasound Images by Fine-Tuning Deep Convolutional Neural Network," *Journal of Digital Imaging*, vol. 30, no. 4, pp. 477–486, 2017.

[36] L. Pedraza, C. Vargas, F. Narváez, O. Durán, E. Muñoz, and E. Romero, "An open access thyroid ultrasound-image Database," in *Proceedings of the 10th International Symposium on Medical Information Processing and Analysis*, Colombia, October 2014.

[37] A. Jaina, K. Nandakumara, and A. Rossb, "Score normalization in multimodal biometric systems," *Pattern Recognition*, vol. 38, no. 12, pp. 2270–2285, 2005.

Research Article

A High Frequency Geometric Focusing Transducer Based on 1-3 Piezocomposite for Intravascular Ultrasound Imaging

Xiaohua Jian, Zhile Han, Pengbo Liu, Jie Xu, Zhangjian Li, Peiyang Li, Weiwei Shao, and Yaoyao Cui

Suzhou Institute of Biomedical Engineering and Technology, Chinese Academy of Sciences, Suzhou, China

Correspondence should be addressed to Xiaohua Jian; simplejane1982@gmail.com and Yaoyao Cui; cuiyy@sibet.ac.cn

Due to the small aperture of blood vessel, a considerable disadvantage to current intravascular ultrasound (IVUS) imaging transducers is that their lateral imaging resolution is much lower than their axial resolution. To solve this problem, a single-element, 50 MHz, 0.6 mm diameter IVUS transducer with a geometric focus at 3 mm was proposed in this paper. The focusing transducer was based on a geometric-shaped 1-3 piezocomposite. The impedance/phase, pulse echo, acoustic intensity field, and imaging resolution of the focusing transducer were tested. For comparison, a flat IVUS transducer with the same diameter and 1-3 piezocomposite was made and tested too. Compared with their results, the fabricated focusing transducer exhibits broad bandwidth (107.21%), high sensitivity (404 mV), high axial imaging resolution (80 μm), and lateral imaging resolution (100 μm). The experimental results demonstrated that the high frequency geometric focusing piezocomposite transducer is capable of visualizing high axial and lateral resolution structure and improving the imaging quality of related interventional ultrasound imaging.

1. Introduction

Intravascular ultrasound (IVUS) allows us to see a coronary artery from the inside-out, which has evolved to an important research tool of modern invasive cardiology [1]. In order to get high resolution image, an IVUS transducer usually has a high center frequency (20~60 MHz) [2], like 20 MHz IVUS (Eagle Eye, Volcano Corporation), 40 MHz IVUS (OptiCross, Boston Scientific), and 60 MHz IVUS (Kodama, ACIST Medical Systems). A limitation to current IVUS transducer is that their lateral imaging resolution (200~300 μm) is much lower than their axial resolution (40~100 μm) [3, 4]. This is mainly caused by its small dimension [5, 6], which is extremely limited by the blood vessel.

Usually higher frequency transducer can provide higher lateral resolution, but it will cause a higher attenuation and decrease penetration capability. For example, to get 100 μm lateral resolution at 3 mm, the central frequency of a 0.6 mm diameter IVUS transducer needs to be more than 100 MHz, so it is not a very efficient method. Another possible method to a single-element IVUS transducer is synthetic aperture focusing, which has been shown to be able to improve the

imaging resolution and SNR outside focus area by focusing the received signal from several emissions for rotating movements [7]. But it requires large sum data processing and decreases the imaging frame rate. Therefore, it is beneficial to try focusing transducer to get high lateral resolution IVUS image. The traditional method is to use acoustic lens, but fabricating a suitable acoustic lens to focus the ultrasound on IVUS is particularly challenging, since the IVUS catheter outer diameter is limited in the range of 3F~9F (1 mm~ 3 mm), and the focusing length should be smaller than the coronary artery diameter (3~5 mm).

Therefore, self-focusing transducer will be a good choice. Fresnel Half-Wave-Band sources method was widely used for self-focusing, but its radius will be larger than 3 mm for getting better performance with enough loops at 20~60 MHz [8]. One possible method is to fabricate high frequency PMN-PT single crystal focusing transducer by a mechanical dimpling technique. The reported dimpled 30 MHz single crystal focusing transducer with a diameter of 1.6 mm can prove 139 μm lateral resolution [9]. Similarly, oblong-shaped focused IVUS transducers using PZT were also able to

Table 1: The design parameters of 1-3 piezocomposite.

Frequency	Kerf width	Pillar width	Composite thickness	Volume fraction
50 MHz	12 μm	18 μm	33 μm	36%

improve the lateral resolution [10]. Angled-focused single-element transducer was another choice to improve IVUS lateral imaging resolution. As reported, the lateral resolution was improved from 270 μm to 120 μm with the angled-focused 45 MHz PMN-PT single-element transducer [11]. But the single crystal or PZT are fragile and easy to crack in the process, which would affect the transducer performance and yield, while 1-3 piezocomposite will be an alternative choice for the active material, which can have high frequency, low acoustic impedance, and wide bandwidth [12, 13]. It has been reported for IVUS imaging and other high frequency endoscopic ultrasound imaging research [14–16]. There are many advantages to use a 1-3 piezocomposite as the IVUS transducer active substrate. First of all, the acoustic impedance of a 1-3 piezocomposite is significantly lower than common pure bulk ceramic, which can effectively decrease the acoustic mismatch between transducer and tissue and avoid the need for more matching layers [17, 18]. Secondly, the electromechanical coupling coefficient of 1-3 composite is much higher than common piezoelectric ceramic, which is helpful to improve the imaging sensitivity. Furthermore, 1-3 piezocomposite consists of a large percentage epoxy, which made it easy to be geometrically shaped. Therefore, 1-3 piezocomposite was suitable for making geometric focusing IVUS transducer. Even in an early patent, the related proposal has been described [14]. Therefore, in this paper we proposed a geometric focusing 50 MHz piezocomposite transducer for intravascular ultrasound imaging. For comparing, a flat IVUS transducer with the same 1-3 piezocomposite was also fabricated and tested following the same experiments; the results are described below in more detail.

2. Design and Fabrication

The focal length of the transducer was designed to 3 mm, which is close to the natural focus F corresponding to the near field range of flat IVUS transducer [5]:

$$F = \frac{D^2}{4\lambda}, \qquad (1)$$

where the diameter D of the transducer is 0.6 mm, the wavelength λ is about 30 μm in our situation, and then the natural focal length of flat IVUS transducer is about 3 mm.

The first step in the fabrication procedure was to make a high frequency 1-3 piezocomposite. Considering our laboratory experimental facilities, the design parameters of the 1-3 composite were listed in Table 1.

A two-dice and filling process was applied to fabricate this 1-3 composite. Firstly, a grid pattern was diced into a ceramic PZT-5H with 500 μm thickness using a 12 μm dicing saw. The depth of cuts is about 120 μm, and the pitch is 60 μm.
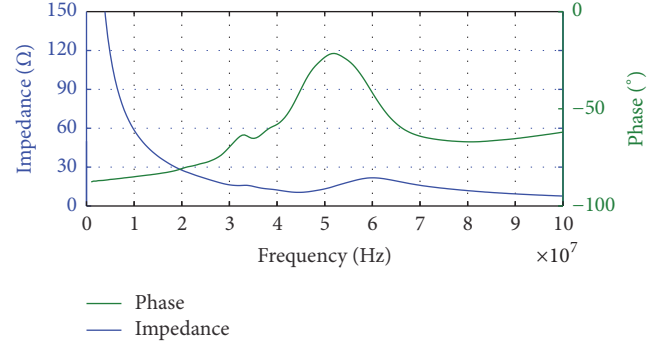

Figure 1: The measured impedance/phase of fabricated 1-3 piezocomposite.

The cuts were then filled with epoxy (Epo-Tek 301-2, Epoxy Technologies, Billerica, MA). After curing, the second set of cuts was made through the center of the PZT-5H pillars to create a composite pattern with 18 μm pillars and 12 μm kerfs as designed. The composite was filled and cured with Epo-Tek 301-2 again and then lapped to 33 μm thick. After that, a 200 Å chrome/gold layer as the electrode was sputtered.

The electrical impedance of fabricated 1-3 piezocomposite was measured with an impedance analyzer E4991A (1 MHz~ 3 GHz, Agilent Technologies, USA), just as Figure 1 shows. The measured center frequency is 52.76 MHz.

Its electromechanical coupling coefficient K_t can be calculated as [15]

$$K_t = \sqrt{\frac{\pi}{2} \times \frac{f_s}{f_p} \times \tan\left(\frac{\pi}{2} \times \frac{f_p - f_s}{f_p}\right)}, \qquad (2)$$

where f_p is the parallel resonant frequency at which the resistance reaches the maximum and f_s is the resonant frequency at which the conductance reaches the minimum. For our sample, f_s is 44.05 MHz and f_p is 60.36 MHz, so according to (2), K_t is about 0.70, which was higher than pure bulk ceramic (~0.5).

In the shaping process, the composite was firstly heated at 60°C for 1 hour to make it more flexible and then quickly mounted on a 3 mm radius PTFE ball with wax. The PTFE ball was used as the curving jig, which decides the focal length of the transducer. Conductive silver epoxy E-Solder 3022 was applied to the composite as the backing material in a PDMS (polydimethylsiloxane) mold. After curing at room temperature, the sample was heated to remove the PTFE ball. Then the sample was diced into the size of 0.6 mm × 0.6 mm. The individual piece was placed in a 1.2 mm diameter needle housing; the center core and mesh wire of a coaxial wire were connected to the piezocomposite surface and backing layer, respectively, with silver conductive. The gap between the transducer and the stainless steel needle was filled in by an insulating epoxy. At last, a 9 μm Parylene C layer was coated as its matching layer. The final fabricated focusing transducer was shown in Figure 2.
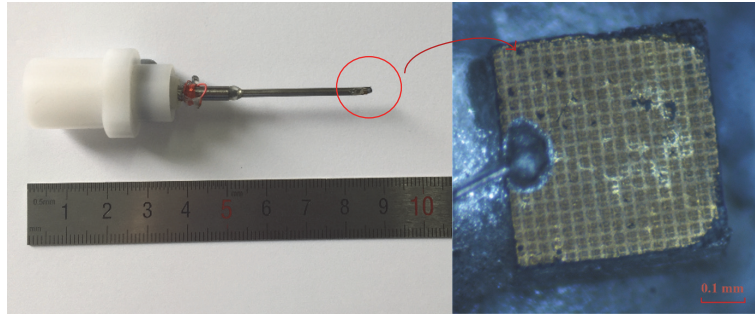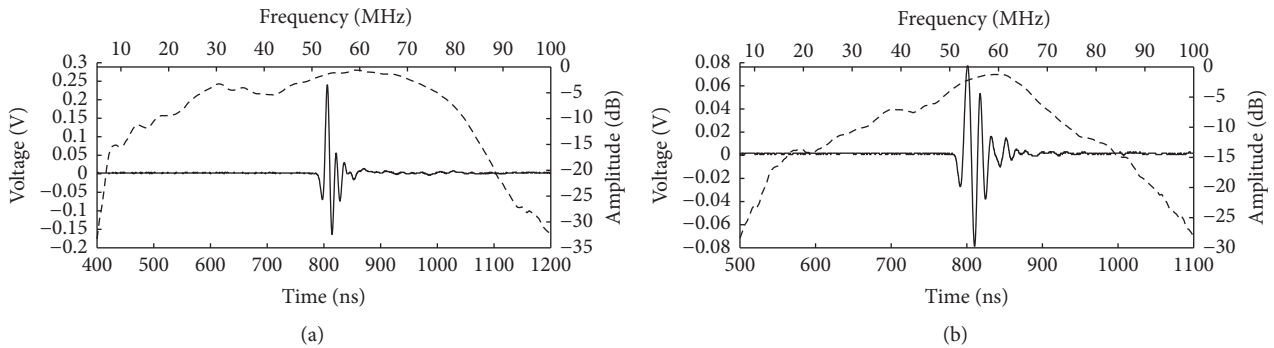
Figure 2: The fabricated focusing IVUS transducer.

(a)

(b)

Figure 3: Pulse echo response and spectrum of (a) fabricated focusing IVUS transducer and (b) fabricated flat IVUS transducer.

3. Results and Discussion

A DPR500 (pulse amplitude: 90 V, gain: 0 dB, filter: 5~ 300 MHz, RPF: 200 Hz, JSR Ultrasonics, USA) was used as the pulser-receiver to measure the center frequency, −6 dB bandwidth, and pulse echo amplitude of the fabricated focusing transducer and flat transducer. The pulse echo response was measured by recording the reflection from a quart polyethylene plastics flat placed at 3 mm in front of the transducer. The measured center frequency is 51.78 MHz, the −6 dB bandwidth is 107.21%, and the pulse half width is 17.37 ns just as Figure 3(a) shows. And the transducer pulse echo amplitude was measured as 404 mV with 50 Ω coupling impedance setting. For comparison, a flat IVUS transducer (unfocused) with the same diameter 0.6 mm was fabricated. This flat transducer was composed of the same 1-3 piezocomposite material, a Parylene C matching layer, and E-Solder 3022 backing layer. According to its pulse echo waveform and corresponding frequency spectrum as shown in Figure 3(b), its measured center frequency, −6 dB bandwidth, pulse half width, and amplitude were 53.77 MHz, 64.77%, 29.86 ns, and 156 mV, respectively.

The acoustic distribution was measured by a 3D scanning system UMS III (scan step resolution 0.001 mm, Precision Acoustics Ltd., Dorchester, UK) with a specially calibrated HGL-0085 hydrophone (20~60 MHz), as shown in Figure 4.

The hydrophone measurement step size was 30 μm. The acoustic intensity distribution of this fabricated transducer along z-axis was measured as shown in Figure 5. For avoiding the collision between the tested hydrophone and transducer,

the recorded data was beginning at 0.5 mm away from the transducer. The measured focal length along the axial direction is 2.98 mm, which is very close to the designed focal length 3 mm. While the intensity of a flat IVUS transducer oscillates sharply in the near field range, then because of the attenuation, it will decrease linearly with the distance.

Because the lateral resolution is determined by the beam width perpendicular to the direction of wave propagation in an imaging plane, the transducer's acoustic intensity distributions in the focal plane (X-Y plane) were scanned with UMS III. According to the focal plane result in Figure 6(a), the diameter of the focal point of the fabricated focusing IVUS transducer (at −6 dB) is about 100 μm, which is one-third of the flat IVUS transducer's 300 μm, just as Figure 6(b) shows. These results indicate that the focusing IVUS transducer can achieve a higher lateral imaging resolution than usual flat ones.

The imaging resolution was tested by our IVUS system [16]. The transducer was fixed on the top of a catheter, and the catheter is driven by a motor, which is in the IVUS catheter interface module (CIM), to do a rotary scan. The block diagram of CIM is shown in Figure 7(b). A single-element rotary scanning catheter is utilized to fix and rotate the transducer, which can spin at a speed of 1800 RPM. In the CIM, a contactless coupler with a flatten transfer curve from 10 to 110 MHz with an attenuation better than −1 dB is designed and manufactured to transfer high frequency signals between rotary and stationary side. For each cycle the catheter have turned, a frame composed of 512 scan lines would be captured. 12 bits analog to digital converter rate with
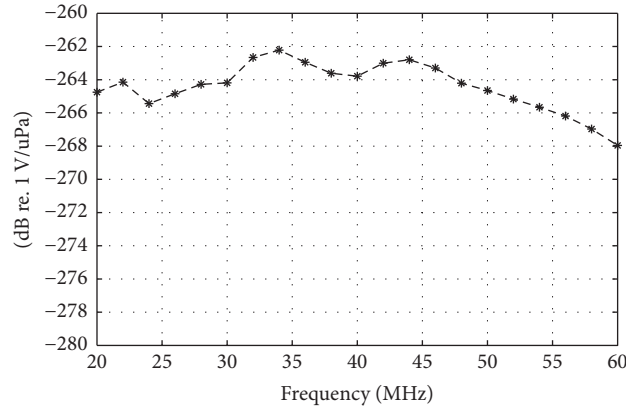
FIGURE 4: The response of HGL-0085 hydrophone with special calibration in the range of 20~60 MHz. Measurement uncertainty: 20~40 MHz, 2.2 dB; 40~60 MHz, 3.0 dB.
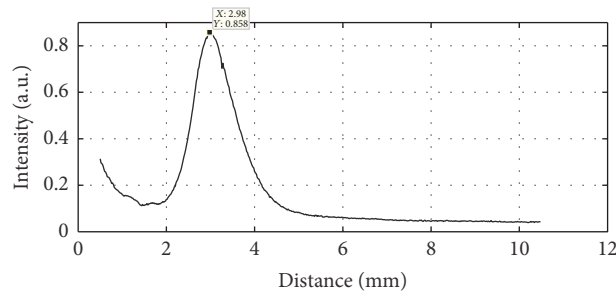

FIGURE 5: The acoustic intensity distribution of fabricated focusing IVUS transducer along z-axis.
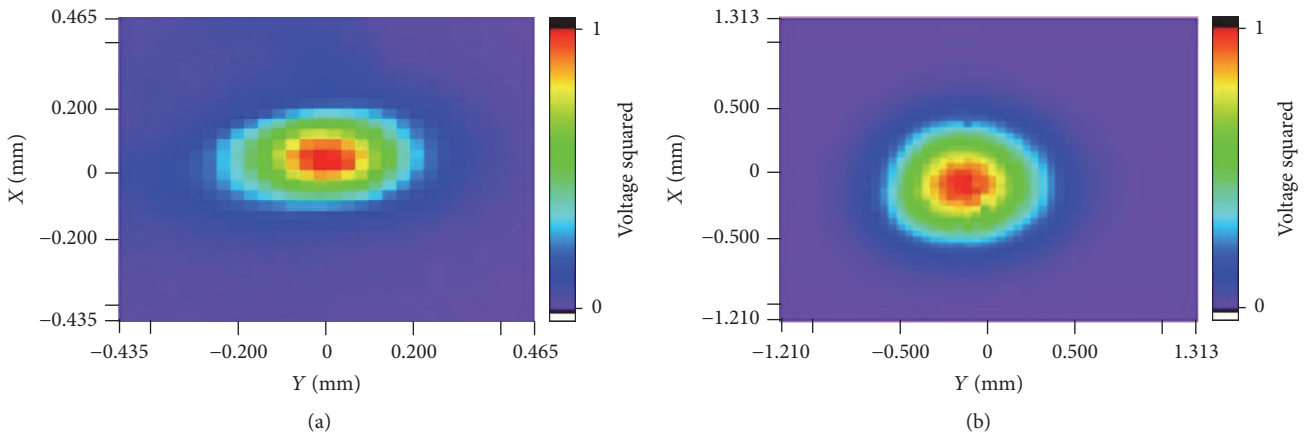

(a)

(b)

FIGURE 6: Measured acoustic intensity distribution of (a) fabricated focusing IVUS transducer; (b) fabricated flat IVUS transducer in the natural focus plane (X-Y plane).

a sampling rate of 220 MSPS ensure the echo information in enough frequency range could be recorded and provide a 25 fps imaging speed. More details of our IVUS system can be found in our published [16].

The imaging targets were some resolution test jigs with fixed interval tungsten wires, including 50 μm, 60 μm, 70 μm, 80 μm, 90 μm, 100 μm, 200 μm, 300 μm, and 400 μm, just as Figure 8 shows. The diameter of tungsten wires is 10 μm. When testing the axial resolution, the transducer was adjusted to be perpendicular to the wire phantom, while

for lateral resolution testing it will be parallel to the wire phantom, just as Figure 7(a) shows. For getting the best lateral resolution, the distance between the phantom wires and transducer was set to be 3 mm just as the focal length.

Figure 9 showed the lateral resolution testing results of the fabricated focusing and flat IVUS transducer, respectively. The bright arcs in the images represent the tungsten wires, while the center black hole and rings are caused by the transducer rotating. When using the 100 μm interval tungsten wire phantom, the image of three tungsten wires is only a
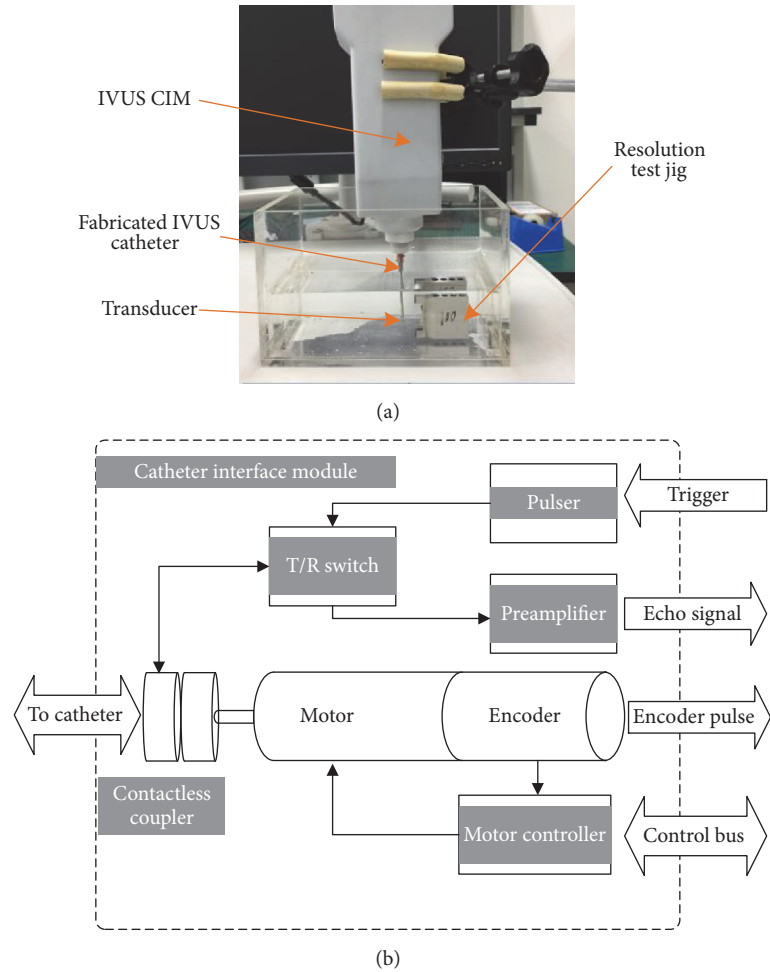
(a)

(b)

FIGURE 7: The imaging resolution test system: (a) experimental setup and (b) the block diagram of IVUS CIM (catheter interface module) [16].
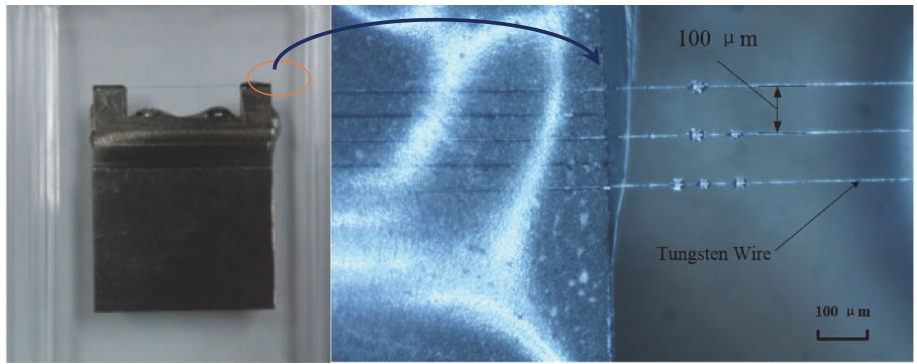

FIGURE 8: The imaging resolution test jig and tungsten wire phantom (100 μm).

blurred curve in Figure 9(b) detected by the flat transducer. It is impossible to distinguish each line in this image. Until the 300 μm interval tungsten wire phantom was used, the lines can be clearly separated in detected image in Figure 9(c). Therefore, the lateral resolution of flat IVUS transducer is tested as 300 μm.

In the same way, the lateral resolution of fabricated focusing IVUS transducer is tested as 100 μm, just as Figure 9(a)

showed, which is three times of the flat IVUS transducer. That is because the lateral beam width is greatly reduced by adjusting the focal performance of focused transducer [19]. Therefore, it is beneficial to try focused transducer to get high lateral resolution IVUS image.

Similarly, Figures 10(a) and 10(b) showed the axial resolution testing images of the focusing and flat IVUS transducer, respectively. According to the results, the axial resolution of
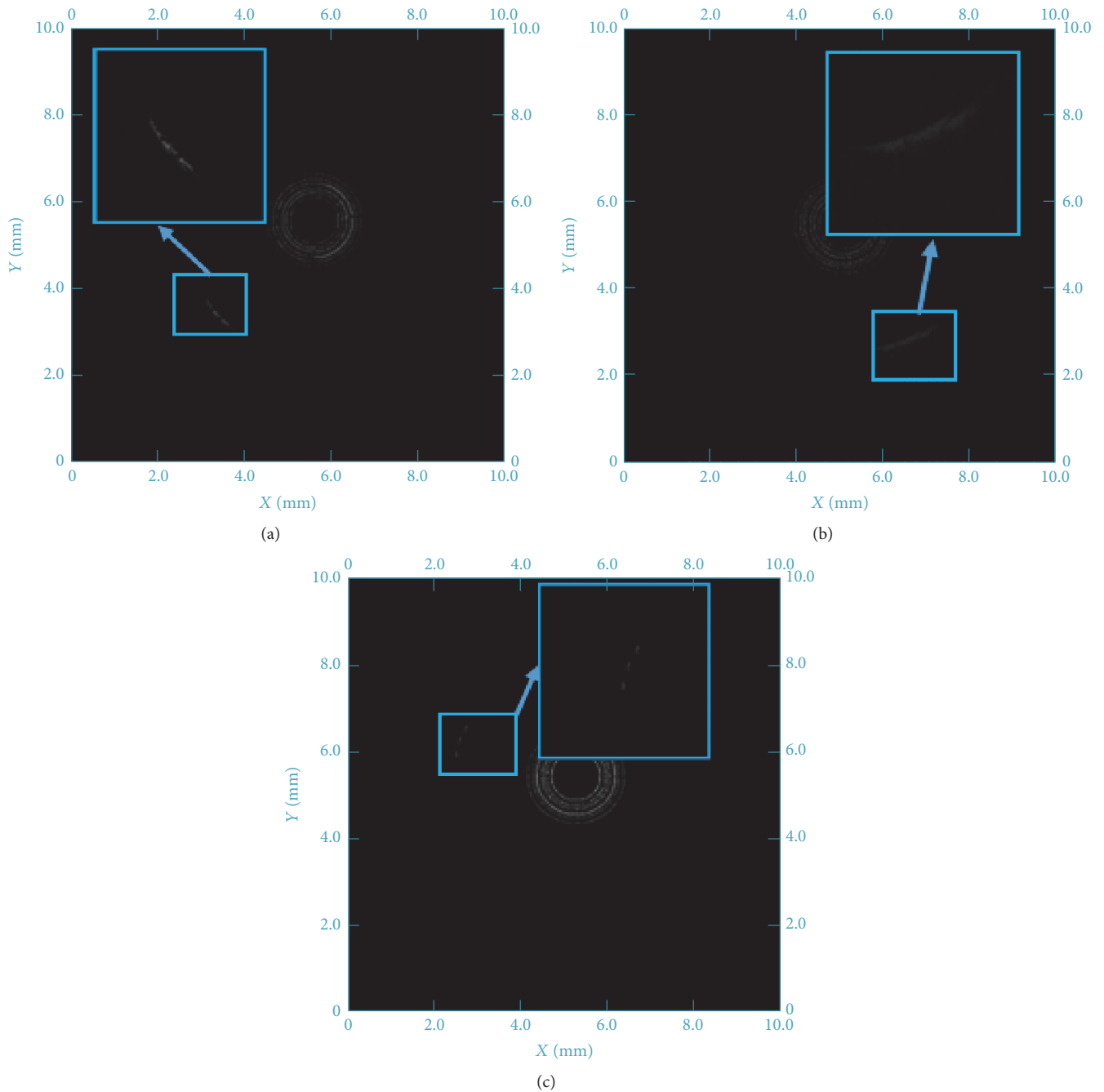
(a)

(b)

(c)

FIGURE 9: The lateral imaging resolution test images of (a) 100 μm interval tungsten wire phantoms with focusing IVUS transducer; (b) 100 μm interval tungsten wire phantoms with flat IVUS transducer; (c) 300 μm interval tungsten wire phantoms with flat IVUS transducer.

focusing IVUS transducer is 80 μm, and the flat IVUS transducer is 80 μm too. That is because the axial imaging resolution is mainly decided by center frequency of the transducer.

Furthermore, a hexagon hole phantom with 3 mm side length was used to test the imaging performance. The phantom was made by mixing 9 μm silicon carbide (2% by weight) and 3 μm aluminum oxide (2% by weight) with PDMS. When testing, the hexagon hole was filled with degas water, and the catheter distal with transducer was immersed into the hole. Figure 11 shows the phantom images detected by the fabricated focusing and flat IVUS transducer, respectively. Two images were both displayed in 12 dB dynamic range. Because of the high resolution and sensitivity, it is obvious that the image obtained by the focusing IVUS transducer was more clear and in a better shape. Particularly, the average contrast with respect to the locations of boundary and background in the images obtained by focusing and flat IVUS transducer were −13.1 dB and −16.2 dB, respectively.

(a)

(b)

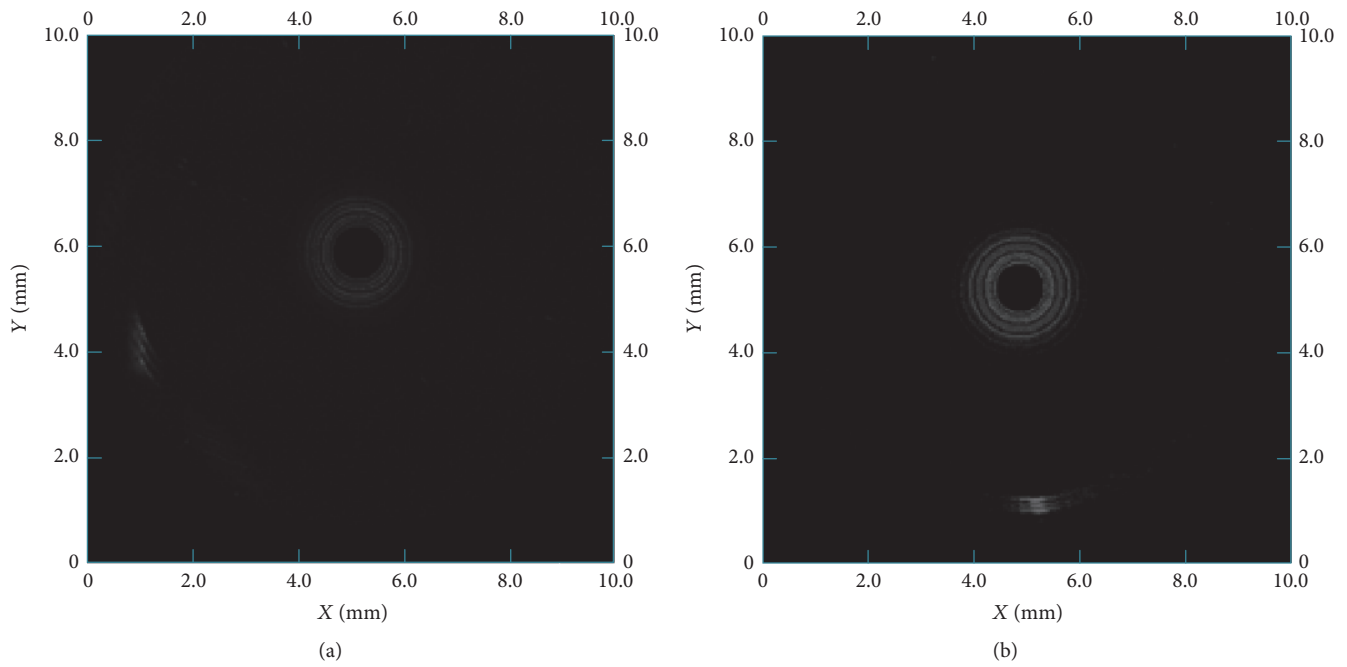FIGURE 10: The axial resolution test images of 80 μm interval tungsten wire phantoms with (a) focusing IVUS transducer and (b) flat IVUS transducer.
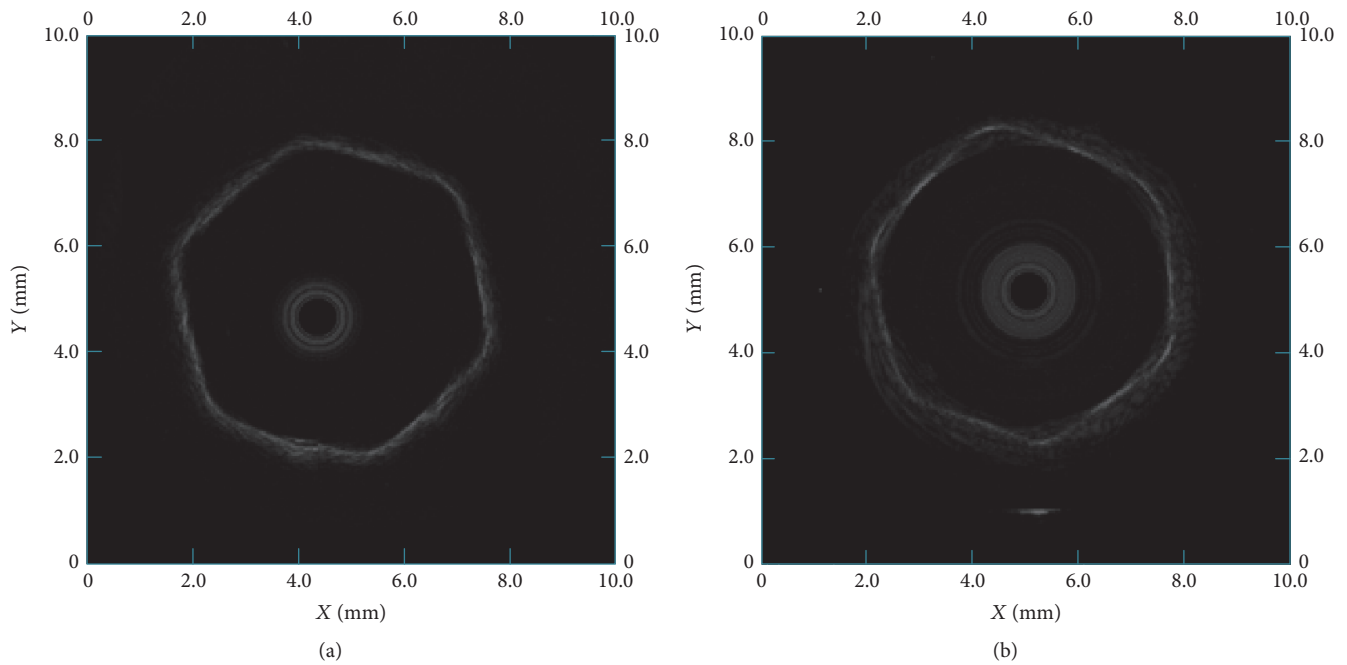

(a)

(b)

FIGURE 11: The image of hexagon phantom detected by (a) focusing IVUS transducer and (b) flat IVUS transducer.

At last, the main testing results were summarized in Table 2.

4. Conclusion

In this study, a micro high frequency IVUS transducer with spherical focusing was successfully produced using PZT/epoxy 1-3 composite. The prototyped focusing IVUS transducer has a small size (0.6 × 0.6 mm), short focal length (3 mm), and high lateral imaging resolution (100 μm). The image obtained by our homemade IVUS system with the fabricated focusing transducer had a high signal to noise ratio and image quality. Based on these results, this micro high frequency focusing transducer has the potential for

Table 2: The comparison of measured focusing and flat IVUS transducer performance.

Properties	Flat IVUS transducer	Focusing IVUS transducer
Center frequency	53.77 MHz	51.78 MHz
Aperture	0.6 mm	0.6 mm
Bandwidth	64.77%	107.21%
Echo peak	156 mV	404 mV
Axial resolution	80 μm	80 μm
Lateral resolution	300 μm	100 μm

intravascular ultrasound imaging and various high frequency endoscopic ultrasound imaging.

Conflicts of Interest

The authors declare that there are no conflicts of interest regarding the publication of this paper.

Acknowledgments

References

[1] B. N. Potkin, A. L. Bartorelli, J. M. Gessert et al., "Coronary artery imaging with intravascular high-frequency ultrasound," *Circulation*, vol. 81, no. 5, pp. 1575–1585, 1990.

[2] P. Schoenhagen, A. DeFranco, S. Nissen, and E. Tuzcu, *IVUS Made Easy*, CRC Press, 2005.

[3] F. Prati, E. Regar, G. S. Mintz et al., "Expert review document on methodology, terminology, and clinical applications of optical coherence tomography: physical principles, methodology of image acquisition, and clinical application for assessment of coronary arteries and atherosclerosis," *European Heart Journal*, vol. 31, no. 4, pp. 401–415, 2010.

[4] F. S. Foster, L. K. Ryan, and G. R. Lockwood, "High Frequency Ultrasound Scanning of the Arterial Wall," in *Intravascular Ultrasound*, Developments in Cardiovascular Medicine, pp. 91–108, Springer Netherlands, 1993.

[5] J. S. Suri, D. L. Wilson, and S. Laxminarayan, *Handbook of Biomedical Image Analysis*, Springer US, Boston, Ma, USA, 2005.

[6] S. Rhee, "High frequency (IVUS) ultrasound transducer technology - Applications and challenges," in *Proceedings of the 2007 16th IEEE International Symposium on the Applications of Ferroelectrics, ISAF*, pp. 856-857, jpn, May 2007.

[7] H. Andresen, S. I. Nikolov, and J. A. Jensen, "Synthetic aperture focusing for a single-element transducer undergoing helical motion," *IEEE Transactions on Ultrasonics, Ferroelectrics, and Frequency Control*, vol. 58, no. 5, pp. 935–943, 2011.

[8] D. Huang and E. S. Kim, "Micromachined acoustic-wave liquid ejector," *Journal of Microelectromechanical Systems*, vol. 10, no. 3, pp. 442–449, 2001.

[9] Y. Chen, K. H. Lam, D. Zhou et al., "High frequency PMN-PT single crystal focusing transducer fabricated by a mechanical dimpling technique," *Ultrasonics*, vol. 53, no. 2, pp. 345–349, 2013.

[10] J. Lee, J. Jang, and J. H. Chang, "Oblong-Shaped-Focused Transducers for Intravascular Ultrasound Imaging," *IEEE Transactions on Biomedical Engineering*, vol. 64, no. 3, pp. 671–680, 2017.

[11] S. Yoon, J. Williams, B. J. Kang et al., "Angled-focused 45 MHz PMN-PT single element transducer for intravascular ultrasound imaging," *Sensors and Actuators, A: Physical*, vol. 228, pp. 16–22, 2015.

[12] X. Li, T. Ma, J. Tian, P. Han, Q. Zhou, and K. K. Shung, "Micromachined PIN-PMN-PT crystal composite transducer for high-frequency intravascular ultrasound (IVUS) imaging," *IEEE Transactions on Ultrasonics, Ferroelectrics, and Frequency Control*, vol. 61, no. 7, pp. 1171–1178, 2014.

[13] J. R. Yuan, X. Jiang, P.-J. Cao et al., "High frequency piezo composites microfabricated ultrasound transducers for intravascular imaging," in *Proceedings of the 2006 IEEE International Ultrasonics Symposium, IUS*, pp. 264–268, can, October 2006.

[14] J. Yuan, P. Cao, and R. Romley, "Piezocomposite transducers," 2006, Google Patents.

[15] A. Safari and E. K. Akdoğan, "Piezoelectric and acoustic materials for transducer applications," *Piezoelectric and Acoustic Materials for Transducer Applications*, pp. 1–481, 2008.

[16] Y. Xiang, J. Xu, T. Lv, T. Gu, Z. Han, and Y. Cui, "A graphic processing unit based intravascular ultrasound (IVUS)," in *Proceedings of the IEEE International Ultrasonics Symposium, IUS 2015*, twn, October 2015.

[17] J. A. Brown, F. S. Foster, A. Needles, E. Cherin, and G. R. Lockwood, "Fabrication and performance of a 40-MHz linear array based on a 1-3 composite with geometric elevation focusing," *IEEE Transactions on Ultrasonics, Ferroelectrics, and Frequency Control*, vol. 54, no. 9, pp. 1888–1894, 2007.

[18] X. Jiang, J. R. Yuan, A. Cheng et al., "Microfabrication of piezoelectric composite ultrasound transducers (PC-MUT)," pp. 918–921.

[19] Y. Saijo and A. F. W. Van der Steen, *Vascular ultrasound*, Springer Science and Business Media, 2003.